UNIVERSITY OF CALIFORNIA

Santa Barbara

Quantifying the distribution of time in sedimentary basins: integrative approaches and applications

A dissertation submitted in partial satisfaction of the requirements for the degree Doctor of Philosophy in Earth Science

by

Eliel Simpson Clendenin Anttila

Committee in charge:

Professor Francis A. Macdonald, Chair

Professor John Cottle

Professor Susannah Porter

June 2024

The dissertation of Eliel Simpson Clendenin Anttila is approved.

_____

John Cottle

_____

Susannah Porter

_____

Francis A. Macdonald, Committee Chair

February 2024

Quantifying the distribution of time in sedimentary basins:

integrative approaches and applications

Eliel Simpson Clendenin Anttila

ACKNOWLEDGEMENTS

The work summarized in the following dissertation reflects an unforgettable array of experiences, adventures, and opportunities, all of which were made possible by a community of scientists, colleagues, friends, and family to whom I am exceedingly grateful.

I thank my advisor, Francis Macdonald, for his boundless and infectious enthusiasm for geology, his scientific creativity and critical eye, and for his support, advice, and motivation throughout my graduate school experience. I deeply appreciate the opportunities to become fully immersed in some of the most beautiful and interesting corners of the world, to expand my scientific network and skillset, and to cut my teeth as a scientist in a learning environment with enough freedom to make (and correct) my own mistakes, but with enough guidance to never feel isolated.

I thank my committee members, John Cottle and Susannah Porter, for their insight and guidance throughout my graduate school experience. I thank Nicholas Swanson-Hysell, Michael Manga, Dave Johnston, Ann Pearson, Blair Schoene, Dawid Szymanowski, Uyanga Bold, Davey Jones, Paul Renne, Steve Self, Jim Boles, Sean Mulcahey, Brad Hacker, Phil Gans, Andrew Kylander-Clark, and Gareth Seward and many others for inspiration, mentorship, and for being scientific and academic role models at crucial points throughout my undergraduate and graduate school experience.

Thanks to Judy Pu, Adrian Tasistro-Hart, and Sam LoBianco for being the best lab mates I could have asked for. I thank Erdene Baiarsaikhan, Ekv Erdene, and Mogi for being my Mongolian field family whom I trust implicitly, respect deeply, and miss greatly; I hope to see you all again soon. Thank you to the Erdene family for welcoming us into your home with such generosity and kindness; the hospitality and resourcefulness of the people around

Lake Khuvsgul was truly incredible, and I am so thankful to have experienced this part of the world through such a positive lens.

Thank you to Ryan Eden, Alex Wrobel, Devin Rand, Cameron Gernant, Chandler Adamaitis, Jeremy Francour, Paul Alessio, Yiming Zhang, Cansu Culha, Mason Perry, Ian Ekblaw, Michael Chamberlain, and so many others for the adventures, debates, fish, and countless waves.

I will always be grateful for the places and experiences that geology has ushered into my life over the past few years: the constantly evolving, perennially stunning California coastline and Channel Islands; the aspens, sage, and thunderstorms of eastern Nevada; the curiously familiar sights, sounds, and smells of Tigray and Addis Ababa; the bright southern hemisphere constellations above the Namibian desert; the first rays of sun over the Khoridol Saridag Range to start another long Mongolian summer day. I loved it all.

To my parents: thank you for your love, your unwavering support of all my endeavors, your timely, wise, and honest advice, and for living with conviction and purpose; I will always look up to you.

To my best friend, confidant, and wife, Ellen: thank you for being the brightest part of my day, for your sage insights, level head, and boundless kindness, and for your constant curiosity and hunger to explore the ends of the world and everything in between… we'll go there together. Te amo!

CURRICULUM VITAE OF ELIEL SIMPSON CLENDENIN ANTTILA
June 2024

Education

University of California, Santa Barbara *Santa Barbara, CA* Aug. 2018 – Jun. 2024 (expected)
Ph.D. Candidate, Department of Earth Science
Thesis: Quantifying the distribution of time in sedimentary basins: integrative approaches and applications
Advisor: Francis Macdonald

Harvard University *Cambridge, MA* Aug. 2017 – Aug. 2018
Graduate Student Researcher, Department of Earth and Planetary Sciences
Advisor: Francis Macdonald

University of California, Berkeley *Berkeley, CA* Aug. 2012 – May 2016
B.A. in Geology with Highest Honors, Department of Earth and Planetary Science
Thesis: Newly differentiated Neoproterozoic strata in Tigray, Ethiopia
Advisor: Nicholas Swanson-Hysell

Publications

In preparation:

9. **Anttila, E.**, Cottle, J.M., and Macdonald, F.A. *Zircon Hafnium isotopes of the Coast Range Volcanics and provenance of ashfall tuffs in the Miocene Californian borderland.* In prep.

8. **Anttila, E.**, Swanson-Hysell, N., Macdonald, F.A. *Order from CAOS: Paleomagnetic constraints on the Tuva-Mongolian Terrane and implications for crustal growth in the Central Asian Orogenic System.* American Journal of Science, in prep.

In review:

7. **Anttila, E.**, Macdonald, F.A., Zinto, J., and Britt, M.D. *The Real McCoy: Great Unconformity source-to-sink on the rifted passive margin of Laurentia.* Earth and Planetary Science Letters.

6. **Anttila, E.**, Macdonald, F.A., Schoene, B., Gaynor, S., Baiarsaikhan, E., and Erdene, E., 2023. *Cambrian foreland phosphogenesis in the Khuvsgul Basin of Mongolia.* American Journal of Science.

Accepted and published:

5. **Anttila, E.**, Macdonald, F.A., Szymanowski, D., Schoene, B., Kylander-Clark, A., Danhof, C. and Jones, D.S., 2023. *Timing and tempo of organic carbon burial in the Monterey Formation of the Santa Barbara Basin and relationships with Miocene climate.* Earth and Planetary Science Letters, v.620, 118343.

4. **Anttila, E.**, Macdonald, F. and Bold, U., 2021. *Stratigraphy of the Khuvsgul Group, Mongolia*. Mongolian Geoscientist, 26(52), pp.2-15.

3. Park, Y., Maffre, P., Goddéris, Y., Macdonald, F.A., **Anttila, E.** and Swanson-Hysell, N.L., 2020. *Emergence of the Southeast Asian islands as a driver for Neogene cooling.* Proceedings of the National Academy of Sciences, 117(41), pp. 25319-25326.

2. Park, Y., Swanson-Hysell, N.L., MacLennan, S.A., Maloof, A.C., Gebreslassie, M., Tremblay, M.M., Schoene, B., Alene, M., **Anttila, E.**, Tesema, T. and Haileab, B., 2020. *The lead-up to the Sturtian Snowball Earth: Neoproterozoic chemostratigraphy time-calibrated by the Tambien Group of Ethiopia*. GSA Bulletin, 132(5-6), pp. 1119-1149.

1. MacLennan, S., Park, Y., Swanson-Hysell, N., Maloof, A., Schoene, B., Gebreslassie, M., **Anttila, E.**, Tesema, T., Alene, M. and Haileab, B., 2018. *The arc of the Snowball: U-Pb dates constrain the Islay anomaly and the initiation of the Sturtian glaciation.* Geology, 46(6), pp. 539-542.

Presentations

14. **Anttila, E.**, and Macdonald, F., Szymanowski, D., Schoene, B., Kylander-Clark., A., Danhof, C., and Jones, D., 2023. "A new chronostratigraphic framework for the Miocene Monterey Formation of the Santa Barbara Basin". Geochronology Gordon Research Conference.

13. ***Anttila, E.**, and Macdonald, F., Szymanowski, D., Schoene, B., Kylander-Clark., A., Danhof, C., and Jones, D., 2022. "A geochronologically-constrained test of the Monterey hypothesis for Miocene climate change". AAPG Pacific Section CGS Monterey Conference.

12. ***Anttila, E.**, and Macdonald, F., Szymanowski, D., Schoene, B., Kylander-Clark., A., and Jones, D., 2022. "Production vs. preservation: a geochronologically-constrained test of the Monterey hypothesis for Miocene climate change". GSA Fall Meeting. Paper 227-6.

11. **Anttila, E.**, and Macdonald, F., 2022. "Testing the Monterey Hypothesis: a new age and stratigraphic model for the Miocene Monterey Formation along the Santa Barbara Coast". SoCal Geobiology Conference.

10. ***Anttila, E.**, Macdonald, F., and Bold, U., 2021. "Phosphorites of the Khuvsgul Basin, Mongolia: Insights into the late Neoproterozoic to early Paleozoic phosphorus cycle". UC Santa Barbara Earth Science Department Colloquium.

9. ***Anttila, E.**, and Macdonald, F., 2021. "Testing the Monterey Hypothesis: a new age and stratigraphic model for the Miocene Monterey Formation along the central coast of California". GSA Fall Meeting. Paper 38-1.

8. ****Anttila, E.**, and Macdonald, F., 2020. "Cryogenian to Cambrian evolution of the phosphorite-bearing Khovsgol Basin, Mongolia". GSA Fall Meeting. Paper 174-17.

7. **Anttila, E.**, 2019. "Evolution of the Khovsgol Paleobasin: new geological mapping, chemostratigraphy, and geochronology from the Khovsgol Group, Mongolia." GSA Fall Meeting. Paper 123-26.

6. **Anttila, E.**, Macdonald F., 2019. "Geological context of phosphorite lagerstätten in the Khovsgol Group, Mongolia." SoCal Geobiology Conference.

5. ***Anttila, E.**, LoBianco, S.J., Brenner, A.R. and Macdonald, F.A., 2018. Neogene to present changes in CO2 sources and sinks due to the growth and tectonic evolution of Indonesia. AGU Fall Meeting. Abstra V51A-03.

4. ***Anttila, E.**, 2018. "Temporally and spatially constraining a Doushantuo-style microfossil-bearing phosphorite, Khubsugul Group, Mongolia." GSA Fall Meeting. Abstract 150-6.

3. **Anttila, E.**, Macdonald F., 2018. "Geological context of Cryogenian glacial deposits and Ediacaran phosphorite lagerstatten in the Khubsugul Group, northern Mongolia." Northeast Geobiology Conference.

2. ***Anttila, E.,** 2016. "New records of global change leading into the first Neoproterozoic snowball Earth event in Tigray, Ethiopia." UC Berkeley Earth and Planetary Science Undergraduate Honors Colloquium.

1. **Anttila, E.**, Wray, M., Knappe, E., Ogasawara, T., Tholt, A., Cliffe, B., Oshun, J., 2014: "Species type controls root strength and influences slope stability in coastal Ecuador." AGU Fall Meeting. Abstract EP31C-3582.

*oral presentation
**oral presentation, virtual only

Teaching Experience

Teaching Assistant, UCSB *EARTH 118 Summer Field Course* Summer 2021, 2022, 2023
Assisted with instruction during field mapping and other field exercises near Ely, NV and Santa Cruz Island, CA; integrated new digital mapping technology into curriculum

Teaching Assistant, UCSB *EARTH 104 Field Studies in Geological Methods* Spring 2021
Taught field skills, including digital mapping, section measurement, and sample collection, during field classes held in the Santa Ynez Mountains.

Teaching Assistant, UC Berkeley *EPS 118 Advanced Field Course* Summer 2016
Assisted with instruction during field mapping, geophysical surveys, and other field exercises near Bishop, CA

Teaching Assistant, UC Berkeley *EPS 101 Field Geology and Digital Mapping* Fall 2014, 2015
Taught field skills and map production/interpretation during twice-weekly field classes in the Berkeley Hills; assisted with implementation of new digital mapping technology into curriculum

Outreach experience

Externship mentor, Research Experience for Teachers, UCSB 2023-present
Trained and mentored a high school teacher during her participation in field and lab work associated with a current research project on the Monterey Fm; continued collaboration will result in the creation of a highschool-level course centered around observations made during field trips to Monterey Fm localities on the Central Coast of California.

Course design and co-instruction, School for Scientific Thought, UCSB Fall 2022
Designed, planned, and co-taught coursework ('*Geological Climate Change'*) targeted at highschool science students; coursework integrated field, laboratory, and classroom components to illustrate how geologists use a variety of observations and approaches to document, interpret, and model climate change in Earth's past, present, and future.

Mobile Science Educator, University of Montana Fall 2016 – Spring 2017
Designed and presented Earth science curriculum to schools (grades K-12) around the state of Montana

Mentoring experience

Trained and mentored students during their undergraduate thesis work with the Macdonald lab:

Caroline Newell – *Geochemical cyclostratigraphy of the Tonian Chuar Group, Grand Canyon* 2023
Joneel Zinto – *Detrital zircon geochronology of the McCoy Creek Group, Nevada* 2022
Brian Mo – *Carbon and oxygen isotope chemostratigraphy of the Monterey Formation, California* 2021
Camille Preece – *Detrital zircon geochronology of northern Mongolia* 2021

Funding

ETH Zürich Postdoctoral Fellowship *215,200 CHF* 2024
Earth Research Institute Graduate Research Fellowship *$5,203.00* 2020
NSF Graduate Research Fellowship Program *$132,000.00* 2017
UC Berkeley Summer Undergraduate Research Fellowship *$4,100.00* 2015
Evolving Earth Foundation Grant *$2,700.00* 2015
Charles H. Ramsden Scholarship *$1,050.00* 2014
Charles H. Ramsden Scholarship *$2,350.00* 2013

Awards and Honors

UCSB Department of Earth Science Graduate Student Opportunity Award 2022
SEPM/SDG Best Student Poster Winner, GSA Annual Meeting 2019
Departmental Citation, Department of Earth and Planetary Science, UC Berkeley 2016
Dean's Honors, UC Berkeley College of Letters and Science Fall 2016, Spring 2016
Co-President, Geological Association at Berkeley 2015 – 2016

ABSTRACT

Quantifying the distribution of time in sedimentary basins:

integrative approaches and applications

by

Eliel Simpson Clendenin Anttila

This dissertation utilizes a combination of field geology, geochronology, and geochemistry to contextualize stratigraphic and chemostratigraphic data in both time and space, and to assess the relative influence of local, regional, and global drivers on sedimentary records during periods of global change.

In my first project chapter, I develop a source-to-sink test of two prevalent hypotheses for the generation of the Great Unconformity by interrogating Tonian-Cambrian stratigraphic records from the distal Cordilleran margin of Laurentia. I utilize a combination of geological mapping, U-Pb zircon geochronology, and stable carbon isotope chemostratigraphy to build a new chronostratigraphic framework for the Tonian-Cryogenian Trout Creek Sequence and Ediacaran McCoy Creek Group of eastern Nevada and western Utah. Integration of these data into a tectonic subsidence model demonstrates that these strata were accommodated by a single rifting event and a Cryogenian transition to thermal subsidence on a passive margin. I show that the distal sedimentary record of western Laurentia records the progressive erosion of the Proterozoic sedimentary cover of Laurentia throughout the Tonian-Cambrian, consistent with extant thermochronological data documenting diachronous erosion and

exhumation across Laurentia over hundreds of millions of years along the Great Unconformity.

My next chapter utilizes similar observational and analytical approaches to assess putative drivers and mechanisms of phosphogenesis across the Ediacaran-Cambrian boundary. I amalgamate field observations, U-Pb zircon geochronology, and carbonate chemostratigraphy into a new stratigraphic framework, age model, and tectonostratigraphic model for the Cryogenian-Cambrian Khuvsgul Group of northern Mongolia, which hosts one of the largest sedimentary phosphate deposits on Earth. These data demonstrate that phosphorites of the Khuvsgul Group were deposited in a proforeland basin between 534-531 Ma, and that tectonically-mediated basinal evolution and paleotopography controlled the timing, locus, and style of phosphogenesis in the Khuvsgul region. Furthermore, this work suggests that taphonomic effects associated with redox-mediated shifts in phosphogenic environment, rather than changes in marine phosphate concentration, were responsible for the apparent global increase in phosphorite abundance across the Ediacaran-Cambrian boundary.

In my final thesis chapter, I present a radiometrically-constrained test of hypotheses linking organic carbon burial in circum-Pacific basins to Miocene climate change. I utilize high-precision U-Pb zircon geochronology to generate a new chronostratigraphic framework for the organic-carbon-rich Miocene Monterey Formation of central California, which I combine with total organic carbon data to constrain the timing and tempo of organic carbon burial in the Monterey Formation. Rather than driving climate, organic carbon burial in the Monterey Formation was controlled by changes in sedimentation rate, which was in turn controlled by a combination of local tectonics and eustasy. Thus, I demonstrate that organic carbon deposition in the Monterey Formation was largely a response to basin formation and climate change.

TABLE OF CONTENTS

LIST OF FIGURES

CHAPTER II

CHAPTER III, PART 1

CHAPTER III, PART 2

CHAPTER IV

LIST OF TABLES

CHAPTER II

CHAPTER III, PART 1

CHAPTER I. FOREWORD

1.1. Introduction

The stratigraphic record provides our best window, albeit inherently fragmented, into Earth history. The rock record hosts physical and chemical signatures of myriad events at a variety of scales, including nonuniformitarian changes in biology, surface chemistry, and global climate that represent fundamental shifts in the evolution of our planet. Some of the most valuable and information-rich records of Earth surface processes, including evidence of global change, are hosted by sedimentary strata. However, all sedimentary records of global change have been influenced, to varying degrees, by the local, regional, and marginal processes inherent to the basin in which those sediments were deposited. An understanding of these processes, and their relative influence on the observed features of a given sedimentary sequence, is therefore critical to a holistic interpretation of the stratigraphic record.

In this dissertation, I leverage a combination of field geology, geochemistry, and geochronology to explore, contextualize, and constrain sedimentary basins containing the stratigraphic records of three distinct phenomena (the generation of the Great Unconformity, the Ediacaran-Cambrian increase in phosphorite abundance, and the Miocene burial of organic carbon in circum-Pacific basins) that have been previously associated with global change. I develop four-dimensional (three-dimensional space, plus time) geological context to parse the impact of local, regional, and global drivers on the stratigraphic records hosted by each basin, provide mechanistic explanations for the observed features of those stratigraphic records, and generate quantitative constraints on each record that improve our

understanding of the relationships between each phenomenon and the respective global changes to which they have been previously linked.

In **Chapter II,** I utilize the distal sedimentary record of western Laurentia to test two distinct hypotheses for the generation of the Great Unconformity. The temporal and physical gap encompassed by the Great Unconformity, which juxtaposes Proterozoic crystalline basement of the cratonic core of North America (Laurentia) with overlying Paleozoic sedimentary strata, has been proposed to be associated with widespread sub-glacial erosion (Keller et al., 2019; McDannell et al., 2022; McDannell and Keller, 2022) across Laurentia during the global Cryogenian Snowball Earth glaciations (Kirschvink, 1992; Hoffman and Schrag, 2002; Hoffman et al., 2017). Alternatively, thermochronologic data supports diachronous geodynamically and tectonically forced exhumation and erosion of Laurentia through the late Neoproterozoic and Cambrian (Flowers et al., 2020; Macdonald et al., 2022; Sturrock et al., 2021; Peak et al., 2023). Both hypotheses provide discrete predictions for the timing and tempo of the delivery of eroded material to the accommodation space provided by marginal basins surrounding Laurentia. However, a test of these predictions is complicated by evidence of active rifting along Laurentian margins during the Cryogenian, necessitating the characterization of the tectonic setting and basinal evolution of the Laurentian margin in question.

To achieve this, I combine geological mapping and field observations with U-Pb zircon geochronology and $\delta^{13}C$ chemostratigraphy to constrain the age, depositional setting, and tectonostratigraphic history of the Trout Creek Sequence and McCoy Creek Groups of northeastern Nevada and western Utah. I show that these strata were deposited on the

Tonian-Cambrian distal western margin of Laurentia, and that this margin experienced Cryogenian rifting and a ca. 650 Ma transition to a long-lived thermally subsiding passive margin. Within this marginal and basinal context, I demonstrate that sedimentation rates during the Cryogenian global glaciations were meagre, providing a negative test of sub-glacial erosion hypotheses for the generation of the Great Unconformity. Instead, the distal stratigraphic record of western Laurentia is consistent with the prolonged erosion and removal of the Proterozoic sedimentary cover of North America, corroborating hypotheses for the diachronous development of the Great Unconformity over hundreds of millions of years.

In **Chapter III**, I explore the nature of the global increase in the appearance of ore-grade sedimentary phosphorus deposits, known as phosphorites, in the Ediacaran and Cambrian stratigraphic record. This apparent increase in phosphorite abundance has been tied to putatively concomitant global increases (Papineau, 2010) in the marine abundance of phosphate, a limiting nutrient for bioproductivity (Tyrell, 1999), with associated implications for the oxygenation of Earth's surface (Reinhard et al., 2017; Laakso et al., 2020) and the rise and diversification of animals (Shields et al., 2000). However, sedimentological (Föllmi, 1990; Föllmi et al., 2017), paleotopographic (Föllmi et al., 2017), and biogenic (Sanders, 2023; Schultz and Schultz, 2005) factors can also control the locus and style of phosphorite deposition. Moreover, the ages of many late-Neoproterozoic and early Phanerozoic phosphorites remain uncertain, calling into question the assertion of a synchronous global rise in phosphogenesis in the Ediacaran-Cambrian boundary.

For my second project, I constrain the age, depositional environment, and tectonostratigraphic context of the Khuvsgul Group of Mongolia, which hosts one of the largest sedimentary phosphate ore bodies in the world. In **Chapter III, Part 1,** I establish a new stratigraphic framework for the Khuvsgul Group and adjacent stratigraphy to streamline the geologic mapping and stratigraphic work required to characterize Khuvsgul Group exposures in the remote mountains of northern Mongolia. In **Chapter III, Part 2**, I amalgamate three seasons of field work, an extensive $\delta^{13}C$ chemostratigraphic framework, and U-Pb zircon geochronology to create new models for the age, depositional environment, and tectonic setting of the Khuvsgul Group. The phosphorites of the Kheseen Formation of the Khuvsgul Group, which host a Doushantuo-Pertatataka-Type microfossil assemblage, were deposited in a pro-foreland basin ca. 534-531 Ma. I show that tectonically-mediated basinal topography was a key factor in determining the locus and timing of primary phosphogenesis, which occurred along the crest of a migrating forebulge in the Khuvsgul pro-foreland. Incorporation of the newly-constrained Kheseen phosphatic strata into a compilation of Ediacaran and Cambrian phosphorites demonstrates the diachroneity of phosphogenesis throughout the Proterozoic-Phanerozoic transition. Rather than an increase in nutrient delivery to the oceans, I suggest that the rise in phosphorite abundance in this portion of the stratigraphic record reflects the opening of a taphonomic window in which the increasing redox potential of Earth's surface favored phosphate accumulation, dominantly controlled by tectonically-mediated paleotopography and sedimentological processes, in marginal marine environments.

In **Chapter IV,** I develop a geochronologically-constrained test of the Monterey Hypothesis (Vincent and Berger, 1985), which proposes a mechanistic link between organic carbon burial in the organic-rich Monterey Formation of central California and equivalent rocks, a positive carbon isotope excursion in marine benthic foraminiferal records, and global cooling in the wake of the Miocene Climatic Optimum. With chemostratigraphic (Flower and Kennett, 1993) and biostratigraphic (John et al., 2002; Föllmi et al., 2005) age controls for the Monterey Formation compromised by diagenesis and basinal restriction, I leverage the precision and accuracy of U-Pb zircon geochronology to date zircons derived from ash horizons intercalated within the organic rich shales of the Monterey Formation. These ages are integrated into a new chronostratigraphic framework for the Miocene Santa Barbara Basin, which is combined with total organic carbon data to develop organic carbon mass accumulation rate curves. The timing and tempo of organic carbon deposition in the Monterey Formation does not correspond with the positive $\delta^{13}C$ excursion of the Monterey event from a timing or mass balance perspective. I demonstrate that total organic carbon content is inversely correlated with sedimentation rate, which was in turn driven by a combination of eustasy and the tectonically-mediated evolution of the Miocene Santa Barbara Basin. As a result, organic carbon burial in the Monterey Formation is best described as a response to, rather than a driver of, global climate.

Although these three project chapters each address sedimentary basinal records of three distinct phenomena separated by both space and time, all three projects are united in the utilization of a broad geological toolkit to provide the context required to interpret each record. Together, these chapters underscore the importance of an integrative approach,

beginning with comprehensive field observations and incorporating an array of geochemical and geochronological analytical techniques, in effectively interrogating and interpreting the stratigraphic record of sedimentary basins.

* * *

REFERENCES, CHAPTER I

Flower, B.P. and Kennett, J.P., 1993, Relations between Monterey Formation deposition and middle Miocene global cooling: Naples Beach section, California: Geology, 21(10), p. 877-880. doi: 10.1130/0091-7613(1993)021<0877:RBMFDA>2.3.CO;2

Flowers, R. M., Macdonald, F. A., Siddoway, C. S., & Havranek, R. (2020). Diachronous development of great unconformities before Neoproterozoic snowball Earth. *Proceedings of the National Academy of Sciences*, *117*(19), 10172-10180. https://doi.org/10.1073/pnas.1913131117

Föllmi, K. B. (1990). Condensation and phosphogenesis: example of the Helvetic mid-Cretaceous (northern Tethyan margin). *Geological Society, London, Special Publications*, *52*(1), 237-252. https://doi.org/10.1144/GSL.SP.1990.052.01.17

Föllmi, K.B., Badertscher, C., de Kaenel, E., Stille, P., John, C.M., Adatte, T. and Steinmann, P., 2005, Phosphogenesis and organic-carbon preservation in the Miocene Monterey Formation at Naples Beach, California—The Monterey hypothesis revisited: Geological Society of America Bulletin, 117(5-6), p. 589-619.

Föllmi, K.B., Thomet, P., Lévy, S., De Kaenel, E., Spangenberg, J.E., Adatte, T., Behl, R.J. and Garrison, R.E., 2017: The impact of hydrodynamics, authigenesis, and basin morphology on sediment accumulation in an upwelling environment: the Miocene Monterey Formation at Shell Beach and Mossel Rock (Pismo and Santa Maria Basins, Central California, USA): Journal of Sedimentary Research, 87(9), p.986-1018. doi:https://doi.org/10.2110/jsr.2017.57

Hoffman, P. F., & Schrag, D. P. (2002). The snowball Earth hypothesis: testing the limits of global change. *Terra nova*, *14*(3), 129-155.

Hoffman, P. F., Abbot, D. S., Ashkenazy, Y., Benn, D. I., Brocks, J. J., Cohen, P. A., ... & Warren, S. G. (2017). Snowball Earth climate dynamics and Cryogenian geology-geobiology. *Science Advances*, *3*(11), e1600983.

John, C.M., Follmi, K.B., De Kaenel, E., Adatte, T., Steinmann, P. and Badertscher, C., 2002, Carbonaceous and phosphate-rich sediments of the Miocene Monterey formation at El Capitan State Beach, California, USA: Journal of Sedimentary Research, 72(2), p. 252-267. doi:https://doi.org/10.1306/080701720252

Keller, C. B., Husson, J. M., Mitchell, R. N., Bottke, W. F., Gernon, T. M., Boehnke, P., ... & Peters, S. E. (2019). Neoproterozoic glacial origin of the Great Unconformity. *Proceedings of the National Academy of Sciences*, *116*(4), 1136-1145. https://doi.org/10.1073/pnas.180435011

Kirschvink, J. L. (1992). Late Proterozoic low-latitude global glaciation: The snowball Earth.

Laakso, T. A., Sperling, E. A., Johnston, D. T., & Knoll, A. H. (2020). Ediacaran reorganization of the marine phosphorus cycle. *Proceedings of the National Academy of Sciences*, *117*(22), 11961-11967. https://doi.org/10.1073/pnas.1916738117

Macdonald, F. A., Yonkee, W. A., Flowers, R. M., & Swanson-Hysell, N. L. (2022). Neoproterozoic of laurentia. In *Laurentia: Turning Points in the Evolution of a Continent*. Geological Society of America. https://doi.org/10.1130/2022.1220(19)

McDannell, K. T., Keller, C. B., Guenthner, W. R., Zeitler, P. K., & Shuster, D. L. (2022). Thermochronologic constraints on the origin of the Great Unconformity. *Proceedings of the National Academy of Sciences*, *119*(5), e2118682119. https://doi.org/10.1073/pnas.2118682119

McDannell, K. T., & Keller, C. B. (2022). Cryogenian glacial erosion of the central Canadian Shield: The "late" Great Unconformity on thin ice. *Geology*, *50*(12), 1336-1340. https://doi.org/10.1130/G50315.1

Papineau, D. (2010). Global biogeochemical changes at both ends of the Proterozoic: insights from phosphorites. *Astrobiology*, *10*(2), 165-181. https://doi.org/10.1089/ast.2009.0360

Peak, B. A., Flowers, R. M., & Macdonald, F. A. (2023). Ediacaran-Ordovician tectonic and geodynamic drivers of Great Unconformity exhumation on the southern Canadian Shield. *Earth and Planetary Science Letters*, *619*, 118334. https://doi.org/10.1016/j.epsl.2023.118334

Reinhard, C. T., Planavsky, N. J., Gill, B. C., Ozaki, K., Robbins, L. J., Lyons, T. W., ... & Konhauser, K. O. (2017). Evolution of the global phosphorus cycle. *Nature*, *541*(7637), 386-389. https://doi.org/10.1038/nature20772

Sanders, C. B. (2023). *Geological and Geochemical Explorations of the Salitre Formation Phosphorite, Eastern Brazil* (Doctoral dissertation, California Institute of Technology). https://doi.org/10.7907/rd4m-7x08

Schulz, H. N., & Schulz, H. D. (2005). Large sulfur bacteria and the formation of phosphorite. *Science*, *307*(5708), 416-418. https://doi.org/10.1126/science.1103096

Shields, G., Stille, P., & Brasier, M. D. (2000). Isotopic records across two phosphorite giant episodes compared: the Precambrian-Cambrian and the late Cretaceous-recent. https://doi.org/10.2110/pec.00.66.0103

Sturrock, C. P., Flowers, R. M., & Macdonald, F. A. (2021). The late great unconformity of the Central Canadian Shield. *Geochemistry, Geophysics, Geosystems*, *22*(6), e2020GC009567. https://doi.org/10.1029/2020GC009567

Tyrrell, T. (1999). The relative influences of nitrogen and phosphorus on oceanic primary production. *Nature*, *400*(6744), 525-531. https://doi.org/10.1038/22941

Vincent, E. and Berger, W.H., 1985, Carbon dioxide and polar cooling in the Miocene: The Monterey hypothesis: The carbon cycle and atmospheric CO2: Natural variations Archean to present, *32*, p. 455-468. doi:https://doi.org/10.1029/GM032p0455

* * *

CHAPTER II. THE REAL MCCOY: GREAT UNCONFORMITY SOURCE-TO-SINK ON THE RIFTED PASSIVE MARGIN OF WESTERN LAURENTIA

A version of this work has been submitted for publication as:

[**Anttila, E.**, Macdonald, F.A., Zinto, J., and Britt, M.D. *The Real McCoy: Great Unconformity source-to-sink on the rifted passive margin of Laurentia.* Earth and Planetary Science Letters.]

ABSTRACT

The Great Unconformity separates Archean and Proterozoic basement rocks of the Laurentian cratonic core of North America from overlying Paleozoic sedimentary strata. Hypotheses for the generation of the Great Unconformity make predictions that can be tested within a source-to-sink depositional framework: kilometer-scale bottom-up exhumation from Neoproterozoic to Cambrian tectonics and dynamic topography predicts protracted delivery of sediments to Laurentian marginal basins, whereas top-down exhumation driven by Cryogenian sub-glacial erosion predicts rapid syn-glacial deposition outboard of Snowball Earth ice grounding lines. However, distinguishing between these hypotheses in North America is complicated by evidence for Cryogenian rifting during Snowball Earth. Here, we develop a new depositional model, age model, and tectonic framework for the Trout Creek Sequence and McCoy Creek Group of northeast Nevada and western Utah. We combine geological mapping, stratigraphy, geochemistry, and U-Pb zircon geochronology to demonstrate that these strata represent some of the most distal marine deposits preserved on the western margin of Laurentia, and that they were deposited outboard of Cryogenian

Snowball Earth ice grounding lines. Subsidence analysis supports a ca. 656 Ma Cryogenian rift-drift transition, without evidence for Ediacaran-Cambrian reactivation previously invoked to accommodate the Sauk transgressive sequence. Nonetheless, sedimentation rates during the Cryogenian Snowball Earth glaciations were low, providing a negative test of the sub-glacial erosion hypothesis. Deepening across the glacial intervals, and high sedimentation rates in their aftermath, suggest that Laurentian marginal basins were starved during Snowball Earth glaciations. Detrital zircon age spectra through the early Ediacaran McCoy Creek Group display limited up-section variability, consistent with the development and long-term stability of a prograding western Laurentian margin and the progressive erosion and redeposition of the Proterozoic sedimentary cover of North America. The dearth of Grenville-age zircon in the uppermost McCoy Creek Group and appearance of jasper clasts derived from Proterozoic units in the Midcontinent, along with detrital mica and carbonate that are the products of first-generation weathering of crystalline basement, are interpreted to be associated with the ca. 570 Ma emergence of the Transcontinental Arch. These data are consistent with thermochronological data documenting diachronous erosion and exhumation across Laurentia over hundreds of millions of years along the Great Unconformity.

2.1. Introduction

The Great Unconformity is a disconformity between Archean-Mesoproterozoic basement of the Laurentian craton and overlying Paleozoic sedimentary strata. First recognized in the Grand Canyon in the late 19th century (Powell et al., 1875), the Great Unconformity represents the amalgamation of multiple overlapping unconformities

(Karlstrom and Timmons, 2012), the presence of which have since been identified across much of North America. The Tonian-Middle Cambrian (ca. 1000-510 Ma) lacuna of the Great Unconformity spans breakup of the supercontinent Rodinia, assembly of Gondwana, Cryogenian Snowball Earth glaciations, the second rise of oxygen, and the origin and diversification of animals. These milestones in Earth history have been variably linked through an increase in global erosion, weathering, and sedimentation across the Great Unconformity (e.g. Campbell et al., 2010; Peters & Gaines, 2012; Husson et al., 2017; Keller et al., 2019), yet the timing and genesis of the Great Unconformity remain unknown. Erosion across the Great Unconformity has been attributed to a variety of driving mechanisms, including exhumation driven by tectonic or geodynamic forcings (Flowers et al., 2020; Macdonald et al., 2022; Sturrock et al., 2021; Peak et al., 2023), eustasy (Peters and Gaines, 2012), and erosion during Snowball Earth glaciations (Keller et al., 2019; McDannell et al., 2022; McDannell and Keller, 2022). These previous attempts to constrain the timing and magnitude of exhumation across the Great Unconformity have focused on thermochronology from the craton, but records of erosion and sedimentation are also preserved on continental margins.

In a source-to-sink framework (e.g. Driscoll and Nittrouer, 2000; Nyberg et al., 2018), the amount of rock exhumed and physically eroded from the continents is balanced by deposition in basins. In the case of the Great Unconformity, the accommodation space for eroded supracontinental material was provided by the rifted passive margins of Laurentia (Macdonald et al., 2022). End-member hypotheses for the timing of exhumation provide predictions for the timing and tempo of sedimentation recorded in the marine slope and basin floor stratigraphic record: Snowball sub-glacial erosion predicts Cryogenian syn-glacial

peaks in sedimentation rate in these marginal marine environments, whereas tectonic and geodynamic exhumation predicts protracted sedimentary delivery to Laurentian marginal basins throughout the late Neoproterozoic and early Paleozoic. However, the feasibility of testing these predictions is challenged by the limited preservation of Tonian-Cambrian deep marine or distal marginal strata, a vast majority of which have since been subducted, or were subsequently destroyed by later tectonism. Furthermore, quantitative tests of these predictions require i) a distal marine Laurentian margin sequence that ii) spans the Cryogenian, at minimum, iii) can produce an age model with sufficient resolution to quantify sedimentation rates on million-year timescales before, during, and after Cryogenian glaciations, and iv), exists within a broadly-constrained tectonic context. This last point is critical for interpreting variability in sedimentation rates, which can change as a function of tectonic accommodation space.

Strata of the Trout Creek Sequence and McCoy Creek Group (Gp) of northeastern Nevada and western Utah formed in an embayment on the western margin of Laurentia and, along with exposures of the Windermere Supergroup in southern British Columbia (Ross, 1991) preserve the most distal Neoproterozoic deposits in North America (Fig. 1a,b; Macdonald et al., 2022). Broadly, these strata record Cryogenian Snowball Earth glaciations (Crittenden et al., 1983; Prave, 1999; Macdonald et al., 2013) and the break-up of the supercontinent Rodinia (Stewart, 1972; Bond et al., 1985; Levy and Christie-Blick, 1991; Lund, 2008; Yonkee et al., 2014). However, a basin analysis of these units has been limited by uncertainties in age, depositional setting, and regional correlations. Here, we combine new geological mapping with sedimentological and stratigraphic data to generate a depositional model for the Trout Creek Sequence and McCoy Creek Gp.

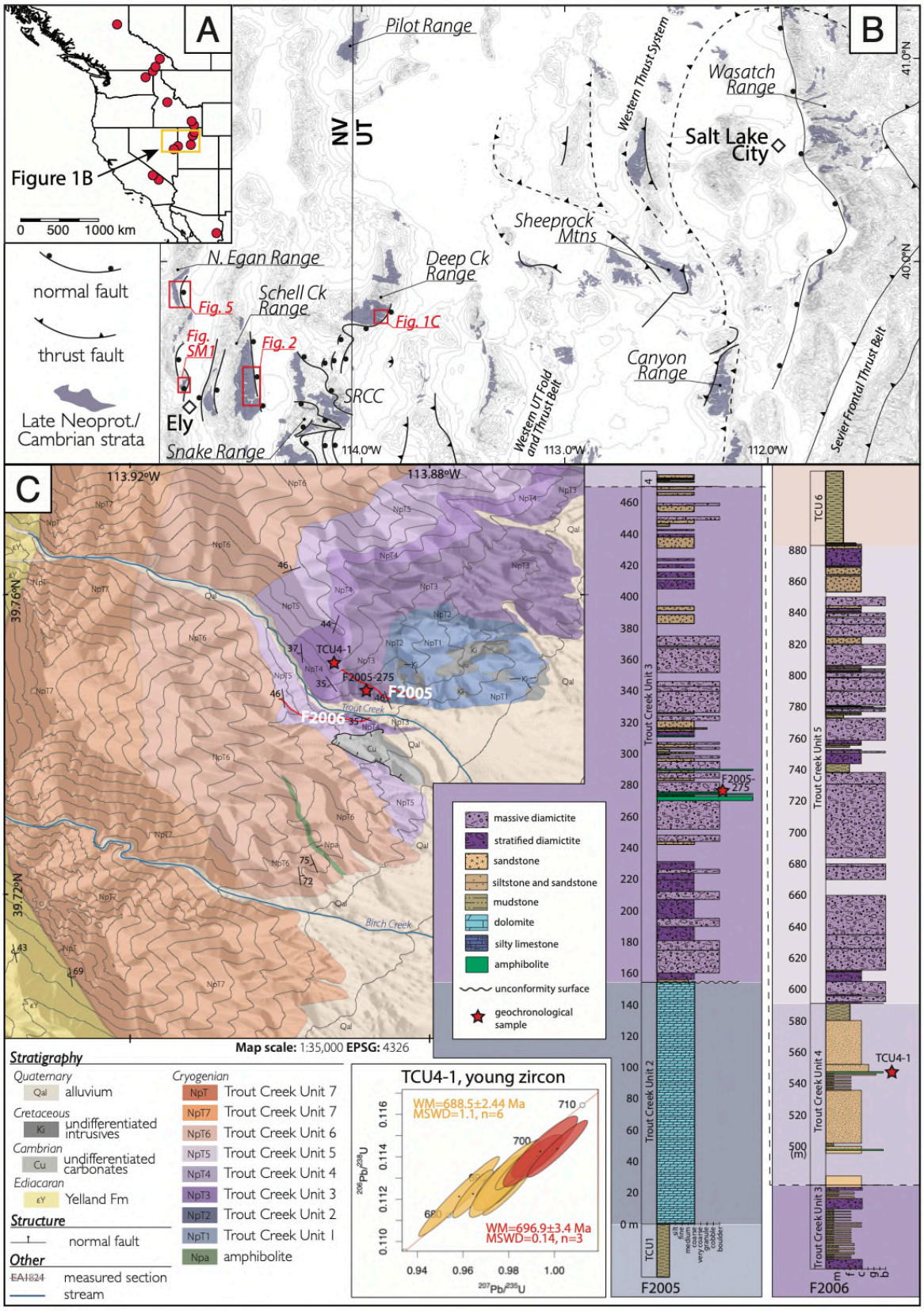
A
Figure 1B
0 500 1000 km
normal fault
thrust fault
Late Neoprot./
Cambrian strata
B
Pilot Range
NV
UT
Western Thrust System
Wasatch
Range
Salt Lake
City
Sheeprock
Mtns
N. Egan Range
Deep Ck
Range
Schell Ck
Range
Fig. 5
Fig. 1C
Fig.
SM1
Fig. 2
Canyon
Range
SRCC
Ely
Snake Range
Western UT Fold
and Thrust Belt
Sevier Frontal Thrust Belt
114.0°W
113.0°W
112.0°W
41.0°N
40.0°N
C
113.92°W
113.88°W
39.76°N
39.72°N
TCU4-1
F2005-275
F2005
F2006
Trout Creek
Birch Creek
massive diamictite
stratified diamictite
sandstone
siltstone and sandstone
mudstone
dolomite
silty limestone
amphibolite
unconformity surface
geochronological
sample
Map scale: 1:35,000 EPSG: 4326
Stratigraphy
Quaternary
Qal alluvium
Cretaceous
Ki undifferentiated intrusives
Cambrian
Cu undifferentiated carbonates
Ediacaran
eY Yelland Fm
Cryogenian
NpT Trout Creek Unit 7
NpT7 Trout Creek Unit 7
NpT6 Trout Creek Unit 6
NpT5 Trout Creek Unit 5
NpT4 Trout Creek Unit 4
NpT3 Trout Creek Unit 3
NpT2 Trout Creek Unit 2
NpT1 Trout Creek Unit 1
Npa amphibolite
Structure
normal fault
Other
measured section
stream
TCU4-1, young zircon
WM=688.5±2.44 Ma
MSWD=1.1, n=6
WM=696.9±3.4 Ma
MSWD=0.14, n=3
206Pb/238U
207Pb/235U
Trout Creek Unit 3
Trout Creek Unit 2
TCU1
F2005
Trout Creek Unit 5
Trout Creek Unit 4
TCU6
F2006

Figure 1: A) Locations of Neoproterozoic diamictite-bearing successions (red circles) along the western margin of Laurentia. **B)** Outcrop belt of the Trout Creek Sequence, McCoy Creek Group, and Cambrian Prospect Mountain Quartzite and equivalents in blue. Locations of Trout Creek Sequence and McCoy Creek Group strata discussed in this paper are indicated with red boxes; all labeled ranges are incorporated into the transect depicted in Fig. 9. **C)** Geological map of the Southern Deep Creek Range, modified from Rodgers (1984) and Monroe (2023). Stratigraphy of Units 1-6 of the Trout Creek Sequence in the Southern Deep Creek Range is shown at right, with the position of measured sections depicted on the map. The stratigraphic height of sample TCU4-1, sampled from the ridge north of Trout Creek, is correlated to a height within section F2006. A concordia diagram of the youngest grains from TCU4-1 is shown in the lower center inset; the weighted mean ages of two distinct populations are shown in red and orange, and are composed of analyses represented by concordia ellipses of the same color.

New U-Pb geochronology and carbonate chemostratigraphy are integrated into an age model, which we use to create a new regional correlation framework and assess the tectonic evolution of the Tonian-Cambrian western Laurentian margin. With the age, depositional environment, and tectonic context of these strata constrained, we examine the timing, tempo, and provenance of sedimentation in the Trout Creek Sequence and McCoy Creek Gp as a source-to-sink test of hypotheses for the formation of the Great Unconformity.

2.2. Geological Background

Late Neoproterozoic strata are present in the deepest structural levels of the Deep Creek, Snake, Schell Creek, and Egan ranges along the Nevada-Utah border (Fig. 1b). Within these ranges, the Trout Creek Sequence and McCoy Creek Gp are preserved as greenschist facies rocks, but are locally upgraded to amphibolite facies (andalusite ± staurolite-bearing assemblages) around Mesozoic plutons (Miller and Gans, 1989). Local kyanite-grade metamorphism of the McCoy Creek Gp is present in the northern Snake Range metamorphic core complex (Fig. 1), and is associated with Late Cretaceous shortening and an elevated geothermal gradient (Miller et al., 1983; Wrobel et al., 2021). This structural culmination of

the Sevier hinterland feeds into the Western Utah Fold and Thrust Belt to the east (Fig. 1; (Greene, 2014; Wrobel et al., 2021). Metamorphic fabrics consist of an older, east-dipping cleavage and a younger, more pervasive regional west-dipping cleavage, which has been dated with Ar-Ar on muscovite and phlogopite in the Schell Creek Range at 61 and 82 Ma (Miller et al., 1988; Miller and Gans, 1989). The west-dipping cleavage has been interpreted as recording subhorizontal, layer-parallel simple shear, indicating top-to-the-east transport (Miller and Gans, 1989). Significant tectonic attenuation is limited to the lower units of the Trout Creek Sequence in the Deep Creek Range, where they are thinned around a Mesozoic intrusion (Rodgers, 1984; Monroe, 2023). These units were exhumed primarily during Eocene to Oligocene extension, which was associated with abundant magmatism (Gans, 1989) and detachments along the Cambrian Pioche Shale and the base of the Ordovician Eureka Quartzite (Wrobel et al., 2021) in the Snake Range metamorphic core complex. Extension was accommodated by westward tilting and down to the east normal faulting (Gans, 1989, Long et al., 2022), which provided excellent exposures of thick, continuous packages of Neoproterozoic strata along the eastern flanks of the Deep Creek, Snake, Schell Creek, and Egan ranges.

The Trout Creek Sequence is a ~3500-m-thick package of meta-sedimentary rocks exposed in the Deep Creek Range (Figs 1b,c), which were divided into seven map units by Misch and Hazzard (1962). It is overlain by the ~2800-m-thick McCoy Creek Gp, which was defined in the McCoy Creek drainage on the west flank of the Schell Creek Range, and also recognized in the southern Snake Range (Misch and Hazzard, 1962), the northern and the southern Deep Creek Range (Woodward, 1965; Rodgers, 1984; Monroe, 2023), at Heusser Mountain in the central Egan Range (Woodward, 1963), the northern Egan Range (Schneck,

1986), and the Pilot Range (Woodward, 1967; Miller, 1983; Miller and Lush, 1994) (Fig. 1b). Correlations of units within the McCoy Creek Gp have remained uncertain, in part because of inconsistent nomenclature and subdivision (Fig. 2). To eliminate potential confusion from generations of inconsistent alphabetical unit schemes, we follow the formation nomenclature of Misch and Hazzard (1962) and Schneck (1986), and define two additional formations (Table 1a,b) that were not included in previous studies.

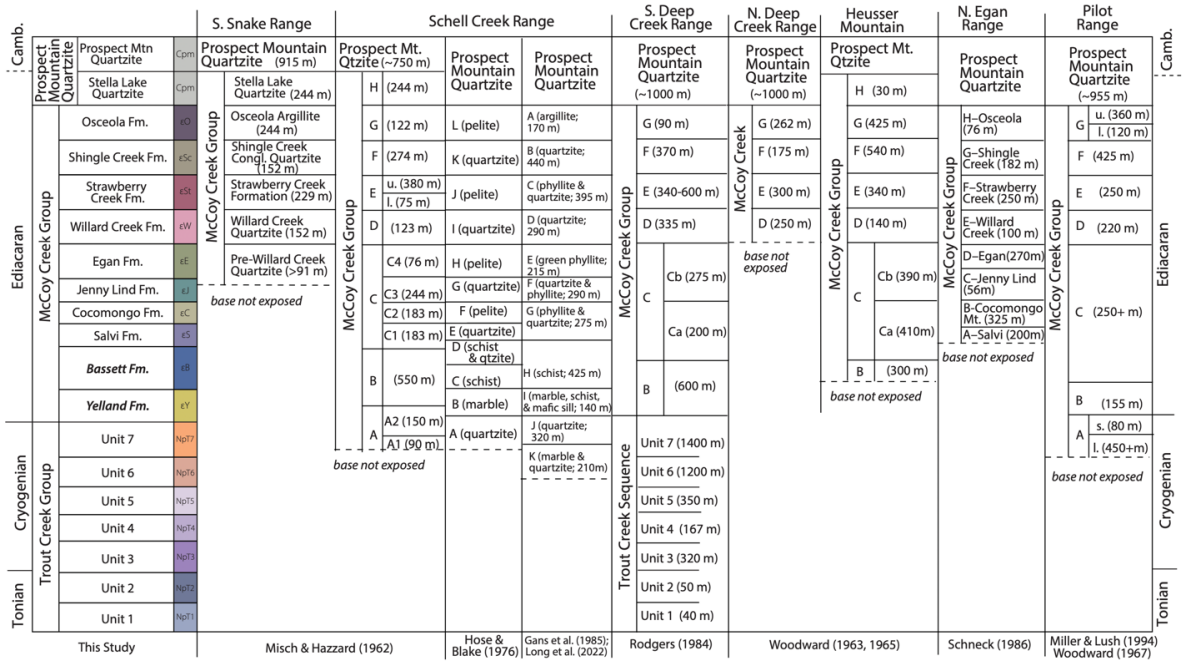

Figure 2: Unit nomenclature for the Trout Creek Sequence and McCoy Creek Group, including previous naming schemes (right) and the full stratigraphic nomenclature (including map unit colors and symbols) used in this study (left). Note that the new nomenclature is an amalgamation of the naming schemes of Misch and Hazzard (1962), Rodgers (1984), and Schneck (1986); two new formalized units are highlighted with bold italicized text. Formalization tables for the newly-defined Yelland Fm and Bassett Fm can be found in Table 1.

Table 1: Formalization tables for the newly defined Yelland (A) and Bassett (B) Formations.

A	
Name	**Yelland Formation**
Name Derivation	Type section at McCoy Creek, directly west of Yelland Ranch, located in Spring Valley to east of Schell Creek Range
Category and Rank	Lithostratigraphic Formation
Type Area	lower eastern slopes of the Schell Creek Range, White Pine County, Nevada, USA
Unit Type Section	F2002 (base of section at 39.372786ºN, 114.528115ºW)
Unit Description	The Yelland Fm consists of ~200 m of interbedded carbonates and thin graded beds of pelite that conformably overly the upper diamictite of Trout Creek Sequence Unit 7 diamictite. Previously incorporated into portions of McCoy Creek Gp Units A2 and B (Misch and Hazzard, 1962; Fig. SM1), the type section of the Yelland Fm section F2002 (Fig. 3) is located on the ridge south of McCoy Creek. At McCoy Creek, the upper Unit 7 diamictite is overlain by 11 m of white- to buff-colored dolomite with tubestone stromatolite cements near the base. The tubestone stromatolite interval is ~1 m thick, with cm-scale, circular in plan-view, sparry to micritic void fill cements. The tubestone stromatolite interval is overlain by fine-laminated, massive dolostone. The dolostone is thickest just north of McCoy Creek within section F2003 and F2004, and south of Taft Creek, where it is over 10 m-thick. Elsewhere along strike, the basal dolomite, interpreted to represent the Marinoan cap carbonate, is thin to absent. At the McCoy Creek type section, the cap dolomite is succeeded by ~20 m of cm-scale graded beds of quartzite, lutite and limestone. Above this lower limestone interval, ~100 m of pelitic schist, quartzite, and minor limestone is overlain by a second ~40-m-thick allodapic limestone interval; the upper limestone is cm-bedded, but often sucrosic, with limited evidence of primary bedding fabrics or textures preserved in outcrop. A paraconformable contact with pelitic schist of the overlying Bassett Fm marks the top of the Yelland Fm.
Unit Reference Localities	Sections F2003 (base of section at 39.374616ºN, 114.528761ºW) and F2004 (base of section at 39.376142ºN, 114.528664ºW), both north of McCoy Creek; Ridges south of Taft Creek drainage (ca. 39.3201ºN, 114.51378ºW)
Dimensions	~170m thick across most of the Schell Creek Range exposures
Geologic Age	basal Ediacaran
Regional Correlations	lowermost Kelley Canyon Fm of the Sheeprock Mountains (Christie-Blick, 1982), lowermost Unit 2 of the Canyon Range (Christiansen, 1952), and the lowermost Kelley Canyon Fm of the northern Wasatch Range

B	
Name	**Bassett Formation (Debrah Member)**
Name Derivation	Type section on ridge north of Bassett Creek, eastern Schell Creek Range
Category and Rank	Lithostratigraphic Formation
Type Area	eastern slopes of the Schell Creek Range and Egan Range, White Pine County, Nevada, USA
Unit Type Section	EA2312 (base of section at 39.420938ºN, 114.537247ºW), Bassett Creek, Schell Creek Range
Unit Description	The Bassett Formation comprises ~800 meters of fine-grained siliciclastic rocks, dominated by strongly cleaved black pelitic schist. The base of the Bassett Fm sharply and paraconformably overlies the uppermost recrystallized carbonates of the Yelland Fm at the EA2312 type section and F2002 reference section. Above the contact, black to umber fine-grained phyllite and pelitic schist carries two well-defined cleavages. A shallow, broadly east-dipping cleavage is cut by a west-dipping cleavage that is steeper than bedding, resulting in the development of pervasive crenulations throughout the lower ~50m of the type section. Rare, fine-grained arenitic quartzite beds to 20cm in thickness typically do not carry either cleavage, but are occasionally deformed in cm-scale crenulation-parallel folds. Up-section, the steep, west-dipping cleavage becomes increasingly pervasive and fully overprints east-dipping cleavage planes. Throughout the section, abundant pyrite rhombs (many of which are deformed in a manner consistent with the top-to-the-east shear sense indicated by crenulation asymmetry in the lower portion of the section) suggest an organic-rich shale protolith for the Bassett Fm. Towards upper half of the Bassett Fm, syneresis cracks become pervasive in the black phyllite, which is increasingly intercalated with 2-10cm beds of generally fining-upward subarkosic and arenitic sandstone beds. Within the upper Bassett Fm in both the Schell Creek and Egan Ranges, the first appearance of thick (broadly >1m) arenitic quartzite beds marks the base of the Debrah Mb of the Bassett Fm. The Debrah Mb comprises a variably-thick succession of medium-to-coarse grained arenitic packages, ranging in thickness from .5 to 3m, that outcrop either as massive, often fining-upward beds or weakly laminated beds exhibiting dune-scale cross stratification. Across both the Egan and Schell Creek Ranges, the thickness and continuity of individual quartzite beds within the Debrah Mb varies significantly, with low-aspect-ratio cuspate bedding morphologies at the base of thicker quartzite beds likely indicating syndepostional erosion and channel infilling. While inconsistent in thickness and along-strike continuity, the Debrah Mb serves as a mappable resistant marker bed in a stratigraphic interval dominated by recessive phyllite and schist. In both the Egan and Schell Creek Ranges, the Debrah Mb is typically overlain by a significant (>50m) interval of Bassett Fm pelitic schist, often bearing abundant syneresis cracks and minor intercalated quartzite beds to 10cm. At McCoy Creek, the lowermost quartzites of the Debrah Mb of the Debrah Fm mark the first major sequence boundary (C1-C2 transition; Fig. SM1) of Misch and Hazzard (1962).
Unit Reference Sections	F2002 (base of section at 39.372786ºN, 114.528115ºW), McCoy Creek, Schell Creek Range
Dimensions	~800-m-thick across most of the Schell Creek Range; incompletely exposed in the Egan Range.
Geologic Age	lower Ediacaran
Regional Correlations	lower-middle Kelley Canyon Fm of the Sheeprock Mountains (Christie-Blick, 1982), lower-middle Unit 2 of the Canyon Range (Christiansen, 1952), and the lower-middle Kelley Canyon Fm of the northern Wasatch Range

2.3. Methods

Between 2020-2023, we mapped exposures of the McCoy Creek Gp in the Snake, Schell Creek, and Egan Ranges of Nevada with iPads running FieldMove digital mapping software. Stratigraphic sections were measured using meter-sticks. Samples for carbon isotope chemostratigraphy and U-Pb zircon geochronology were collected within measured stratigraphic sections, or from localities in which the relative stratigraphic height of the sample was easily calculated from map relationships. The location of all measured sections and samples are collated in Tables A1 and A2, in Appendix 1.

2.3.1. Carbonate geochemistry

Carbonate samples were collected from within measured stratigraphic sections, and were subsequently slabbed and microdrilled to procure aliquots of carbonate powder at the University of California, Santa Barbara. Carbonate $\delta^{13}C$ and $\delta^{18}O$ data were acquired at the Center for Stable Isotope Biogeochemistry at the University of California, Berkeley. Between 10-100 microgram subsamples of each powder aliquot were reacted with concentrated H_3PO_4 at 90^{o}C for 10 mins to generate CO_2 gas for coupled $\delta^{13}C$ and $\delta^{18}O$ analysis using a GV IsoPrime mass spectrometer with Dual-Inlet and MultiCarb systems. Several replicates of one international standard NBS19, and two lab standards $CaCO_3$-I & II were measured along with approximately 40 unknowns for each run. The overall external analytical precision was about $\pm$0.05‰ for $\delta^{13}C$ and about $\pm$0.07‰ for $\delta^{18}O$. All carbonate chemostratigraphic data and section locations are collated in Table A1 in Appendix 1.

2.3.2. Zircon geochronology

Sample collection

Samples collected for detrital zircon geochronology are described below, in ascending stratigraphic order:

F2005-273.4/275—Trout Creek Group Unit 3: The sandstone matrix of diamictite with clasts of amphibolite (Fig. 3C) was collected along the north side of Trout Creek in the Deep Creek Range at 39.7466°N, 113.8884°W. Two horizons directly above amphibolite horizons ~120 m above the base of Unit 3 were sampled.

TC4-1—Trout Creek Sequence Unit 4: A poorly sorted arkosic wacke, featuring subangular plagioclase rhombs, was sampled from Trout Creek Sequence Unit 4 on a ridge north of Trout Creek in the Deep Creek Range at 39.7506ºN, 113.8924ºW. The sampled horizon is located just below a fine arenitic sandstone horizon containing isolated dropstones (Fig. 2d).

F2003-3—Trout Creek Group Unit 7: A white, vitreous quartzite with 0.5-meter-scale tabular cross bedding was sampled one meter below the base of the upper diamictite of Trout Creek Unit 7 on the north side of McCoy Creek in the Schell Creek Range at 39.3747°N, 114.5289°W.

F2002-204.9—Yelland Formation: Fine-grained sandstone from a 10-cm-thick graded bed was sampled 91.4 meters above the base of the Yelland Formation on the south side of McCoy Creek in the Schell Creek Range at 39.3723°N, 114.5301°W.

F2002-273.4—*Bassett Formation:* A ~10 cm thick bed of medium-grained arenitic sandstone ~50 m above the base of the Bassett Formation was sampled on the south side of McCoy Creek at 39.3718ºN, 114.5318ºW.

MC_2—*Bassett Formation:* A medium-coarse arenite at the lowest exposure of the Debrah Mb of the Bassett Fm was sampled on the ridge north of McCoy Creek at 39.3778ºN, 114.5361ºW.

Egan 182.0—Egan Formation: A medium-to-coarse subarkosic litharenite bed, ~20cm thick and interbedded within brown-green argillite, was sampled from the slope above the north side of Egan Creek in the Egan Range at 39.8662°N, 114.9228°W.

Egan 233.0—Egan Formation: Coarse grained arkosic grit with basal shale rip-ups and occasional laterally discontinuous grit channels was sampled from the middle Egan Fm along the north side of Egan Creek in the Egan Range at 39.8651ºN, 114.9240°W.

Egan 384.4—Willard Formation: Half meter- to meter-thick beds of coarse arenitic quartzite with minor amalgamated granule-cobble conglomerate was sampled from the Willard Fm at Egan Creek at 39.8659ºN, 114.9256°W.

Egan 564.0—Strawberry Creek Formation: Poorly sorted subarkosic pebble conglomerate with interbeds of coarse litharenitic sandstone was sampled from the middle Strawberry Creek Fm at Egan Creek at 39.8652ºN, 114.9281°W.

Sample preparation

Geochronology samples were trimmed with a rock saw and cleaned to remove potential surficial contamination, and pulverized in an industrial jaw crusher. The resultant

<500 micron grainsize fraction was collected, and subsequently washed in an antiflocculant solution to remove ultrafine material. Samples were then panned to isolate heavy minerals. Samples containing few zircon crystals were further magnetically separated with a Frantz device (0.4A at a 20º incline), and put through a final density separation in methylene iodide. Zircon grains were individually picked from resultant heavy mineral separates, annealed in a muffle furnace for 48 hours at 900ºC, mounted in epoxy, and polished. The internal structures of the grains were mapped with cathodoluminescence (CL) imaging using a Cameca SX-100 Electron Probe Micro-Analyzer (EPMA) with a CL detector.

Laser ablation inductively coupled plasma mass spectrometry (LA-ICPMS) analyses

LA-ICP-MS U-Pb geochronological analyses on zircon were completed at UCSB, using a Cetac/Photon Machines Analyte Excite 193 nm excimer laser attached to a Nu Plasma 3D multicollector ICPMS, following the methods of Kylander-Clark et al. (2013). Each zircon was ablated with a 20µm laser spot. The zircon 91500 (Wiedenbeck et al., 1995) was used for age calibration. Secondary zircon reference materials included 9435, AUSZ, Mudtank, GJ1, and Plesovice (Jackson et al., 2004). *Iolite* (Paton et al., 2010) was used to correct for U-Pb mass bias and drift following the methods of Kylander-Clark et al. (2013) and Horstwood et al. (2016). Dates for each analyzed grain were calculated by importing reduced $^{238}U/^{206}Pb$ and $^{207}Pb/^{206}Pb$ ratios into *IsoplotR* (Vermeesch, 2018). All LA-ICP-MS data is collated in Table A2 in Appendix 1. We also retabulate data from Yonkee et al., 2014, which were integrated into the normalized probability plots described below.

Normalized probability plots

Detrital zircon normalized probability plots were created for all detrital samples. Discordant analyses from detrital samples were removed by excluding all ages exhibiting more than 15% discordance. Concordia ages (Vermeesch, 2020) from the resultant filtered dataset from each sample were combined with other samples from the same formation (including extant data from Yonkee et al., 2014), and were incorporated into a kernel density estimation (KDE) function (full code available in GitHub repository linked in Appendix 1) to generate the normalized probability plots depicted in Fig. 9 of the main manuscript. Maximum depositional ages from detrital samples were calculated by isolating groups of young zircon analyses conforming to the MSWD (Wendt and Carl, 1991) criteria for a single magmatic population of *n* grains (Spencer et al., 2016).

2.3.3. Tectonic subsidence model

Representative stratigraphic thicknesses, lithological information, and inferred depositional environments were utilized to develop a tectonic subsidence curve for the entirety of the Trout Creek Sequence and McCoy Creek Group, as well as the overlying Paleozoic succession (through the Ely Limestone) within the model framework of Zhang et al. (2023a,b). All inputs for this portion of the model can be viewed in the first sheet ("Stratigraphy") of Table A3 in Appendix 1; a detailed discussion of the SubsidenceChron.jl model framework (and parameters therein) can be viewed within Zhang et al. (2023a,b). An expanded discussion of model inputs used in this work can be viewed in Appendix 1.

2.4. Results

2.4.1. Stratigraphy

Trout Creek Sequence

The Trout Creek Sequence, first described by Misch and Hazzard (1962) and Rodgers (1984), is best exposed at the eponymous type locality (Fig. 1c). At Trout Creek, the top of Unit 1 is composed of argillite, while Unit 2 comprises partially calcitized dolomite that is attenuated to ~50 m around a Mesozoic intrusion, but thickens to 147 m on the ridge north of Trout Creek (Fig. 1c). Unit 1 is gradationally separated from Unit 2 by ~2 m of thin-bedded tan dolostone intercalated with argillite. Carbonate of Unit 2, which locally preserves mm-laminated bedding (Fig. 3a), is sharply overlain by Unit 3, which is composed of graded beds of quartzite, stratified diamictite, and minor amphibolite. The diamictite is matrix-supported, with faceted clasts composed of quartzite, crystalline basement (Fig. 3b), pelite, carbonate, and amphibolite (Fig. 3c). Stretched clasts in Unit 3 diamictites are interpreted to be the result of layer-parallel simple shear, resulting in a minimal reduction in apparent thickness. Unit 4 gradationally overlies Unit 3, and consists of quartzite-pelite graded beds with minor diamictite with bed-penetrating dropstones (Fig. 3d). Unit 5 has a gradational contact with the underlying Unit 4, comprises the same lithologies as Units 3 and 4, but is more dominated by granite- and orthogneiss-clast diamictite. Unit 5 is capped by a laterally continuous ~0.2-1 m thick limestone bed (Fig. 3e). Together, Units 3-5 are

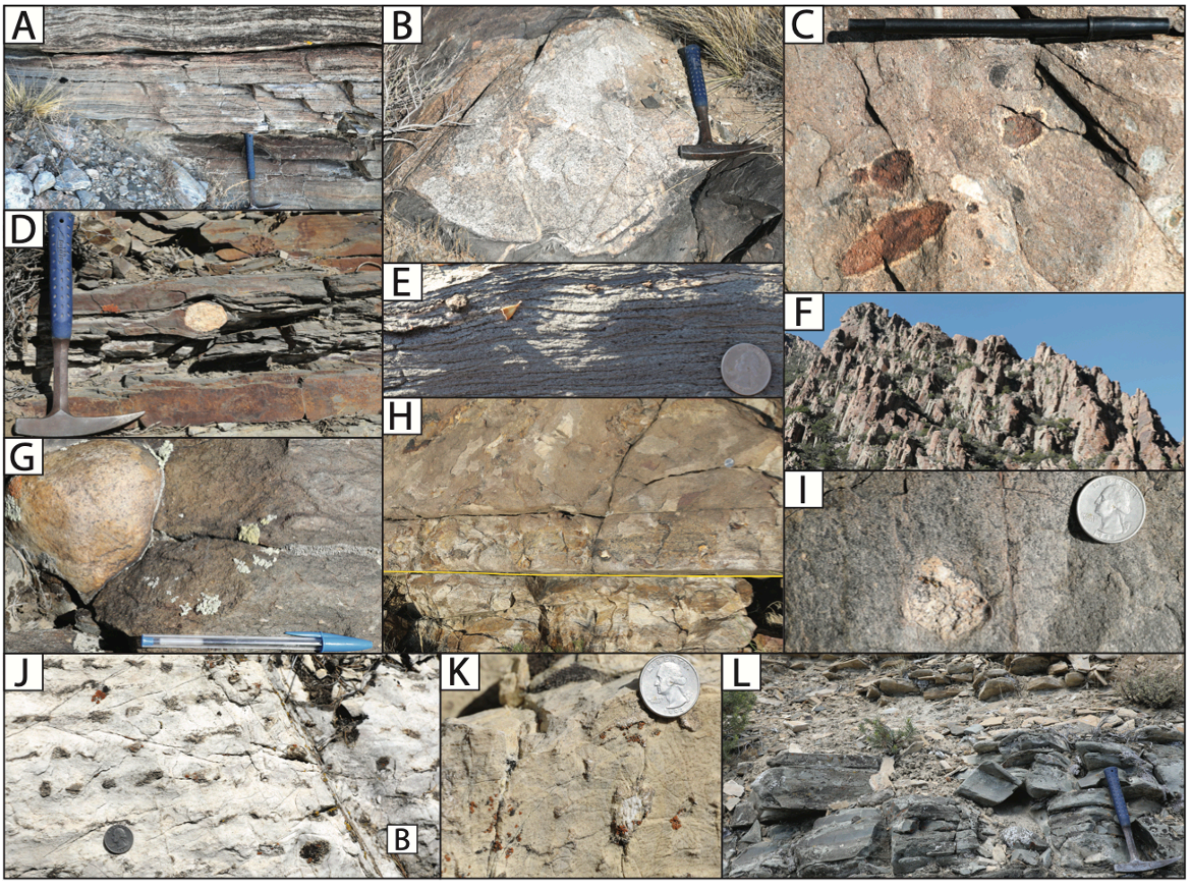

Figure 3: Field photos of Trout Creek Sequence and basal McCoy Creek Group strata in the southern Deep Creek Range and Schell Creek Range. **A)** massive weathering, thinly- laminated dolostone of Unit 2 from section F2005. **B)** Granitic orthogneiss boulder clast in diamictite of Unit 3 from section F2005. Note pebble-to-cobble clasts of quartzites in surrounding outcrop. **C)** Amphibolite clasts with reaction rims in Unit 3 diamictite from section F2005. These clasts occur directly above bedding-parallel amphibolite horizons in Unit 3, suggesting that the amphibolites were originally extrusive mafic volcanic material or mafic sedimentary deposits, and not later sills. **D)** Gneissic dropstone in laminated fine sandstone horizon within Unit 4; this horizon is ~1m stratigraphically above the horizon sampled for geochronological sample TCU4-1. **E)** Basal Unit 6 cap limestone from ridge above section F2005. **F)** Massive ridge forming quartzites of Unit 7, looking from Trout Creek up to northern ridgeline. **G)** Granite clast in uppermost diamictite of Unit 7 at McCoy Creek, section F2003. **H)** Sharp basal contact of uppermost diamictite of Unit 7 overlying clean, bedded quartzites, ridge north of Taft Creek. Contact is indicated with a yellow line, note quarter-dollar coin in upper right for scale. **I)** Granite clast in uppermost diamictite of Unit 7 at McCoy Creek, section F2003. **J)** Plan view of tubestone stromatolite in basal cap carbonate of the Yelland Formation at McCoy Creek, section F2003, showing tubes filled with both sparry and micritic cements. **K)** Cross-sectional view of tubestone stromatolite showing faint lamination and funnel-shaped cements, section F2003. **L)** Laminated, sharp-based, graded fine sandstone to mudstone beds and overlying limestones and lutites of Yelland Formation, section F2004.

~760 m thick. Unit 6 comprises ~400 m of silver-grey to brick-red-weathering pelitic schist, overlain by 800 m of beige vitreous quartzite with interbedded pelite (Rodgers, 1984). The overlying Unit 7 consists of ~1400 m of cliff forming (Fig. 3f) quartz arenite with tabular cross-beds and minor conglomerate. In the Deep Creek Range, the top of Unit 7 is marked by <10 m of diamictite with an arkosic wacke matrix and pebble- to cobble-sized clasts of quartzite.

In the Schell Creek Range (Fig. 4), strata previously identified as McCoy Creek Gp Unit A are correlative with the upper portion of Unit 7 of the Trout Creek Gp (Misch and Hazzard, 1962; Fig. 2). There, the lowest exposures of Unit 7 host two ~30 m-thick light blue-gray sucrosic marbles separated by ~10 m of quartzite. The marbles are succeeded by ~250 m of massive and tabular cross-stratified quartz arenite beds. This thick quartzite interval is overlain by ~50 m of pelitic schist and quartzite featuring m-scale channelization and minor quartzite pebble- to cobble-clast conglomerate (Fig. 3g), and an additional ~50 m of m-scale beds of massive and tabular cross-stratified quartzite. The top of Trout Creek Unit 7 in the Shell Creek Range is marked by a weakly-bedded 5-25 m thick diamictite (Fig. 3h) consisting of poorly-sorted arkosic sandstone with quartzite and crystalline (Fig. 3i) basement clasts ranging in size from pebbles to rare boulders.

McCoy Creek Group

The newly-defined Yelland Fm (Table 1a) consists of ~200 m of interbedded carbonate and thin graded beds of pelite. A distinctive buff-yellow dolostone of the basal Yelland Formation (Fm) sharply overlies the uppermost diamictite of Trout Creek Sequence Unit 7 in both the Deep Creek and Schell Creek Ranges. At McCoy Creek, this interval

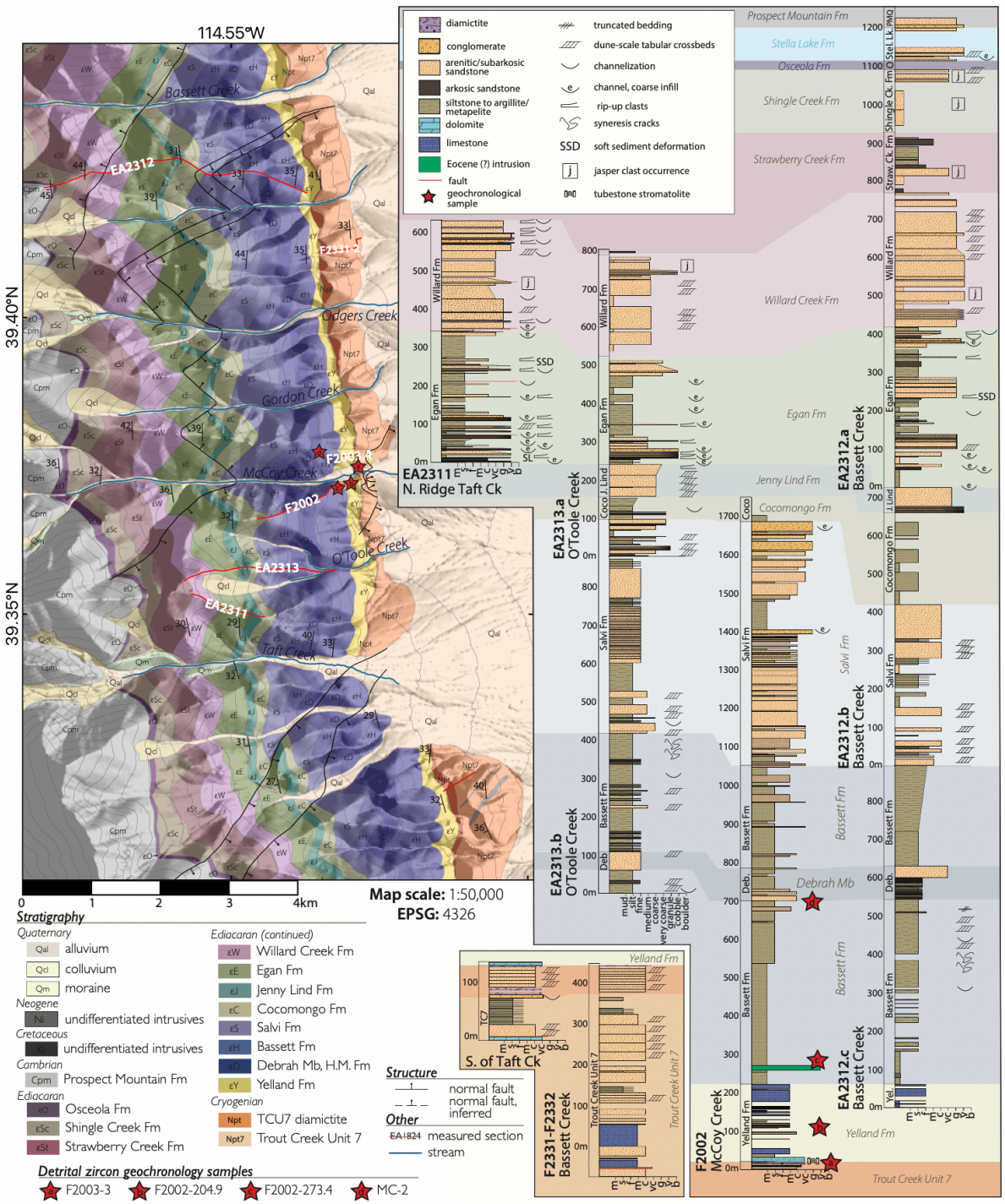

Figure 4: Geological map of the eastern front of the central Schell Creek Range. Stratigraphy of the McCoy Creek Group is shown at right, with the position of measured sections depicted on the map. Stratigraphy of the upper portions of Unit 7 of the Trout Creek Sequence are shown in the lower central inset panel.

comprises 11 m of white- to buff-colored massive and fine-laminated dolostone, with a basal meter-thick horizon of tubestone stromatolites featuring cm-scale sparry to micritic void fill cements that are circular in plan-view (Fig. 3j) and funnel-shaped in cross section (Fig. 3k). The dolostone interval varies from 0-20 m thick along strike, and is overlain by ~20 m of graded fine-grained sandstone, lutite and limestone (Fig. 3l) and ~100 m of pelitic schist, thin graded sandstones, and allodapic limestones.

The newly-defined Bassett Fm (Table 1b) comprises ~800 m of fine-grained siliciclastic rocks, with black phyllite that becomes increasingly intercalated up-section with cm-thick graded beds of fine- to medium-grained sandstone. The appearance of >1 m thick quartz arenite beds marks the base of the informal Debrah member (Mb; Table 1b). The Debrah Mb consists of massive, fining-upwards, or weakly laminated beds of medium-to-coarse grained arenite that occasionally feature planar dune-scale cross-stratification. Although individual quartzite beds vary in thickness and lateral continuity over 10-100 m distances, the Debrah Mb serves as a mappable marker in an otherwise recessive stratigraphic interval. The Debrah Mb is overlain by >50 m of pelitic schist featuring abundant syneresis cracks (Fig. 5a) and minor cm-thick graded quartzites.

In the Egan Range, the Salvi Fm (Schneck, 1986) comprises ~100 m of resistant medium-grained to granule vitreous gray quartz arenite with coarse-tail normal graded beds and tabular cross-beds (Fig. 5b). In the Schell Creek Range, the Salvi Fm consists of ~500 m of 1-4-m-thick beds of coarse-grained arenite intercalated with subsidiary fine-grained arenites, phyllites, and slates. Coarse beds host dune-scale tabular cross stratification and rare interval of granule-to-pebble quartzite conglomerate featuring erosive bases with up to 50 cm of vertical relief.

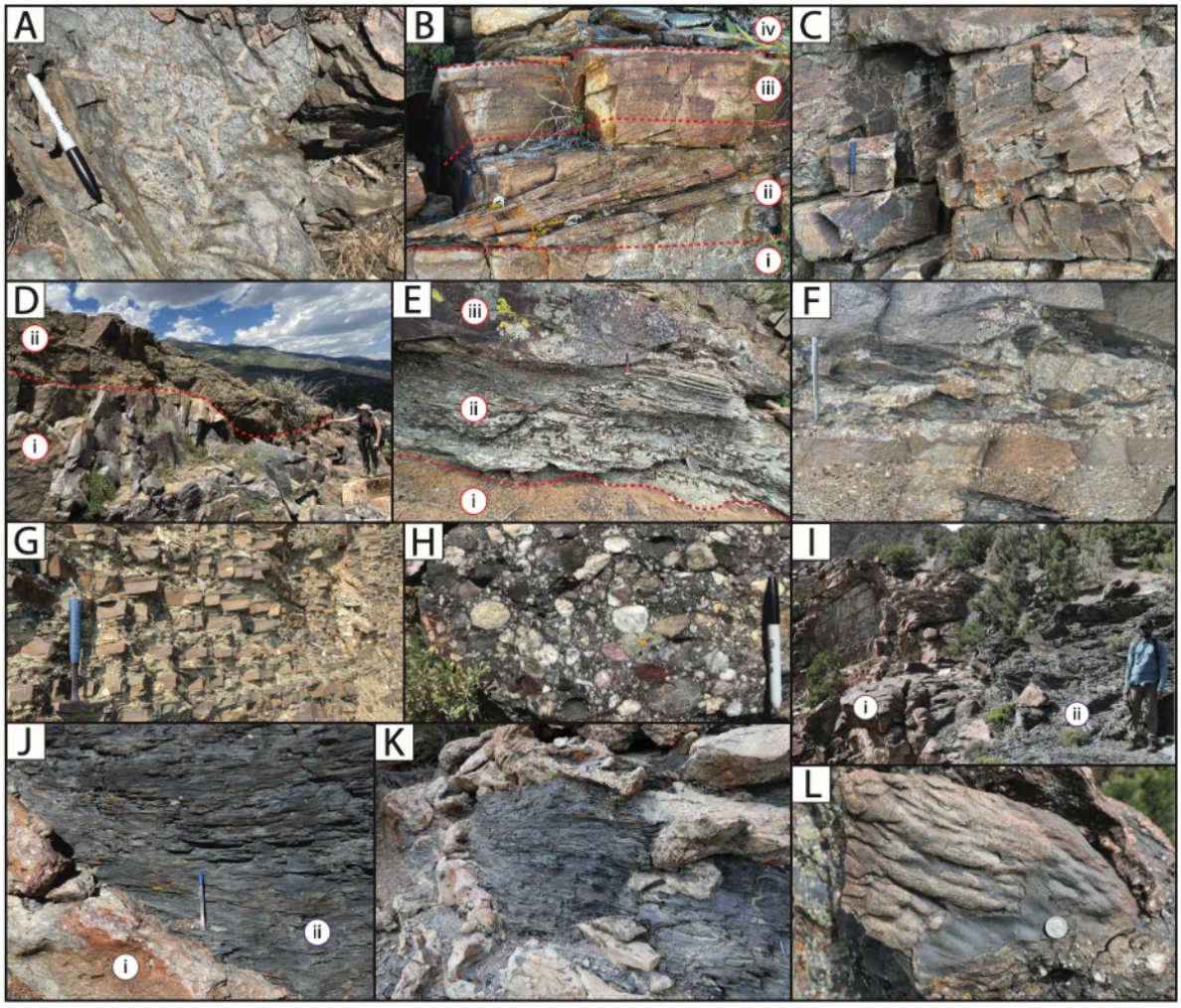

Figure 5: Field photos McCoy Creek Group Units C-F: **A)** Pervasive syneresis cracks in the Bassett Formation at McCoy Creek, section F2002. **B)** Fining-upward sandstone package, Salvi Fm., McCoy Creek, section F2002. Normal-graded coarse arenite (i) conformably underlies tabular dune-scale crossbeds (ii), laminated fining-upward medium to fine arenite (iii) and laminated fine sand and silt (iv). **C)** Dune-scale tabular cross- beds in a laterally-discontinuous, m-scale quartz arenite bed, Jenny Lind Formation, Taft Creek. **D)** Channelization at the Jenny Lind-Egan contact, central Schell Creek Range ridge. A ~2m tall geologist is pointing at an incised channel in the uppermost quartzite of the Jenny Lind Formation (i), which is infilled with massive coarse conglomerates of the overlying Egan Formation (ii). **E)** Basal Egan Formation, northern Taft Creek ridge, section EA2311. An erosional surface above the uppermost Jenny Lind Fm (i) is variably overlain by green argillites (ii) and channel- filling quartz conglomerates and coarse quartzites (iii) of the Egan formation. **F)** Channel fill, including coarse conglomerates, cobble to boulder rip-up clasts of silt and fine sandstone, and coarse-tail normal graded sandstone (at top). Egan Formation, ridge to north of Bassett Creek. **G)** Laterally-continuous packages of normal graded 3 cm-thick medium to fine sandstone, overlain by 2-5cm packages of less-resistant fine sandstone to siltstone of the Strawberry Creek Formation, western ridgecrest of Cocomongo Mountain, northern Egan Range. **H)** Conglomerate of the Shingle Creek Formation, featuring dark jasper clasts, ridge north of McCoy Creek. **I)** Incised paleotopography cutting into the uppermost Shingle Creek

Formation (i) in the northern Deep Creek Range. Channel fill deposits of the Osceola Formation (ii) fill a paleocanyon with ~120m of relief below a disconformable Shingle-Osceola contact. 2-m-tall geologist for scale. **J) Channels**, incised into jasper-bearing conglomerates of the uppermost Shingle Creek Formation (i) are infilled by silts and fine sands of the basal Osceola Formation (ii). Northern Deep Creek Range. **K)** Osceola channel fill, featuring slump-folded pebble-cobble conglomerate, and coarse sandstone chaotically interfingered with siltstones and shales. From a subsidiary channel within a larger paleocanyon in the northern Deep Creek Range. Note quarter for scale at photograph center. **L)** Flute casts, Osceola Formation, northern Deep Creek Range.

The ~50-200-m-thick Cocomongo Fm (Schneck, 1986) coarsens upward from grey argillite to cm-scale graded beds of medium- to fine-grained subarkosic sandstone to siltstone and slate. Rare interstitial intervals of poorly sorted, coarse-grained arenite and granule conglomerate are intercalated within the finer-grained lithologies, and feature erosive, channelized bases.

The Jenny Lind Fm (Schneck, 1986) comprises ~50-115 m of resistant, ridge-forming vitreous quartz litharenite featuring massive 0.5-2-m-thick poorly-sorted sandstone beds with rare tabular dune-scale cross bedding (Fig. 5c) and minor partings of sublitharenitic fine-grained sandstone and slate. Incised channels with m-scale vertical relief (Fig. 5d) are common near the top of the unit, which host granule-pebble conglomerate with subangular to rounded clasts of quartzite and slate, and abundant slump-folds (Fig. 5e).

The Egan Fm (Schneck (1986), comprises a ~165-400-m-thick recessive interval dominated by green slate and argillite, with minor poorly-sorted arkosic to sublitharenitic sandstone in cm- to m-thick graded beds and minor massive granule to pebble conglomerate horizons with channelized bases. The Egan Fm is thickest in the Schell Creek Range, and hosts coarse-grained channel fill deposits with cobble-to-boulder-scale rip-up clasts (Fig. 5f), soft-sedimentary deformation, and slump-folds.

The Willard Creek Quartzite (Misch and Hazzard 1962; Schneck, 1986) is 30-130 m thick in the Egan Range and 260-340 m thick in the Schell Creek Range. It outcrops as a resistant band of massive, 1-2-m-thick beds of white vitreous arenitic quartzite with granule-to-pebble quartz conglomerate containing rare dune-scale tabular cross-bedding, pebble stringers, quartz granule to cobble conglomerate, and discontinuous shale partings.

The Strawberry Creek Fm (Misch and Hazzard 1962) comprises a ~220-350 m, broadly-coarsening-upward sequence of green-blue-gray slate, siltstone, and purple-gray fining-upwards packages of granule conglomerate and arkosic to sublitharenitic sandstone. Channel-filling conglomerates with rip-ups and soft-sedimentary folds are common near the base, while the upper Strawberry Creek Fm contains repeated sharp-based, laterally continuous fining-upwards packages of medium-grained sandstone to siltstone (Fig. 5g).

In the Schell Creek Range, the Shingle Creek Fm (Misch and Hazzard, 1962) consists of ~150 m of light purple to pink-white cross-bedded sandstone and quartz and jasper clast pebble conglomerate (Fig. 5h). It varies radically in thickness from ~100 m thick in the northern Egan Range (Fig. 6) to over 540 m thick in the central Egan Range at Heusser Mountain (Fig. 7).

The Osceola Fm (Misch and Hazzard, 1962) is exposed in the northern Deep Creek, southern Snake, Schell Creek, Egan, and Pilot Ranges (Fig. 1b). It varies in thickness from ~50-350 m, and consists predominantly of micaceous maroon to olive green slate and thin graded beds of sandstone to siltstone, with minor conglomerate and limestone. In the northern Deep Creek Range, purple slate sandstone, and coarse conglomerate fill an incised erosional surface ~120 m deep and 500 m wide (Fig. 5i; Woodward, 1963). Conglomerates with quartzite, jasper, and shale rip-up clasts fill subsidiary channels (Fig. 5j,k), while fine-

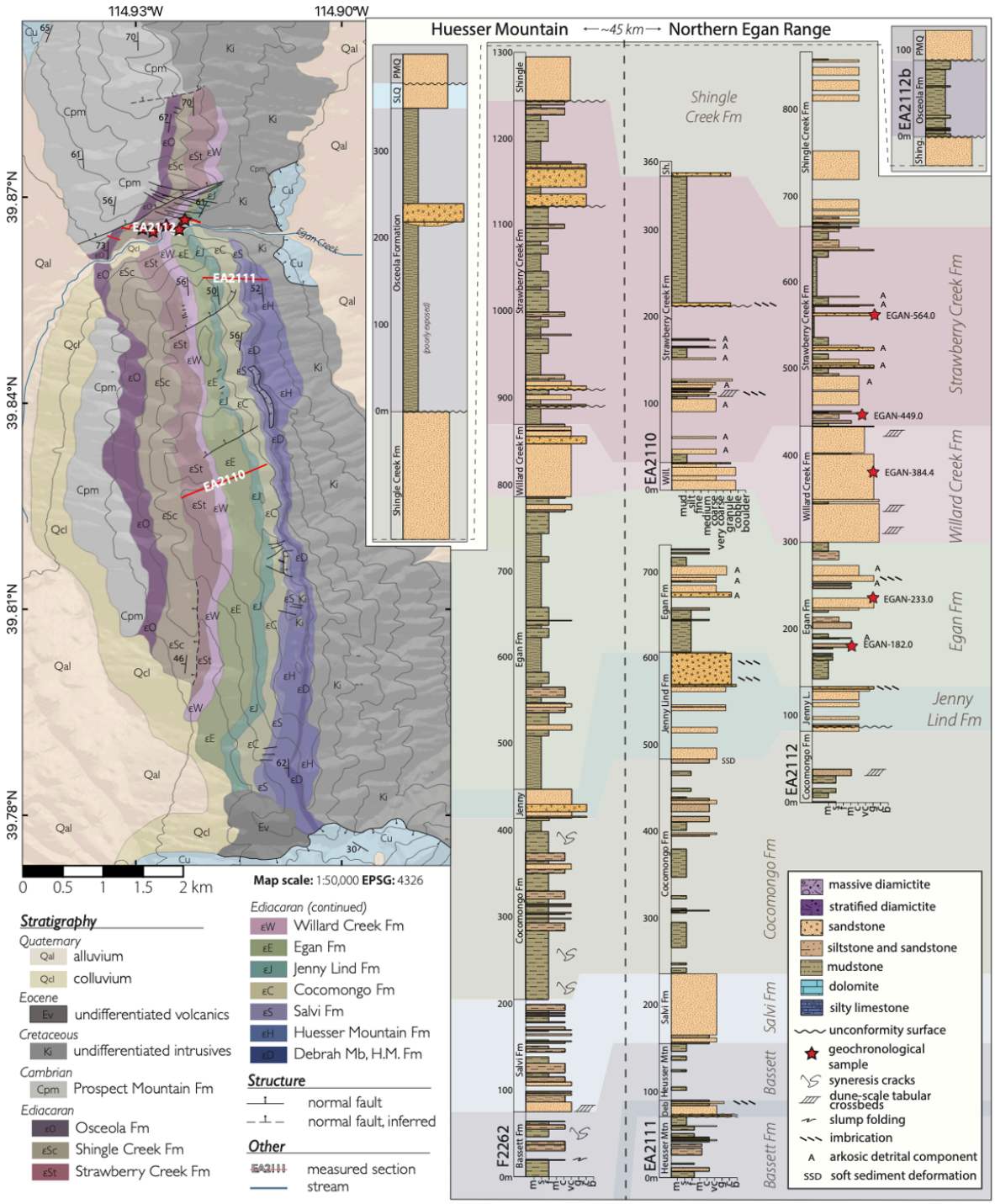

Figure 6: Geological map of the northern Egan Range. Stratigraphy of the McCoy Creek Group is shown at right, with the position of measured sections from the northern Egan Range depicted on the map. Section F2262 and the schematic Osceola Fm section were measured at Huesser Mountain, ~45km south of Cocomongo Mountain; a geological map of the Huesser Mountain field area, including the location of Section F2262, can be found in Figure 7.

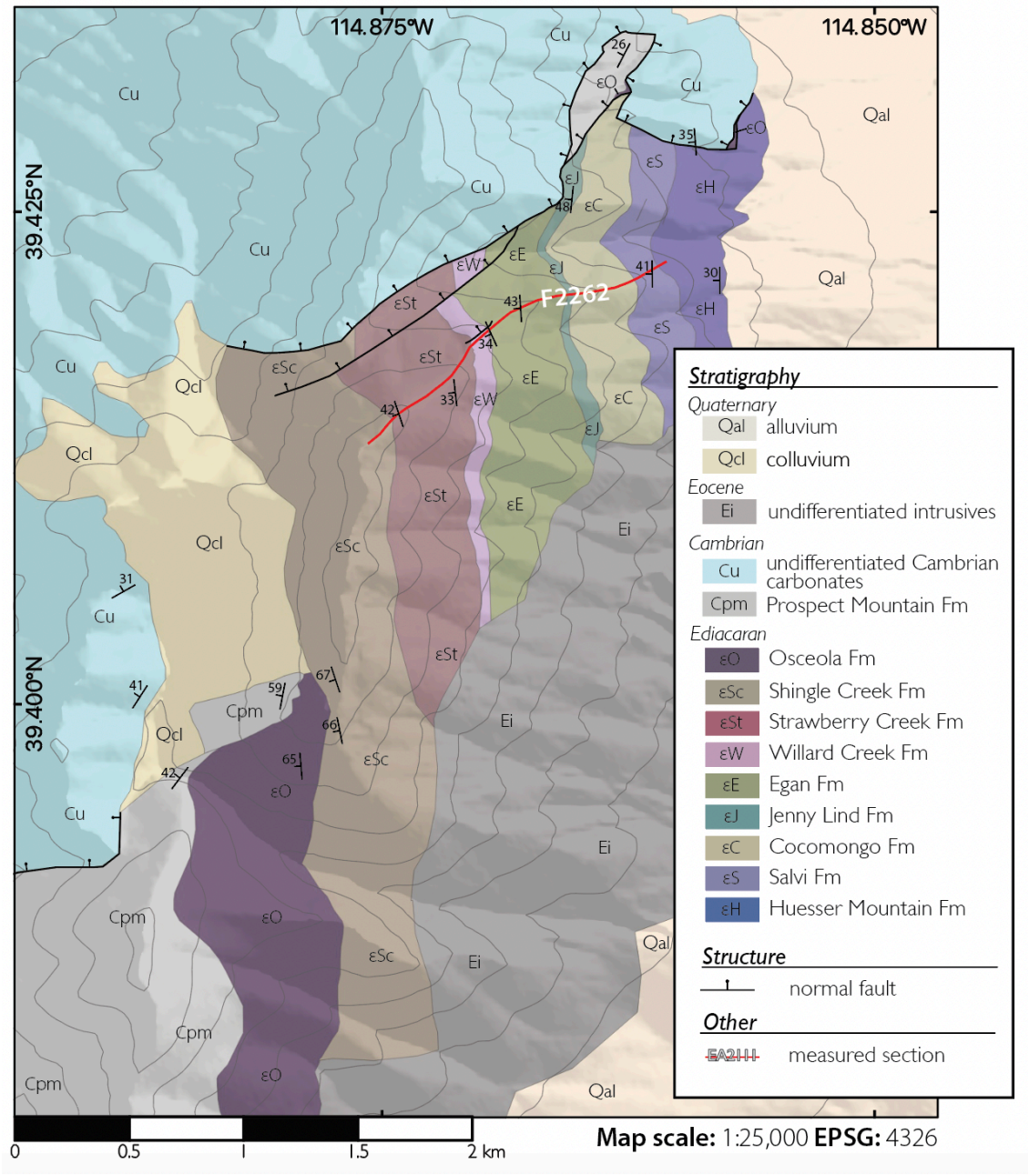

Figure 7: Geologic map of the Heusser Mountain study area (see Fig. 1b). In addition to measured section F2262, a schematic section through the Osceola Fm (Fig. 6 inset) at this locality was approximated from map relationships and geometries.

grained sediments host flute casts (Fig. 5l). Above the basal channels, the Osceola Fm is composed of ~140 m of maroon to olive green slate with thin graded beds of sandstone to siltstone. Stacked channels ~50 m deep and ~100 m wide also occur near the top of the

Osceola Fm, but below the Prospect Mountain Quartzite, and are filled with white vitreous quartzite.

In the northern Egan Range, hummocky cross-stratification occurs within slates of the uppermost Osceola Fm, which are unconformably overlain by conglomerate at the base of the Prospect Mountain Quartzite. In the Pilot Range (Fig. 1b), the upper Osceola Fm (Miller and Lush, 1994) consists of cm-scale allodapic limestone beds interbedded with thin white to light grey sandstone and maroon siltstone. Sandstone beds become more common upward, and conformably grade into starkly-white vitreous quartzite.

The Prospect Mountain Quartzite comprises a thick succession of dominantly-arenitic, tan-buff weathering quartzites that host herringbone cross stratification, lunate ripples exposed on dip-plane surfaces, and flaser bedding within finer-grained intervals. The Prospect Mountain Quartzite is underlain by an unconformity surface. Clean blue-white vitreous quartzites, likely equivalent to the Stella Lake Quartzite as defined in the Snake Range by Misch and Hazzard (1962), are intermittently present below this unconformity in the Egan, Schell Creek, northern Deep Creek, and Pilot ranges, and exhibit variably-conformable relationships with the underlying Osceola Fm.

2.4.2. Carbonate geochemistry

We report 164 carbonate carbon ($\delta^{13}C$) and oxygen ($\delta^{18}O$) isotope analyses from the Trout Creek Sequence and the McCoy Creek Gp; all carbonate carbon and oxygen isotopic data is collated in Table A1 of Appendix I. $\delta^{13}C$ values from Unit 2 of the Trout Creek Sequence vary from 0 to +4 ‰, and average +1.8 ‰. $\delta^{18}O$ values vary from -5 to -16 ‰, average -9.3 ‰, and do not show significant covariance with $\delta^{13}C$. Three measurements from

carbonates in the ~20 cm thick cap carbonate have $\delta^{13}C$ values between -4.2 and -6.4 ‰, and $\delta^{18}O$ values that average -16.5 ‰ (Table A1, Appendix 1). Two carbonate intervals within the upper portions Unit 7 of the Trout Creek Sequence were sampled for carbonate chemostratigraphy, and host $\delta^{13}C$ values between +5 and +9‰, with most values clustering between +7 and +8‰. The 8 m-thick cap dolostone of the basal Yelland Fm of the McCoy Creek Gp was sampled at 0.5 m resolution. These 16 samples have consistent $\delta^{13}C$ values between -2.3 and -2.9 ‰, and $\delta^{18}O$ values between -9.4 and -11.2 ‰ (Table A1, Appendix 1). Higher in unit B, $\delta^{13}C$ values in limestones become more variable, but remain negative and do not covary with $\delta^{18}O$.

The Osceola Fm of the McCoy Creek Gp was sampled for carbonate chemostratigraphy in the S. Snake Range and the Pilot Range. In the S. Snake Range, four samples were analyzed from the ~20 cm thick limestone horizon. The lower horizon yielded $\delta^{13}C$ values of -11.37 and -11.24 ‰, and the upper horizon yielded $\delta^{13}C$ values of -9.19 and -9.39. In the Pilot Range, $\delta^{13}C$ values increase up-section from ~-9.5 to -8.5 ‰ over a 70m interval.

2.4.3. Zircon geochronology

Sandstone samples were collected through the Trout Creek Gp and McCoy Creek Gp in the Deep Creek, Schell Creek, and Egan Ranges to compliment the previous detrital zircon geochronological dataset of Yonkee et al. (2014) from the Deep Creek Range; sample locations and new LA-ICPMS zircon data are collated in Table A2 in Appendix 1. Zircon geochronological data are graphically presented in Figures 1 and 11.

2.5. Discussion

2.5.1. Depositional environments and sequence stratigraphy

Trout Creek Sequence

The bedded diamictite and graded sandstone of Units 3-5 are typical of redeposited glaciomarine subaqueous flow tills that form in front of ice-grounding lines (Domack et al., 1999, Fielding et al., 2011). Units 3-5 host quartz-rich syn-glacial facies, putatively representing the erosional product of the underlying latest-Tonian quartz-arenite- to subarkose-dominated Uinta Mountain Gp (Dehler et al., 2010). Similar syn-glacial quartzites are present in the Pocatello Group of Idaho and Utah (Christie-Blick, 1982; Christie-Blick, 1997; Crittenden et al., 1983). There is no evidence for local grounded ice, such as ubiquitously massive diamictite or glacio-tectonism, within Units 3-5. Instead, the entire sequence is interpreted to represent distal glaciomarine subaqueous deposition below an ice-shelf, offboard of an ice-grounding line. However, the presence of granite clasts throughout Units 3-5 indicates ice grounding somewhere to the east: granite clasts in Unit 5 are consistent with progressive subglacial erosion through the Uinta Mountain Gp to basement. Paleocanyons in Big Cottonwood Canyon in the Wasatch Range of Utah are candidate subglacial channels that may have provided basement clasts (Christie-Blick, 1983; Vandyk et al., 2021). Deglaciation is recorded in the upper 30 m of Unit 5, which is dominated by stratified diamictite that includes boulder lonestones interpreted as ice rafted debris.

The Unit 5-6 contact records a major sequence boundary interpreted as a post-glacial flooding surface, and marked by a ~20 cm thick cap limestone (Fig. 3e). Unit 6 beds are flat-

bedded and graded, and are interpreted to have formed in a deep-water basin to lower slope environment, with a broad coarsening-upward trend recording the progressive filling of a starved basin. This trend continues into Unit 7, where quartzite beds, laterally discontinuous on 10-100 m length scales and bearing dune-scale tabular cross-beds, are intercalated with minor carbonate and channel-fill deposits of quartzite clast conglomerate. However, all unidirectional tabular cross-beds are closely associated with graded beds, and there is no evidence for storm wave base or shoreface deposition in any of these deposits. These facies associations are consistent with deposition on the slope of an aggrading deep-water shelf margin delta (Porebski & Steel, 2003).

Towards the top of Unit 7 in the Schell Creek Range, the stratigraphy reverts to pelite with minor diamictite-filled channels, which records glaciation in a pro-grounding line environment. Deglaciation is marked by the return of coarse-grained sedimentation with interspersed diamictite, followed by a glacio-eustatic transgression at the base of the Yelland Fm.

McCoy Creek Group

The cap dolostone at the base of the Yelland Fm records elevated alkalinity and glacio-eustatic transgression in the aftermath of glaciation. The persistence of basinal facies for hundreds of meters above the Yelland transgressive sequence, in deeper-water facies than the upper slope deposits in the pre-glacial Trout Creek Unit 7, suggests that the basin was sediment-starved during the glaciation recorded by the uppermost Unit 7 stratigraphy.

Although previous workers have affiliated Neoproterozoic quartzites of western Utah and northeastern Nevada with a fluvial or fluvio-deltaic depositional setting (Levy et al.,

1994), we propose that quartzites of the McCoy Creek Group were deposited in a marine basin-floor to slope environment: coarse clastic material was deposited within laterally discontinuous lobe complexes (e.g. Terlaky et al., 2016) associated with sediment delivery through submarine canyons and channels amidst a background of fine-grained siliciclastic sedimentation. Quartzites of the McCoy Creek Gp are similar, in terms of scale, morphology, and sedimentary structure, to slope-basin lobate sandstone deposits elsewhere along the Neoproterozoic-Cambrian western Laurentian margin (Terlaky, 2014; Fraino et al., 2022) and throughout the stratigraphic record (Walker, 1978; Normark et al., 1979; Piper et al., 1999; Deptuck et al., 2008; Prélat et al., 2009; 2010).

Quartzite-dominated units of the McCoy Creek Gp exhibit lateral thickness variability on km-scale distances across both the eastern Egan and Schell Creek range-fronts, consistent with the dimensions of lobes and lobe complexes from other slope-basin depositional systems (see Terlaky et al., 2016, and references therein). Thicker quartzite units, which are typically decameters to hundreds of meters thick, comprise stacked packages of laterally-discontinuous quartzite beds, typically between 1-3 m thick. These include massive and coarse-tail normal graded beds containing pebble and rare cobble clasts, as well as beds with dune-scale planar-tabular-crossbedding. The majority of coarse-tail graded and planar-crossbedded horizons are sharply capped by another quartzite bed with an erosive base. However, in rare instances, laminated finer-grained sandstones fining upwards into planar-laminated very fine sandstone and siltstone are found conformably above coarse-tail graded and tabular-cross-bedded quartzite packages (Fig. 5b), consistent with the idea that each package of quartzite represents a single density flow, with the delivery of subsequent erosive-

based flows removing evidence of finer-grained deposition during the terminal stages of each flow.

The close association of dune-scale tabular cross beds with underlying massive or coarse-tail normal graded beds corroborates existing models for dune-scale cross-bedding in turbidity currents (e.g. Terlaky et al., 2016), which suggest that such features are the result of sufficiently sediment-dilute flows that fall into flow stability fields permitting the formation of dune bedforms (Talling et al., 2012). Dune-scale cross-bedding has been observed in deep-marine sandstones throughout the stratigraphic record (Bouma, 1962, Allen, 1970, Sylvester and Lowe, 2004; Sumner et al., 2012; Fraino et al., 2022).

Across the length of the Schell Creek Range and Egan Range, and throughout the entire stratigraphy of the McCoy Creek Gp, foreset orientation indicates paleoflow direction directly west (Fig. 9), with limited variability across a statistically-significant sample size collected across both time (different stratigraphic heights) and space. The unimodality of paleoflow direction is consistent with the deposition of the McCoy Creek Gp in slope-basin lobate deposits forming perpendicularly to the axis of a west-facing margin.

In the upper McCoy Creek Gp, quartzite-dominated intervals become thicker, and meter- to decimeter-deep channelization and channel-fill deposits become more frequent. Although isolated channelization is observed throughout the McCoy Creek Gp above the Salvi Fm, complexes of stacked channels (each channel being between 1 and 10 m deep and 10-100m wide) are observed at the base of and throughout the Egan Fm, within the Willard Creek Fm, within the basal Strawberry Creek Fm, and within the Osceola Fm. These channels are infilled with poorly sorted pebble to boulder conglomerate, sandstone, and shale, with occasional cobble-to-boulder-scale shale rip-up clasts observed within

conglomeratic channel fill. These lithologies are consistent with facies associations observed within the proximal distributary or feeder channels of lobe complex deposits (Terlaky et al., 2016), well as those expected during the progradation of deep-water delta margin clinoforms across a low-angle slope (sensu Porebski and Steele, 2003), and indicate the progressive up-section shallowing of McCoy Creek Group facies.

This broad up-section shallowing trend continues through deposition of the Osceola Fm. Dramatic incision occurs near the top of the McCoy Creek Gp, best represented by the ~120 m deep incised paleotopography observed at the base of the Osceola Fm in the N. Deep Creek Range. The lower Osceola Fm in the Pilot Range and at Heusser Mountain in the Central Egan Range also fills incised paleotopography cut into the underlying Shingle Creek Fm. There is no evidence for subaerial exposure below or within these incisions, and they are filled with turbidites, sedimentary breccia, and ubiquitous slump folding (Fig. 5 j-l), all of which indicate a submarine origin.

However, the ~100 m scale of incision at the basal Osceola contact is much larger than that typically observed for individual channels (~ 1-10 m) within distributary channel complexes in deep-water lobe complexes. Feeder channels, which represent higher-order sediment pathways located more proximally to an avulsion node than distributary channels (Terlaky et al., 2016) may exist at scales similar to the relief observed at the basal Osceola contact. Submarine canyons incising through the slope, and acting as coarse sediment delivery pathways (e.g. Covault and Graham, 2010; Fraino et al., 2022), can also achieve or exceed similar scales of incision in a submarine environment. Thus, the sub-Osceola unconformity surface could be an expression of the continued progradation of the western

Laurentian margin or glacio-eustatic sea-level fall, and represents the formation of a submarine canyon in an upper slope or shelf-margin environment.

Canyon-fill deposits of the lowermost Osceola Fm are succeeded by graded beds of purple and green slate and fine-grained sandstone that paraconformably or disconformably overly non-incised portions of the underlying Shingle Creek Fm. Carbonate appears in the upper Osceola Fm in the S. Snake Range and the Pilot Range. In the Southern Snake Range, rip-up clasts of carbonate suggest these strata formed above storm wave base, and were associated with early cementation, further corroborating the interpretation of continued progradation and progressive shallowing through Osceola deposition. In the Pilot Range, the carbonates form cm-scale graded beds interbedded with siliciclastic turbidites, suggestive of a deeper depositional environment, likely below fair-weather wave base. In the uppermost Osceola Fm in the northern Egan Range, hummocky cross-stratification is present, again pointing towards deposition within storm wave base.

The Osceola Fm is variably unconformably, disconformably, and paraconformably overlain by the vitreous and arenitic Stella Lake Quartzite. A >50 m-deep paleocanyon incising into the Osceola Fm in the northern Deep Creek Range is filled with clean white arenitic sandstone, interpreted to be Stella Lake Quartzite. In the Pilot Range, turbidites of the uppermost Osceola Fm become coarser-grained and increasingly arenitic up-section, culminating in quartzites that are potentially correlative with the Stella Lake Fm, and suggesting the presence of a correlative conformity in deeper water sections. This relationship further highlights the need for caution when correlating individual erosional unconformity surfaces in the McCoy Creek Gp across regional or margin-wide length scales.

Fluviodeltaic sandstones of the Prospect Mountain Quartzite unconformably overly the Stella Lake Quartzite above a low-relief erosional surface observed at exposures across northeastern Nevada and western Utah, with the exception of in the northern Egan Range, where the Prospect Mountain Quartzite directly overlies the Osceola Fm. Flaser bedding, point-bar morphologies, and herringbone cross-stratification, conspicuously absent throughout the McCoy Creek Gp, are present in the Prospect Mountain Quartzite. These features are consistent with a shallow-water to subaerial depositional environment, and reflect the culmination of the broad shallowing-upward trend observed throughout the McCoy Creek Gp.

2.5.2. Age model and regional correlations

The strata of the Trout Creek Sequence and McCoy Creek Gp along the Nevada Utah border can be correlated south to the Death Valley region, and east across Utah. Neoproterozoic units in Nevada between the Egan Range and Death Valley are limited to Patterson Mountain, Caliente, and Delamar, and do not get stratigraphically lower than quartzite units potentially equivalent to the Stirling Quartzite of Death Valley and Stella Lake Quartzite of the basal Prospect Mountain Quartzite (Stewart, 1974). To the east, across Utah, Trout Creek Sequence and McCoy Creek Gp equivalents are present along a transect in the Sheeprock Mountains (Christie-Blick, 1982; Cohenour, 1959), Canyon Range (Christiansen, 1952), and the Northern (Balgord et al., 2013) and Central Wasatch Range (Ehlers and Chan, 1999; Provow et al., 2021). Situated west of the Western thrust system (Yonkee et al., 2014), the Egan, Schell Creek, and Deep Creek Ranges, Sheeprock Mountains and Canyon Range

are all allocthonous. Parautochthonous sections are present in the Wasatch mountains, which are separated from the autochthon by the Eastern thrust system (Yonkee et al., 2014).

Tonian

$\delta^{13}C$ values through Unit 2 of the Trout Creek Gp vary from 0 to +4 ‰ and average +1.8 ‰ (Fig. 8), comparable to values derived from both the marbleized Beck Spring Dolomite (Smith et al., 2016) and the Virgin Spring Limestone (Tucker, 1986) in the Panamint Range of California. The Beck Spring Dolomite has been correlated via chemostratigraphy and microfossil biostratigraphy to the Callison Lake dolostone in the Yukon, which has been bracketed with Re/Os dates on organic-rich mudstones between 752.7 ± 5.5 and 739.8 ± 6.5 Ma (Strauss et al., 2014; Rooney et al., 2015). The Virgin Spring Limestone was deposited ca. 732-717 Ma, after the Islay carbon isotope excursion, but prior to the onset of the Sturtian glaciation. We tentatively correlate Unit 2 with the Virgin Spring Limestone (Fig. 8).

Cryogenian Sturtian glaciation

Units 3-5 of the Trout Creek Sequence were previously interpreted to record two glaciations (Rodgers, 1984; Yonkee et al., 2014). Here, we demonstrate that Unit 4, comprising stratified diamictites, dropstones, and gradational upper and lower contacts, is a quartzite-rich continuation of the glacial facies of Units 3 and 5. Units 3-5 of the Trout Creek Sequence are correlative with ca. 717-662 Ma Sturtian glacial deposits throughout the Cordillera (Figs. 6, 7), which commonly show evidence for rifting and magmatism (Macdonald et al., 2022; Nelson et al., 2020; Isakson et al., 2022). A volcaniclastic horizon

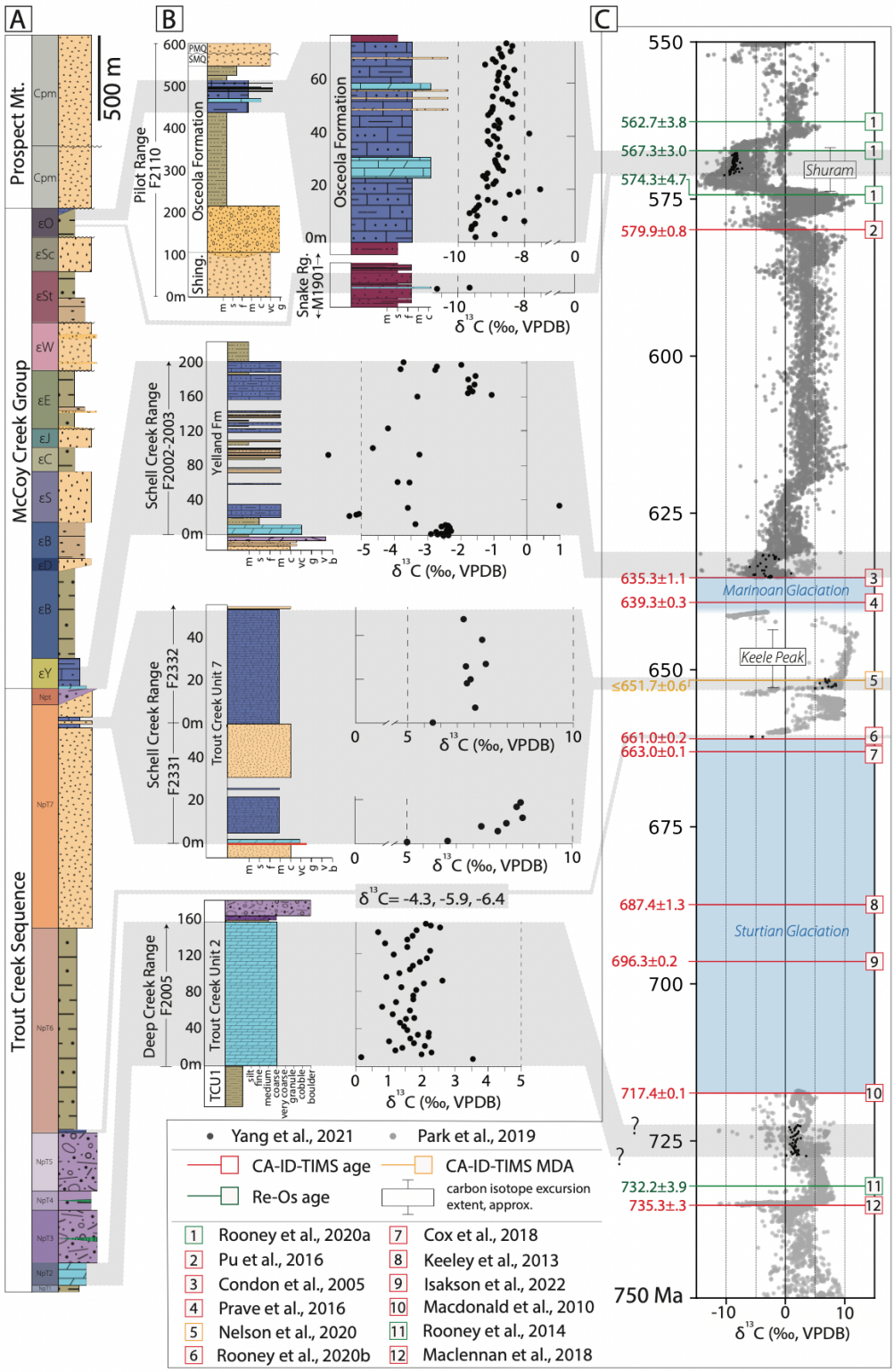

Figure 8: A) Generalized lithostratigraphy of the Trout Creek Sequence and McCoy Creek Group. **B)** Carbonate $\delta^{13}C$ chemostratigraphy of the Trout Creek Sequence and McCoy Creek Group, correlated with **C)** a compiled global Tonian-Ediacaran $\delta^{13}C$ chemostratigraphy, amalgamated from the compilations of Yang et al. (2021) and Park et al. (2019). All chemostratigraphic data from this study, including sampling location coordinates, are compiled in Table A1 in Appendix 1.

in Unit 4 yielded a young group of 9 zircons, with a population of 3 grains yielding a weighted mean age of 696.9 ± 3.4 Ma, and a population of 6 zircons yielding a weighted mean age of 688.5 ± 2.4 Ma (Fig. 1c). These populations are indistinguishable from CA-ID-TIMS ages on zircon from a tuff below the lower Scout Mountain diamictite of the Pocatello Fm (696.4 ± 0.2 Ma, Isakson et al., 2022) and from the Oxford Mountain locality of the Pocatello Fm (687.4 ± 1.3 Ma; Keeley et al., 2013) respectively, further corroborating the syn-Sturtian affiliation of these strata.

We correlate units 3-5 of the Trout Creek Sequence in the Deep Creek Range with the lower diamictite of the Otts Canyon Fm in the Sheeprock Mountains (Fig. 9). In the northern Wasatch Range, the Sturtian Glaciation is recorded by diamictites of the Perry Canyon Fm (Balgord et al., 2013), while in the central Wasatch Range, the Sturtian glaciation is recorded by an erosional unconformity between the uppermost Big Cottonwood Fm and the basal Mineral Fork Diamictite. Given the preservation of Sturtian syn-glacial strata in more margin-distal exposures and the development of a syn-Sturtian unconformity surface in Central Wasatch Range exposures, we suggest that the Sturtian ice grounding line on the western margin of Laurentia was located offboard of the paleolocation of the Big Cottonwood Canyon exposures in the Central Wasatch Range (Fig. 9).

Cryogenian non-glacial interval

Unit 6 of the Trout Creek Sequence hosts a basal cap limestone (Fig. 3e) with $\delta^{13}C$ values between -4.2 and -6.4 ‰ (Fig. 8). This range of values overlaps with those derived from the base of the Sourdough limestone in the Panamint Mountains of California, which

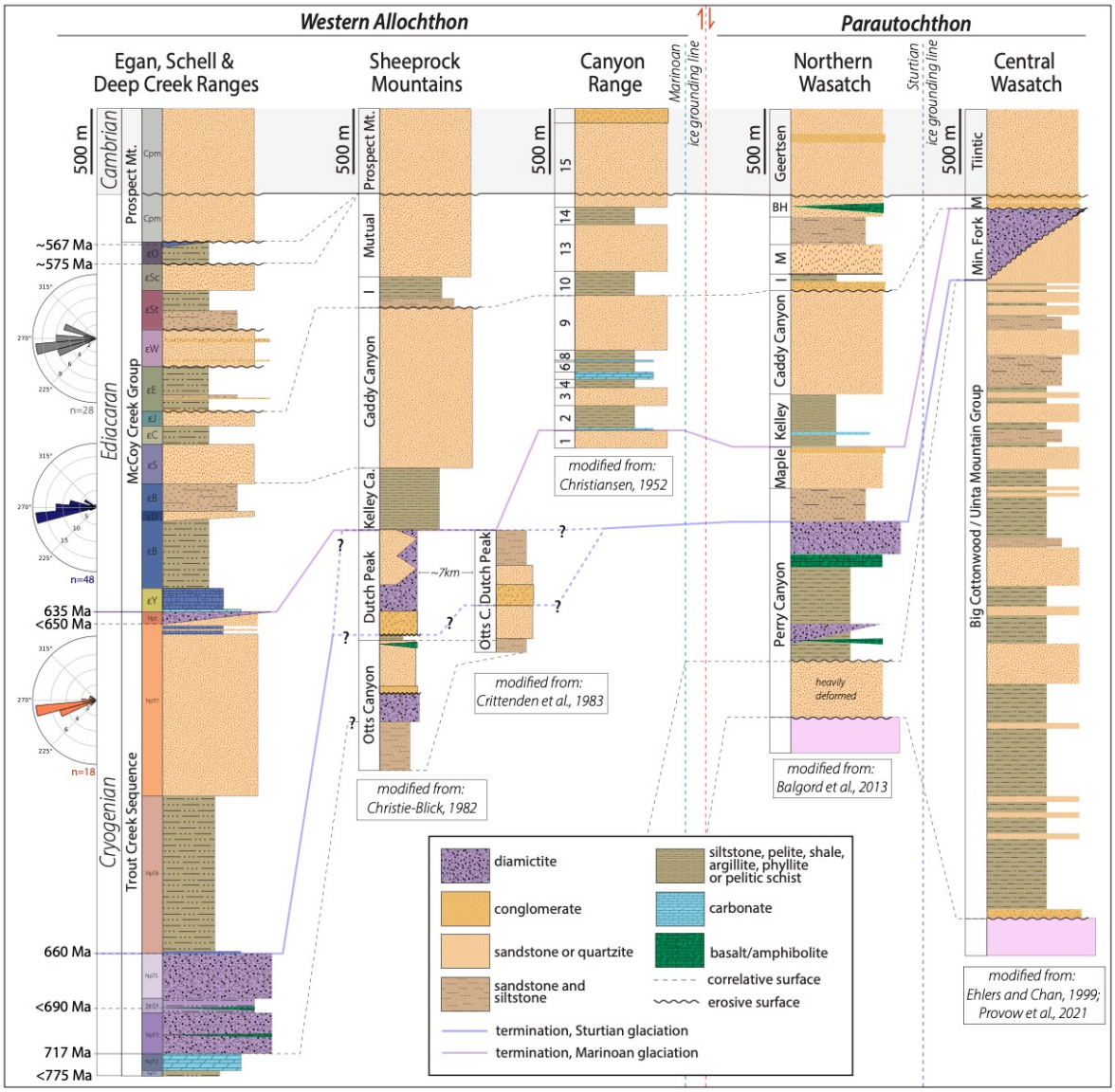

Figure 9: Regional stratigraphic correlations across an E-W transect from northeastern Nevada to central Utah. The generalized locations of each range depicted with a generalized stratigraphic column above are noted in Figure 1. Note the inferred relative positions of the Marinoan (light blue vertical dashed line) and Sturtian (dark blue vertical dashed line) ice grounding lines. Paleocurrent directions from Trout Creek Sequence Unit 7, the lower McCoy Creek Group (Salvi Fm and below), and the upper McCoy Creek Group (Jenny Lind and above) are depicted with the orange, blue, and gray rose diagrams.

has values between -4 and -6 ‰ in southern Wildrose Canyon (Nelson et al., 2021). U-Pb CA-TIMS geochronology demonstrates that the Sourdough limestone is correlative with ca. 661 Ma Sturtian cap dolostones globally (Nelson et al., 2020).

The thick, broadly shoaling upwards succession of Trout Creek Sequence Units 6 and 7 is reminiscent of the ~1300 m-thick shoaling upwards sequence of the Twitya and Keele formations of the Mackenzie Mountains (Eisbacher, 1978; Eisbacher, 1981), which culminates in cyclic fluvial delta deposits (Day et al., 2004). In the Panamint Mountains, the post-Sturtian transgressive to shallowing upwards sequence is recorded in the Middle Park to Mountain Girl submembers of the South Park Mb of the Kingston Peak Fm (Nelson et al., 2021). A similar shallowing-upwards motif is expressed in the Northern Wasatch Range, where fine-grained siliciclastic rocks of the uppermost Perry Canyon Fm are found above a carbonate and mudstone sequence that directly overlies the Perry Canyon diamictite (Balgord et al., 2013). These fine-grained siliciclastics are overlain by sandstones and conglomerates of the Maple Canyon Fm. In the Central Wasatch Range, Cryogenian non-glacial interlude strata are not preserved beneath the Marinoan diamictite of the Mineral Fork Fm, which directly overlies an erosional unconformity (Fig. 9).

$\delta^{13}C$ values from carbonates near the top of Unit 7 of the Trout Creek Sequence range between +5 and +9‰ (Fig. 11), and are equivalent to the extremely positive values in the McCoy Creek Group previously identified by Wickham & Peters (1993). These are interpreted to be correlative to similar $\delta^{13}C$ values from Cryogenian non-glacial interlude carbonates deposited during the Keele Peak positive carbon isotope excursion (Kauffman et al., 1997). Similarly positive $\delta^{13}C$ values from the Thorndike submember of the South Park Mb of the Kingston Peak Fm in the Panamint Range of Death Valley (Nelson et al., 2021) occur stratigraphically just below a zircon CA-ID-TIMS maximum depositional age constraint of ≤651.7±0.6 Ma (Nelson et al., 2020).

Cryogenian Marinoan glaciation

A Marinoan age for the diamictite at the top of Trout Creek Unit 7 is supported by its position above Sturtian-age deposits and the Keele Peak carbon isotope excursion, its association with the distinctive ca. 635 Ma (Condon et al., 2005) basal Ediacaran cap carbonate (Figs. 3j, k, 8), and its position below a broadly-correlatable lower Ediacaran transgressive interval (Fig. 9).

In the Sheeprock Mountains, the Marinoan glaciation is represented by the Dutch Peak Fm (Christie-Blick, 1997), although the basal Ediacaran cap carbonate is absent. In the Canyon Range and northern Wasatch Range in Utah, Marinoan diamictites are not present; the Marinoan horizon is inferred beneath carbonates and fine-grained siliciclastics of Unit 2 of the Canyon Range and the basal Kelly Canyon Fm of the northern Wasatch Range (Balgord et al., 2013). Given the preservation of syn-Marinoan glacial strata without evidence for grounded ice in localities in allochthonous sections, the Marinoan ice grounding line is inferred to have been located between the restored locations of the Sheeprock Mountains and the Wasatch Range (Fig. 9). Marinoan diamictite is preserved inboard of the grounding line in the central Wasatch Range, where the Mineral Fork Fm fills a paleocanyon bounded by an erosive surface that represents the combined erosive expression of the Sturtian and Marinoan glaciations.

Ediacaran

In Nevada and Utah, Unit 7 of the Trout Creek Sequence is capped by a dolostone with tubestone stromatolites (Fig. 3j,k), characteristic of basal Ediacaran cap carbonates globally (Hoffman, 2011) and, more specifically, of the Noonday Dolomite of Death Valley

(Cloud et al., 1974; Corsetti and Grotzinger, 2005). Along with the distinctive tubestone stromatolite facies, the carbon isotope profile of the dolostone to limestone of the basal Yelland Fm through the post-glacial transgression (Fig. 8) is indistinguishable from that of the Noonday Dolomite (Petterson et al., 2011). Particularly, in the thicker reef facies of the tubestone stromatolite in the Sentinel Peak Mb of the Noonday Dolostone in Death Valley, $\delta^{13}C$ values range from -1.8 to -3.5 ‰ (Petterson et al., 2011), compared to -2.3 and -2.9 ‰ in the cap dolostone of the basal Yelland Fm of the McCoy Creek Gp. Similarly, in the overlying Radcliffe Mb, limestone in deeper-water mixed carbonate-siliciclastic facies extend below -6 ‰ (Petterson et al., 2011), paralleling trends observed in the lowermost Yelland Fm.

The Yelland Fm records a post-Marinoan transgressive sequence that is identifiable in contemporaneous strata throughout Nevada and Utah. In the Schell Creek Range, the Yelland Fm shales out to black graphitic schist with minor carbonate for hundreds of meters. This distinctive sequence is interpreted to record a glacioeustatic transgression above a starved basin, and is interpreted to be correlative with grey to green slate and carbonate successions in the Kelley Canyon Fm of the Sheeprock Mountains, Units 2-8 of the Canyon Range, and the Kelley Canyon Fm of the N. Wasatch Range (Fig. 9).

The first major quartzite interval in the McCoy Creek Gp is the Salvi Fm, which is overlain by pelite of the Cocomongo Fm, and the vitreous amalgamated quartzites of the Jenny Lind Fm. Together, these strata indicate the incipience of abundant coarse clastic sedimentation in the distal slope and basinal environments of the Ediacaran margin. This interval of the McCoy Creek Gp is interpreted to be broadly equivalent to the Caddy Canyon Fm (Christie-Blick, 1982; Provow et al., 2021). These units record the first deposition of

heterogeneous siliciclastic sedimentation across the margin following the post-Marinoan transgressive sequence. In Central and Southern Idaho, the Caddy Canyon and equivalent lower Ediacaran strata consist of a mix of fine-grained siliciclastic rocks, minor conglomerate, and carbonates.

The base of the Egan Fm is marked by erosional incision and channel fill deposits at the top of the Jenny Lind Fm. Much of the lower Egan Fm is composed of laterally discontinuous channelized bodies, interpreted to be associated with the migration of distributary channels near the avulsion node of a deep marine lobe complex. This facies change may potentially be mechanistically decoupled from baselevel-change-related drivers: while it is possible that many of the lithological transitions observed in the McCoy Creek Group may have been driven by eustatic changes along the margin, we note that these transitions could also have been i) the result of short-lived erosional processes at canyon heads that can occur at a variety of baselevels (e.g. Covault and Graham, 2010), or ii) result from the stochastic migration of channels within the lobe-complex depositional system (Terlaky et al., 2016), or, higher in the section, within a deepwater shelf-margin delta (Porebski and Steele, 2003).

However, the progradation of avulsion-node-proximal lobe-complex facies of the Egan Fm atop the amalgamated terminal splay deposit quartzites of the Jenny Lind Fm is broadly consistent with a relative regression, which may be expressed in more proximal marginal settings as an unconformity surface at the top of the Caddy Canyon Fm. This surface outcrops as a conglomeratic (interpreted to be fluvial) channel fill interval above a surface interpreted as an incised valley (Levy et al., 1994).

In margin-proximal localities throughout Utah, a distinctive transition to the fine-grained siliciclastics of the Inkom Fm may be equivalent to the fine green, purple, and maroon argillite of the middle and upper Egan Fm, or to similar lithofacies present within the overlying Strawberry Creek Fm, which is separated from the Egan Fm by massive white quartzites and conglomerates of the Willard Creek Fm. It is worth noting that this correlation (Fig. 9) differs from that of Christie-Blick (1982), who drew tentative equivalencies between the Inkom Fm of central Utah and the Osceola Fm of the McCoy Creek Gp. However, Christie-Blick (1982) notes the presence of vitreous white quartzites and conglomerates interstitially associated with finer siliciclastics in the basal Inkom Fm of the Sheeprock Mountains, which is a sequence of channel-filling conglomerates broadly equivalent to the uppermost channel-fill deposits of the Caddy Canyon described elsewhere in Utah (Levy et al., 1994). This association of lithologies broadly parallels those within the Egan-Strawberry Creek interval of the McCoy Creek Gp, with the purple, green, and maroon slates of the uppermost Strawberry Creek Fm likely equivalent to the Inkom Fm.

Above the Strawberry Creek Fm, the Shingle Creek Fm comprises distinctive light purple-to-pink vitreous quartzites and jasper clast conglomerates, which we suggest is the upper slope equivalent of shelf to shoreface deposits of jasper-bearing rocks of the Mutual Fm in the Sheeprock Mountains (Christie-Blick, 1982) and the Wasatch Range, and equivalents in the Canyon Range and Beaver Mountains of central Utah (Woodward, 1968; Crittenden et al., 1971).

Erosional incision at the top of the Shingle Creek Fm/base of the Osceola Fm is potentially correlative to an amalgamated unconformity surface, situated above the Mutual and Brown's Hole formations (Fig. 7). In this scenario, the Osceola Fm does not have an

equivalent in central Utah, but is equivalent to the Rainstorm Mb of the Johnnie Fm in California . $\delta^{13}C$ values in the upper Osceola Fm (between -11 and -8‰, Fig. 6) are similar to those of the Rainstorm Mb (Bergmann et al., 2011; Witkosky and Wernicke, 2018, and references therein), and are equivalent to those of the globally-synchronous Shuram negative carbon isotope excursion, which has been constrained by Re-Os geochronology to have occurred between 574.3 ± 4.7 and 567.3 ± 3.0 Ma (Rooney et al., 2020).

Additional decimeter-scale channelization and incision observed within the upper Osceola Fm in the northern Deep Creek Range is filled by vitreous white quartzites of the Stella Lake Mb of the Prospect Mountain Fm., equivalents of which are observed to conformably overly the Shuram-correlative carbonates of the Osceola Fm in the Pilot Range. This implies the development of significant incision and erosive topography in the uppermost McCoy Creek Gp after the Shuram nadir, c.a. >567 Ma. Potential equivalents of this erosional surface are also observed in the Rainstorm Mb of the Johnnie Fm, stratigraphically above the syn-Shuram strata in the Nopah Range (Clapham & Corsetti, 2005; Giles et al., 2023).

2.5.3. Tectonic evolution of the Tonian-Cambrian western Laurentian margin

Previous studies of the McCoy Creek Gp at the eponymous locality in the Schell Creek Range interpreted the stratigraphy to be fault repeated (Misch and Hazzard, 1962). Our mapping demonstrates that this is not the case, and that the inferred fault was due to a miscorrelation between the Egan and Strawberry Creek formations (Fig. 4). This miscorrelation resulted in an underestimate of the true thickness of Ediacaran strata in the McCoy Creek Gp, and these approximate thicknesses were propagated through the literature.

Critically, in previous subsidence models, Yonkee et al. (2014) use a thickness of ~1.5 km, compared to the ~2.5 km of Ediacaran strata reported here. This underestimate, combined with errors in the age model and inferred lacunas led to an apparent Ediacaran levelling of subsidence curves, and the inference of a failed Cryogenian rift on the western Laurentian margin, followed by a second rift-drift transition in the latest Ediacaran/earliest Cambrian to accommodate thick Cambrian successions associated with the Sauk transgressive sequence.

Here, we utilize our new age model, generalized stratigraphic thicknesses informed by multiple Trout Creek Sequence/McCoy Creek Gp localities in Utah and Nevada, and interpreted depositional environments as inputs for a new tectonic subsidence model (Fig. 10a). Critically, the resultant tectonic subsidence curve is well-matched (Fig. 10b) by a single idealized thermal subsidence curve (McKenzie, 1978), with a transition to thermal subsidence occurring c.a. 656 Ma, and a crustal stretching factor (β) of ~5.9 (Fig. 10C). This model requires a single Cryogenian rifting event on the western Laurentian margin, consistent with the presence of ca. 685 Ma volcanism in Idaho (Isakson et al., 2022) and observations of syn-extensional deposition in Cryogenian strata in Death Valley (Macdonald et al., 2013; Nelson et al., 2020). The crustal stretching factor (β≈5.9) required to fit the model subsidence curve is consistent with values expected for attenuated crust adjacent to a continental margin (Roberts et al., 2013), in line with our interpretation of the study area as a distal marginal depozone. Our findings broadly agree with those of Witkosky and Wernicke (2018), who argued that margin-proximal localities (e.g. Bond et al., 1985, Levy and Christie-Blick, 1991; Yonkee et al., 2014) may not fully capture the expression of tectonic subsidence along the Laurentian rifted margin due to the development of unconformities

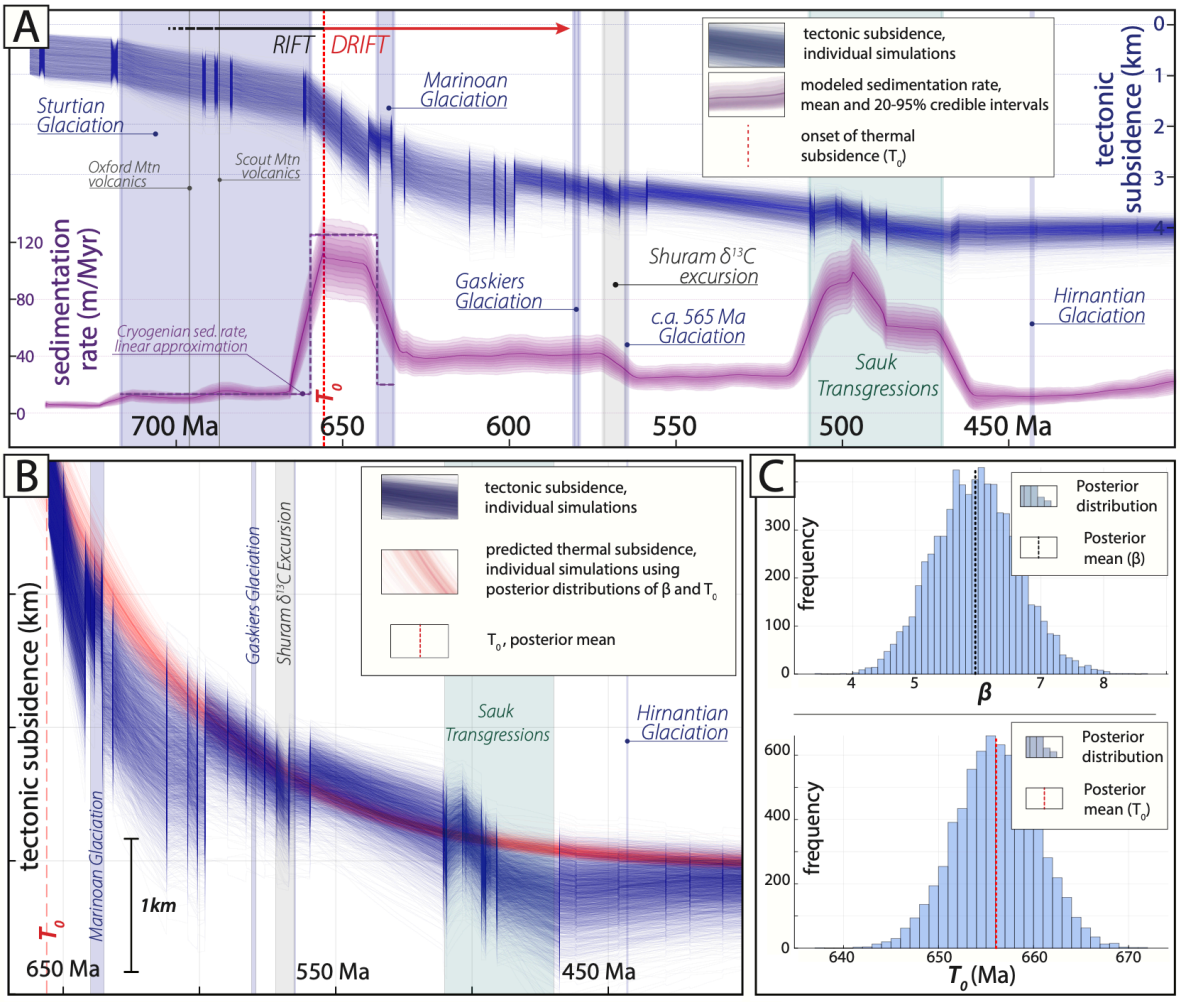

Figure 10: Model tectonic subsidence and sedimentation rates for the Trout Creek Sequence, McCoy Creek Group, and overlying units. **A)** A modeled tectonic subsidence curve, comprising 4000 individual Monte Carlo simulations (thin blue lines). Modeled undecompacted sedimentation rates, including the model mean (dark line) and 20 to 95% credible interval envelopes, are depicted in violet. Linear approximations of Cryogenian undecompacted sedimentation rates are depicted with a dashed violet line. The inferred temporal position of the transition from rifting to thermal subsidence along a passive margin (rift-drift transition) is indicated with the vertical red dashed line. **B)** A late Cryogenian transition from active rifting to thermal subsidence along the margin is corroborated by the exponentially-decreasing rates of tectonic subsidence observed in the Cryogenian-Cambrian modeled tectonic subsidence curve (blue curve), which are coincident with those predicted by idealized thermal subsidence models (sensu McKenzie, 1978), depicted by the red curve, which comprises 3000 individual simulations calculated from distributions of posterior values, output from a Bayesian backstripped tectonic subsidence model, for crustal stretching factor (β) and thermal subsidence initiation (T_0), both of which are shown in panel **C)**. The tectonic subsidence curve can be fit by a thermal subsidence curve with a rift-drift transition c.a. 656 Ma, and a crustal stretching factor of ~5.9 All model parameters and inputs are tabulated in Table A3, Appendix 1. Bayesian age, sedimentation rate, backstripping, and subsidence models utilize the SubsidenceChron.jl (Zhang et al., 2023) framework.

with temporal lacunas of unknown duration, and that more complete deeper water Ediacaran successions can account for the apparent misfit between Cryogenian rifting and Cambrian subsidence. Thus, we infer that the western Laurentian rift-drift transition occurred in the Cryogenian, and that the uppermost Trout Creek Sequence, the McCoy Creek Gp, and overlying Cambrian strata were deposited on the thermally-subsiding, progressively-prograding passive margin of western Laurentia, and that the Sauk sequence was the result of eustasy rather than local tectonic accommodation (Tasistro-Hart & Macdonald, 2023).

2.5.4. Incision and channelization on the Ediacaran western Laurentian margin

Channels and paleo-canyons in Ediacaran units in Utah and California have been previously interpreted to record singular glacioeustatic sea-level fall (Abolins et al., 2000; Christie-Blick, 1997; Levy et al., 1994; Witkosky and Wernicke, 2018; Giles et al., 2023), variably correlated with the Marinoan (Varanger) or Gaskiers glaciations. Here, we show that there are multiple levels of incision throughout the Ediacaran McCoy Creek Gp of northeastern Nevada, with major erosional features and channel complexes present at the base of the Egan, Strawberry Creek, and Osceola Fms, as well as within the Osceola Fm itself. Displaying tens to hundreds of meters of vertical relief, these individual and composite erosional features are consistent with magnitudes of glacioeustatic sea-level fall comparable to or larger than Quaternary glaciations. However, as discussed above, many of the erosional features in the McCoy Creek Gp can also be interpreted as submarine channelization events that may be partially or fully mechanistically decoupled from base-level changes associated with glacioeustasy. In the McCoy Creek Gp, the position of these surfaces >1 km above ca. 635 Ma basal Ediacaran cap carbonates rules out correlation with the Marinoan glaciation

and Snowball Earth. Instead, these surfaces occur both below and above the ca. 570-565 Ma Shuram negative carbon isotope excursion. The inferred age of several of these surfaces broadly overlap with the ca. 580 Ma Gaskiers glaciation on Avalonia (Pu et al., 2016) and the ca. 565 Ma Late Ediacaran glaciations on Cadomia and Gondwana (Linnemann et al., 2018; Linnemann et al., 2022). Thus, it is likely that some of these ca. 580-560 Ma incision and erosional surfaces were partially or fully driven by forced regressions associated with glacioeustatic sea-level fall. Given its pre-Shuram timing and large topographic magnitude, the dramatic channelization of the Shingle Creek Fm at the sub-Osceola unconformity is a particularly compelling prospect for incision associated with a syn-Gaskiers forced regression.

2.5.5. Detrital zircon provenance and recycling of Laurentian sedimentary cover

Detrital zircon age spectra through much of the upper Trout Creek Sequence and lower McCoy Creek Gp are self-similar, consistent with deposition along a prograding Ediacaran passive margin (Fig. 11). Age peaks in the detrital zircon age spectra of these rocks (Yonkee et al., 2014), as well as Tonian strata in the Wasatch Range (Dehler et al., 2010; Spencer et al., 2012) have been previously interpreted to indicate the erosion and direct transport of material from basement sources of the same age. However, the presence of an age peak in DZ spectra does not necessitate a single-stage transport pathway between a crystalline basement source and the sedimentary detrital sample, but can instead reflect erosion and redeposition of older strata. Sedimentary sources of the quartzites in the Trout Creek Sequence and McCoy Creek Gp are evidenced by extreme compositional maturity, including through the glacial sequences, and the ubiquity of quartzite clasts. We posit that

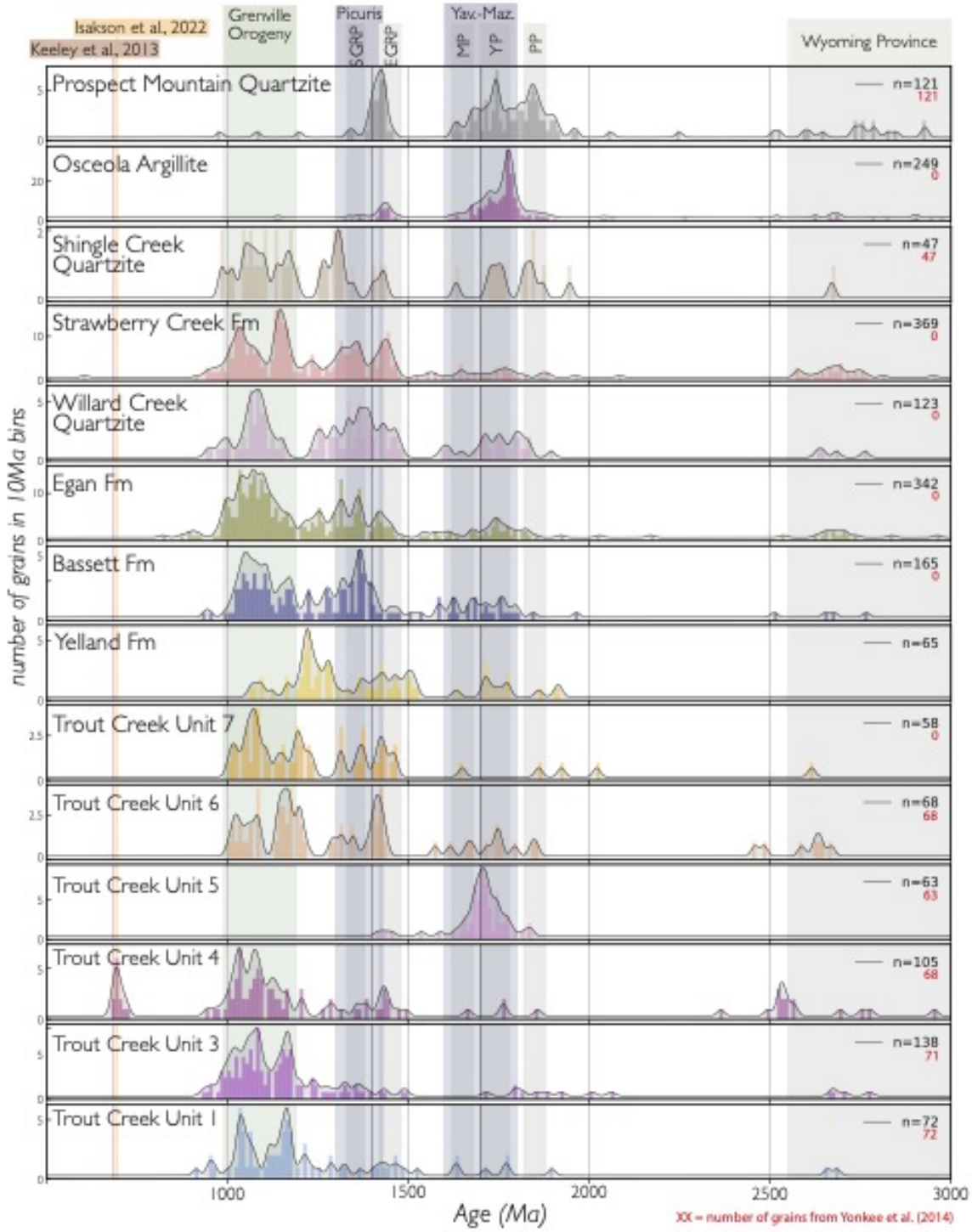

Figure 11: Normalized probability density plots depicting the relative abundances of detrital zircon (in 10Ma age bins) from units within the Trout Creek Sequence, McCoy Creek Group and Prospect Mountain Quartzite. Note the conspicuous dearth of Stenian, syn-Grenville Orogeny grains in the Osceola Formation and Prospect Mountain Quartzite. Locations sampled for geochronology are shown in previous figures, and are compiled, along with all LA-ICPMS data, in Table A2, Appendix 1. Red numbers denote the number of grains in the detrital spectrum from the data of Yonkee et al. (2014). Vertical bars span the putative ages of local volcanic sources (red and yellow bars at left), cratonic basement ages (gray bars at center and right), and the durations of putative orogenic events (green and blue vertical bars at center).

the detrital zircon age records of the Trout Creek Sequence and McCoy Creek Gp broadly record the progressive dissection, remobilization, and redeposition of the once-expansive Proterozoic sedimentary cover of cratonic Laurentia.

Many of the crystalline basement provinces that make up the core of the Laurentian craton are associated with collisional tectonic events that generated tectonic topography, abundant sediment, and accommodation space, including the ca. 1.6-1.8 Ga Yavapai-Mazatzal Orogeny (Hillenbrand et al., 2023), the ca. 1.3-1.5 Ga Picuris Orogeny (Medaris et al., 2021), and the ca. 950-1300 Ma Grenville Orogeny (Rivers, 2015). These foreland deposits are variably preserved in the stratigraphic record: the superposition of multiple events reworked and redistributed the sedimentary products of earlier collisions. The putative extent of pre- and syn-Grenville foreland basin deposits are shown in Fig. 12a.

A prominent Stenian detrital zircon age peak is present in most of the Trout Creek Sequence and lower McCoy Creek Gp, and suggests that these strata were derived from the recycling of syn- to post-Grenville sedimentary cover. Cryogenian units of the Trout Creek Sequence may have cannibalized sediments of the Big Cottonwood Canyon Fm and Uinta Mountain Gp (Dehler et al., 2010; Spencer et al., 2012; Yonkee et al., 2014). This is broadly supported by the documentation of isolated instances of putatively glacial incision through these units in the Wasatch Range: a ~500 m deep, U-shaped canyon was previously documented in Cottonwood Canyon (Christie-Blick, 1983; Christie-Blick, 1997; Vandyk et al., 2021). Although Vandyk et al. (2021) argued that this surface need not be glacial, the geometry of this surface, and its subsequent infill by glacial diamictites, makes a glacial origin the most parsimonious interpretation. The occurrence of this feature in the Wasatch Range also provides evidence against widespread Cryogenian subglacial erosion: despite

being located inboard of the putative ice grounding lines of the Sturtian and Marinoan glaciations (Fig. 9), the Big Cottonwood Canyon Fm preserves nearly 5 km of Tonian strata, only the uppermost extent of which appears to have been affected by glacial incision.

Basement-derived clasts within Cryogenian diamictites of the Trout Creek Sequence indicate that syn-glacial erosion encountered crystalline basement along the western Laurentian margin. This incision and erosion was likely isolated to ice-streams, as evidenced by the U-shaped canyons in the Wasatch Range, and may have resulted in localized variability in sediment provenance, such as that observed in Trout Creek Unit 5 (Fig. 11). Yonkee et al (2014) interpreted the lack of a Stenian peak in this interval to reflect broad subglacial erosion across the crystalline basement of the Yavapai and Mazatzal provinces. However, likelihood of some Stenian grains being encountered and transported during putative widespread subglacial erosion makes this an unlikely explanation for the lack of Grenvillian material in TCU5. We suggest that the detrital zircon spectrum of Unit 5 of the Trout Creek Sequence resulted from the localized incision of basement material and isolated delivery of this sediment by subglacial channels (melt-streams), directly analogous to sub-glacial erosion processes in modern Antarctica (Jamieson et al., 2005). Local basement highs may have also formed due to syn-sedimentary faulting during active rifting.

Following the Cryogenian, detrital zircon spectra throughout the lowermost portions of the McCoy Creek Gp record recycling and redeposition of the Proterozoic sedimentary cover of Laurentia. As Grenvillian-age cover was progressively dissected, underlying sedimentary sources were accessed (Fig. 12). The appearance of rare jasper clasts in quartzites of the Willard and Strawberry Creek formations, and abundant jasper clasts in the Shingle Creek (Fig. 5h) and Osceola formations may provide insight into the increased

dominance of a possible sediment source: the Sioux Quartzite, which extends through Minnesota, Iowa, South Dakota, and into the subsurface in Nebraska, is a pre-Grenville red orthoquartzite with abundant jasper clasts (Southwick et al., 1986; Medaris et al., 2021). In Nevada, as jasper clasts appear and become more common, Stenian detrital zircons disappear.

2.5.6. Disappearance of Stenian zircons in late Ediacaran and Early Cambrian units

Detrital zircon age spectra from the Osceola Fm and Prospect Mountain Quartzite conspicuously lack the Stenian peak observed in underlying units of the McCoy Creek Gp (Fig. 11). Similar trends are observed in equivalent units across Utah and southern Idaho (Yonkee et al., 2014). We attribute the dearth of Stenian zircon in these units to the removal of Late Mesoproterozoic and Tonian sedimentary cover, with the exception of outliers preserved in the Midcontinent rift and the ChUMP basins (e.g. Dehler et al., 2010). The emergence of the Transcontinental Arch (TCA, Sloss, 1988; Carlson, 1999) provided a topographic barrier to westerly sediment transport (Brennan et al., 2021a). The appearance of mica and carbonate in fine-grained lithologies of the Osceola Fm reflects the regional removal of supracratonic sedimentary cover and the incipience of first-generation chemical weathering and erosion of a basement source. This is further supported by the strong syn-Yavapai basement-age peak observed in the Osceola Fm DZ spectrum (Fig. 11), as Yavapai basement underlies the western flank of the portion of the TCA that is directly east of the McCoy Creek Gp (Fig. 12a).

Thus, the Osceola Fm records the exhumation the TCA east of northern Nevada, implying that relative uplift or topographic relief along a portion of the TCA inboard of had

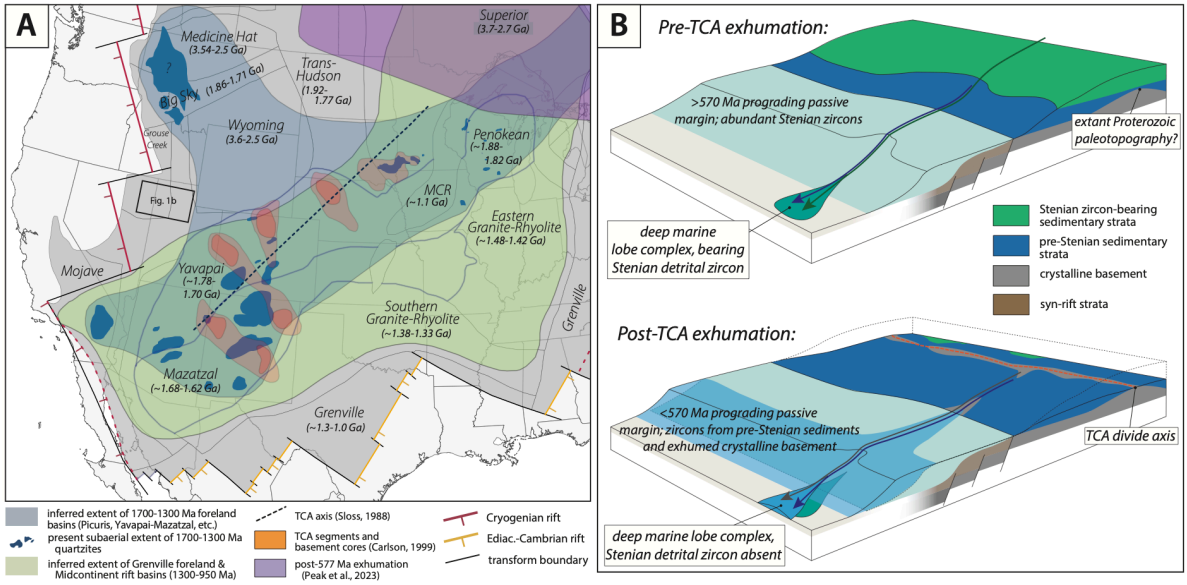

Figure 12: A) Proterozoic sedimentary cover of Laurentia, depicting the inferred extent of pre-Grenville foreland deposits (transparent blue polygon) and overlying Grenville foreland deposits (green polygon). Remnant pre-Grenville sedimentary cover is depicted in dark blue (modified from Carlson, 1970; Southwick et al., 1986; Jones III and Thrane, 2012, Medaris et al., 2021, Mahatma et al., 2022, and Brennan et al., 2021b). Remnant syn-Grenville foreland deposits, including the Middle Run Fm (Clay et al., 2021) in the subsurface of Indiana Ohio, and Kentucky, the Jacobsville Fm (Hodgin et al., 2022) of the Midcontinent, the Hazel and Lanoria Formations (Spencer et al., 2014) of Texas, the Unkar Group (Timmons et al., 2012) of Arizona, the Crystal Springs Formation (Mahon et al., 2014) of California, and distal basins in the Canadian Arctic (Rainbird et al., 2012), are not pictured here for graphical clarity, but were used to approximate the extent of the green polygon. The areal extents of basement highs of the Transcontinental Arch (modified from Carlson, 1999) and uplift and exhumation of the Canadian Shield and Superior province (modified from Peak et al., 2023) are indicated with orange and purple polygons, respectively. The extent of the Laurentian craton (dark gray) and rift positions/extents are modified from Macdonald et al., 2022 and Poole et al., 2005; ages and extents of cratonic basement provinces (italicized labels) are compiled from Clay et al., 2021 and Brennan et al., 2021b. **B)** Cartoon depicting the progressive erosion and removal of Grenvillian and pre-Grenville foreland sediments. Erosion of supracratonic sedimentary cover down to preexisting basement structures may have resulted in drainage isolation and the creation of a continental divide (TCA), preventing the westward transport of remnant Grenvillian material from the Midcontinent, and resulting in the dearth of Stenian zircons observed in late Ediacaran-Cambrian strata along the Cordilleran Laurentian margin.

occurred by ca. 570 Ma. This age constraint is significantly older than that inferred for exhumation of the TCA in Arizona and New Mexico, which is argued to have occurred ca. 525 Ma, with Stenian grains largely absent in the ≤509 Ma upper Sixtymile Fm (Holland et

al., 2023). One possible explanation for the diachroneity of Stenian zircon disappearance along the TCA axis is the variable thickness and extent of Proterozoic sedimentary cover across Laurentia. The erosional products of a relatively-synchronously-uplifted TCA would thus be spatially and temporally variable across the western Laurentian margin; thicker packages of Grenville-derived material proximal to the southern Grenville margin would plausibly take longer to erode and remove, resulting in the later disappearance of Stenian grains from basins adjacent to the southern TCA.

Our inferred age of TCA exhumation of ca. 570 Ma broadly overlaps with the timing of uplift (and ≥5-6 km of exhumation) of the sedimentary cover of the Superior Province (Fig. 12a, Peak et al., 2023) and elsewhere on the Canadian Shield (Sturrock et al., 2021), which was broadly concomitant with plume-related magmatism in the Canadian Shield and evidence of mantle upwelling under the broader Laurentian continent, including the ca. 610 Ma Central Iapetus magmatic province (Tegner et al., 2019), the ca. 585 Ma Grenville dikes and Callendar complex (Halls et al., 2015), and the ca. 540 Ma Wichita complex (Wall et al., 2021). An alternative explanation for the generation of the TCA is the tilting and beveling of the craton as a response to uplift associated with sub-cratonic mantle upwelling, resulting in the formation of a retreating escarpment that progressively eroded back to the newly-formed continental divide of the TCA axis (Fig. 12b), analogous to the Mesozoic-Cenozoic exhumation of southern Africa (Baby et al., 2020; Stanley et al., 2015). It is notable that the axis of the TCA broadly traces the known extent of Yavapai basement (Fig. 12a), which could suggest that the axis of the TCA followed preexisting structure in the Yavapai basement and its overlying erodible Proterozoic sedimentary cover (Fig. 12b). This hypothesis is consistent with the observation that the axis of the TCA was likely segmented

by E-W trending faults, which could have represented syn- or post-Iapetan rift reactivation of preexisting syn-Midcontinent-Rift-related structures (Brennan et al., 2021a; Holland et al., 2023).

2.5.7. The distal sedimentary record of Great Unconformity exhumation

Kilometer-scale Cryogenian sub-glacial erosion (Keller et al., 2019; McDannell and Keller, 2022; McDannell et al., 2021) predicts the delivery of eroded material to marginal accommodation space. Despite forming along an actively rifting margin, Sturtian glacial strata in the Trout Creek Sequence display meagre undecompacted sedimentation rates of 13.3 m/Myr. Thicknesses of Sturtian glacial deposits elsewhere in the Cordillera are highly variable and fault controlled (Macdonald et al., 2022, and references therein), but tend to be <1 km thick, which would result in undecompacted sedimentation rates of <20 m/Myr. Similarly, a conservative linear approximation of syn-Marinoan undecompacted sedimentation rates, utilizing the maximum observed thickness of the Unit 7 diamictite of 100 m and an approximate duration of the Marinoan glaciation of 5 Myr, yields a rate of 20 m/Myr. Marinoan glacial deposits are thin to absent through much of the Canadian Cordillera, but are locally present, with thicknesses also up to 100 m, in the Wildrose diamictite of California (Nelson et al., 2020), and the upper Scout Mountain member in Idaho (Isakson et al., 2022). This finding agrees with previous assessments of low sedimentation accumulation rates during Snowball Earth (Partin and Sadler, 2016; Hoffman, 2022).

The highest sedimentation rates observed in the Trout Creek Sequence and McCoy Creek Gp occur during the Cryogenian non-glacial interval (undecompacted rates of ~125

m/Myr), and can be attributed to the rapid generation of accommodation space due to active rifting and rapid thermal subsidence associated with a ca. 650 Ma rift-drift transition (Fig. 10). Similar thicknesses and a coarsening-upward succession are preserved in the nonglacial interval of NW Canada in the Twitya and Keele formations (Day et al., 2004). Thick black pelite-dominated successions above the terminations of both Cryogenian glaciations along the Nevada-Utah border are interpreted to reflect basinal starvation, with sediment supply lagging accommodation space generated by tectonic subsidence. Through both the Cryogenian nonglacial interval and the Ediacaran succession, facies assemblages record a coarsening up from basin to upper slope delta front environments, filling the starved basins.

The timing, tempo, and composition of sedimentation in both the Trout Creek Sequence and McCoy Creek Gp records the progressive removal of supra-cratonal sedimentary cover to the Laurentian margin across the Tonian-Cambrian time, supporting the notion that erosion along the Great Unconformity was diachronous. The accumulation of the thick Ediacaran McCoy Creek Gp along a distal prograding passive margin corroborates the occurrence of Ediacaran erosion and exhumation in the Canadian Shield, consistent with post-Cryogenian intracratonic exhumation driven by rifting and mantle upwelling (Sturrock et al., 2021; Peak et al., 2023). As upwelling and magmatism under Laurentia declined during the Cambrian, the Great unconformity was sealed by the Sauk eustatic transgression associated with downwelling under Gondwana (Tasistro-Hart & Macdonald, 2023).

2.6. Conclusions

New geological mapping, field observations, geochemistry, and geochronology are integrated into a new depositional model and age model for the Trout Creek Sequence and

McCoy Creek Gp of northeastern Nevada and western Utah, and establish these rocks as some of the most distal Tonian-Ediacaran strata preserved on the Cordilleran margin of western Laurentia. The Trout Creek sequence spans the Tonian-Cryogenian, and hosts strata associated with the Sturtian and Marinoan Snowball Earth glaciations and the Cryogenian non-glacial interlude. The McCoy Creek Gp spans most of the Ediacaran: dolomites of the basal Yelland Fm are equivalent to ca. 635 Ma post-Marinoan cap carbonate sequences around the world, while carbonates of the Osceola Fm host $\delta^{13}C$ values correlative with the nadir of the ca. 570-565 Ma Shuram carbon isotope excursion. Facies associations throughout much of the Trout Creek Sequence and McCoy Creek Gp demonstrate deposition on a slope to basinal environment, with coarse sandstone deposition occurring in lobe-complex deposits and distal shelf margin clinoforms. A new tectonic subsidence model for the distal Tonian-Cambrian strata of northeastern Nevada and western Utah suggests that a single Cryogenian rift, transitioning to a thermally subsiding passive margin c.a. 656 Ma, is necessary to explain the subsidence history of the western Laurentian margin. These modeling results corroborate our interpretation of McCoy Creek Gp deposition occurring along a distal prograding passive margin throughout the Ediacaran.

The distal stratigraphic record of the Trout Creek Sequence and McCoy Creek Gp provides a source-to-sink test of the timing and tempo of Laurentian exhumation and the generation of the Great Unconformity. Meagre sedimentation rates observed across both Cryogenian Snowball Earth glaciations provide a negative test of hypotheses for extensive syn-glacial exhumation and erosion. Conversely, prolonged delivery of supracratonically-sourced material throughout the Cryogenian and Ediacaran, culminating with source-isolation associated with the ca. 570 Ma exhumation of the Transcontinental Arch, supports

tectonically and geodynamically-forced exhumation and erosion across Laurentia, with the Great Unconformity surface reflecting the amalgamation of erosive events distributed across both space and time.

* * *

ACKNOWLEDGMENTS

We thank the UCSB Earth Science department for support, Ryan Eden, Sam LoBianco and Evan Monroe for their help as teaching assistants, and Phil Gans for fruitful discussions. We thank Bob Eldridge for water, chard, and memorable insights into the history of Spring Valley and the Schell Creek Range. ESCA was additionally supported by National Science Foundation (NSF) Graduate Research Fellowship Program (GRFP) 2139319 and NSF Frontier Research in Earth Science (FRES) Grant FRES1925990 to FAM.

* * *

REFERENCES, CHAPTER II

Abolins, M., Oskin, R., Prave, T., Summa, C., & Corsetti, F. (2000). Neoproterozoic glacial record in the Death Valley region, California and Nevada. https://doi.org/10.1130/0-8137-0002-7.319

Allen, J. R. L. (1970). The sequence of sedimentary structures in turbidites, with special reference to dunes. *Scottish Journal of Geology*, *6*(2), 146-161. https://doi.org/10.1144/sjg06020146

Baby, G., Guillocheau, F., Braun, J., Robin, C., & Dall'Asta, M. (2020). Solid sedimentation rates history of the Southern African continental margins: Implications for the uplift history of the South African Plateau. *Terra Nova*, *32*(1), 53-65. https://doi.org/10.1111/ter.12435

Balgord, E. A., Yonkee, W. A., Link, P. K., & Fanning, C. M. (2013). Stratigraphic, geochronologic, and geochemical record of the Cryogenian Perry Canyon Formation,

northern Utah: Implications for Rodinia rifting and snowball Earth glaciation. *Bulletin*, *125*(9-10), 1442-1467. https://doi.org/10.1130/B30860.1

Bergmann, K. D., Zentmyer, R. A., & Fischer, W. W. (2011). The stratigraphic expression of a large negative carbon isotope excursion from the Ediacaran Johnnie Formation, Death Valley. *Precambrian Research*, *188*(1-4), 45-56. https://doi.org/10.1016/j.precamres.2011.03.014

Bond, G. C., Christie-Blick, N., Kominz, M. A., & Devlin, W. J. (1985). An early Cambrian rift to post-rift transition in the Cordillera of western North America. *Nature*, *315*(6022), 742-746. https://doi.org/10.1038/315742a0

Bouma, A. H. (1962). Sedimentology of some flysch deposits. *A graphic approach to facies interpretation*, *168*.

Brennan, D. T., Mitchell, R. N., Spencer, C. J., Murphy, J. B., & Li, Z. X. (2021a). A tectonic model for the Transcontinental Arch: Progressive migration of a Laurentian drainage divide during the Neoproterozoic–Cambrian Sauk Transgression. *Terra Nova*, *33*(4), 430-440. https://doi.org/10.1111/ter.12528

Brennan, D. T., Mahoney, J. B., Li, Z. X., Link, P. K., Evans, N. J., & Johnson, T. E. (2021b). Detrital zircon U–Pb and Hf signatures of Paleo-Mesoproterozoic strata in the Priest River region, northwestern USA: A record of Laurentia assembly and Nuna tenure. *Precambrian Research*, *367*, 106445. https://doi.org/10.1016/j.precamres.2021.106445

Carlson, M. P. (1999). Transcontinental Arch—A pattern formed by rejuvenation of local features across central North America. *Tectonophysics*, *305*(1-3), 225-233. https://doi.org/10.1016/S0040-1951(99)00005-0

Carlson, M. P. (1999). Transcontinental Arch—A pattern formed by rejuvenation of local features across central North America. *Tectonophysics*, *305*(1-3), 225-233. https://doi.org/10.1016/S0040-1951(99)00005-0

Christiansen, F. W. (1952). Structure and stratigraphy of the Canyon Range, central Utah. *Geological Society of America Bulletin*, *63*(7), 717-740. https://doi.org/10.1130/0016-7606(1952)63[717:SASOTC]2.0.CO;2

Christie-Blick, N. (1982). Upper Proterozoic and Lower Cambrian rocks of the Sheeprock Mountains, Utah: regional correlation and significance. *Geological Society of America Bulletin*, *93*(8), 735-750. https://doi.org/10.1130/0016-7606(1982)93<735:UPALCR>2.0.CO;2

Christie-Blick, N. (1983). Glacial-marine and subglacial sedimentation Upper Proterozoic Mineral Fork Formation, Utah. *Glacial-marine sedimentation*, 703-776.

Christie-Blick, N. (1997). Neoproterozuic Sedimentation and Tectonics in West-Central Utah. *Brigham Young University Geology Studies*, *42*, 1-30.

Clapham, M. E., & Corsetti, F. A. (2005). Deep valley incision in the terminal Neoproterozoic (Ediacaran) Johnnie Formation, eastern California, USA: Tectonically or glacially driven?. *Precambrian Research*, *141*(3-4), 154-164. https://doi.org/10.1016/j.precamres.2005.09.002

Crittenden Jr, M. D., Schaeffer, F. E., Trimble, D. E., & Woodward, L. A. (1971). Nomenclature and correlation of some upper Precambrian and basal Cambrian sequences in western Utah and southeastern Idaho. *Geological Society of America Bulletin*, *82*(3), 581-602.

Crittenden Jr, M. D., Christie-Blick, N., & Karl Link, P. (1983). Evidence for two pulses of glaciation during the late Proterozoic in northern Utah and southeastern Idaho. *Geological Society of America Bulletin*, *94*(4), 437-450.

Campbell, I. H., & Squire, R. J. (2010). The mountains that triggered the Late Neoproterozoic increase in oxygen: the Second Great Oxidation Event. *Geochimica et Cosmochimica Acta*, *74*(15), 4187-4206. https://doi.org/10.1016/j.gca.2010.04.064

Clay, J. M., Moecher, D. P., & Bowersox, J. R. (2021). Detrital zircon U-Pb geochronology of the Precambrian Middle Run Formation (eastern North America basement): implications for Grenvillian foreland basin evolution and midcontinent rifting. *Precambrian Research*, *364*, 106332. https://doi.org/10.1016/j.precamres.2021.106332

Cloud, P., Wright, L. A., Williams, E. G., Diehl, P., & Walter, M. R. (1974). Giant stromatolites and associated vertical tubes from the Upper Proterozoic Noonday Dolomite, Death Valley region, eastern California. *Geological Society of America Bulletin*, *85*(12), 1869-1882.

Cohenour, R. E. (1959). *Sheeprock Mountains: Tooele and Juab Counties*. University of Utah.

Condon, D., Zhu, M., Bowring, S., Wang, W., Yang, A., & Jin, Y. (2005). U-Pb ages from the neoproterozoic Doushantuo Formation, China. *Science*, *308*(5718), 95-98. DOI: 10.1126/science.1107765

Corsetti, F. A., & Grotzinger, J. P. (2005). Origin and significance of tube structures in Neoproterozoic post-glacial cap carbonates: example from Noonday Dolomite, Death Valley, United States. *Palaios*, *20*(4), 348-362. https://doi.org/10.2110/palo.2003.p03-96

Covault, J. A., & Graham, S. A. (2010). Submarine fans at all sea-level stands: Tectono-morphologic and climatic controls on terrigenous sediment delivery to the deep sea. *Geology*, *38*(10), 939-942.

Cox, G. M., Isakson, V., Hoffman, P. F., Gernon, T. M., Schmitz, M. D., Shahin, S., ... & Nordsvan, A. (2018). South Australian U-Pb zircon (CA-ID-TIMS) age supports globally synchronous Sturtian deglaciation. *Precambrian Research*, *315*, 257-263. https://doi.org/10.1016/j.precamres.2018.07.007

Crittenden Jr, M. D., Christie-Blick, N., & Karl Link, P. (1983). Evidence for two pulses of glaciation during the late Proterozoic in northern Utah and southeastern Idaho. *Geological Society of America Bulletin*, *94*(4), 437-450. https://doi.org/10.1130/0016-7606(1983)94<437:EFTPOG>2.0.CO;2

Day, E. S., James, N. P., Narbonne, G. M., & Dalrymple, R. W. (2004). A sedimentary prelude to Marinoan glaciation, Cryogenian (Middle Neoproterozoic) Keele Formation, Mackenzie Mountains, northwestern Canada. *Precambrian Research*, *133*(3-4), 223-247. https://doi.org/10.1016/j.precamres.2004.05.004

Dehler, C. M., Fanning, C. M., Link, P. K., Kingsbury, E. M., & Rybczynski, D. (2010). Maximum depositional age and provenance of the Uinta Mountain Group and Big Cottonwood Formation, northern Utah: Paleogeography of rifting western Laurentia. *Bulletin*, *122*(9-10), 1686-1699. https://doi.org/10.1130/B30094.1

Deptuck, M. E., Piper, D. J., Savoye, B., & Gervais, A. (2008). Dimensions and architecture of late Pleistocene submarine lobes off the northern margin of East Corsica. *Sedimentology*, *55*(4), 869-898.

Domack, E. W., Jacobson, E. A., Shipp, S., & Anderson, J. B. (1999). Late Pleistocene–Holocene retreat of the West Antarctic Ice-Sheet system in the Ross Sea: Part 2—sedimentologic and stratigraphic signature. *Geological Society of America Bulletin*, *111*(10), 1517-1536. https://doi.org/10.1130/0016-7606(1999)111<1517:LPHROT>2.3.CO;2

Driscoll, N., & Nittrouer, C. (2000). Source to sink studies. *Margins*, *11*, 14.

Ehlers, T. A., & Chan, M. A. (1999). Tidal sedimentology and estuarine deposition of the Proterozoic Big Cottonwood Formation, Utah. *Journal of Sedimentary Research*, *69*(6), 1169-1180. https://doi.org/10.2110/jsr.69.1169

Eisbacher, G. H. (1978). *Re-definition and subdivision of the Rapitan Group, Mackenzie Mountains* (Vol. 77, No. 35). Department of Energy, Mines and Resources.

Eisbacher, G. H. (1981). Sedimentary tectonics and glacial record in the Windermere Supergroup, Mackenzie Mountains, northwestern Canada.

Fielding, C. R., Browne, G. H., Field, B., Florindo, F., Harwood, D. M., Krissek, L. A., ... & Pekar, S. F. (2011). Sequence stratigraphy of the ANDRILL AND-2A drillcore, Antarctica: A long-term, ice-proximal record of Early to Mid-Miocene climate, sea-level and glacial dynamism. *Palaeogeography, Palaeoclimatology, Palaeoecology*, *305*(1-4), 337-351.

Flowers, R. M., Macdonald, F. A., Siddoway, C. S., & Havranek, R. (2020). Diachronous development of great unconformities before Neoproterozoic snowball Earth. *Proceedings of the National Academy of Sciences*, *117*(19), 10172-10180. https://doi.org/10.1073/pnas.1913131117

Fraino, P. E., Arnott, R. W. C., & Navarro, L. (2022). The influence of sediment supply on the stratigraphic evolution of an ancient passive margin deep-marine slope channel system, Windermere Supergroup, British Columbia, Canada. *Journal of Sedimentary Research*, *92*(3), 232-256. https://doi.org/10.2110/jsr.2021.007

Gans, P. B. (1989). *Synextensional magmatism in the Basin and Range province: A case study from the eastern Great Basin* (Vol. 233). Geological Society of America.

Giles, S. M., Christie-Blick, N., & Lankford-Bravo, D. F. (2023). A subaerial origin for the mid-Ediacaran Johnnie valleys, California and Nevada: Implications for a diachronous onset of the Shuram excursion. *Precambrian Research*, *397*, 107187.

Greene, D. C. (2014). The Confusion Range, west-central Utah: Fold-thrust deformation and a western Utah thrust belt in the Sevier hinterland. *Geosphere*, *10*(1), 148-169. https://doi.org/10.1130/GES00972.1

Halls, H. C., Lovette, A., Hamilton, M., & Söderlund, U. (2015). A paleomagnetic and U–Pb geochronology study of the western end of the Grenville dyke swarm: Rapid changes in paleomagnetic field direction at ca. 585 Ma related to polarity reversals?. *Precambrian Research*, *257*, 137-166.

Hillenbrand, I. W., Karlstrom, K. E., Williams, M. L., Gilmer, A., Premo, W., & Davis, P. (2023). Geochemical evidence for evolving Proterozoic crustal thickness and orogenic styles in southwestern Laurentia. *Earth and Planetary Science Letters*, *622*, 118417.https://doi.org/10.1016/j.epsl.2023.118417

Hodgin, E. B., Swanson-Hysell, N. L., DeGraff, J. M., Kylander-Clark, A. R., Schmitz, M. D., Turner, A. C., ... & Stolper, D. A. (2022). Final inversion of the Midcontinent Rift during the Rigolet Phase of the Grenvillian Orogeny. *Geology*, *50*(5), 547-551.

Hoffman, P. F. (2011). Strange bedfellows: glacial diamictite and cap carbonate from the Marinoan (635 Ma) glaciation in Namibia. *Sedimentology*, *58*(1), 57-119. https://doi.org/10.1111/j.1365-3091.2010.01206.x

Hoffman, P. F. (2022). Glacial erosion on a snowball Earth: testing for bias in flux balance, geographic setting, and tectonic regime. *Canadian Journal of Earth Sciences*.

Holland, M. E., Mohr, M., Schmitz, M., Madronich, L., & Karlstrom, K. Source-to-sink tandem geochronology reveals tectonic influences on the Cambrian Transcontinental Arch of Laurentia. *Terra Nova*. https://doi.org/10.1111/ter.12692

Horstwood, M.S., Košler, J., Gehrels, G., Jackson, S.E., McLean, N.M., Paton, C., Pearson, N.J., Sircombe, K., Sylvester, P., Vermeesch, P. and Bowring, J.F., 2016, Community-derived standards for LA-ICP-MS U-(Th-) Pb geochronology–Uncertainty propagation, age interpretation and data reporting: Geostandards and Geoanalytical Research, 40(3), p. 311-332.

Husson, J. M., & Peters, S. E. (2017). Atmospheric oxygenation driven by unsteady growth of the continental sedimentary reservoir. *Earth and Planetary Science Letters*, *460*, 68-75. https://doi.org/10.1016/j.epsl.2016.12.012

Isakson, V. H., Schmitz, M. D., Dehler, C. M., Macdonald, F. A., & Adolph Yonkee, W. (2022). A robust age model for the Cryogenian Pocatello Formation of southeastern Idaho (northwestern USA) from tandem in situ and isotope dilution U-Pb dating of volcanic tuffs and epiclastic detrital zircons. *Geosphere*, *18*(2), 825-849. https://doi.org/10.1130/GES02437.1

Jackson, S.E., Pearson, N.J., Griffin, W.L. and Belousova, E.A., 2004, The application of laser ablation-inductively coupled plasma-mass spectrometry to in situ U–Pb zircon geochronology: Chemical geology, 211(1-2), p. 47-69.

Jamieson, S. S. R., Hulton, N. R. J., Sugden, D. E., Payne, A. J., & Taylor, J. (2005). Cenozoic landscape evolution of the Lambert basin, East Antarctica: the relative role of rivers and ice sheets. *Global and Planetary Change*, *45*(1-3), 35-49. https://doi.org/10.1016/j.gloplacha.2004.09.015

Jones III, J. V., & Thrane, K. (2012). Correlating Proterozoic synorogenic metasedimentary successions in southwestern Laurentia: New insights from detrital zircon U-Pb geochronology of Paleoproterozoic quartzite and metaconglomerate in central and northern Colorado, USA. *Rocky Mountain Geology*, *47*(1), 1-35. https://doi.org/10.2113/gsrocky.47.1.1

Karlstrom, K. E., & Timmons, J. M. (2012). Many unconformities make one 'Great Unconformity'. *Grand Canyon Geology; Two Billion Years of Earth's History*, 73-79.

Kaufman, A. J., Knoll, A. H., & Narbonne, G. M. (1997). Isotopes, ice ages, and terminal Proterozoic earth history. *Proceedings of the National Academy of Sciences*, *94*(13), 6600-6605. https://doi.org/10.1073/pnas.94.13.6600

Keller, C. B., Husson, J. M., Mitchell, R. N., Bottke, W. F., Gernon, T. M., Boehnke, P., ... & Peters, S. E. (2019). Neoproterozoic glacial origin of the Great Unconformity. *Proceedings of the National Academy of Sciences*, *116*(4), 1136-1145. https://doi.org/10.1073/pnas.180435011

Keeley, J. A., Link, P. K., Fanning, C. M., & Schmitz, M. D. (2013). Pre-to synglacial rift-related volcanism in the Neoproterozoic (Cryogenian) Pocatello Formation, SE Idaho: New

SHRIMP and CA-ID-TIMS constraints. *Lithosphere*, *5*(1), 128-150. https://doi.org/10.1130/L226.1

Kylander-Clark, A.R., Hacker, B.R. and Cottle, J.M., 2013, Laser-ablation split-stream ICP petrochronology: Chemical Geology, 345, p. 99-112.

Levy, M., & Christie-Blick, N. (1991). Tectonic subsidence of the early Paleozoic passive continental margin in eastern California and southern Nevada. *Geological Society of America Bulletin*, *103*(12), 1590-1606.

Levy, M., Christie-Blick, N., & Link, P. K. (1994). Neoproterozoic incised valleys of the eastern Great Basin, Utah and Idaho: Fluvial response to changes in depositional base level.

Linnemann, U., Pidal, A. P., Hofmann, M., Drost, K., Quesada, C., Gerdes, A., ... & Horak, J. (2018). A~ 565 Ma old glaciation in the Ediacaran of peri-Gondwanan West Africa. *International Journal of Earth Sciences*, *107*, 885-911.

Linnemann, U., Hofmann, M., Gärtner, A., Gärtner, J., Zieger, J., Krause, R., ... & Vickers-Rich, P. (2022). An Upper Ediacaran Glacial Period in Cadomia: the Granville tillite (Armorican Massif)–sedimentology, geochronology and provenance. *Geological Magazine*, *159*(7), 999-1013.

Long, S. P., Lee, J., & Blackford, N. R. (2022). The low-angle breakaway system for the Northern Snake Range décollement in the Schell Creek and Duck Creek Ranges, eastern Nevada, USA: Implications for displacement magnitude. *Geosphere*, *18*(4), 1194-1222.

Lund, K. (2008). Geometry of the Neoproterozoic and Paleozoic rift margin of western Laurentia: Implications for mineral deposit settings. *Geosphere*, *4*(2), 429-444.

Macdonald, F. A., Schmitz, M. D., Crowley, J. L., Roots, C. F., Jones, D. S., Maloof, A. C., ... & Schrag, D. P. (2010). Calibrating the cryogenian. *science*, *327*(5970), 1241-1243.

Macdonald, F. A., Prave, A. R., Petterson, R., Smith, E. F., Pruss, S. B., Oates, K., ... & Fallick, A. E. (2013). The Laurentian record of Neoproterozoic glaciation, tectonism, and eukaryotic evolution in Death Valley, California. *Bulletin*, *125*(7-8), 1203-1223. https://doi.org/10.1130/B30789.1

Macdonald, F. A., Yonkee, W. A., Flowers, R. M., & Swanson-Hysell, N. L. (2022). Neoproterozoic of laurentia. In *Laurentia: Turning Points in the Evolution of a Continent*. Geological Society of America. https://doi.org/10.1130/2022.1220(19)

MacLennan, S., Park, Y., Swanson-Hysell, N., Maloof, A., Schoene, B., Gebreslassie, M., ... & Haileab, B. (2018). The arc of the Snowball: U-Pb dates constrain the Islay anomaly and the initiation of the Sturtian glaciation. *Geology*, *46*(6), 539-542. https://doi.org/10.1130/G40171.1

Mahatma, A. A., Kuiper, Y. D., & Holm-Denoma, C. S. (2022). Evidence for the~ 1.4 Ga Picuris orogeny in the central Colorado Front Range. *Precambrian Research*, *382*, 106878. https://doi.org/10.1016/j.precamres.2022.106878

Mahon, R. C., Dehler, C. M., Link, P. K., Karlstrom, K. E., & Gehrels, G. E. (2014). Geochronologic and stratigraphic constraints on the Mesoproterozoic and Neoproterozoic Pahrump Group, Death Valley, California: A record of the assembly, stability, and breakup of Rodinia. *Bulletin*, *126*(5-6), 652-664.

McDannell, K. T., Keller, C. B., Guenthner, W. R., Zeitler, P. K., & Shuster, D. L. (2022). Thermochronologic constraints on the origin of the Great Unconformity. *Proceedings of the National Academy of Sciences*, *119*(5), e2118682119. https://doi.org/10.1073/pnas.2118682119

McDannell, K. T., & Keller, C. B. (2022). Cryogenian glacial erosion of the central Canadian Shield: The "late" Great Unconformity on thin ice. *Geology*, *50*(12), 1336-1340. https://doi.org/10.1130/G50315.1

McKenzie, D. (1978). Some remarks on the development of sedimentary basins. *Earth and Planetary science letters*, *40*(1), 25-32. https://doi.org/10.1016/0012-821X(78)90071-7

Medaris Jr, L. G., Singer, B. S., Jicha, B. R., Malone, D. H., Schwartz, J. J., Stewart, E. K., ... & Reiners, P. W. (2021). Early Mesoproterozoic evolution of midcontinental Laurentia: Defining the geon 14 Baraboo orogeny. *Geoscience Frontiers*, *12*(5), 101174. https://doi.org/10.1016/j.gsf.2021.101174

Miller, E. L., Gans, P. B., & Garing, J. (1983). The Snake Range decollement: An exhumed mid-Tertiary ductile-brittle transition. *Tectonics*, *2*(3), 239-263.

Miller, D. M., & Lush, A. P. (1994). *Geologic map of the pilot peak quadrangle, box Elder County, Utah, and Elko County, Nevada*. The Survey.

Miller, E. L., Gans, P. B., Wright, J. E., Sutter, J. F., & Ernst, W. G. (1988). Metamorphic history of the east-central Basin and Range province: Tectonic setting and relationship to magmatism. *Metamorphism and crustal evolution, western conterminous United States, Rubey*, *7*, 649-682.

Miller, E. L., & Gans, P. B. (1989). Cretaceous crustal structure and metamorphism in the hinterland of the Sevier thrust belt, western US Cordillera. *Geology*, *17*(1), 59-62. https://doi.org/10.1130/0091-7613(1989)017<0059:CCSAMI>2.3.CO;2

Misch, P., & Hazzard, J. C. (1962). Stratigraphy and metamorphism of late Precambrian rocks in central northeastern Nevada and adjacent Utah. *AAPG Bulletin*, *46*(3), 289-343. https://doi.org/10.1306/BC743823-16BE-11D7-8645000102C1865D

Monroe, E. B. (2023). *Late Cretaceous Tectonic Evolution of the Deep Creek-Kern Mountains, Eastern Nevada and Western Utah: Magmatically Induced Large-Scale Folding, Dynamothermal Metamorphism and Ductile Strain at Mid-to Upper-Crustal Levels in the Sevier Hinterland* (Doctoral dissertation, University of California, Santa Barbara).

Nelson, L. L., Smith, E. F., Hodgin, E. B., Crowley, J. L., Schmitz, M. D., & Macdonald, F. A. (2020). Geochronological constraints on Neoproterozoic rifting and onset of the Marinoan glaciation from the Kingston Peak Formation in Death Valley, California (USA). *Geology*, *48*(11), 1083-1087. https://doi.org/10.1130/G47668.1

Nelson, L. L., Ahm, A. S. C., Macdonald, F. A., Higgins, J. A., & Smith, E. F. (2021). Fingerprinting local controls on the Neoproterozoic carbon cycle with the isotopic record of Cryogenian carbonates in the Panamint Range, California. *Earth and Planetary Science Letters*, *566*, 116956. https://doi.org/10.1016/j.epsl.2021.116956

Normark, W. R., Piper, D. J. W., & Hess, G. R. (1979). Distributary channels, sand lobes, and mesotopography of Navy Submarine Fan, California Borderland, with applications to ancient fan sediments. *Sedimentology*, *26*(6), 749-774.

Nyberg, B., Helland-Hansen, W., Gawthorpe, R. L., Sandbakken, P., Eide, C. H., Sømme, T., ... & Leiknes, S. (2018). Revisiting morphological relationships of modern source-to-sink segments as a first-order approach to scale ancient sedimentary systems. *Sedimentary Geology*, *373*, 111-133.

Park, Y., Swanson-Hysell, N. L., MacLennan, S. A., Maloof, A. C., Gebreslassie, M., Tremblay, M. M., ... & Haileab, B. (2020). The lead-up to the Sturtian Snowball Earth: Neoproterozoic chemostratigraphy time-calibrated by the Tambien Group of Ethiopia. *GSA Bulletin*, *132*(5-6), 1119-1149.

Partin, C. A., & Sadler, P. M. (2016). Slow net sediment accumulation sets snowball Earth apart from all younger glacial episodes. *Geology*, *44*(12), 1019-1022. https://doi.org/10.1130/G38350.1

Paton, C., Woodhead, J.D., Hellstrom, J.C., Hergt, J.M., Greig, A. and Maas, R., 2010, Improved laser ablation U-Pb zircon geochronology through robust downhole fractionation correction: Geochemistry, Geophysics, Geosystems, *11*(3).

Peak, B. A., Flowers, R. M., & Macdonald, F. A. (2023). Ediacaran-Ordovician tectonic and geodynamic drivers of Great Unconformity exhumation on the southern Canadian Shield. *Earth and Planetary Science Letters*, *619*, 118334. https://doi.org/10.1016/j.epsl.2023.118334

Peters, S. E., & Gaines, R. R. (2012). Formation of the 'Great Unconformity'as a trigger for the Cambrian explosion. *Nature*, *484*(7394), 363-366. https://doi.org/10.1038/nature10969

Petterson, R., Prave, A. R., Wernicke, B. P., & Fallick, A. E. (2011). The Neoproterozoic Noonday Formation, Death Valley region, California. *Bulletin*, *123*(7-8), 1317-1336. https://doi.org/10.1130/B30281.1

Piper, Hiscott, & Normark. (1999). Outcrop-scale acoustic facies analysis and latest Quaternary development of Hueneme and Dume submarine fans, offshore California. *Sedimentology*, *46*(1), 47-78.

Poole, F. G., Perry, W. J., Madrid, R. J., & Amaya-Martínez, R. (2005). Tectonic synthesis of the Ouachita-Marathon-Sonora orogenic margin of southern Laurentia: Stratigraphic and structural implications for timing of deformational events and plate-tectonic model. https://doi.org/10.1130/0-8137-2393-0.543

Porębski, S. J., & Steel, R. J. (2003). Shelf-margin deltas: their stratigraphic significance and relation to deepwater sands. *Earth-Science Reviews*, *62*(3-4), 283-326. https://doi.org/10.1016/S0012-8252(02)00161-7

Powell, J. W. (1875). *Exploration of the Colorado River of the West and its Tributaries*.

Prave, A. R. (1999). Two diamictites, two cap carbonates, two δ13C excursions, two rifts: the Neoproterozoic Kingston Peak Formation, Death Valley, California. *Geology*, *27*(4), 339-342.

Prave, A. R., Condon, D. J., Hoffmann, K. H., Tapster, S., & Fallick, A. E. (2016). Duration and nature of the end-Cryogenian (Marinoan) glaciation. *Geology*, *44*(8), 631-634. https://doi.org/10.1130/G38089.1

Prélat, A., Hodgson, D. M., & Flint, S. S. (2009). Evolution, architecture and hierarchy of distributary deep-water deposits: a high-resolution outcrop investigation from the Permian Karoo Basin, South Africa. *Sedimentology*, *56*(7), 2132-2154.

Prelat, A., Covault, J. A., Hodgson, D. M., Fildani, A., & Flint, S. S. (2010). Intrinsic controls on the range of volumes, morphologies, and dimensions of submarine lobes. *Sedimentary Geology*, *232*(1-2), 66-76.

Provow, A. W., Newell, D. L., Dehler, C. M., Ault, A. K., Yonkee, W. A., Thomson, S. N., ... & Billi, A. (2021). Revised maximum depositional age for the Ediacaran Browns Hole Formation: Implications for western Laurentia Neoproterozoic stratigraphy. *Lithosphere*, *2021*(1). https://doi.org/10.2113/2021/1757114

Pu, J. P., Bowring, S. A., Ramezani, J., Myrow, P., Raub, T. D., Landing, E., ... & Macdonald, F. A. (2016). Dodging snowballs: Geochronology of the Gaskiers glaciation and the first appearance of the Ediacaran biota. *Geology*, *44*(11), 955-958. https://doi.org/10.1130/G38284.1

Rainbird, R., Cawood, P., & Gehrels, G. (2011). The great Grenvillian sedimentation episode: record of supercontinent Rodinia's assembly. *Tectonics of sedimentary basins: Recent advances*, 583-601. https://doi.org/10.1002/9781444347166.ch29

Rivers, T. (2015). Tectonic setting and evolution of the Grenville Orogen: An assessment of progress over the last 40 years. *Geoscience Canada*, *42*(1), 77-124.

Roberts, A. M., Kusznir, N. J., Corfield, R. I., Thompson, M., & Woodfine, R. (2013). Integrated tectonic basin modelling as an aid to understanding deep-water rifted continental margin structure and location. https://doi.org/10.1144/petgeo2011-046

Rodgers, D. W. (1984). Stratigraphy, correlation, and depositional environments of Upper Proterozoic and Lower Cambrian rocks of the southern Deep Creek Range, Utah.

Rooney, A. D., Macdonald, F. A., Strauss, J. V., Dudás, F. Ö., Hallmann, C., & Selby, D. (2014). Re-Os geochronology and coupled Os-Sr isotope constraints on the Sturtian snowball Earth. *Proceedings of the National Academy of Sciences*, *111*(1), 51-56. https://doi.org/10.1073/pnas.1317266110

Rooney, A. D., Strauss, J. V., Brandon, A. D., & Macdonald, F. A. (2015). A Cryogenian chronology: Two long-lasting synchronous Neoproterozoic glaciations. *Geology*, *43*(5), 459-462. https://doi.org/10.1130/G36511.1

Rooney, A. D., Cantine, M. D., Bergmann, K. D., Gómez-Pérez, I., Al Baloushi, B., Boag, T. H., ... & Strauss, J. V. (2020a). Calibrating the coevolution of Ediacaran life and environment. *Proceedings of the National Academy of Sciences*, *117*(29), 16824-16830. https://doi.org/10.1073/pnas.2002918117

Rooney, A. D., Yang, C., Condon, D. J., Zhu, M., & Macdonald, F. A. (2020b). U-Pb and Re-Os geochronology tracks stratigraphic condensation in the Sturtian snowball Earth aftermath. *Geology*, *48*(6), 625-629. https://doi.org/10.1130/G47246.1

Ross, G. M. (1991). Tectonic setting of the Windermere Supergroup revisited. *Geology*, *19*(11), 1125-1128.

Schneck, W. M. (1986). *Lithostratigraphy of the McCoy Creek Group and Prospect Mountain Quartzite (upper Proterozoic and Lower Cambrian), Egan and Cherry Creek Ranges, White Pine County, Nevada* (Doctoral dissertation, Eastern Washington University).

Sloss, L. L. (1988). Tectonic evolution of the craton in Phanerozoic time. *The Geology of North America*, *2*, 25-51.

Smith, E. F., MacDonald, F. A., Crowley, J. L., Hodgin, E. B., & Schrag, D. P. (2016). Tectonostratigraphic evolution of the c. 780–730 Ma Beck Spring Dolomite: Basin Formation in the core of Rodinia. *Geological Society, London, Special Publications*, *424*(1), 213-239. https://doi.org/10.1144/SP424.6

Southwick, D. L., Morey, G. B., & Mossler, J. H. (1986). Fluvial origin of the lower Proterozoic Sioux Quartzite, southwestern Minnesota. *Geological Society of America Bulletin*, *97*(12), 1432-1441. https://doi.org/10.1130/0016-7606(1986)97<1432:FOOTLP>2.0.CO;2

Spencer, C. J., Hoiland, C. W., Harris, R. A., Link, P. K., & Balgord, E. A. (2012). Constraining the timing and provenance of the Neoproterozoic Little Willow and Big Cottonwood Formations, Utah: Expanding the sedimentary record for early rifting of Rodinia. *Precambrian Research*, *204*, 57-65. https://doi.org/10.1016/j.precamres.2012.02.009

Spencer, C. J., Prave, A. R., Cawood, P. A., & Roberts, N. M. (2014). Detrital zircon geochronology of the Grenville/Llano foreland and basal Sauk Sequence in west Texas, USA. *Bulletin*, *126*(7-8), 1117-1128.

Spencer, C. J., Kirkland, C. L., & Taylor, R. J. (2016). Strategies towards statistically robust interpretations of in situ U–Pb zircon geochronology. *Geoscience Frontiers*, *7*(4), 581-589.

Stanley, J. R., Flowers, R. M., & Bell, D. R. (2015). Erosion patterns and mantle sources of topographic change across the southern A frican P lateau derived from the shallow and deep records of kimberlites. *Geochemistry, Geophysics, Geosystems*, *16*(9), 3235-3256.

Stewart, J. H. (1972). Initial deposits in the Cordilleran geosyncline: Evidence of a late Precambrian (< 850 my) continental separation. *Geological Society of America Bulletin*, *83*(5), 1345-1360.

Stewart, J. H. (1974). Correlation of uppermost Precambrian and Lower Cambrian strata from southern to east-central Nevada. *US Geological Survey Journal of Research*, *2*(5), 609-618.

Strauss, J. V., Rooney, A. D., Macdonald, F. A., Brandon, A. D., & Knoll, A. H. (2014). 740 Ma vase-shaped microfossils from Yukon, Canada: Implications for Neoproterozoic chronology and biostratigraphy. *Geology*, *42*(8), 659-662.

Sturrock, C. P., Flowers, R. M., & Macdonald, F. A. (2021). The late great unconformity of the Central Canadian Shield. *Geochemistry, Geophysics, Geosystems*, *22*(6), e2020GC009567. https://doi.org/10.1029/2020GC009567

Sumner, E. J., Talling, P. J., Amy, L. A., Wynn, R. B., Stevenson, C. J., & Frenz, M. (2012). Facies architecture of individual basin-plain turbidites: Comparison with existing models and implications for flow processes. *Sedimentology*, *59*(6), 1850-1887.

Sylvester, Z., & Lowe, D. R. (2004). Textural trends in turbidites and slurry beds from the Oligocene flysch of the East Carpathians, Romania. *Sedimentology*, *51*(5), 945-972.

Talling, P. J., Masson, D. G., Sumner, E. J., & Malgesini, G. (2012). Subaqueous sediment density flows: Depositional processes and deposit types. *Sedimentology*, *59*(7), 1937-2003. https://doi.org/10.1111/j.1365-3091.2012.01353.x

Tasistro-Hart, A. R., & Macdonald, F. A. (2023). Phanerozoic flooding of North America and the Great Unconformity. *Proceedings of the National Academy of Sciences*, *120*(37), e2309084120. https://doi.org/10.1073/pnas.2309084120

Tegner, C., Andersen, T. B., Kjøll, H. J., Brown, E. L., Hagen-Peter, G., Corfu, F., ... & Torsvik, T. H. (2019). A mantle plume origin for the Scandinavian dyke complex: A "piercing point" for 615 Ma plate reconstruction of Baltica?. *Geochemistry, Geophysics, Geosystems*, *20*(2), 1075-1094.

Terlaky, V. (2014). *Sedimentology, stratigraphy, architecture and origin of deep-water, basin-floor deposits: Middle and upper Kaza Group, Windermere Supergroup, BC, Canada*(Doctoral dissertation, Université d'Ottawa/University of Ottawa).

Terlaky, V., Rocheleau, J., & Arnott, R. W. C. (2016). Stratal composition and stratigraphic organization of stratal elements in an ancient deep-marine basin-floor succession, Neoproterozoic Windermere Supergroup, British Columbia, Canada. *Sedimentology*, *63*(1), 136-175. https://doi.org/10.1111/sed.12222

Timmons, J. M., Bloch, J., Fletcher, K., Karlstrom, K. E., Heizler, M., & Crossey, L. J. (2012). The Grand Canyon Unkar Group: Mesoproterozoic basin formation in the continental interior during supercontinent assembly. *Grand Canyon Geology*, *2*, 25-48.

Tucker, M. E. (1986). Formerly aragonitic limestones associated with tillites in the Late Proterozoic of Death Valley, California. *Journal of Sedimentary Research*, *56*(6), 818-830. https://doi.org/10.1306/212F8A5D-2B24-11D7-8648000102C1865D

Vandyk, T. M., Kettler, C., Davies, B. J., Shields, G. A., Candy, I., & Le Heron, D. P. (2021). Reassessing classic evidence for warm-based Cryogenian ice on the western Laurentian margin: The "striated pavement" of the Mineral Fork Formation, USA. *Precambrian Research*, *363*, 106345. https://doi.org/10.1016/j.precamres.2021.106345

Vermeesch, P., 2018, IsoplotR: A free and open toolbox for geochronology: Geoscience Frontiers, 9(5), p. 1479-1493.

Vermeesch, P. (2020). On the treatment of discordant detrital zircon U–Pb data. *Geochronology Discussions*, *2020*, 1-19. https://doi.org/10.5194/gchron-3-247-2021

Walker, R. G. (1978). Deep-water sandstone facies and ancient submarine fans: models for exploration for stratigraphic traps. *AAPG Bulletin*, *62*(6), 932-966.

Wall, C. J., Hanson, R. E., Schmitz, M., Price, J. D., Donovan, R. N., Boro, J. R., ... & Toews, C. E. (2021). Integrating zircon trace-element geochemistry and high-precision U-Pb

zircon geochronology to resolve the timing and petrogenesis of the late Ediacaran–Cambrian Wichita igneous province, Southern Oklahoma Aulacogen, USA. *Geology*, *49*(3), 268-272.

Wendt, I. and Carl, C., 1991, The statistical distribution of the mean squared weighted deviation: Chemical Geology: Isotope Geoscience Section, 86(4), p. 275-285

Wiedenbeck, M.A.P.C., Alle, P., Corfu, F.Y., Griffin, W.L., Meier, M., Oberli, F.V., Quadt, A.V., Roddick, J.C. and Spiegel, W., 1995, Three natural zircon standards for U-Th-Pb, Lu-Hf, trace element and REE analyses: Geostandards newsletter, 19(1), p. 1-23.

Wickham, S. M., & Peters, M. T. (1993). High δ13C Neoproterozoic carbonate rocks in western North America. *Geology*, *21*(2), 165-168.

Witkosky, R., & Wernicke, B. P. (2018). Subsidence history of the Ediacaran Johnnie Formation and related strata of southwest Laurentia: Implications for the age and duration of the Shuram isotopic excursion and animal evolution. *Geosphere*, *14*(5), 2245-2276. https://doi.org/10.1130/GES01678.1

Woodward, L. A. (1963). Late Precambrian metasedimentary rocks of Egan range, Nevada. *AAPG Bulletin*, *47*(5), 814-822.

Woodward, L. A. (1965). Late Precambrian stratigraphy of northern Deep Creek Range, Utah. *AAPG Bulletin*, *49*(3), 310-316.

Woodward, L. A. (1967). Stratigraphy and correlation of late Precambrian rocks of Pilot Range, Elko County, Nevada, and Box Elder County, Utah. *AAPG Bulletin*, *51*(2), 235-243.

Woodward, L. A. (1968). Lower Cambrian and Upper Precambrian strata of Beaver Mountains, Utah. *AAPG Bulletin*, *52*(7), 1279-1290.

Wrobel, A. J., Gans, P. B., & Womer, J. B. (2021). Late Cretaceous Crustal Shortening in the Northern Snake Range Metamorphic Core Complex: Constraints on the Structural Geometry and Magnitude of Pre-Extensional Footwall Burial. *Tectonics*, *40*(8), e2020TC006460. https://doi.org/10.1029/2020TC006460

Yang, C., Rooney, A. D., Condon, D. J., Li, X. H., Grazhdankin, D. V., Bowyer, F. T., ... & Zhu, M. (2021). The tempo of Ediacaran evolution. *Science advances*, *7*(45), eabi9643.

Yonkee, W. A., Dehler, C. D., Link, P. K., Balgord, E. A., Keeley, J. A., Hayes, D. S., ... & Johnston, S. M. (2014). Tectono-stratigraphic framework of Neoproterozoic to Cambrian strata, west-central US: Protracted rifting, glaciation, and evolution of the North American Cordilleran margin. *Earth-Science Reviews*, *136*, 59-95. https://doi.org/10.1016/j.earscirev.2014.05.004

Zhang, T., Keller, C. B., Hoggard, M. J., Rooney, A. D., Halverson, G. P., Bergmann, K. D., ... & Strauss, J. V. (2023a). A Bayesian framework for subsidence modeling in sedimentary

basins: A case study of the Tonian Akademikerbreen Group of Svalbard, Norway. *Earth and Planetary Science Letters*, *620*, 118317. https://doi.org/10.1016/j.epsl.2023.118317

Zhang, T., Keller, C.B., Strauss, J.V. (2023b), SubsidenceChron.jl. https://doi.org/10.17605/OSF.IO/ZW5GA

* * *

CHAPTER III. THE KHUVSGUL GROUP

Part 1 of this chapter has been published as:

[Anttila, E., Macdonald, F., & Bold, U. (2021). Stratigraphy of the Khuvsgul Group, Mongolia. *Mongolian Geoscientist*, *26*(52), 2-15.]

Part 2 of this chapter has been submitted for publication as:

[**Anttila, E.**, Macdonald, F.A., Schoene, B., Gaynor, S., Baiarsaikhan, E., and Erdene, E., 2023. *Cambrian foreland phosphogenesis in the Khuvsgul Basin of Mongolia.* American Journal of Science.]

CHAPTER III, PART 1: STRATIGRAPHY OF THE KHUVSGUL GROUP

ABSTRACT

The Khuvsgul Group (Khuvsgul Province, Mongolia) is a Late Neoproterozoic to Cambrian carbonate-dominated succession that includes minor glacial diamictite and one of the largest known ore-grade phosphate deposits in the world. These strata, which have experienced low-grade metamorphism, are exposed in the Khoridol- Saridag Range on the western margin of Lake Khuvsgul. Since 2017, new geologic mapping and field studies have been conducted in the Khuvsgul region. During the course of this work, it has become necessary to restructure the stratigraphic framework of the Khuvsgul Group in order to better facilitate geologic mapping, stratigraphic observations, and regional correlations. We have divided the lower Khuvsgul Group into four distinct formations spanning the

Cryogenian and Ediacaran, each of which encompass strata associated with the Sturtian glaciation, Cryogenian non-glacial interlude, Marinoan glaciation, and basal Ediacaran transgression respectively. The phosphorites of the Khuvsgul Group are now included within a new distinct formation, while the overlying Cambrian carbonates and siliciclastic rocks have been further subdivided to streamline mapping and correlation efforts. The stratigraphic framework outlined below will simplify identification and differentiation of Khuvsgul Group rocks in the field and provide a foundation for the interpretation of Khuvsgul Group strata within the context of the changing climatic, tectonic, and paleoenvironmental conditions of the late Neoproterozoic and early Cambrian.

3.1. Introduction

Located on the northern Tuva-Mongolia terranes (Ilyin, 1971; Kuzmichev, 2015; Bold et al., 2019), and exposed in a north-south belt along the ridgelines above the west shores of Lake Khuvsgul (Figs 1 and 2), the Khuvsgul Basin hosts the late Neoproterozoic to Cambrian Khuvsgul Group (Ilyin and Ratnikova, 1981; Macdonald and Jones, 2011). The Khuvsgul Group is a ~3 km-thick succession composed predominantly of limestone and dolostone, with minor diamictite, phosphorite, and siliciclastic rocks. Early geological investigation of the Khuvsgul Group centered around the ore-grade Khuvsgul phosphorite (Ilyin, 1973; Ilyin and Ratnikova, 1981). More recent work has focused on Cryogenian Snowball Earth glaciations recorded by the diamictite units (Macdonald and Jones, 2011) and the late Ediacaran to Cambrian Doushantuo-Pertatanka-type microfossil assemblage within the phosphatic strata (Anderson et al., 2017; 2019). Over the past half-century, workers have developed a variety of stratigraphic schemes for the Khuvsgul Group, with

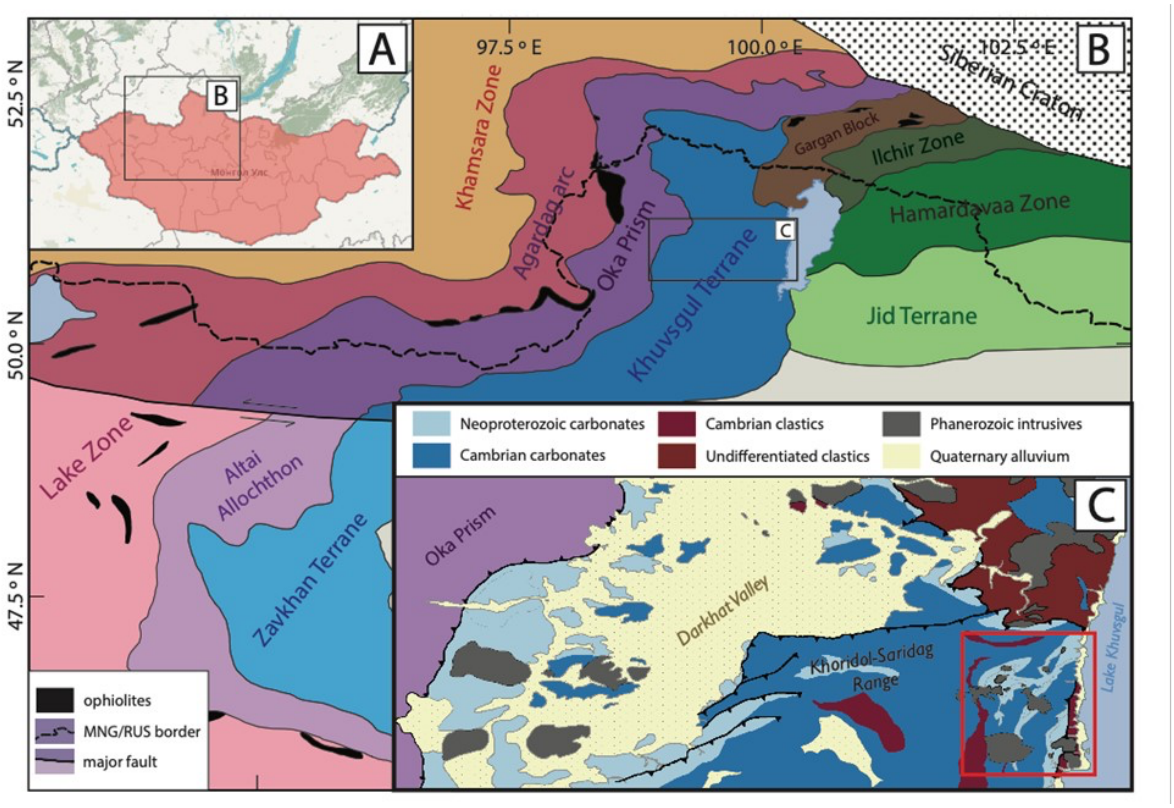

Figure 1: Location and geologic context of northern Mongolia. **A:** Geopolitical map of northern Mongolia. **B:** Tectonic map of the northern Mongolian portion of the Central Asian Orogenic Belt, modified from Bold et al. (2016b, 2019) and Kuzmichev (2015). **C:** Generalized geologic map of the Khoridol-Saridag Range and Darkhat Valley. A detailed geologic map of the area outlined in red is shown in Figure 2.

Figure 2: Geologic map of the eastern and central Khoridol-Saridag Range, Khuvsgul Aimag, Mongolia. Locations of measured stratigraphic sections are depicted with lavender lines. Only type-locality measured sections are labeled, as are river drainages or gorges ("gols") relevant to locations discussed in this work. Note that the Shar Formation and Khirvesteg Formation are depicted in this figure as a single unit, as the Khirvisteg Formation is generally too thin to be clearly discernible at the map scale presented here.

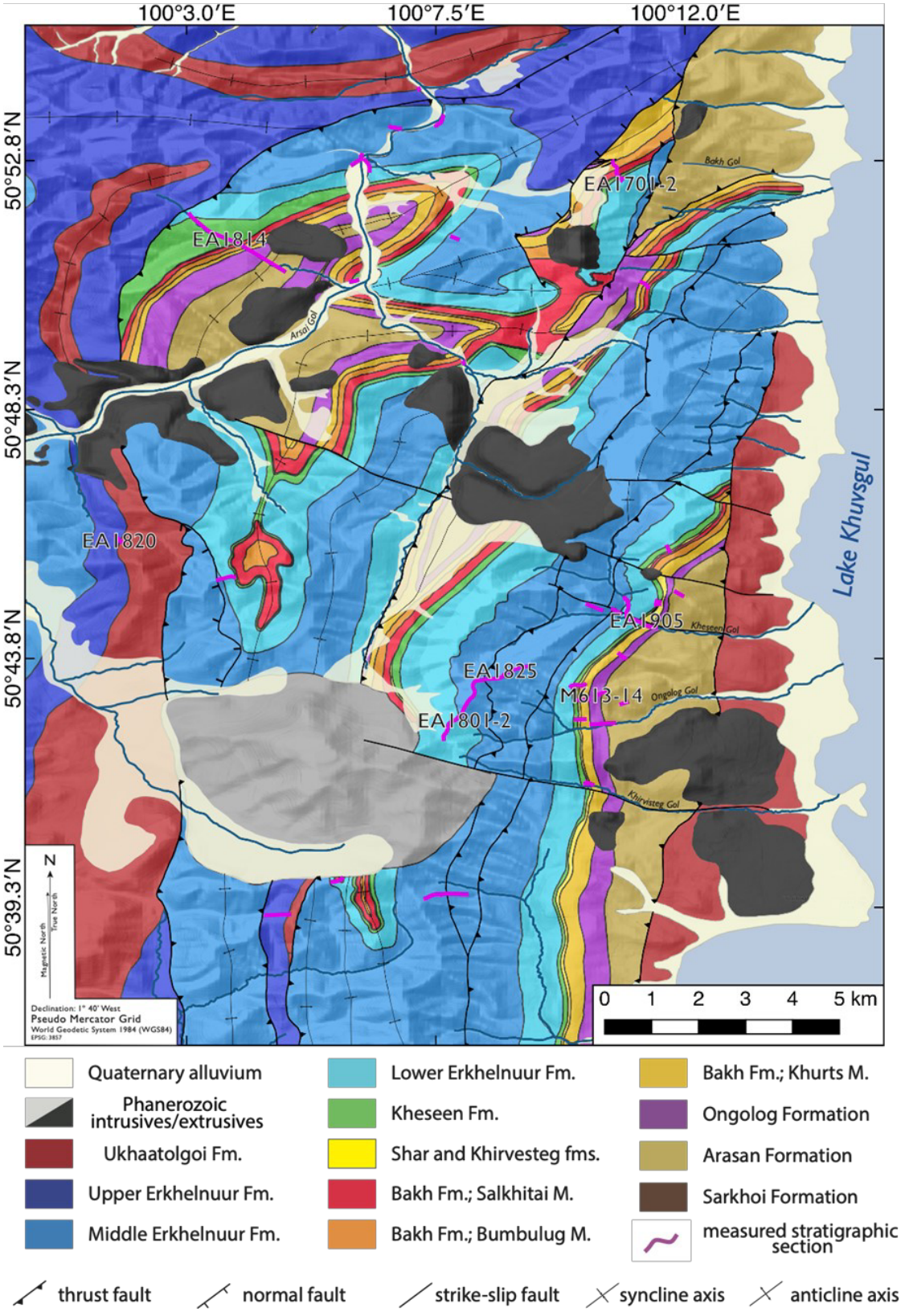
100°3.0′E
100°7.5′E
100°12.0′E
50°52.8′N
50°48.3′N
50°43.8′N
50°39.3′N
EA1814
EA1701-2
EA1820
EA1905
EA1825
M613-14
EA1801-2
Bakh Gol
Arsai Gol
Khesseen Gol
Ongolog Gol
Khirvisteg Gol
Lake Khuvsgul
N
Magnetic North
True North
Declination: 1° 40' West
Pseudo Mercator Grid
World Geodetic System 1984 (WGS84)
EPSG: 3857
0 1 2 3 4 5 km
Quaternary alluvium
Phanerozoic intrusives/extrusives
Ukhaatolgoi Fm.
Upper Erkhelnuur Fm.
Middle Erkhelnuur Fm.
Lower Erkhelnuur Fm.
Kheseen Fm.
Shar and Khirvesteg fms.
Bakh Fm.; Salkhitai M.
Bakh Fm.; Bumbulug M.
Bakh Fm.; Khurts M.
Ongolog Formation
Arasan Formation
Sarkhoi Formation
measured stratigraphic section
thrust fault
normal fault
strike-slip fault
syncline axis
anticline axis

correlations to putatively equivalent units on the Siberian side of the Russian- Mongolian border (Osokin and Tyzhinov, 1998; Kuzmichev et al., 2001; Vishnevskaya and Letnikova, 2013), or the southwest margin of the Zavkhan terrane (Macdonald and Jones, 2011, Smith et al., 2016, Bold et al., 2016 a,b). Stratigraphic frameworks proposed by previous workers are summarized in Fig. 3. Here we propose an updated stratigraphic framework based on new geological mapping, lithostratigraphic observations, and biostratigraphic constraints.

Based on the regional basinal stratigraphic divisions outlined by Macdonald and Jones (2011), our new stratigraphy further divides map units on the basis of discrete lithostratigraphic trends observed throughout the Khuvsgul paleobasin. First, we propose that the Ongolog Formation, which includes diamictite and carbonate, be separated into the Ongolog Formation (glacial facies) and Bakh Formation (non-glacial facies). The Bakh Formation is further subdivided, based on basinally-consistent lithological changes, into the Khurts, Bumbulug, and Salkhitai members. Next, strata formerly incorporated into the Kheseen Formation (Macdonald and Jones, 2011) are subdivided: the newly defined Shar Formation includes a diamictite and breccia sequence, while a cap carbonate and overlying transgressive sequence form the Khirvesteg Formation. The newly-defined Kheseen Formation (spelling adapted to conform to Mongolian anglicized spelling standardization) includes the Khuvsgul phosphorite and overlying carbonate grainstones and mass-flow deposits. We then define Lower, Middle, and Upper members of the Erkhelnuur Formation based on regional lithostratigraphic trends in order to streamline mapping, field identification, and structural relationships. Finally, varied siliciclastic rocks overlying the Erkhelnuur Formation are incorporated into the Ukhaatolgoi Formation.

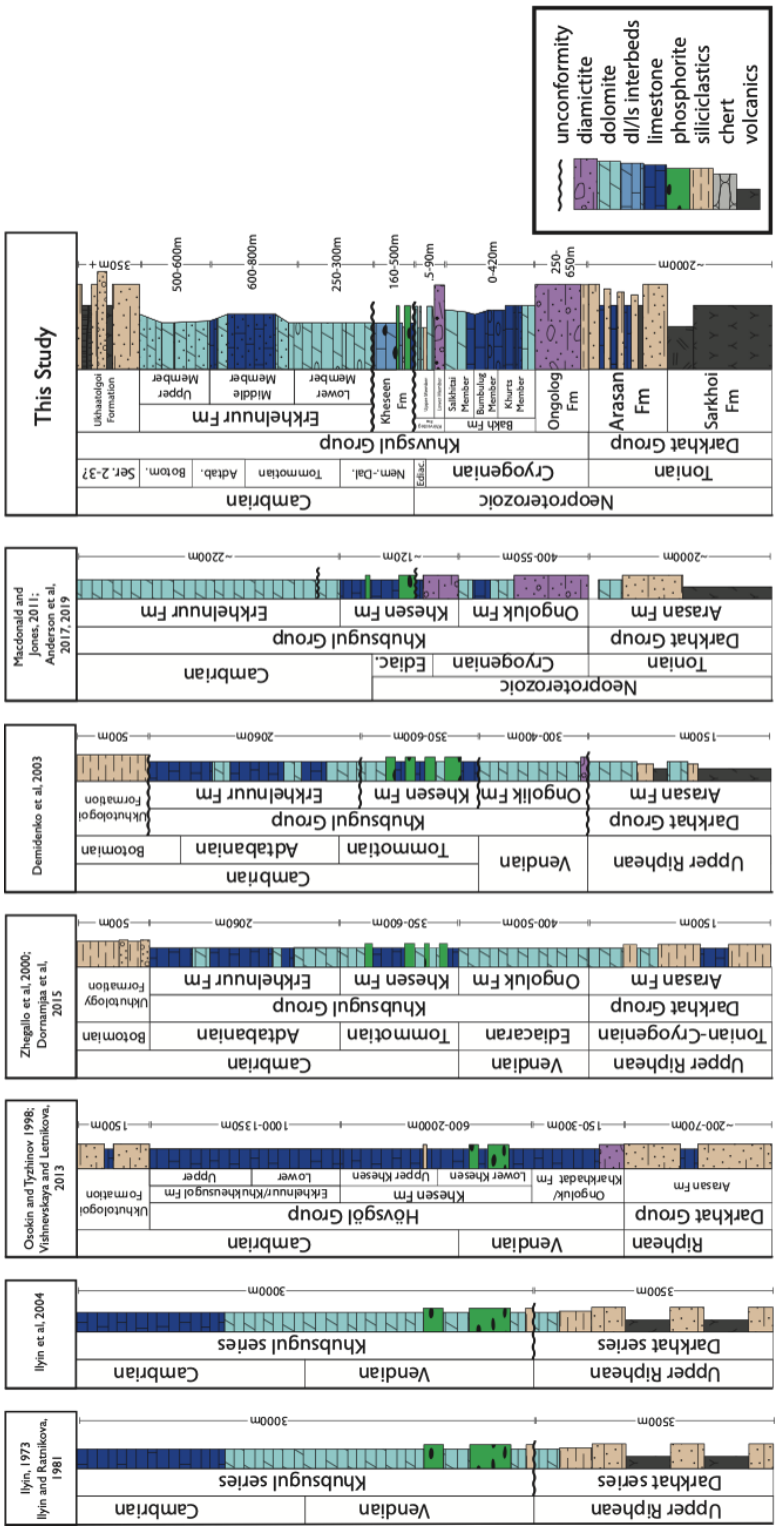

Figure 3: Compilation of previous stratigraphic frameworks, including nomenclature, cartoon representations of reported lithology, and approximate thickness. A schematic representation of the new framework outlined in this study is shown in the column at right (top).

3.2. Methods

During the course of a geological mapping campaign spanning three field seasons (summers of 2017-2019), we measured more than 8,000 m of stratigraphic section at sub-meter resolution through Khuvsgul Group exposures in the Khoridol Saridag Range and Darkhat Valley. Section locations are depicted in Fig. 2, while representative stratotype sections are plotted in Fig. 5. By combining our lithostratigraphic and facies observations (both from measured sections and from outcrop encountered during the course of geologic mapping) with structural relationships from our mapping efforts, we discretized constituent formations of the Khuvsgul Group into a stratigraphic framework that will streamline future work in the region. Formalized unit names, type section locations, thicknesses, age constraints, and correlations are summarized in Table 1.

3.3. Stratigraphy

Ongolog Formation: Composed of poorly sorted sandstone, siltstone, conglomerate, and diamictite, the Ongolog Formation is 250-650 m thick, with changes in both thickness and facies observed in north- south along-strike exposures west of Lake Khuvsgul. The Ongolog Formation is well exposed on the northern slopes of Ongolog Gorge (Fig. 2), with recessive, poorly outcropping clast-free sequences of fine to medium-grained lithic arenites giving way up-section to more resistant matrix-supported stratified diamictite, with the matrix composed of the same material that makes up the clast-free interval below. On a ridge north of Kheseen Gorge (Fig. 2), a continuous section preserves the gradual transition from clast-free siliciclastic material to massive diamictite (see sections M613 and M614 in Macdonald and Jones, 2011). At both localities, the formation culminates in massive, dark-colored, argillite

matrix diamcitite with clasts of carbonate, sandstone, and crystalline basement ("perforated shales" of Ilyin, 1973), depicted in in Fig. 4a.

Bakh Formation: Named for its type locality on a ridgeline above Bakh Gorge (EA1701 and EA1702, Fig. 5), the Bakh (бах; tr. "toad") Formation is composed of platformal and upper slope carbonate sequences that are subdivided into three distinct members.

Khurts Member: Dolomite wackestone and fine- laminated grainstone of the lowermost Khurts (хурц; tr. "sharp") Member of the Bakh Formation directly overly the Ongolog Formation, with a sharp, conformable or paraconformable contact. Although most Khurts Member exposures are heavily recrystallized, a generally shallowing-upward trend is suggested by the increase of coarse grainstone and grainflow deposits containing ooids and microbial mat rip-up clasts towards the top of the member. The Khurts Member is 20-120 m thick, and thickens to the southwest.

Bumbulug Member: A conformable transition to repeating shallowing-upward parasequences of limestone mudstone, marl (mixed carbonate and fine-graded siliciclastic rocks), and rhythmite (graded calcisiltite to micrite) interbeds marks the beginning of the Bumbulug (бөмбөлөг; tr. "bubbly") Member. Vitreous black-grey ellipsoidal chert nodules from 1-3 cm are distributed throughout thicker, tawny-brown mudstone beds, giving outcrops a bubbly, almost sponge-like appearance. Thinner laminated mudstone, marl, and rhythmite are more frequent up-section, with mm- to cm-scale bedded chert interspersed throughout; the Bumbulug Member is 50-150 m thick.

Table 1: Formalization of newly defined stratigraphic units of the Khuvsgul Group.

Name	**Ongolog Formation**
Name Derivation	Good, albeit incomplete, exposures in and around Ongolog Gorge, Khuvsgul Aimag, Mongolia; previously used as the name for a broader formation that included the now-differentiated Ongolog and Bakh Formations
Category and Rank	Lithostratigraphic Formation
Type Area	South-facing slopes north of Kheseen Gorge, Khuvsgul Aimag, Mongolia
Unit Type Section	Composite section M613 and M614 (Macdonald and Jones, 2011; Fig. 2, this paper). South-facing slope near top of ridge/treeline north of Kheseen Gorge; near northeasternmost exploratory trench visible on satellite imagery. Gradational basal contact begins just west of section start (50.74887N, 100.19923E), ends just below first exposure of allodapic limestones to WNW
Unit Description	Poorly sorted litharenites, silts, and gritty lags grade into matrix supported, beige-green to purple-weathering matrix-supported diamictite hosting sub angular to subrounded clasts (dominantly carbonates, with minor quartzite and granitic clasts) ranging from pebbles to boulders. Reported striated and faceted clasts (Osokin and Tyzhinov, 1998) suggest a glacigenic origin. Massive and stratified diamictite facies present in varying abundance throughout exposures, with rapid facies and thickness variability apparent between along-strike exposures at sub-km length scales. Uppermost strata of the Ongolog Formation include a massive diamictite with sub-rounded to sub angular carbonate, granite, and quartzite clasts supported by a dark grey argillitic matrix
Unit Reference Sections	1. M605 (50.710609N, 100.178601E) 2. M610 (50.72995N, 100.18197E) (Macdonald and Jones, 2011), located in Ongolog Gol and on ridge north of Ongolog Gol, respectively
Dimensions	~430m in composite type section, estimated thicknesses from ~250m in Ongolog Gorge to up to 650m to north
Geologic Age	Earliest Cryogenian (~719Ma) to end-Sturtian (~660Ma) via correlation with globally distributed Sturtian glacial diamictites
Regional Correlations	Maikhan-Uul Fm, Zavkhan Terrane, Mongolia (Macdonald and Jones, 2011, Bold et al., 2016a)
Name	**Bakh Formation (Khurts, Bumbulug, and Salkhitai Members)**
Name Derivation	Type section located on ridge west of Bakh Gorge, Khuvsgul Aimag, Mongolia, with best access by foot up Bakh Gol. Khurts (хурц; *tr. "sharp")* Member is often a cliff-forming unit; Bumbulug (бомбөлөг; *tr. "bubbly"*) Member contains nodular cherts that are reminiscent of bubbles on exposed weathered surfaces; Salkhitai (салхитай; *tr. "windy"*) Member is often a ridge-forming unit, with a stratotype section on a ridgeline that is particularly exposed to wind and weather
Category and Rank	Lithostratigraphic Formation composed of 3 component Members
Type Area	Ridge on the westernmost rim of the upper northern drainage area of Bakh Gorge, Khuvsgul Aimag, Mongolia
Unit Type Section	EA1701-2 (Figures 2 and 5, this paper). Lower Boundary: lowest continuous exposure of Khurts Member (50.87971N, 100.17848E) above nearby Ongolog Formation outcrop. Section follows exposures along the northern and eastern edges of ridge crests. Upper Boundary: contact with overlying yellow carbonate diamictite of Khirvesteg Formation (50.875802N, 100.179634E)
Unit Description	Khurts Member: dolomite wackestones and laminated grainstones, often heavily recrystallized to the point of destroying primary sedimentary textures. Generally appears to shallow upsection: ooids and microbial textures more frequent towards top of member Bombolog Member: shallowing-upward parasequences of limestone, mudstone, and marl. Ellipsoidal chert nodules (1-3cm) throughout thicker mudstone beds; laminated mudstones, marls, rythmites, and bedded mm-scale cherts become frequent upsection Salkhitai Member: coarse limestone grainstone parasequences, grading into thicker dolomitized grainstones, grainflow deposits, carbonate intraclast breccias, and sedimentary breccias often with lithic grains in matrix material
Unit Reference Sections	1. ~40m into EA1814 (50.85318N, 100.06865E), Arsai Gorge (Figures 2 and 5, this paper) 2. partial exposures in Kheseen and Ongolog Gorges (Fig. 2, this paper)
Dimensions	At the type section, the Khurts Member is at least 20m thick, the Bombolog Member is ~120m thick, and the Salkhitai Member is ~175m thick. Elsewhere in the basin, the Khurts, Bombolog, and Salkhitai Members have been estimated to be a maximum of 120m, 150m, and 175m thick respectively, both at EA1814 and at incomplete exposures in the easternmost Khoridol-Saridag Range
Geologic Age	Cryogenian non-glacial interlude; >660Ma to likely younger than ~657Ma (Rooney et al., 2020)
Regional Correlations	Taishir Fm., Zavkhan Terrane, Mongolia (Macdonald and Jones, 2011; Bold et al., 2016a)
Name	**Khirvesteg Formation**
Name Derivation	Good exposure in outcrop on the south-facing hillsides west of Khirvesteg Gorge, Khuvsgul Aimag, Mongolia
Category and Rank	Lithostratigraphic Formation
Type Area	Ridge on the westernmost rim of the upper northern drainage area of Bakh Gorge
Unit Type Section	~300m into EA1701-2 (50.875683N, 100.179771E), Bakh Gorge ridge (Figures 2 and 5, this paper). Lower Boundary: locally conformable contact with underlying dolomite grainstone of Salkhitai Member, Bakh Formation (50.875802N, 100.179634E). Section continues through outcrop exposure on northern edge of ridgeline. Upper Boundary: unconformity surface at contact with Kheseen Formation (50.875516N, 100.179958E)
Unit Description	Yellow-weathering, massive matrix-supported diamictite, containing angular to sub-angular carbonate clasts in a dolomite matrix. Often interfingered with angular dolomite boulder breccias; thickness of diamictite/breccia package highly variable in along-strike exposures. The diamictite is overlain by a 3m thick, cream-colored dolomite grainstone, often bearing sheetcrack cements and barite fans., interpreted to be a cap carbonate paired with the underlying diamictite. Above the cap carbonate, a transgressive sequence of marls, mudstones, and thinly laminated carbonaceous shales, ranging in color from white to tawny brown on weathered surfaces, is found at most exposures
Unit Reference Sections	1. M611 (50.692094N, 100.172123E), Khirvesteg Gorge, (Macdonald and Jones, 2011). 2. M607-M609 composite section (50.691558N, 100.171421E), northern Ongolog Gorge. 3. ~200m into EA1814 (50.85510N, 100.06526E), Arsai Gorge (Figures 2 and 5, this paper)
Dimensions	At the type section, the diamictite/dolomite breccia unit is ~25m thick, the Marinoan cap is ~3m thick, and the overlying Ediacaran strata are ~20m thick. Diamictites at Reference Section 2 approach 50m in thickness, with a ~2m thick cap carbonate sequence and nearly 50m of overlying Ediacaran strata. Around the basin, thicknesses range from 0.5 to ~70m for the Khirvesteg diamictite, 1-3m for the Marinoan cap carbonate, and 0 to 50m for the Ediacaran strata
Geologic Age	Onset of Marinoan Glaciation (younger than 657Ma; Rooney et al., 2020) to early Ediacaran (younger than 635Ma)
Regional Correlations	Khongor Formation and lower Ol Formations, Zavkhan Terrane, Mongolia (Macdonald and Jones, 2011; Bold et al., 2016a)

Table 1(cont.): Formalization of newly defined stratigraphic units of the Khuvsgul Group.

Name	**Kheseen Formation**
Name Derivation	Good exposure in and around Kheseen Gorge, Khuvsgul Aimag, Mongolia; previously used as the name for a broader formation (frequently spelled "Khesen") containing the now-differentiated Khirvesteg Formation and the new Kheseen Formation
Category and Rank	Lithostratigraphic Formation
Type Area	Ridge on the westernmost rim of the upper northern drainage area of Bakh Gorge
Unit Type Section	~345m into EA1701-2, (50.875516N, 100.179958E) Bakh Gol Ridge (Figures 2 and 5, this paper). Lower Boundary: carbonates directly above unconformity surface at contact with Kheseen Formation (50.875516N, 100.179958E). Section continues along fall-line exposure directly up ridge to east. Upper Boundary: end of continuous exposure before contact with overlying Erkhelnuur Formation
Unit Description	Thin, interbedded limestone and dolomite mudstones, fetid marls, and phosphatic and silicified hardgrounds form discontinuous beds frequently truncated by cm-scale channelization and autoclastic debris flows. These lower Kheseen Formation strata contain abundant primary phosphate precipitates, and, in addition to hosting a DPT-type microfossil assemblage (Anderson et al., 2017,2019), also contain stromatolitic and microbial mat textures. Thin interbeds of the lower Kheseen Formation are usually overlain by a marker bed of amorphous chert, which is subsequently overlain by allodapic carbonate grainstones bearing phosphatic and siliceous allochems. While exposure at the type section locality ends within the allodapic carbonate sequence, exposures at Reference Section 1 reveal an expanded carbonate grainstone sequence in which phosphatic and siliceous allochems become sparse upsection before the occurrence of a second thick bed of amorphous chert. At Reference Section 2, the uppermost allodapic carbonates begin to exhibit a strong siliciclastic allochemical component, eventually giving way to graded lithic grainflows and larger debris flows with up to boulder-sized clasts. Here, the contact with the overlying Erkhelnuur Formation is a microkarstic disconformable exposure surface
Unit Reference Sections	1. ~ 230m into EA1814 (50.855144N, 100.065221E), Arsai Gorge (Figures 2 and 5, this paper); 2. EA1905 (50.855144N, 100.18400E), Kheseen Gorge (Figures 2 and 5, this paper)
Dimensions	At least 130m thick at the type locality; at least 500m thick at Reference Section 1, and between 120 and 400m at other exposures around the basin
Geologic Age	Latest Ediacaran to earliest Cambrian via correlation with Zavkhan equivalents (Macdonald et al, 2009; Macdonald and Jones, 2011)
Regional Correlations	Zuun Arts Formation, Zavkhan Terrane, Mongolia (Macdonald and Jones, 2011; Smith et al., 2016)
Name	**Lower, Middle and Upper Members of the Erkhelnuur Formation**
Name Derivation	Relative stratigraphic heights of differentiable units of the Erkhelnuur Formation
Category and Rank	3 constituent Members of a Lithostratigraphic Formation
Type Area	Lower Member: ridges west of Khirvesteg Gorge; Middle Member: ridges west of Khirvesteg and Ongolog Gorges; Upper Member: ridges west of Ongolog and Kheseen Gorges, as well as in several locations in the upper Arsai Gorge drainage
Unit Type Section	Lower Member: EA1801-2 (50.70571N, 100.12742E), ridge west of Khirvesteg Gol (Figures 2 and 5, this paper). Lower Boundary: base of EA1801-2, located ~20 m above contact with Kheseen Formation, which is covered by vegetation. Section follows ridgecrest to North. Upper Boundary: ~280m into EA1801-2 Middle Member: begins at upper boundary of Lower Member. Section continues north, following ridge crest, before turning east at (50.723044N, 100.136873E) and continuing along the ridgeline to the east, into EA1825, which follows the same ridge. Upper Boundary: ~650m into EA1825 (50.724445N, 100.1366252E), ridge west of Ongolog and Kheseen Gorges (Figures 2 and 5, this paper). Upper Member: begins at upper boundary of Middle Member. Exposure continues until EA1825 ends at core of syncline. Uppermost Upper Member is exposed in EA1920 (50.76544N, 100.03005E), Upper Arsai Gorge drainage (Figures 2 and 5, this paper). Section continues up gully until conformable contact with overlying Ukhaatolgoi Formation
Unit Description	Lower Member: bounded below by a disconformable exposure surface at the top of the Kheseen Formation, the Lower Member of the Erkhelnuur Formation is composed of dolomite and dolomitized limestone shallowing-upward parasequences (typically laminated mudstones and grainstones, coarser grainstones with infrequent stromatolitic horizons, and allodapic packstones and coarse grainstones containing ooids and oncoids. Occasional silicified surfaces Middle Member: abrupt transition to parasequences dominated by dark-grey-weathering limestone grainstone beds; this gray band is easy to identify on satellite or aerial imagery. Ichnofossils begin to appear, with abundant bioturbation increasing up section, eventually obfuscating all primary sedimentary structures and bedding features. Archaeocyathid reefs and hash appear ~300m above the base of the Middle Member Upper Member: base of the member is demarcated by an abrupt transition to white-cream dolomite grainstone beds. Heavy recrystallization throughout, with occasionally discernible laminated grainstones and rhythmites. White dolomites are also visible in satellite and aerial imagery, and serve as a valuable marker bed. The uppermost portion of the Upper Member begins to incorporate lithic grains and fragments in grainstone beds, with the frequency of lithics increasing upsection until carbonate deposition is overwhelmed at the conformable contact with the overlying Ukhaatolgoi Formation
Unit Reference Sections	1. ~119m into EAGC1905 (50.741915N, 100.183101E), Kheseen Gol (Figures 2 and 5, this paper), which includes the disconformable contact at the base of the Lower Member of the Erkhelnuur Formation
Dimensions	Lower Member: ~300m thick; Middle Member: 600-800m thick; Upper Member: 500-600m thick
Geologic Age	Archaeocyathid appearances constrain the Middle Member to within the Tommotian and Toyonian Stages (~525-511Ma)
Regional Correlations	Putative correlation with Bayangol Formation, Zavkhan Terrane, Mongolia (Smith et al., 2016)

Salkhitai Member: The uppermost portion of the Bakh Formation, the Salkhitai (салхитай; tr. “windy”) Member, conformably overlies the Bumbulug Member and contains coarse limestone grainstone-dominated parasequences that transition into a coarsening-upward stack of dolomitized grainstone, grainflow deposits, and intraclast breccia with a minor siliciclastic granular component. The top of the Salkhitai Member is marked by a coarse, carbonate- cemented sandstone with carbonate granules that is overlain by a massive unit of dolomite grainstone. The Salkhitai Member ranges between 100 m and 150 m in thickness.

Shar Formation: The Shar (шар; tr. “yellow") Formation is composed of a massive matrix-supported diamictite with a distinctive yellow-ochre dolomite matrix (Fig. 4b), often closely associated with coarse, gray-weathering angular dolomite breccia. Around the basin, thickness of diamictite-breccia packages ranges from 0.5-70 m. The base of the member is defined as the transition from dolomite grainstone of the uppermost Bakh Formation to diamictite or dolomite breccia. At the stratotype locality above Bakh Gorge, the Shar Formation is approximately 20 m thick, with nearly ten meters of angular dolomite breccia overlain by the eponymous yellow diamictite (EA1701-2, Fig. 5).

Khirvesteg Formation: Conformably above the diamictite and breccia, the base of the Khirvesteg Formation is defined by a 1-3 m thick dolomite grainstone containing barite fans and sheetcrack cements (Hoffman et al., 2011). The cap carbonate is overlain by thin dolomitic marl, mudstone, and carbonaceous shale. Although exposures to the south are locally only 2-3 m thick, 25 m of marl, shale, and dolomite mudstone are found in the stratotype section on the ridge above Bakh Gorge (EA1701-2, Fig. 5). Note that in Fig. 2, the Shar and Khirvesteg Formations are shown as a single map unit for visual clarity at the presented map scale.

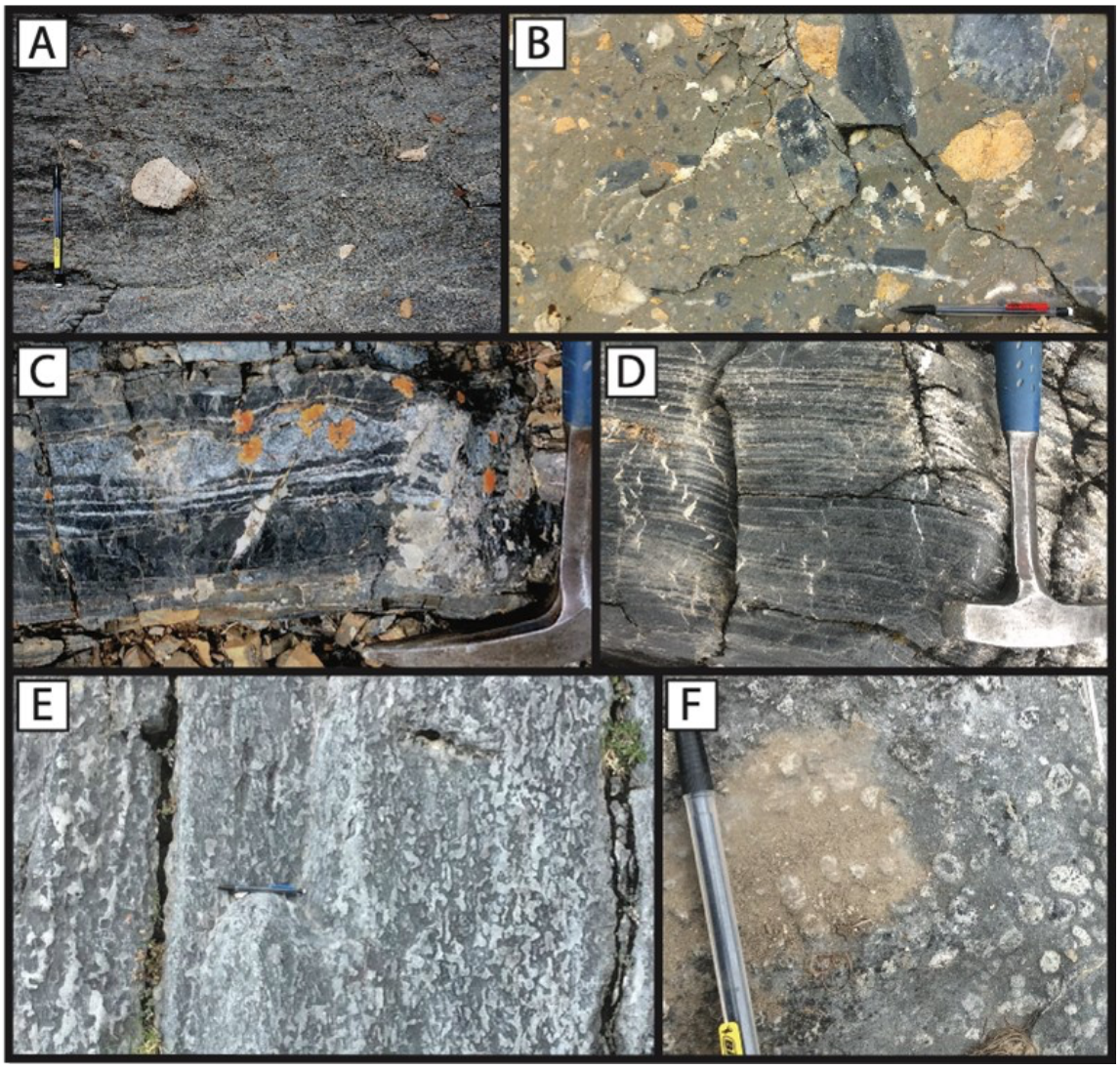

Figure 4: Khuvsgul Group rocks in outcrop and hand-sample. **A:** Matrix-supported diamictite of the Ongolog Formation, featuring sub-angular to sub-rounded carbonate and granitic clasts. **B:** Yellow, dolomite-matrix-supported diamictite of the Shar Formation, with angular to sub-angular carbonate clasts, many of which are lithologically similar to strata of the underlying Bakh Formation. **C:** phosphorite of the lower phosphatic units of the Kheseen Formation observed in EA1701, with discontinuous layers of primary phosphatic material weathering blue-white between darker chert and limestone beds. **D:** Dolomite grainstones of the Kheseen Formation bearing phosphatic allochems, EA1814. **E:** Bed-penetrating bioturbation within grainstones of the Middle Member of the Erkhelnuur Formation. **F:** Archaeocyathid hash in grainstones of the Middle Member of the Erkhelnuur Formation.

Kheseen Formation: Ranging from 160-500 m in thickness, the Kheseen Formation is separated from the Khirvesteg Formation by a prominent erosional unconformity. Above this surface, the basal Kheseen Formation is composed of interbedded black micritic

limestone and dolomite mudstone, foetid marl and shale, and phosphatic and silicified hardgrounds (Fig. 4c. Bedding is largely discontinuous along strike, and is often truncated by channelization or autoclastic debris flows, while thicker carbonate beds contain stromatolitic and thrombolitic textures. Phosphatic hardgrounds and phosphatic grainflows in these strata contain a Doushantuo- Pertatanka-Type microfossil assemblage, described by Anderson et al. (2017; 2019). This sequence, referred to in previous works as the lower phosphate unit (Ilyin and Ratnikova, 1981; Ilyin, 1998), is 10-60 m thick, and contains the most concentrated phosphate ore (average of 22% and up to 34% P_2O_5; Dorjnamjaa and Altanshagai, 2015) in the region. This phosphatic unit is capped by 1-5 m of massive amorphous black chert. Above this, granular phosphorite is present in graded allodapic limestone and dolomite grainstone (Fig. 4d). This facies forms the majority of phosphorite exposure in the Khuvsgul Basin. In the Western Khoridol Saridag Range (KSR), the Kheseen Formation is capped by a second chert bed, whereas in the easternmost KSR it is composed of grainstone and coarse conglomerate with a large siliciclastic component not observed elsewhere in the basin. The stratotype section for the Upper Kheseen Formation is on the ridge above Bakh Gorge (EA1701-2) with reference sections in Arsai Gorge (EA1814), which includes an expanded upper phosphorite sequence, and in Ongolog Gorge (EA1905), which contains conglomerate with abundant lithic clasts at the top of the formation. All sections are depicted in Fig 5.

Erkhelnuur Formation: The Erkhelnuur Formation (Zhegallo, 2000) is a 2 km thick carbonate sequence separated from the Kheseen Formation by a hiatal surface, observed in the Eastern KSR (EA1905) as a disconformable exposure surface, with the base of the Erkhelnuur Formation defined as the carbonate grainstones overlying this surface. In order

to simplify structural interpretation and lithological differentiation of Erkhelnuur Formation carbonates in the field, we propose the subdivision of the formation into Lower, Middle, and Upper Members, which are summarized below.

Lower Member: The Lower Member includes repetitive dolomite and dolomitized limestone parasequences, composed of laminated mudstone and grainstone interbeds, dolomitized grainstone beds containing domal stromatolites, and allodapic packstone and coarse grainstone containing ooids and oncoids. Parasequences are commonly capped by horizons of lenticular grey -black chert. The Lower Member is 250-300 m thick, with a stratotype exposure on a ridge above Khirvesteg Gorge (EA1801-2, Fig. 5).

Middle Member: The base of the Middle Member of the Erkhelnuur Formation is defined by an abrupt transition to parasequences dominated by dark grey limestone grainstone beds. While the parasequences include stromatolitic mudstone and dolo-rhythmite, this transition is visible both in the field and on satellite imagery, where limestone-dominated parasequences appear as a dark blue-gray band. In most sections, bed-penetrating ichnofossils appear 20-50 m above the base of the Middle Member, consisting of irregular 1-2 cm diameter tubes. The density of bioturbation increases up-section to the point of obfuscating primary bedding features (Fig. 4e). Approximately 300 m above the base of the Middle Member, archaeocyathid reefs and hash can be observed in bioturbation-free zones (Fig. 4f), constraining the strata to a window of the early Cambrian between the Tommotian and Toyonian Stages (~525-511 Ma, or mid- Terreneuvian Age 2 to Cambrian Series 2, Age 4; Peng et al., 2020). The Middle Member of the Erkhelnuur Formation ranges from 600-

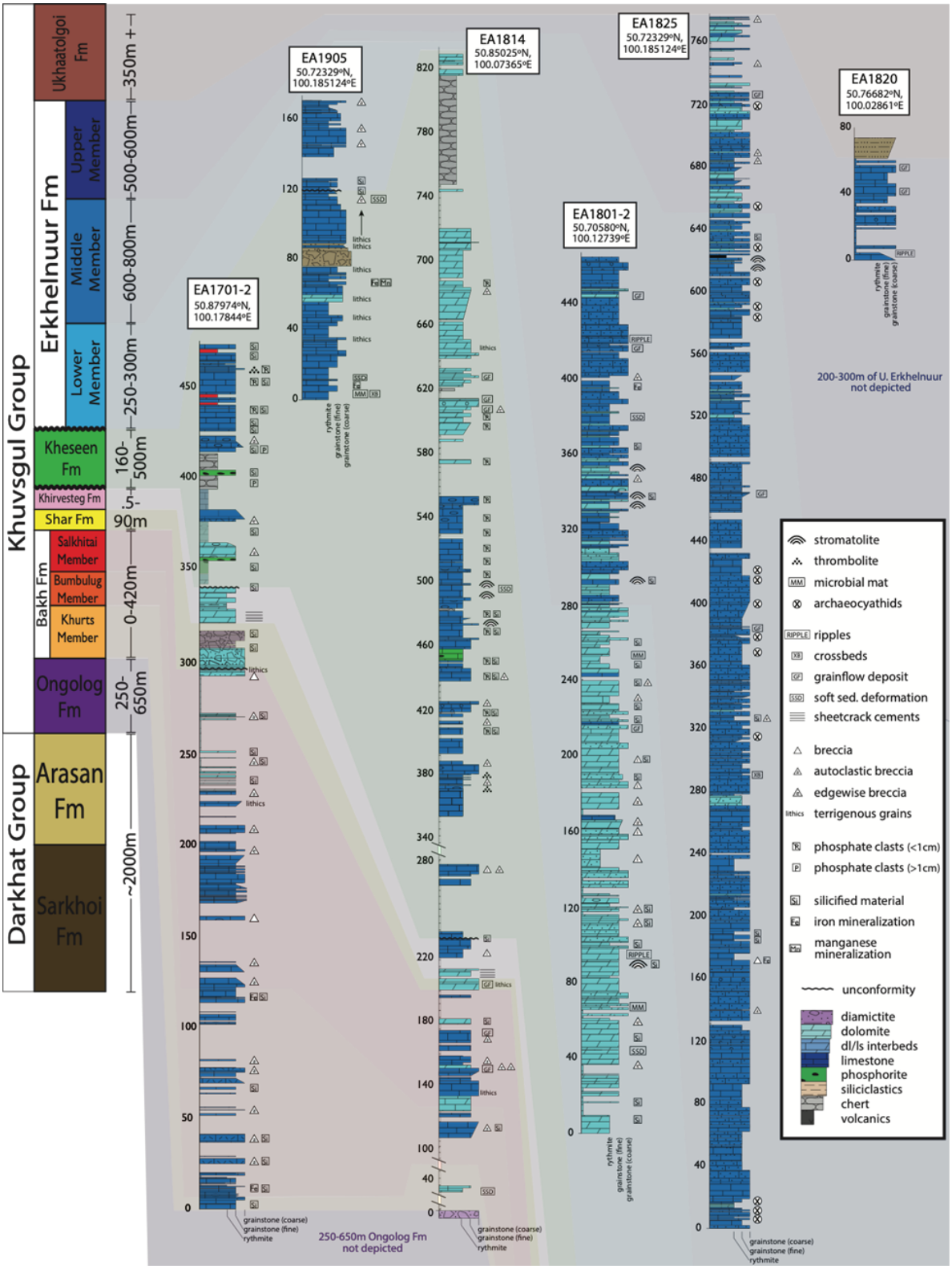

Figure 5: Measured stratigraphic sections from Khuvsgul Group type-localities. All section locations are depicted in Fig. 2, while coordinate locations shown above are from the stratigraphic base of each section.

800 m thick, and is best exposed in sections EA1801- 1802 (see Fig. 5) on the ridges above Khirvesteg Gorge.

Upper Member: The base of the Upper Member of the Erkhelnuur Formation is demarcated by a sequence of >50 m thick white- to cream- colored dolomite grainstone beds. Although the white beds locally preserve laminated grainstone and rhythmite, in most exposures, primary bedding features are obliterated by recrystallization. Like the dark beds at the base of the Middle Member, the basal white dolomite of the Upper Member forms a reliable marker bed that is easily visible in the field and satellite imagery. Above the white dolomite, grey dolomite and limestone laminite-grainstone- grainflow parasequences continue, with ichnofossils present in fine grainstone beds. Up- section, coarser-grained grainstone and grainflows incorporate terrigenous lithic fragments, which increase in frequency and size toward the top of the section. The Upper Member is 500-600 m thick; the base of the Member is best exposed in EA1825, while the uppermost grainflows are prominently exposed in section EA1820 (Fig. 5).

UkhaatolgoiFormation: The >350 m thick Ukhaatolgoi Formation conformably overlies the Erkhelnuur Formation and is composed of siliciclastic rocks dominated by greywacke with minor siltstone, sandstone, and conglomerate. Carbonate parasequences of the uppermost Erkhelnuur Formation contain allochems that are gradationally succeeded by greywacke of the basal Ukhaatolgoi Formation. Previously referred to as the Ukhutologoy Formation (Zhegallo et al., 2000; Demidenko et al., 2003) and excluded from the Khuvsgul Group, the Ukhaatolgoi Formation is dominated by green greywacke, with rare granule to pebble lithic clasts, angular quartz and plagioclase grains, and carbonate fragments in a green siltstone

matrix. The base of the formation is best documented in section EA1820, and the formation is best exposed at the cores of synclines in upper Arsai Gorge. Note that we do not include the formalization of this Formation in Table 1, as this nomenclature has been applied to these rocks by previous workers (Dorjnamjaa et al., 2015).

3.4. Discussion

While the stratigraphic divisions outlined above are largely based on lithological characteristics that can be easily differentiated in the field by future workers, our stratigraphic framework is also reflective of significant changes in paleoenvironment and paleoclimate that occurred during the deposition of the Khuvsgul Group. For example, the Ongolog, Bakh, Shar, and Khirvesteg formations can be correlated with the Sturtian glaciation, Cryogenian non-glacial interlude, Marinoan glaciation, and basal Ediacaran transgression respectively, with diamictites associated with both glaciations separated by a platformal carbonate sequence (Macdonald and Jones, 2011). A glaciogenic origin for the Ongolog Formatiton is established via the observation of exotic clasts in matrix-supported diamictite, as well as striated and faceted clasts (Osokin and Tyzhinov, 1998). Typically exhibiting sheetcrack cements and crystal fans, the basal carbonate of the Khirvesteg Formation is interpreted as a cap carbonate sequence (Hoffman et al., 2011), coupled with the underlying diamictite of the putatively Marinoan Shar Formation. Additionally, these units can be correlated with Cryogenian and Ediacaran successions on the Zavkhan Terrane in southwest Mongolia (Macdonald and Jones, 2011; Bold et al., 2016b).

Bound above and below by unconformities, the newly-defined Kheseen Formation records a depositional environment that resulted in the precipitation and eventual reworking

of the Kheseen phosphorites, which may be condensed equivalents of the phosphatic shales of the Zuun Arts Formation on the Zavkhan Terrane (Macdonald and Jones, 2011). The lower units of the Kheseen Formation record precipitation of primary phosphatic material in a very shallow, energetic depozone, whereas phosphatic material in the upper parts of the formation has been redeposited in carbonate grainstones (Fig. 5). Importantly, the newly defined lower bound of the Kheseen Formation isolates the phosphatic strata from the underlying Khirvesteg and Shar formations, highlighting the lack of a previously-postulated genetic relationship between the Marinoan glaciation and phosphogenesis (Osokin and Tyzhinov, 1998). Furthermore, the disconformable exposure surface at the top of the formation separates the Kheseen Formation in time from the nearly 2 km of overlying Erkhelnuur Formation carbonates, introducing the possibility that the Kheseen and Erkhelnuur formations were accommodated by distinct basin-forming events. Additional petrographic, geochronological and chemostratigraphic data are necessary to better constrain the ages and depositional environments of the Kheseen phosphorites and Khuvsgul Group strata as a whole. The stratigraphic framework presented here provides a necessary foundation for future work in the Khuvsgul region.

3.5. Conclusions

A new stratigraphic framework for the Khuvsgul Group divides strata spanning nearly 200 My of Earth history into seven formations. Cryogenian strata are divided into the Ongolog, Bakh, Shar, and Khirvesteg formations, discretizing units associated with the Sturtian glaciation, Cryogenian non-glacial interlude, Marinoan Glaciation, and basal Ediacaran transgression respectively. Phosphatic strata, bounded above and below by depositional hiatuses, are included in the newly defined Kheseen Formation. In order to

streamline mapping and correlation, the Erkhelnuur Formation is divided into Lower, Middle, and Upper Members, while the overlying siliciclastic sequences are discretized as the Ukhaatolgoi Formation.

* * *

ACKNOWLEDGEMENTS

Thanks to Erdene Bayarsaikhan, Ekv Erdene, Sam Lobianco, Peter Otness, and Judy Pu for assistance, companionship, and camaraderie in the field, to M. Munkhbaatar, Batsukh Erdene, and Set for transportation and friendship, to Ariunsanaa Dorj and the Earth Science Center of Mongolia for logistic help, and to the Ministry of Environment of Mongolia and the rangers and staff of the Khuvsgul Nuur National Park and Khoridol Saridag Protected Zone for access. This work was funded by grant funds from Nasa Astrobiology: Exobiology and Evolutionary Biology, NNH10ZDA001N-EXO. ESCA was additionally supported by National Science Foundation (NSF) Graduate Research Fellowship Program (GRFP) 2139319.

* * *

REFERENCES, CHAPTER III, PART 1

Anderson, R.P., Macdonald, F.A., Jones, D.S., McMahon, S., Briggs, D.E. 2017. Doushantuo -type microfossils from latest Ediacaran phosphorites of northern Mongolia: Geology, v. 45(12), p. 1079-1082. https://doi.org/10.1130/G39576.1

Anderson, R.P., McMahon, S., Macdonald, F.A., Jones, D.S. Briggs, D.E. 2019. Palaeobiology of latest Ediacaran phosphorites from the upper Khesen Formation, Khuvsgul Group, northern Mongolia: Journal of Systematic Palaeontology, v. 17(6), p. 501-532. https://doi.org/10.1080/14772019.2018.1443977

Bold, U., Smith, E.F., Rooney, A.D., Bowring, S.A., Buchwaldt, R., Dudás, F.Ő., Ramezani, J., Crowley, J.L., Schrag, D.P., Macdonald, F.A. 2016a. Neoproterozoic stratigraphy of the Zavkhan terrane of Mongolia: The backbone for Cryogenian and early Ediacaran chemostratigraphic records: American Journal of Science, v. 316(1), p. 1-63. https://doi.org/10.2475/01.2016.01

Bold, U., Crowley, J.L., Smith, E.F., Sambuu, O., Macdonald, F.A. 2016b. Neoproterozoic to early Paleozoic tectonic evolution of the Zavkhan terrane of Mongolia: Implications for continental growth in the Central Asian orogenic belt: Lithosphere, v. 8(6), p. 729- 750. https://doi.org/10.1130/L549.1

Bold, U., Isozaki, Y., Aoki, S., Sakata, S., Ishikawa, A., Sawaki, Y., Sawada, H. 2019. Precambrian basement, provenance implication, and tectonic evolution of the Gargan block of the Tuva-Mongolia terranes, Central Asian Orogenic Belt: Gondwana Research, v. 75, p. 172-183. https://doi.org/10.1016/j.gr.2019.05.003

Demidenko, Y.E., Zhegallo, E.A., Parkhaev, P.Y., Shuvalova, Y.V. 2003. Age of phosphorites from the Khubsugul basin (Mongolia): Dolkady Earth Sciences C/C of Dolkady Akademiia Nauk, v. 389, p. 317-321.

Dorjnamjaa, D., Altanshagai, G. 2015. Concerning the original viewpoint of biogeologic accumulation of the old bedded phosphorites in the Khubsugul and Zavkhan basins of Mongolia: Open Journal of Geology, v. 5(09), p 666. https://doi.org/10.4236/ojg.2015.59059

Dorjnamjaa, D., Enkhbaatar, B., Altanshagai, G. 2015. Concerning Precambrian and Cambrian regional stratigraphy of Mongolia: Mongolian Geoscientist, v. 42, p.2-11.

Hoffman, P.F., Macdonald, F.A., Halverson, G.P. 2011. Chemical sediments associated with Neoproterozoic glaciation: iron formation, cap carbonate, barite and phosphorite: Geological Society, London, Memoirs, v. 36(1), p.67-80. https://doi.org/10.1144/M36.5

Ilyin, A.V. 1971. About the Tuva-Mongolian massif: Materials about the Regional Geology of Africa and Asia: Zarubezhgeologiya, v. 22, p.67-73.

Ilyin, A.V. 1973. Khubsugul phosphorite- bearing basin: Moscow, Geolgicheskiy Institut, Doklady Akademiya Nauk SSSR, p. 167 (in Russian).

Ilyin, A.V. 1998. Rare-earth geochemistry of old phosphorites and probability of syngenetic precipitation and accumulation of phosphate: Chemical Geology, v. 144(3-4), p. 243-256. https://doi.org/10.1016/S0009-2541(97)00134-4

Ilyin, A.V., Ratnikova, G.I. 1981. Primary, bedded, structureless phosphorite of the Khubsugul Basin, Mongolia: Journal of Sedimentary Research, v. 51(4), p. 1215- 1222. https://doi.org/10.1306/212F7E69-2B24- 11D7-8648000102C1865D

Kuzmichev, A.B., Bibikova, E.V., Zhuravlev, D.Z. 2001. Neoproterozoic (~ 800 Ma) orogeny in the Tuva-Mongolia Massif (Siberia): island arc-continent collision at the northeast Rodinia mar-gin: Precambrian Research, v. 110(1-4), p. 109-126. https://doi.org/10.1016/S0301-9268(01)00183-8

Kuzmichev, A.B. 2015. Neoproterozoic accretion of the Tuva-Mongolian massif, one of the Precambrian terranes in the Central Asian Orogenic Belt: The Central Asian Orogenic Belt, p. 66-92.

Macdonald, F.A., Jones, D.S. 2011. The Khubsugul Group, northern Mongolia: Geological Society, London, Memoirs, v. 36 (1), p. 339-345. https://doi.org/10.1144/M36.30

Osokin, P.V., Tyzhinov, A.V. 1998. Precambrian tilloids of the Oka-Khubsugul phosphorite-bearing basin (eastern Sayany, northwestern Mongolia): Lithology and Mineral Resources, C/C of Litologiia I Polezyne Iskopaemye, v. 33, p. 142-154.

Peng, S.C., Babcock, L.E., Ahlberg, P. 2020. The Cambrian period in Geologic Time Scale 2020, Elsevier, p. 565-629. https:// doi.org/10.1016/B978-0-12-824360-2.00019-X

Smith, E.F., Macdonald, F.A., Petach, T.A., Bold, U., Schrag, D.P. 2016. Integrated stratigraphic, geochemical, and paleontological late Ediacaran to early Cambrian records from southwestern Mongolia: GSA Bulletin, v. 128(3-4), p.442- 468. https://doi.org/10.1130/B31248.1

Vishnevskaya, I.A., Letnikova, E.F. 2013. Chemostratigraphy of the Vendian-Cambrian carbonate sedimentary cover of the Tuva- Mongolian microcontinent: Russian Geology and Geophysics, v. 54(6), p. 567-586. https://doi.org/10.1016/j.rgg.2013.04.008

Zhegallo, E.A., Rozanov, A.Y., Ushatinskaya G.T., Hoover, R.B., Gerasimenko, L.M., Ragozina, A.L. 2000. Atlas of microorganisms from ancient phosphorites of Khubsugul (Mongolia): Huntsville, AL, National Aeronautics and Space Administration, Marshall Space Flight Center, 166 p.

* * *

CHAPTER III, PART 2: CAMBRIAN FORELAND PHOSPHOGENESIS IN THE KHUVSGUL BASIN OF MONGOLIA

ABSTRACT

Ediacaran-Cambrian phosphorite deposits in northern Mongolia have been associated with a putative increase in nutrient delivery to the global oceans that drove oxygenation and the rise of animals. However, like many phosphorites from this ~100 Myr interval, the precise age and depositional setting of these deposits remain poorly constrained. Here, we integrate new geological mapping, lithostratigraphy, chemostratigraphy, and U-Pb zircon geochronology to develop a new age and tectonic basin model for the Cryogenian to Cambrian Khuvsgul Group of northern Mongolia. We propose that Cambrian strata were deposited into two composite foreland basins. A ~535-524 Ma pro-foreland basin formed during collision of the Khantaishir-Agardag oceanic arc, and a younger ~523-505 Ma retro-arc foreland developed behind the Ikh-Mongol continental arc. The phosphorites, which include a Doushantuo-Pertatataka-type microfossil assemblage, were deposited in the pro-foreland basin between 534 and 531 Ma, at least 40 million years later than the phosphatized Weng'an Biota of the Doushantuo Formation of South China. Tectonically-mediated basinal topography associated with foreland development was a necessary condition for phosphogenesis along the Tuva-Mongolia-Zavkhan margin, with different styles of phosphate mineralization associated with sediment starvation and migrating redox boundaries across the margin. The apparent Ediacaran-Cambrian increase in preserved phosphorite deposits was not an event associated with an increase in nutrient delivery to the

oceans, but rather represents the opening of a taphonomic window in which increasing redox potential favored phosphate accumulation in marginal marine environments.

3.6. Introduction

On geological timescales, phosphate is thought to be a limiting nutrient of bioproductivity (Tyrell, 1999), with phosphorus fluxes in Earth's surface environments responding to changes in both silicate weathering (Hartmann and Moosdorf, 2011; Horton, 2015) and environmental redox state (Dodd et al., 2023; Ruttenberg, 2003; Colman and Holland, 2000). The stratigraphic record preserves an apparent global increase in the size, grade, and frequency of concentrated phosphate deposits, or phosphorites, near the Ediacaran-Cambrian boundary (Cook, 1992; Cook and McIlhenny, 1979). Ediacaran-Cambrian phosphorites have been found in Asia (Ilyin and Zhuraleva, 1968; Ilyin and Ratnikova, 1981; Anttila et al, 2021; Meert et al., 2011; Xiao and Knoll, 1999; Sergeev et al., 2020; Banerjee et al., 1980; Mazumdar et al., 1999), Africa (Flicoteaux and Trompette, 1998; Bertrand-Sarfarti et al., 1997), Australia (Valetich et al., 2022; Southgate, 1980) and South America (Misi and Kyle, 1994; Shiraishi et al., 2019; Sanders and Grotzinger, 2021; Morais et al., 2021), and include some of the largest known phosphate deposits in the world (Cook and Shergold, 1986). These occurrences have inspired hypotheses that link a global increase in phosphate deposits around the Ediacaran-Cambrian boundary to changes in nutrient fluxes to the oceans (Papineau, 2010), concomitant oxygenation of the Earth's surface (Reinhard et al., 2017; Laakso et al., 2020), and the rise and expansion of life (Shields et al., 2000).

However, phosphorus delivery to the oceans (Follmi, 1996) is only one potential controlling aspect of phosphogenesis: sedimentological (Follmi, 1990; Follmi et al 2005; 2017), paleotopographic (Follmi et al., 2017), and biogenic (Sanders, 2023; Schultz and Schultz, 2005) factors have been shown to control the locus and concentration of phosphate accumulation in phosphogenic environments. To this end, detailed investigations that constrain the age, duration, and depositional context of individual phosphorite localities are a prerequisite of any holistic model for the drivers of Ediacaran-Cambrian phosphogenesis. Furthermore, constraining the age of Ediacaran-Cambrian phosphorites is particularly important given the taphonomic potential of phosphogenic environments: early authigenic precipitation of phosphate minerals (dominantly calcium fluorapatite, or CFA) can result in the exceptional preservation of biogenous material, including soft-bodied organisms and putative animal embryos (Xiao et al., 1998). Phosphatized lagerstätten, such as the Weng'an biota of the Doushantuo Formation (Fm, Xiao and Knoll, 2000) and the Portfjeld Fm, northern Greenland (Willman et al., 2020) provide some of the best windows into the evolution and expansion of metazoans around the Ediacaran-Cambrian boundary.

The Khuvsgul Group of northern Mongolia (Ilyin and Ratnikova, 1981; Anttila et al., 2021) contains one of the largest ore-grade phosphorites in the world (Ilyin, 1973; Munkhtsengel et al., 2021), and hosts glacial diamictites associated with Cryogenian Snowball Earth glaciations (Macdonald and Jones, 2011) as well as a diverse Doushantuo-Pertatataka-Type microfossil assemblage (Anderson et al., 2017; 2019). Although the Khuvsgul Group has been the subject of geological investigation for more than half a century (Donov et al., 1967), age models for these strata rely on biostratigraphy (Ilyin and Zhuraleva, 1968; Korobov, 1980; 1989; Zhegallo et al., 2000; Demidenko et al., 2003,

Korovnikov and Lazarev, 2021), which is of limited used in the Neoproterozoic and Early Cambrian. Lithostratigraphic correlations to radiometrically-dated sections elsewhere provide additional age constraints on the Khuvsgul Group (Macdonald and Jones, 2011).

Here, we develop a new age model for the Khuvsgul Group by combining new lithostratigraphic observations, carbonate chemostratigraphy, and U-Pb zircon geochronology from the Khuvsgul region. This framework is paired with new geologic mapping and structural data to create a tectonic basin model for the Khuvsgul Group. Within the context of this model, we compare Khuvsgul Group strata to adjacent Cryogenian to Cambrian strata of the Zavkhan Terrane in southwest Mongolia (Bold et al. 2016a, b, Smith et al. 2016, Macdonald and Jones, 2011, Macdonald et al., 2009), and explore how differences in sedimentology and basin morphology may have impacted the mode of phosphogenesis observed in each basin. Finally, our chronostratigraphic model provides new age constraints on the phosphatic lagerstätten of the Kheseen Fm of the Khuvsgul Group, which are then discussed in relation to other Doushantuo-Pertatataka-Type microfossil assemblages and Ediacaran-Cambrian phosphorites from around the world.

3.7. Geologic Background

3.7.1. Tectonic setting of the Khuvsgul Group

The Khuvsgul Group comprises the Cryogenian-Cambrian sedimentary cover of the Khuvsgul Terrane, which forms the central component of an amalgamated composite terrane previously referred to as the Tuva-Mongolia Massif (Ilyin, 1971) the Tuva-Mongolia Microcontintent (TMM; Kuzmichev, 2015), Central Mongolian Terranes (CMT; Domieier, 2018), and our preferred nomenclature of the Tuva-Mongolia Terrane (TMT; Bold et al.,

2019). The TMT (Fig. 1) is embedded within the Central Asian Orogenic System (CAOS; Kroner et al., 2007; Windley et al., 2007; Kroner et al., 2014), which formed through collision and accretion of arcs, oceanic tracts, and microcontinental fragments from the late Mesoproterozoic (Khain et al., 2002) to late Paleozoic (Xiao et al., 2003; Windley et al., 2007; Wilde, 2015).

The oldest rocks in the TMT are the 2702 ± 6 Ma basement gneisses (the Salig Complex) of the Gargan Block (U-Pb LA-ICPMS on zircon, Bold et al., 2019). During the Tonian Period, volcanic and ophiolitic rocks associated with the ~1000 Ma Dunzhugur arc (Khain et al., 2002) were obducted along the northern TMT margin prior to the emplacement of the Sumsunur Complex, which includes tonalite-trondjeimites that have been dated to 785 ± 11 Ma (Kuzmichev et al., 2001), and potentially during 814 ± 10 Ma metamorphism of the Salig Complex (Bold et al., 2019). The Sumsunur Complex is an intrusive complement to the coeval Sarkhoi volcanics (Kuzmichev and Larionov, 2011), which have also been correlated with the Zavkhan Volcanics (see Bold et al., 2016b) in southwest Mongolia. Geochemical data suggests the Zavkhan and Sarkhoi volcanics formed a continental arc system across both terranes (Kheraskova et al., 1995; Kuzmichev et al., 2001; Kuzmichev, 2015, Bold et al. 2016b).

3.7.2. Cryogenian-Cambrian stratigraphy of the Tuva Mongolia Terranes: The Khuvsgul Group

Carbonate, siliciclastic, and volcaniclastic rocks of the Khuvsgul Group overlie the Sarkhoi volcanics (and coeval siliclastic and volcaniclastic rocks of the Darkhat Group).

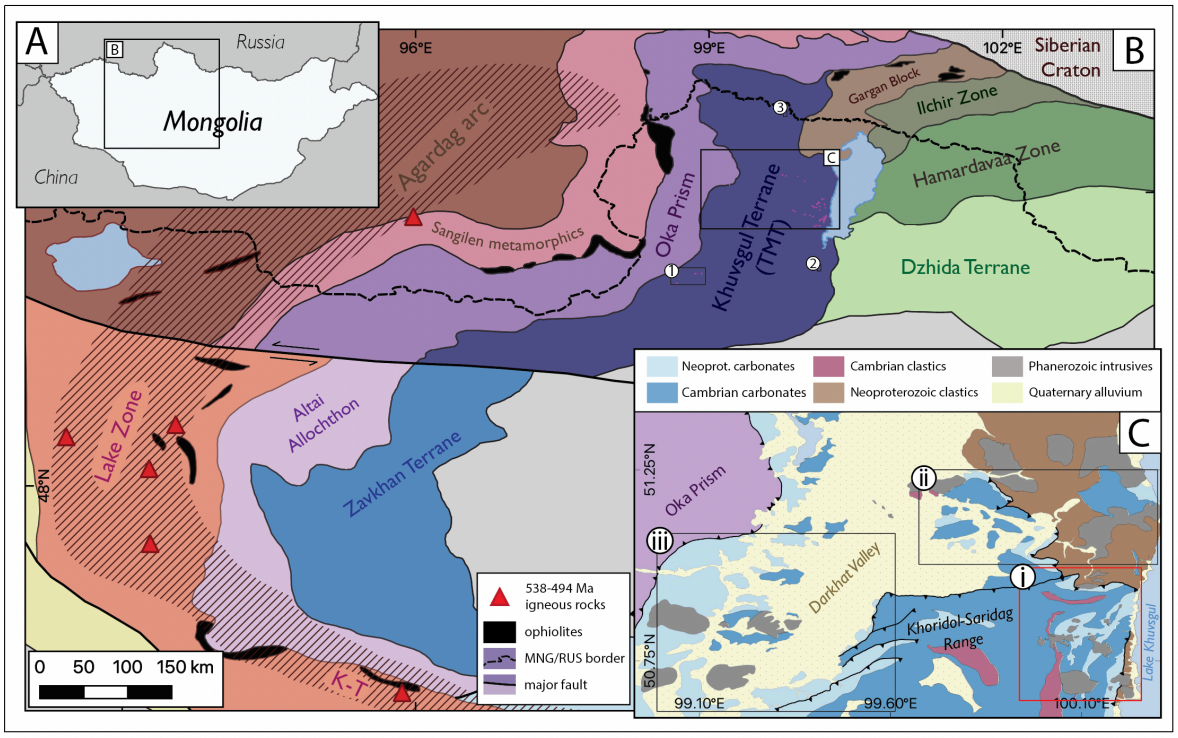

Figure 1: Location and geological context of study area. **A)** geopolitical overview map, contextualizing **B)** the Mongolian Central Asian Orogenic Belt, modified from Bold et al. (2016b; 2019) and Kuzmichev (2015). The Khuvsgul Terrane forms the core of the composite Tuva Mongolia Terrane (TMT). The location of 538-494 Ma igneous rocks, as well as the hashed area indicating the putative extent of the Ikh-Mongol continental arc, are modified from Janousek et al. (2018). The numerals 1, 2, and 3 indicate the positions of the Bayan Zurgh, Eg Gol, and Khoroo Gol study areas, respectively. **C)** Generalized geologic map of the main Khuvsgul study area, compiled from both original and extant geological mapping (Buihover et al., 1968). Boxes with numerals i, ii, and iii indicate the extent of the Khoridol Saridag, Northern, and Darkhat Valley mapping regions, respectively. A 1:100,000 geological map of the Khoridol Saridag mapping area can be found in Figure 3; geologic maps of the Northern and Darkhat Valley mapping areas can be found as Figures X and Y, respectively.

Here, we build on the stratigraphic framework developed from the Khuvsgul region of the TMT (Fig. 2; Anttila et al., 2021) with new chemostratigraphic, lithostratigraphic, and sequence stratigraphic data.

The Cryogenian strata of the Khuvsgul Group include two diamictites separated by a carbonate sequence, which have been correlated with the Cryogenian Sturtian and Marinoan Snowball Earth glaciations and the non-glacial interlude, respectively (Macdonald and

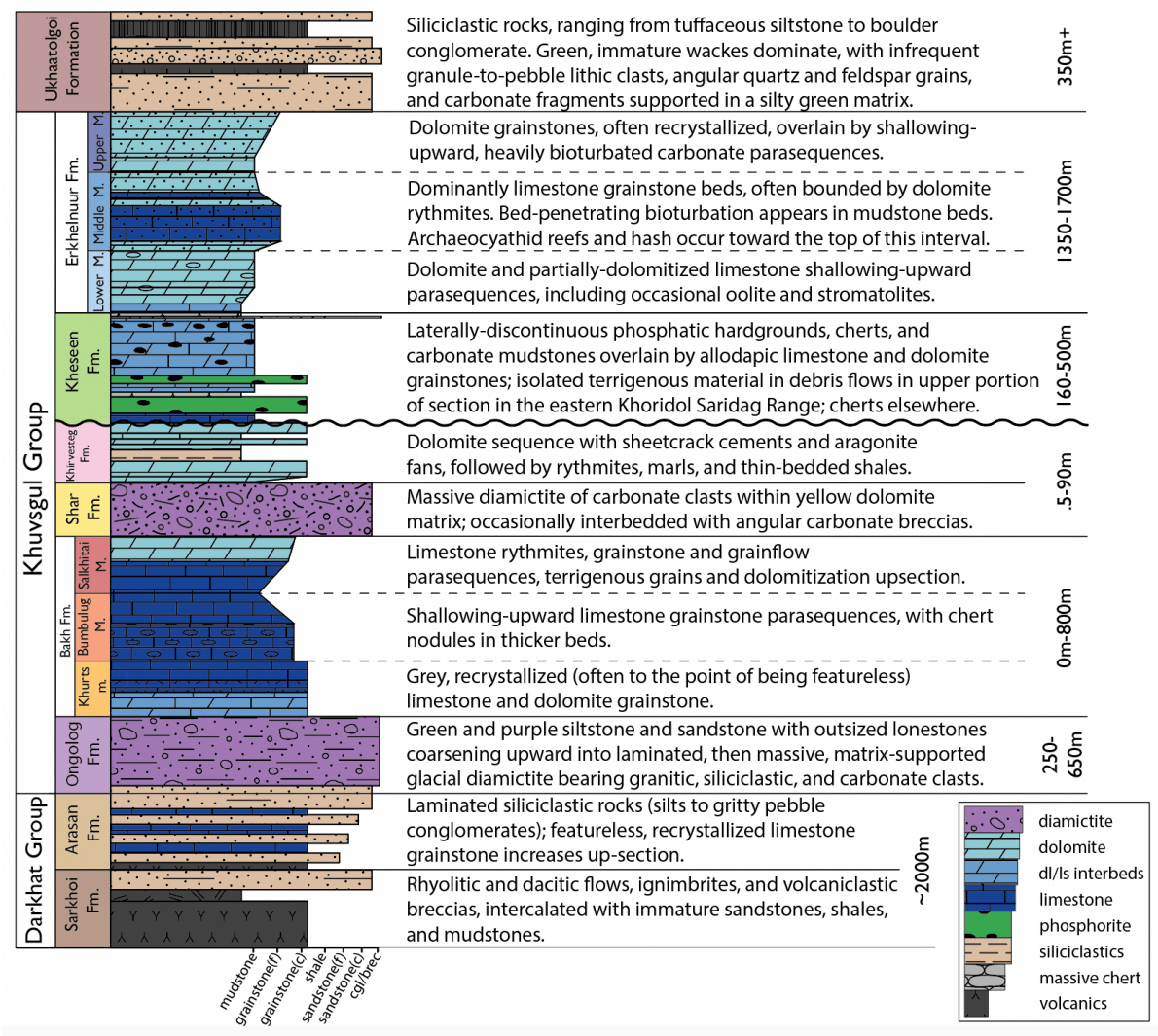

Figure 2. Generalized stratigraphy of the Khuvsgul Group and adjacent strata, after Anttila et al. (2021).

Jones, 2011). The laterally-variable thicknesses of Cryogenian strata on the Khuvsgul Block have been interpreted to represent syn-depositional topography. In particular, it has been proposed that the Sturtian Ongolog diamictite was deposited along active Tonian to Cryogenian rift shoulders (Osokin and Tyzhinoff, 1998; Macdonald and Jones, 2011).

Much of the early geologic inquiry in the Khuvsgul region (Donov, et al., 1967; Ilyin, 1973, 2004; Osokin and Tyzhinof, 1998) focused on the phosphatic strata of the

Kheseen Fm, which are found stratigraphically above the Cryogenian sequence and make up one of the largest economic-grade phosphorite deposits in the world (Cook and Shergold, 1984). Trenches and roadcuts from prospecting are still visible, but economic development of mineral resources in the area was prevented initially by the remote location of the Khuvsgul region, and more recently by the recognition of the environmental fragility of the surrounding ecosystem. In addition to their economic significance, phosphorites of the Kheseen Fm host a Doushantuo-Pertatanka-Type microfossil assemblage (Anderson et al., 2017, 2019), with fossiliferous strata located in the eastern Khoridol Saridag mountain range, on the western shores of Lake Khuvsgul (Fig. 3).

The phosphatic strata of the Kheseen Fm are separated from the underlying Cryogenian units by a thin package of Ediacaran carbonate, lutite, and shale (Fig. 2). For this reason, previous workers (Sheldon, 1984; Osokin and Tyzhinov, 1998; Ilyin, 2004) argued for a genetic relationship between Cryogenian glacial episodes and the phosphorite deposits. However, a disconformity surface first recognized by Ilyin (2004) at several sites around the basin may be potentially correlative to an Ediacaran hiatus observed in the Zavkhan Terrane (Macdonald et al., 2009; Bold et al., 2016a), casting doubt upon glaciogenic interpretations of phosphogenesis in the Khuvsgul basin.

The upper Khuvsgul Group includes the ~2 km-thick carbonate succession of the Erkhelnuur Fm, which disconformably overlies the Kheseen Fm. Reported trilobite and archaeocyathid occurrences within the Erkhelnuur Fm (Korobov, 1989) suggest a Cambrian age for this interval. A coarse siliciclastic unit, the Ukhaatolgoi Fm, overlies the Erkhelnuur Fm carbonates, and is the youngest pre-Cenozoic sedimentary sequence on the TMT. The

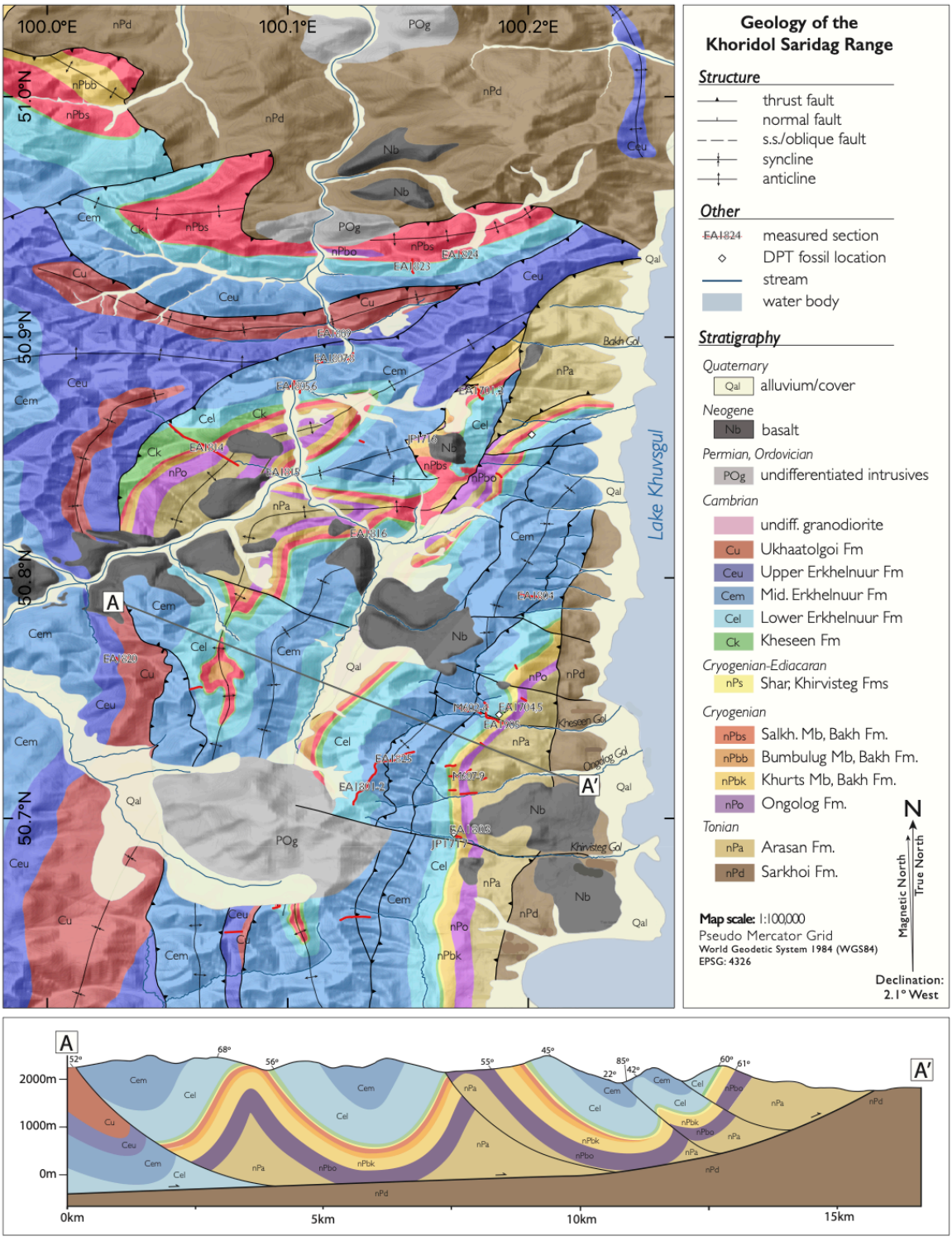

Figure 3: Original geologic map of the Khuvsgul Group in the Khoridol Saridag Range. The location of schematic cross section A-A' is shown in the main map panel. A companion map highlighting the broad structural features of this map area is provided in Figure 7.

accumulation of the Cambrian platformal carbonate sequence of the Khuvsgul basin has been attributed to continued thermal subsidence along the TMT margin (Khukhuudei et al, 2020; Kuzmichev, 2015) and potential deposition into a riftogenic graben (Ilyin, 2004). Conversely, Macdonald and Jones (2011) suggest that, like on the Zavkhan Terrane, Cambrian subsidence on the TMT margin was driven by collisional tectonics related to the Salarian Orogeny (Rhuzentsev and Burashnikov, 1996; Smith et al., 2016; Bold et al., 2016).

3.7.3. Phanerozoic deformation of the Tuva Mongolian Terranes

Khuvsgul Group strata in the Khoridol Saridag Range (Fig. 1) were previously mapped as km-scale south-plunging, north-south-trending anticlinoria (Buihover et al., 1968; Mongolian Survey, 1988), intruded by Ordovician post-metamorphic monzogranites and granodiorites (Kuzmichev, 2015). However, these pre-Ordovician structures have not been explicitly associated with a specific collision or compressional event, highlighting the need for detailed structural characterization of the greater Khuvsgul region. Following early Paleozoic deformation, TMT-Siberian sutures were reactivated and intruded by Carboniferous and early Permian plutons (Buslov et al., 2001; 2009). The Neogene development of the Baikal Rift system resulted in the generation of new N-S trending normal fault structures and basaltic magmatism in the Khuvsgul region. The Neogene extensional regime also reactivated extant older structures, leading to block rotation along older faults in the region. Seismic activity along both normal and sinistral transverse structures in the Khuvsgul region continues today (Liu et al., 2021).

3.8. Methods

3.8.1. Geological mapping and stratigraphy

Over the course of three field seasons, we mapped the geology of the Khuvsgul region of the TMT, with an emphasis on exposures of the Khuvsgul Group in the Khoridol Saridag Range and Darkhat Valley (Fig. 1C). Outcrop mapping was performed on Apple iPads running FieldMove software. Structural measurements and field photographs were also taken and geotagged within the FieldMove program. Shapefiles generated from outcrop mapping and structural measurements were imported into QGIS and used, in addition to satellite imagery and scanned early geologic maps, as constraints for the placement of structures and contacts in our geologic map of the region. Stratigraphic sections were measured with a meter-stick; the locations of all measured sections referenced in this manuscript are collated in Table A1 in Appendix 2.

3.8.2. Bulk carbonate carbon and oxygen isotope analyses

Carbonate rocks were collected for stable carbon and oxygen isotope ($\delta^{13}C$ and $\delta^{18}O$) analyses within measured sections throughout the field area. Limestone and dolomite hand samples (200-500 g) were collected at 0.5 to 2 m intervals within selected measured sections, with samples chosen from outcrops with minimal evidence of late-stage alteration. Each collected sample was shipped back to the University of California, Santa Barbara and cut into slabs with a rock saw, with slab surfaces cut orthogonal to bedding features. ~1 mg of carbonate powder was then procured from each slab via microdrilling (0.5 mm bit on a vertical press), with a focus on producing a representative and reproducible powder aliquot for each sample: samples with laminar bedding features were drilled along single bedding

surfaces whenever possible, and micritic matrix material was targeted for allodapic samples. Drilled slabs were labeled and stored.

Aliquots of carbonate powder from sections EA1701-05, JP1716-17, MG32, EA1801,-02,-05 and -20 were analyzed in the Stable Isotope Laboratory of the Precambrian Research Office at McGill University. Subsamples of each aliquot of carbonate powder were loaded into glass vials and individually dissolved in H_3PO_4 on a NuCarb automated carbonate preparation device. The resultant CO_2 analyte from each sample was measured on a Nu Instruments Perspective IRMS.

Aliquots from all other sections were analyzed at the Center for Stable Isotope Biogeochemistry at the University of California Berkeley. 10-100 microgram subsamples of each powder aliquot were reacted with concentrated H_3PO_4 at 90^{o}C for 10 mins to generate CO_2 gas for coupled $\delta^{13}C$ and $\delta^{18}O$ analysis using a GV IsoPrime mass spectrometer with Dual-Inlet and MultiCarb systems. Several replicates of one international standard NBS19, and two lab standards $CaCO_3$-I & II were measured along with approximately 40 unknowns for each run. The overall external analytical precision was about $\pm$0.05‰ for $\delta^{13}C$ and about $\pm$0.07‰ for $\delta^{18}O$.

All $\delta^{13}C$ and $\delta^{18}O$ data are collated in Table A2 in Appendix 2.

3.8.3. U-Pb zircon geochronology

Samples for U-Pb zircon geochronology were collected during the course of mapping. Samples were cleaned and trimmed to remove potential contamination, and pulverized in an industrial jaw crusher. The resultant <500 micron fraction was collected, and subsequently washed in an antiflocculant solution to remove ultrafine material. Samples

were then panned to isolate heavy minerals. Samples containing few zircon were further magnetically separated with a Frantz device (0.4A at a 20º incline), and put through a final density separation in methylene iodide. Zircon grains were individually picked from resultant heavy mineral separates, annealed in a muffle furnace for 48 hours at 900ºC, mounted in epoxy, and polished. The internal structures of the grains were mapped with cathodoluminescence (CL) imaging using a Cameca SX-100 Electron Probe Micro-Analyzer (EPMA) with a CL detector.

Laser ablation inductively coupled plasma mass spectrometry (LA-ICPMS) analyses

LA-ICPMS U-Pb geochronological analyses on zircon were completed at UCSB, using a Cetac/Photon Machines Analyte Excite 193 nm excimer laser attached to a Nu Plasma 3D multicollector ICPMS, following the methods of Kylander-Clark et al. (2013). Each zircon was ablated with a 20µm laser spot. The zircon 91500 (Wiedenbeck et al., 1995) was used for age calibration. Secondary zircon reference materials included 9435, AUSZ, Mudtank, GJ1 (Jackson et al., 2004), and Plesovice (Sláma et al., 2008). *Iolite* (Paton et al., 2010) was used to correct for U-Pb mass bias and drift following the methods of Kylander-Clark et al. (2013) and Horstwood et al. (2016). The resultant U and Pb isotopic ratios were reduced according to methods outlined in Kylander-Clark et al., 2013. Dates for each analyzed grain were calculated by importing reduced $^{238}U/^{206}Pb$ and $^{207}Pb/^{206}Pb$ ratios into *IsoplotR* (Vermeesch 2018). For appropriate magmatic samples, a weighted mean age for each sample was calculated by isolating a group of analyses that conform to statistical standards of a single magmatic population as outlined in Spencer et al. (2016) and references therein.

Detrital zircon normalized probability plots were created for all detrital samples. Discordant analyses from detrital samples were removed by excluding all analyses exhibiting more than 15% discordance. Reversely-discordant analyses greater than -10% discordant were also included in the compilation, with reverse discordance assumed to be attributed to a range of potential factors (see Mattinson et al., 1996) putatively associated with various metamorphic events in the region. Ages from the resultant filtered dataset were incorporated into a kernel density estimation (KDE) function with 5Ma bins (full code available in the Supplementary Information/GitHub repository). Because the detrital populations of interest in our samples are of Tonian and younger age, we present detrital spectra of ages up to 1Ga, and as such only utilize the Pb^{206}/U^{238} ages of each analysis in the KDE. Maximum depositional ages (MDAs) were determined by using the age of the youngest individual grain in the sample, or the weighted mean of the youngest group of grains in the case of samples with a cluster of young analyses that conform to MSWD criteria for a single magmatic population (Wendt and Carl., 1991; Spencer et al., 2016). Additional CA-ID-TIMS analyses were conducted on a subset of grains used to calculate MDAs, methods for which are outlined below.

Chemical abrasion isotope dilution thermal ionization mass spectrometry (CA-ID-TIMS) analyses

Individual grains from the population of zircons that make up the LA-ICPMS weighted mean age for magmatic samples or the MDA of detrital samples were analyzed with single zircon U-Pb chemical abrasion isotope dilution thermal ionization mass spectrometry (CA-ID-TIMS) at Princeton University, following standard chemical abrasion

methods modified from Mattinson (2005). Previously annealed single zircons were plucked from epoxy mounts, transferred to Teflon beakers, and rinsed with 3N HNO_3. Grains were removed from the acid rinse and loaded into 200 µl Savillex microcapsules with ca. 90 µl 29M HF. Microcapsules were assembled in a Parr bomb and zircons were leached at 180ºC for 12 hours to remove domains in the crystal lattice that may have experienced lead loss. Following the complete dissolution of several grains in the first two batches of leaching, a set of samples in a third Parr bomb were removed from the 180ºC oven after only 4.5 hours in order to avoid complete destruction of the grains. This leaching time resulted in no complete grain dissolution, but introduced the possibility of the incorporation of domains with possible lead-loss into the resultant analyte. Only one zircon (EA1905-46B) from this low-temperature leach appears to have incorporated significant lead loss; as a result, we omit the data from this grain from maximum depositional age calculations for this sample, but have included the data in Table A3, Appendix 2.

Following leaching, zircon grains were moved to Teflon beakers, and repeatedly rinsed in 3N HNO_3 and 6N HCl. The crystals were then transferred back to microcapsules, spiked with the EARTHTIME ^{205}Pb-^{233}U-^{235}U tracer (Condon et al., 2015; McLean et al., 2015) and placed back into a Parr bomb for dissolution in ca. 90 µl 29M HF for 60 h at 210ºC. The resulting solutions were then dried down, converted to chlorides in the Parr bomb overnight, and dried down once more on the hot plate. The samples were then redissolved in 3N HCl and placed into 50 µl microcolumns filled with AG-1 X8 resin, where U-Pb and trace element solutions were separated by anion exchange following methods modified from Krogh (1973). The U-Pb solution was dried down in a Teflon beaker on the hot plate with a microdrop of 0.015M H_3PO_4. Each aliquot was then redissolved in a silica

gel emitter (Gerstenberger and Haase, 1997), and loaded with an ultrafine pipette onto a single outgassed zoned-refined rhenium filament.

Lead and U isotopic measurements were performed with one of two Isotopx Phoenix thermal ionization mass spectrometers (TIMS) at Princeton University. Pb isotopes were measured using peak-hopping mode on a Daly photomultiplier ion-counter, while U isotopes were measured as UO_2 in static mode with Faraday cups connected to traditional 10^{12} Ω amplifiers, or to ATONA amplifiers (Szymanowski and Schoene, 2020). Instrumental mass fractionation for Pb was corrected with a factor (0.14 or 0.18 %/amu) derived from a long-term compilation of in-run $^{202}Pb/^{205}Pb$ values of double-Pb-spiked Daly analyses on each instrument. The dead time of the Daly systems was kept constant throughout the period of the study but was monitored with analyses of NIST SRM 982 Pb isotope standard over a range of intensities. U runs were corrected for fractionation using the known $^{233}U/^{235}U$ of the spike and assuming a sample $^{238}U/^{235}U$ of 137.818 ± 0.045 (2σ; Hiess et al., 2012). An $^{18}O/^{16}O$ value of 0.00205 ± 2 (1σ) was used to correct for interferences in UO_2 analyses.

Data was compiled and reduced in *Tripoli* and *ET_Redux* (Bowring et al., 2011; McLean et al., 2011). Initial ^{230}Th disequilibrium in the $^{206}Pb/^{238}U$ system was corrected for each grain by estimating $(Th/U)_{magma}$ using a fixed $(Th/U)_{zircon\text{-}magma}$ partition coefficient ratio of 0.19 ± 0.06 (1s) based on a compilation of natural zircon–melt pairs, and uncertainties for the $(Th/U)_{magma}$ were propagated into final date uncertainty for each grain. Weighted-mean ages were calculated in *ET_Redux.* Results are summarized below, and are collated, along with sample locations, in Table A3 in Appendix 2.

3.8.4. Backstripping calculations

A representative tectonic subsidence curve for the Khuvsgul Group was calculated by entering stratigraphic thickness estimates, model ages, approximations of lithological composition, and estimated paleo-depths of deposition for all Khuvsgul Group strata into the backstripping model of Müller et al., 2018. All model inputs, as well assumptions about lithological density, porosity, and permeability, are tabulated in Table A4, Appendix 2; full code used to generate the tectonic subsidence curve is available within the GitHub repository linked in Appendix A2.

3.9. Results

3.9.1. Lithostratigraphy and facies associations of the Khuvsgul Basin

The Khuvsgul Group, formalized by Anttila et al. (2021), is divided into the Ongolog, Bakh, Shar, Khirvesteg, Kheseen, and Erkhelnuur formations, with the Bakh and Erkhelnuur formations further divided into three Members. The Khuvsgul Group is underlain by the volcanics, volcaniclastics, and siliciclastics of the Darkhat Group, which includes the Sarkhoi and Arasan formations, and is overlain by siliciclastic rocks of the Ukhaatolgoi Fm.

Lithofacies of the Khuvsgul Group and bounding units are described below. These descriptions inform interpretations of the depositional environments of each unit, which are subsequently incorporated into a general tectonostratigraphic model for the Khuvsgul Group in Section 5.4.

Sarkhoi Formation description. – The Sarkhoi Fm outcrops in the Khoridol Saridag Range and Darkhat Valley, and consists of purple, red, and green fine-grained rhyolite and

rhyodacite flows, ignimbrites, volcaniclastic breccias, siltstone, fine-grained sandstone with linguoid and lunate ripples, and feldspathic and lithic wacke. The Sarkhoi Fm is estimated to be ~4 km thick near the Zabit River of southern Siberia (Kuzmichev, 2015), whereas the maximum thickness in the Khoridol-Saridag Range and Darkhat Valley is ~1.5 km.

Sarkhoi Formation interpretation.–Although the Sarkhoi Fm has been interpreted to have formed in a rift setting (Ilyin 1973, 2004), geochemical characterizations of the Sarkhoi volcanics suggest a continental arc affinity (Kuzmichev and Larionov, 2011), with east-dipping subduction inferred to have occurred along the western margin of the TMT (Kuzmichev, 2015). In the Khuvsgul region, the close association of volcanic flows and ignimbrites with a suite of siliciclastic rocks records volcanic flows interfingering with a marginal marine depositional environment, suggesting the proximity of an actively-subsiding basin adjacent to an active volcanic edifice.

Arasan Formation description. – Above the Sarkhoi Fm, the Arasan Fm outcrops as tan-to-brown laminated siltstone with occasional 1–3 cm fining-upward packages of medium- to coarse-grained quartz arenite to sublitharenite. In the lower Arasan Fm, discontinuous quartz-rich granule to pebble lags occur within fine-grained sandstone or shale layers directly above thicker sandstone beds. 10–20 cm thick recrystallized dolomite beds punctuate the uppermost ~100 m of very fine-grained sandstone and siltstone, with minor coarse-grained sandstone beds intercalated throughout the uppermost portion of the section. Poor exposure precludes both the measurement of a complete stratigraphic section through the Arasan Fm, as well as identification of the basal contact.

Arasan Formation interpretation.–Although the contact with the underlying Sarkhoi Fm is not exposed, the well-sorted, moderately-mature siliciclastic rocks of the Arasan Fm

likely indicate a transition, from mass-wasting-dominated deposition in an actively-subsiding basin, to shoaling and the development of mature sediment sources in a potentially more-quiescent marginal environment. The close association of shales and laterally-continuous graded sandstones in the upper Arasan Fm suggests a marginal marine depozone, with episodic instability on the shelf and upper slope driving both gravity flow and suspension-dominated deposition.

Ongolog Formation description. – Intercalated graded and massive sandstone, siltstone, and shale of the basal Ongolog Fm is gradually populated up-section by increasing numbers of lonestones, forming a stratified, matrix-supported diamictite. The base of the Ongolog Fm is rarely exposed: at Kheseen Gol, the ochre to tawny-brown well-sorted siltstone and sandstone of the upper Arasan Fm grades into poorly-sorted green and purple siltstone and wacke of the overlying Ongolog Fm; however, this contact has been reported to be unconformable elsewhere in the region (Osokin and Tyzhinof, 1998). In some cases, the Arasan Fm is completely absent from the stratigraphy, with the basal Ongolog Fm directly overlying volcanics of the Sarkhoi Fm (Kuzmichev et al, 2001). In the Khoridol Saridag Range, with the exception of the exposures described above, the base of the Ongolog Fm is faulted.

The most complete Ongolog sections outcrop on the easternmost exposures of the Khoridol Saridag Range, where the basal clast-free portion of the Ongolog Fm is up to 400 m thick, and the overlying diamictite ranges from 100 – 250 m thick. The lower, clast-free interval is exposed along the northern ridge bordering the eponymous Ongolog Gol (Fig. 3), with poorly sorted, green to tawny-brown wacke transitioning up-section into olive to dark-brown siltstone with discontinuous lenses of medium-grained sandstone to poorly-sorted

granule conglomerate, and thin beds of blue to dark gray micritic limestone. Arkosic wackes that make up the coarser sandstone beds include subangular quartz plagioclase grains amidst a fine-grained green to brown matrix.

Up-section, sparse, rounded to sub-angular quartzite and carbonate granule-to-cobble lonestones are suspended in laminated green to brown siltstone and fine-grained sandstone beds. The frequency and maximum size of outsized clasts increases dramatically in the top ~200 m of section, with nearly continuous exposure on the ridge north of Kheseen Gol (Macdonald and Jones, 2011). In the easternmost Khoridol Saridag Range, the top ~100 m of the Ongolog Fm is composed of a matrix-supported, polyclastic, stratified diamictite. Clasts include rounded to sub-angular gravel to cobbles of quartzite, plutonic and volcanic rocks, and carbonates, and are locally observed to be faceted and striated (Osokin and Tyzhinof, 1998). The upper 30-50 m of the Ongolog Fm consists of resistant, dark-weathering argillite matrix-supported diamictite dominated by subrounded dolomite clasts with minor quartzite and granite clasts. This facies, termed the "perforated shale" by Ilyin (1973), is most dramatically exposed along the banks of Ongolog Gol, where dolomite clasts are recessively weathered, leaving pockmarked holes in the black argillite matrix (Fig. 4A). A different facies of the uppermost Ongolog diamictite outcrops to the west in the Darkhat Valley, where only the top of the formation is exposed: subangular quartzitic, plutonic, and volcanic cobbles are supported in a dark brown massive sandstone matrix.

Ongolog Formation interpretation. – The Ongolog Fm has been assigned to the ~717-661 Ma Sturtian Snowball Earth glaciation (Macdonald and Jones, 2011). Striated and faceted clasts within diamictites of the Ongolog Fm (Osokin and Tyzhinof, 1998) support a glaciogenic origin. The gradational transition from clast-free shales and wackes at the base

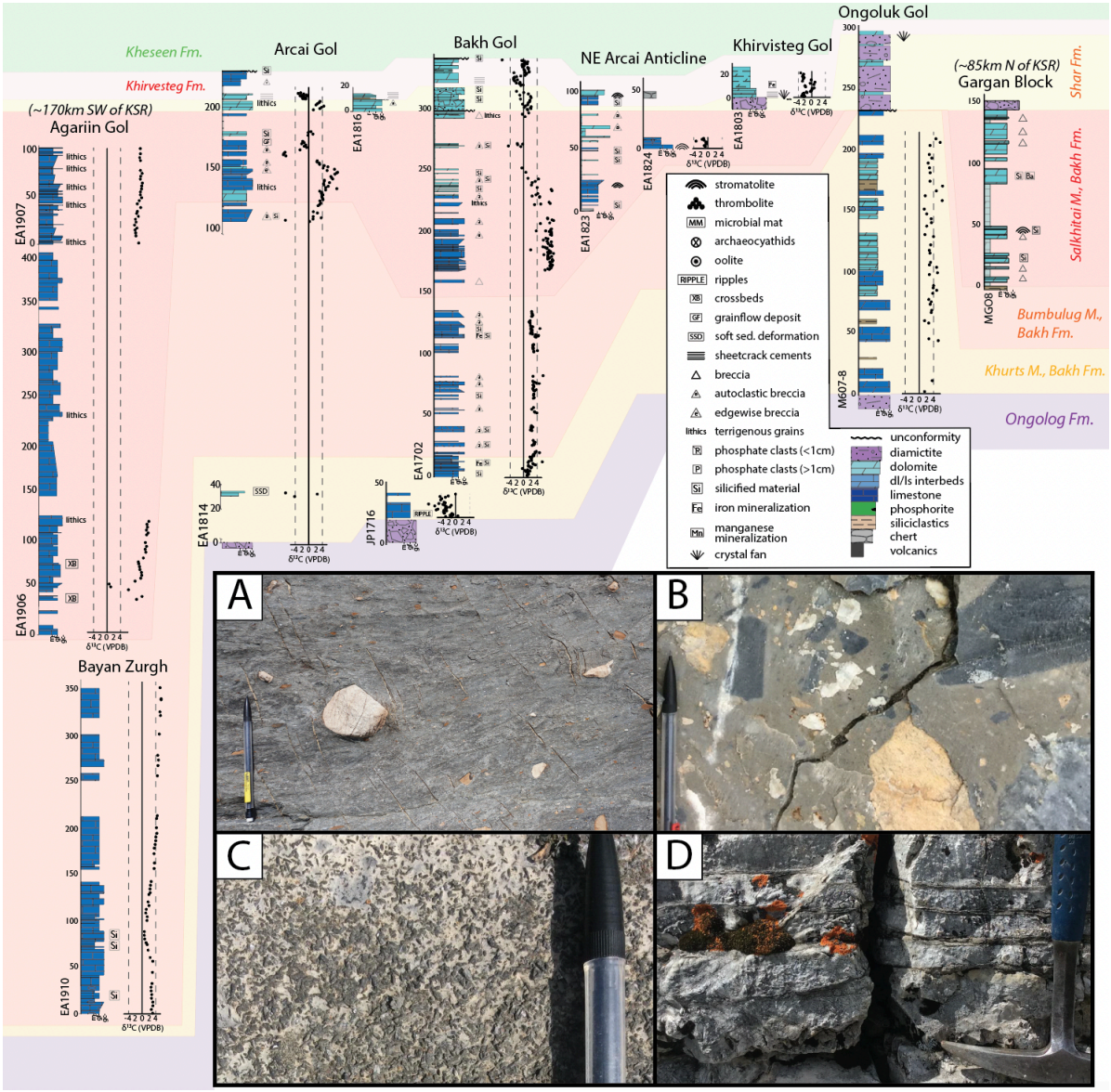

Figure 4: Cryogenian chemostratigraphy of the Khuvsgul Group, with field photographs of Cryogenian lithologies depicted in inset panels A-D. Stratigraphic sections are arranged, from left to right, along a broadly southwest-northeast transect. Geochemical data and section locations are collated in Supplementary Table 3. A) massive, matrix supported diacmictite of the Ongolog Fm. B) massive diamictite of the Shar Fm, featuring carbonate clasts in a dolomite matrix. C) barite pseudomorphs on a dolomite grainstone bedding plane in the basal Khirvisteg Fm. D) sheetcrack cements in dolomite mudstones of the basal Khirvisteg Fm.

of the unit to stratified or massive diamictite at the top of the section likely represents the evolution of a subaqueous glaciomarine depositional environment, with stratified diamictites interpreted as flow tills deposited in front of a marine ice-grounding line. It is unclear if the

clast-free basal portion of the Ongolog Fm was deposited in open water or below an ice shelf, but the gradational contact with the overlying diamictite suggests the latter. Initial sparse outsized clasts seen lower in the section, many of which truncate bedding planes, are likely ice rafted debris. An up-section increase in clast frequency, from isolated lonestone-bearing horizons amidst clast-free laminated shales to stratified diamictite without much evidence for bed-penetrating clasts, indicates the advance of the ice grounding line towards the depozone.

Bakh Formation. – Composed of variably laminated limestone and dolomite grainstone and rhythmite (finely laminated, graded beds of calcisiltite and micrite), the Bakh Fm is subdivided into three lithologically distinct Members.

Khurts Member description. –The Khurts Mb of the Bakh Fm is dominated by heavily recrystallized carbonate that forms resistant ridges in the Khoridol Saridag Range. Its thickness increases, from ~20 to >110 m, east to west across the Khoridol Saridag Range. Dolomite and limestone micrite and calcisiltite of the Khurts Mb sharply overlie the Ongolog diamictite. Above this cap carbonate, the Khurts Mb is composed of homogenous <2 m-thick dolomitized wackestone beds separated by <40 cm-thick allodapic dolomite grainstone beds that occasionally contain sub-rounded < 1 cm carbonate clasts. Up-section, wackestone beds thin to ~1 m, with interstitial 50-70 cm beds composed of finely-laminated, 1-2 cm grainstone beds containing sub-rounded carbonate clasts, small ooids, and rare domal stromatolites. Coarse grainstone beds increase in frequency up-section.

Khurts Member interpretation. – The sharp transition from the Ongolog Fm diamictite to laminated carbonate of the Khurts Mb is interpreted as a flooding surface associated with eustatic sea-level rise following the termination of the Sturtian glaciation.

Facies associations of the Khurts Mb are consistent with deposition in a subtidal marginal marine setting on a carbonate ramp. A shift from laminated micrite in the basal portion of the Khurts Mb to coarser wackestone and grainstone up-section suggests a transition from an outer-ramp to mid-ramp environment (Burchette and Wright, 1992). Infrequent, tabular carbonate allochems in some of the thicker grainstone beds towards the top of the Khurts Mb are interpreted as rip-up clasts, which, along with the occurrence of domal stromatolitic horizons in adjacent grainstone beds, are interpreted to reflect cyclic shoaling in a relatively energetic upper middle-ramp depositional setting. This interpretation is further supported by the appearance of ooids as allochems within some of the larger grainstone beds, suggesting relative proximity and/or intermittent depositional connectivity to shallow, energetic environments above fair-weather-wave base.

Bumbulug Member Description. – The base of the Bumbulug Mb of the Bakh Fm is marked by a sharp transition, from recrystallized dolomite wackestone and grainstone of the uppermost Khurts Mb, to limestone micrite-wackestone, lutite, and rhythmite interbeds. In the eastern Khoridol Saridag Range, grainstone and rhythmite beds are stippled with <3 cm-long ellipsoidal black and grey chert nodules, creating a dappled, almost spongelike appearance on the tan- to grey-weathering limestone beds. Chert nodules are concentrated primarily in micrite beds, and are associated with 1-3 mm-thick chert interbeds in adjacent rhythmite and lutite. Rare chert-free micrite and wackestone beds weather dark grey in contrast to buff-weathering chert-bearing carbonates. Exposures of the Bumbulug Mb in the western Khoridol Saridag Range and the Darkhat Valley contain less chert. Parasequences of micrite and lutite to grainstone and wackestone range in thickness from 0.8-2 m. Towards the top of the Bumbulug Mb, wackestone becomes the dominant component of each

parasequence. Thickness of the Bumbulug Mb is ~100-150 m across an east-west transect of the central Khoridol-Saridag Range (KSR map area, Fig. 3), <50 m in the southern Khoridol Saridag Range and Eg Gol regions (Fig. 1B), and >350 m near Bayan Zurgh (Fig. 1B), south-southwest of the Darkhat Valley.

Bumbulug Member interpretation. – The base of the Bumbulug Mb is marked by an abrupt shift from relatively energetic, peri-to shallow-subtidal grainstone and wackestone to finely-laminated micrite and lutite. This shift is interpreted as a deepening, from a peri- to shallow-subtidal carbonate ramp environment to a deeper, less energetic outer ramp setting, below storm-wave base. This transgressive sequence is followed by abundant wackestone and massive mudstone, interpreted to record a return to more energetic, gravity-driven depositional processes in a mid-ramp environment. Despite a substantial increase in stratigraphic thickness to the south-southwest, up-section facies trends are similar throughout the region, with globular chert-bearing micrite overlain by shallowing-upward parasequences at all complete Bumbulug Mb exposures.

Salkhitai Member description. – The Salkhitai Mb of the Bakh Fm consists of interbedded limestone grainstone, micrite, and occasional dark, fetid rhythmites, transitioning into coarsening-upward dolomitized grainstone, intraclast breccia, and massive carbonate breccia that include scattered lithic grains. Best exposed and preserved in the Khoridol Saridag Range, dark-colored limestone of the Salkhitai Mb consists of ~1.5-2 m-thick parasequences of laminated micrite capped by wackestone and grainstone beds that contain edgewise breccia and ooids in channelized bodies.

Up-section, parasequences are dominated by wackestone and grainstone, and are capped by intraclast breccia. Fining-upward wackestone and grainstone beds with 5-cm

diameter grey chert nodules become increasingly abundant up-section. Fine- to medium-grained, subrounded to subangular quartz and lithic fragments are dispersed throughout the uppermost limestone unit of fining-upwards wackestone and grainstone beds.

This influx of terrigenous material occurs directly before a shift to dolomitized grainstone beds with ~1cm-thick discontinuous bands of nodular black chert, followed by chaotically bedded conglomerates that include dolomite, chert, and quartz and lithic grains. The uppermost portion of the Sakhitai Mb contains massive coarse-grained sandstone with outsized carbonate and lithic clasts, up to granule in size, followed by a dolomite grainstone bed. The sandstone, as well as an erosional surface at the top of the dolomite grainstone, are both best exposed in the eastern Khoridol Saridag Range, particularly at the Bakh Gol section. Thickness of the Salkhitai Mb ranges from ~100-150 m across the basin.

Salkhitai Member interpretation. – Rhythmite-grainstone parasequences (Fig. 5A) at the base of the Salkhitai Mb are consistent with cyclic carbonate shoaling in a sub-tidal, mid-to-upper ramp environment, with facies associations trending up-section towards increasingly energetic, proximal depositional environments. Episodic reworking and incorporation of carbonate and chert into intraclast breccias suggests deposition near or above storm-wave base, and/or repeated shoaling into a more energetic depositional regime, above fair-weather-wave base. Up-section, channelization and an increase in terrigenous allochems indicate continued shallowing into an upper-ramp or shoreface depositional

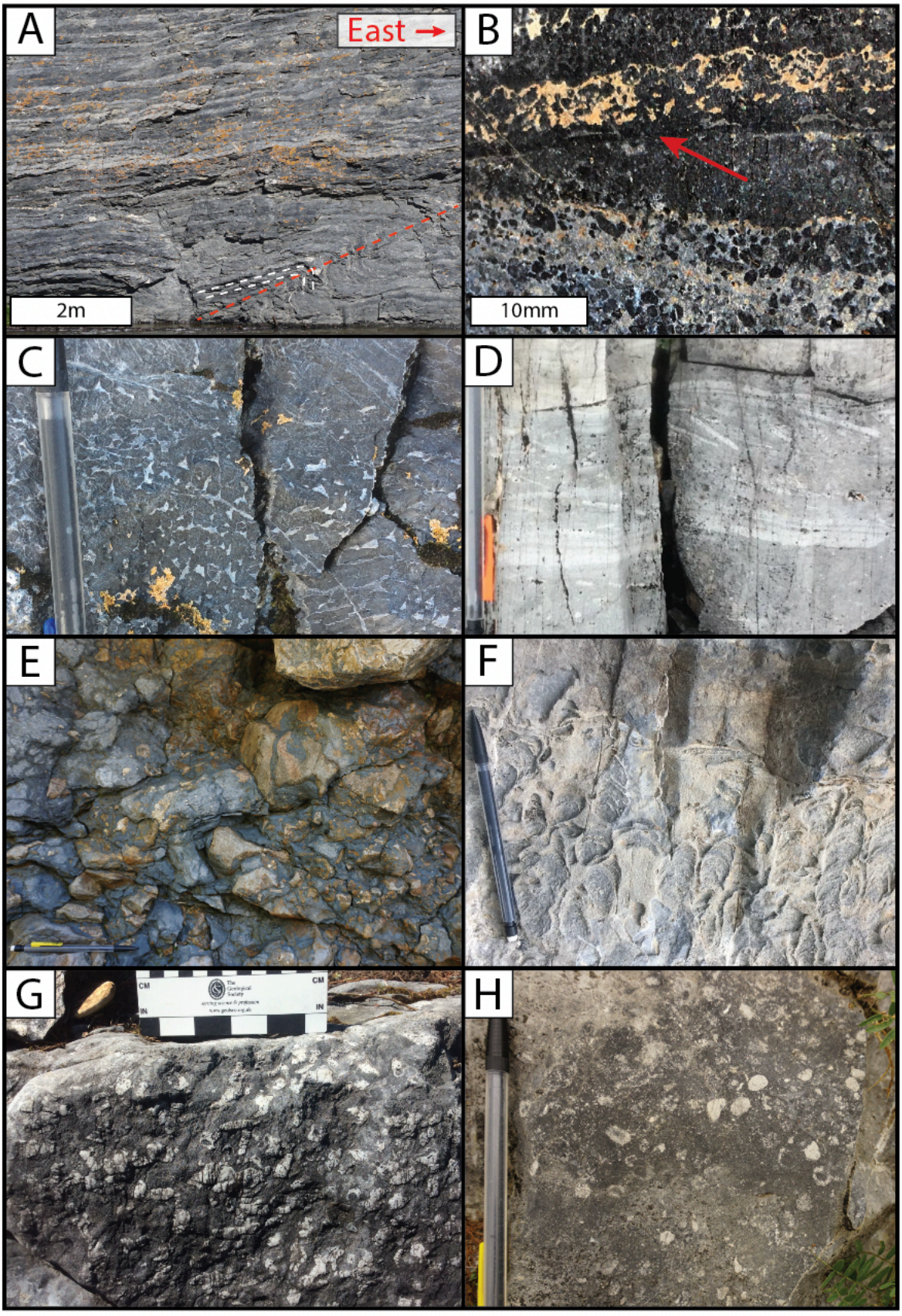
A
East →
2m
B
10mm
C
D
E
F
G
CM
IN
H

Figure 5: Field photographs of Khuvsgul Group strata. **A)** Outcrop-scale photograph of well-bedded mudstone-grainstone parasequences of the Salkhitai Mb of the Bakh Fm near Agariin Gol. White dashed lines highlight bedding planes through a m-scale fold, with elongated west-dipping fold arms indicating top-to-the-east shear. The trend of the fold axis highlighted by the red dashed line is parallel to the trend of D1 structures in the Khoridol Saridag Range. **B)** phosphatic grainstone of the Kheseen Fm, featuring truncated bedding as well as horizons indicative of primary/multigenerational phosphogenesis. The red arrow indicates the location of a multigenerational phosphogenic horizon (phosphatic allochems in authigenic CFA cement). **C)** thrombolytic texture in a phosphatic grainstone interval of the Kheseen Fm. **D)** imbricate, edgewise breccia horizon within the Kheseen Fm. featuring rip-up clasts of underlying strata. **E)** wildflysch of the upper Kheseen Fm at Kheseen Gol. Clasts include material similar to underlying Kheseen strata, suggesting an erosive contact at the base of the interval. **F)** digitate stromatolites in a dolomite grainstone interval of the Middle Mb of the Erkhelnuur Fm. **G)** bed-penetrating ichnofossils in a limestone grainstone bed of the Middle Mb of the Erkhelnuur Fm. **H)** disassociated archaeocyathid allochems in dolomite grainstone bed of the Upper Mb of the Erkhlenuur Fm.

environment. The deposition of grainstones and carbonate conglobreccias indicates the continued influence of mass-wasting processes, caused either by the migration of tidal channels or by sea-level forced banktop instability. Sandstone beds near the top of the Salkhitai Mb have an erosive contact with underlying grainstones, and are interpreted as bypass channels (e.g. Smith et al., 2016).

Shar Formation description. – The Shar Fm is composed of matrix-supported massive diamictite containing carbonate and exotic angular to sub-rounded clasts (0.1–1.2 m) in a cream-to-yellow weathering, gray-when-fresh fine-grained carbonate matrix (Fig. 4B) with minor thin lutite and shale. Although clasts are dominated by angular to sub-angular micritic dolomite, similar to that observed in the most proximal underlying strata, limestone rhythmite, oolite, and grainstone are present, as well as subrounded lithic and quartzite clasts. Significant facies changes occur along strike, with massive diamictite with minor laminated beds containing bed-penetrating lonestones at Kheseen Gol (Macdonald and Jones, 2011) stratigraphically equivalent to sedimentary breccia with sub-angular

carbonate clasts approaching 1.5 m in diameter <4 km south at Khirvesteg Gol (Fig. 3). These massive, ungraded, clast-supported dolomite breccias consist of angular to subangular dolomite clasts up to 30 cm across both above (0-3 m thickness) and below (0-25 m thickness) the Shar Fm diamictite. The matrix of these breccias is micritic and similar to the composition of the clast material, with rare occurrences of terrigenous grains and coarser void-filling grainstone. The Shar diamictite and associated dolomite breccias vary in thickness across the basin from <0.5 m in the central Khoridol Saridag Range to nearly 70 m on the ridge above Ongolog Gol. The base of the Shar Fm is identified by the carbonate breccias and diamictites that occur above an erosional surface that cuts into the upper two members of the Bakh Fm, with Shar Fm diamictite directly overlying Khurts Mb strata in the easternmost Khoridol Saridag Range (Figs. 3,4).

Shar Formation interpretation. – The Shar diamictite is interpreted to be a glaciogenic deposit correlated with the Marinoan Snowball Earth glaciation (Macdonald and Jones, 2011). The clast and matrix composition of the diamictite suggests that glacial erosion sampled material from the underlying Bakh Fm, with minimal input from siliciclastic or basement sources. The dominance of massive, matrix-supported diamictite suggests deposition in a marine peri-glacial environment at or near the ice grounding line. However, the presence of laminated intervals with bed-penetrating lonestones within massive diamictite-dominated intervals (Macdonald and Jones, 2011) suggests movement of the grounding line, with lonestone-bearing strata putatively associated with episodes of grounding-line retreat and a shift towards distal, suspension-dominated sedimentation punctuated by input from ice-rafted debris (Domack and Hoffman, 2011).

Clast-supported breccias are interpreted to be autoclastic or locally-sourced, short-transport-distance breccias that formed as a result of local glacio-isostatic deformation across the carbonate ramp. The erosional surface observed at the Salkhitai Mb-Shar Fm contact in the eastern Khoridol Saridag Range may have formed as the result of a regression at the onset of the Marinoan glaciation, with the overlying diamictite and carbonate breccia variably recording glacial advance and retreat across the basin.

Khirvesteg Formation description. – The basal Khirvesteg Fm includes a ~1-3 m cream-colored dolomite grainstone that overlies the Shar Fm, and hosts twinned barite pseudomorphs (Fig. 4C) and bedding-parallel sheet-crack cements (Fig. 4D). This interval is overlain by a sequence of lutite in the eastern Khoridol Saridag Range, and by thinly-bedded lime- and dolo-micrite in the central Khoridol Saridag Range and Darkhat Valley. These strata are truncated by an unconformity, which outcrops as an identifiable erosional disconformity at many of the easternmost Khoridol Saridag Range exposures, and ubiquitously as a sharp paraunconformable transition from lutite/dolomitized laminated grainstones of the uppermost Khirvesteg Fm to the overlying allodapic phosphatic and siliceous grainstones of the basal Kheseen Fm.

Khirvesteg Formation interpretation. – The dolomite grainstone at the base of the Khirvesteg Fm is interpreted to be a basal Ediacaran cap carbonate sequence: in addition to its proximity with the underlying Shar diamictite, the dolomite bed displays features, including sheet-crack cements and crystalline barite, that have been observed in other Marinoan cap carbonate sequences from around the globe (Hoffman et al., 2011). The fine-grained carbonate and siliciclastic sequences that overly the cap dolomite likely reflect a post-Marinoan transgression, with facies across the basin indicating a shift towards

suspension-dominated deposition in an outer-ramp to bathyal setting. Mirroring trends observed in the Bakh Fm, a relative abundance of siliciclastic material in lutite in the eastern Khoridol Saridag Range compared to micrite in the west is consistent with a west-facing margin and deepening to the west in both the Bakh and Khirvesteg Formations.

Kheseen Formation description.–The Kheseen Fm displays dramatic lithofacies and thickness variability both within outcrop and across the basin, with total thicknesses ranging from 160-170 m in sections in the eastern Khoridol Saridag Range to over 500 m in the central and southern Khoridol Saridag Range and at Eg Gol (Fig. 1B). In the eastern Khoridol Saridag Range, the basal Kheseen Fm disconformably overlies the Khirvesteg Fm above an erosional surface, and is composed of interbedded black micritic limestone and dolomite mudstone, organic-rich lutite and shale, and phosphatic and silicified hardgrounds and allodapic carbonate (Fig. 5B). Hardgrounds are laterally continuous for only a few meters, and are typically in close proximity to cm-scale channels that truncate primary bedding features (Fig. 5B), cross-stratified channel fills, and allodapic carbonate packages consisting of edgewise breccia, granular packstone, and grainstone (Fig. 5D). Grainstone beds include phosphatic and siliceous grains and clasts. The best-preserved examples of Doushantuo-Pertatataka-type fossils are preserved in this lithofacies, in which individual fossils appear in packstone and grainstone beds (Anderson et al., 2017, 2019). Up-section, beds of nodular black chert interrupt the hardground/allodapic carbonate sequence, with stacked 30 cm-thick beds in packages up to 5 m thick. The cherts are superseded by fetid, carbonate-rich shale and thinly bedded lutite with interbedded dolomite grainstone and intraclast conglomerate. Up-section, phosphatic material is found primarily as allochems in graded wackestone and grainstone beds. Chert and phosphorite allochems within limestone

wackestone and grainstone beds decrease in abundance up-section, where micrite with black chert nodules, and laminar grey chert beds become dominant towards the top of the formation. Sharp, uneven boundaries are often observed between carbonate and chert horizons.

In the western Khoridol Saridag Range, Darkhat Valley, and Eg Gol localities, evidence of primary authigenic phosphatic and siliceous deposition is less abundant. Instead, fining-upward packages of grainstone, packstone, and wackestone with phosphatic and siliceous allochems are dominant, and are infrequently punctuated by fetid limestone packstone and wackestone beds containing domal stromatolites and thrombolitic reefs (Fig. 5C). These limestone sequences are superseded by a dolomite interval consisting of laminated micrite, domal stromatolites, and oomicritic wackestone and grainstone. In these localities, a 1–6 m-thick bed of black to maroon-red chert is often found at the top of the Kheseen Fm. The chert bed is largely textureless, and sharply bounded, both above and below, by dolomite wackestone or grainstone.

At Kheseen Gol in the eastern Khoridol Saridag Range, the reworked allodapic carbonates of the uppermost Kheseen Fm are interspersed with siliciclastic deposits: the top of the Kheseen Fm is marked by an influx of siliciclastic material, including a 10-12m thick, cobble-to-boulder clast, matrix-supported conglomerate with an erosive base (Fig. 5E).

Kheseen Formation interpretation. – In the eastern Khoridol Saridag Range, phosphogenesis in the lower Kheseen Fm occurred in a shallow, energetic depositional environment. The co-location of discontinuous, truncated primary bedding surfaces including phosphatic and siliceous hardgrounds, abundant channelization, and cross-stratified allodapic carbonates with angular clasts of phosphatic and siliceous material is

consistent with deposition on a shallow carbonate upper ramp or banktop environment subject to tidal currents. Allodapic carbonates contain evidence of local reworking of primary phosphatic and siliceous material, the primary precipitation of which appears to have been concentrated in the easternmost Khoridol Saridag Range. Up-section, phosphatic grainstone and wackestone beds are reworked, consistent with redeposition as mass-wasting deposits in a mid-ramp setting.

In the western Khoridol Saridag Range and Darkhat Valley, Kheseen Fm deposition occurred in a mid- to upper-ramp environment. In these localities, phosphatic material was redeposited as phosphatic and carbonate allochems. Normal grading in the allodapic carbonates with horizons of stromatolites and thrombolites suggests deposition below fair-weather-wave base, but well within the photic zone.

A transition to micrite and bedded chert in the upper Kheseen Fm marks a shift from grainflow-dominated to suspension-dominated deposition and continued deepening to a more quiescent basinal environment. Sharp, uneven contacts between chert and micrite beds can be attributed to rheological differences between lithologies, dewatering, and soft-sediment deformation. Together with the geochronological data and carbon isotope data described below, the cobble-to-boulder clast, matrix-supported conglomerate at the top of the Kheseen Fm is interpreted as a debrite (Fig. 5E), marking a significant unconformity and major tectonic disturbance to the margin.

Erkhelnuur Formation. – The Erkhelnuur Fm is an ~2 km-thick carbonate sequence with Middle Cambrian ichnofossils, archaeocyatha, and trilobites (Korobov et al., 1985). It is separated into three distinct Members (Lower, Middle and Upper) that can be differentiated both litho- and chemo-stratigraphically.

Lower Member description. – The Lower Mb of the Erkhelnuur Fm is distinguished by repetitive parasequences above the lime-micrite, cherts, and conglomerate of the uppermost Kheseen Fm. These parasequences occur as packages of thick dolomite and partially-dolomitized lime-micrite and grainstone-wackestone interbeds, white laminated dolo-micrite and wackestones containing domal or digitate stromatolites (Fig. 5F), and allodapic packstone and grainstone beds containing ooids, carbonate clasts, and minor black chert clasts. Throughout the Lower Mb, infrequent and recessive tan-to-green silicified fine-grained lutites stand out as bursts of color in an otherwise blue-gray to white expanse of carbonate. The thickness of the Lower Mb is 250–300 m.

Middle Member description. – A transition to limestone-dominated grainstone deposition marks the base of the Middle Mb of the Erkhelnuur Fm. This transition is visible both in the field and on satellite imagery, where the light grey and white dolomites of the Lower Mb give-way to dark blue-grey beds that stand out on ridgetop exposures. Like the Lower Mb, dolo-rhythmites and stromatolite-bearing mudstone beds are bounded by wackestone and grainstone beds in shallowing-upward parasequences. Approximately 20–50 m above the base of the Middle Mb, bed-penetrating bioturbation is more pervasive in micrite and wackestone beds. Irregular tubes, typically 1-2 cm in diameter, increase in frequency and density up-section, eventually obliterating nearly all primary bedding features. Although bioturbation rarely affects the most finely laminated beds, most grainstone beds in the upper Middle Mb are thoroughly perforated with burrows. In the most heavily bioturbated zones, burrows (Fig. 5G) tend to focus on individual 5-6 cm bedding-parallel layers, with rare vertical burrows penetrating 3-6 cm interstitial layers that are more

sparsely bioturbated. The total thickness of the middle Mb is ~800 m in the Khoridol Saridag Range, and at least 600 m in the Darkhat Valley.

Archaeocyatha occur ~300 m into the Middle Mb, with the best-preserved fossils occurring in zones with minimal bioturbation (Fig. 5H). Disassociated, randomly oriented archaeocyathid fossils are present in grainstone beds in the western Arcai Gol drainage and along the ridgeline between Khirvesteg and Ongolog Gol.

Upper Member description. – The base of the Upper Mb of the Erkhelnuur Fm is demarcated by a sequence of white to cream colored dolomite grainstone and wackestone beds, typically more than 50 m thick. Primary bedding features are obfuscated by dolomitization, but relict 10-60 cm bedding is locally apparent. Like the dark base of the Middle Mb, these white bands are visible and traceable both on distant ridge exposures and on aerial and satellite imagery, which aids the mapping of large-scale structures.

Above the white dolomite sequence, micritic laminites and dolo-grainstones form 1-10 m scale coarsening-upward parasequences for up to 500 m. Ichnofossils are frequent and tend to be concentrated in thicker grainstone beds. Where visible in less-bioturbated strata, the Upper Mb contains cross-bedded and channelized grainstone, microbial mat textures, and ripple cross-stratification. At the top of the sequence, lithic grains and fragments are present in coarse-grained, non-bioturbated grainstone beds, becoming more frequent toward the top of the sequence. Thicker sections of the Upper Mb contain more abundant siliciclastic grains, which occur in graded beds that increase in abundance up-section.

Erkhelnuur Formation interpretation. – Repeated, shallowing-upward parasequences of the Lower and Middle Mbs of the Erkhelnuur Fm suggest shoaling in an upper-mid-ramp environment. Interbedded micrite and grainstone beds record repeated gravity deposits. The

association of domal and digitate stromatolites with thinly-laminated micrite and grainstone beds suggests growth of microbial communities during periods of minimal gravity-flow input. Coarser grainstone and wackestone at the top of each parasequence contain allochems, including ooids, likely sourced from an upper ramp setting, and suggest progressive shallowing and increased communication with banktop or inner-ramp depozones at the top of each parasequence. Sparse evidence of tidal or persistent wave action suggests that the Lower and Middle Mbs largely remained below fair-weather-wave base, but within the photic zone, during deposition.

In the Middle Mb, the onset of bed-penetrating bioturbation is broadly associated with an increase in the dominance of wackestone and grainstone; however, in these heavily bioturbated facies, primary depositional fabrics and textures have been destroyed and coarsely recrystallized, potentially causing observational bias towards the apparent dominance of more-energetic carbonate lithofacies. Nonetheless, the appearance of coarser-grained allochems, including archaeocyathid hash, in the Middle Mb indicates an increasing sediment flux from shallow-water environments, and corroborates an inferred shallowing of the depozone through the Middle Mb.

A transgressive sequence at the base of the Upper Mb is marked by an abrupt shift to ichnofossil-free, well-bedded grainstone. The resumption of shallowing-upward parasequences above this interval also marks the return of abundant ichnofossils, suggesting a return to a similar upper-ramp environment as is inferred for the Middle and Lower Mbs. As with the Lower and Middle Mbs, limited textural evidence for ripple cross-stratification, channelization, and microbial-mat-like textures suggests that the Upper Mb formed in a middle to upper ramp environment. In the uppermost Upper Mb, ichnofossils disappear prior

to the influx of the terrigenous allochems and gravity flows that inundate the top of the formation prior to Ukhaatolgoi Fm deposition.

Ukhaatolgoi Formation description.–The Ukhaatolgoi Fm is composed of siliciclastic rocks ranging from tuffaceous siltstone to massive subangular boulder conglomerate. Coarse-grained, immature green arkosic wacke is the dominant lithology, with rare granule-to-pebble lithic clasts, angular quartz and plagioclase grains, and carbonate fragments in a green siltstone matrix (Fig 6A). The contact between the uppermost Erkhelnuur Fm and basal Ukhaatolgoi Fm is rarely exposed, but appears to be a gradational conformable contact: grainstone beds of the uppermost Upper Mb of the Erkhelnuur Fm incorporate increasing siliciclastic material up-section before being drowned out by massive arkosic wacke, intermittently punctuated by siltstone and gravel lag deposits. Elsewhere, the lower Ukhaatolgoi Fm includes maroon and green siltstone with minor lags of granule-to-pebble conglomerate. The siltstone is typically overlain by several meters of immature grit and gravel, which grade into cobble conglomerate. Up-section, green graywacke is interbedded with siliceous siltstone and mudstone and 10 m packages of massive, polyclastic boulder conglomerate.

Ukhaatolgoi Formation interpretation.–The accumulation of a thick package of poorly-sorted, immature sandstone, interspersed with coarser lithofacies, reflects the influx of terrigenous material onto a marine, carbonate ramp environment. Though the Ukhaatolgoi Fm includes siliciclastic facies with a range of grain sizes, the dominantly massive and graded bedding observed across all Ukhaatolgoi lithologies suggests that gravity flows, rather than fluvial or fluvio-deltaic processes, were the dominant depositional mechanism during Ukhaatolgoi deposition. Beds within the Ukhaatolgoi Fm likely reflect repetitive

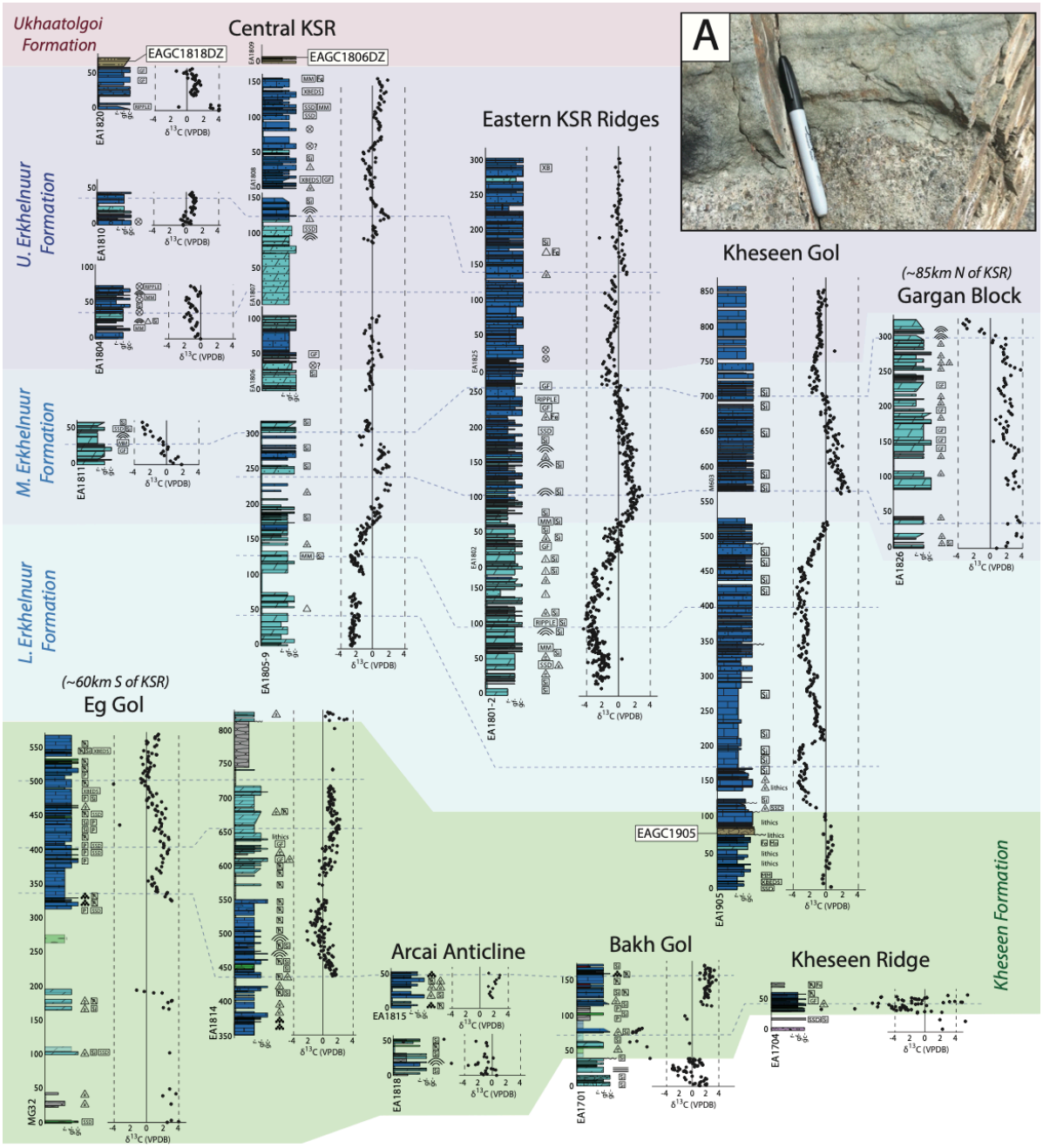

Figure 6: Cambrian chemostratigraphy of the Khuvsgul Group, and a field photograph of the Ukhaatologoi Fm (inset panel A). Stratigraphic sections are arranged, from left to right, along a broadly southwest-northeast transect. A legend defining all lithological and sedimentary symbology can be found in Figure 4. Geochemical data and section locations are collated in Table A3, Appendix 2. The stratigraphic heights of geochronological samples collected within the measured sections presented here are highlighted with white-boxed labels.

failures in the stability of terrigenous material accumulating on what had previously been a carbonate-dominated platform, resulting in extensive siliciclastic gravity flow deposition.

3.9.2. Structure

The greater Khuvsgul map area can be subdivided into three structurally-distinguishable map areas (Fig. 1C): (i) a fold-thrust belt, largely composed of Khuvsgul Group rocks, that makes up most of the Khoridol-Saridag Range (Fig. 3; a structural summary of the Khoridol-Saridag Range map area is presented in Fig. 7); (ii) a region north of Arcai Gol dominated by Sarkhoi Group outcrop, but including exposures of both Khuvsgul Group strata and pre-Sarkhoi gneissic basement (Fig. 9); and (iii) the Darkhat Valley, which includes limited exposures of the Khuvsgul Group and Sarkhoi Group within a regional topographic lowland bounded by both Paleozoic thrusts and small-scale Neogene normal faulting (Fig. 10). All three map areas have experienced Neogene-present extensional deformation and volcanism associated with the generation of the failed Baikal Rift system.

Structure of the Khoridol Saridag map areas

In the Khoridol Saridag Range map area, N-S trending, gently S-plunging km-scale anticlinoria are separated by W-dipping thrust faults that divide the eastern range into discrete N-S panels (Figs. 3, 7). These N-S trending structural elements are hereafter referred to as D1 structures. A second set of km-scale folds, the axes of which trend generally E-W and are hereafter termed D2 structures (Figs. 7, 8), cross-cut and deform the

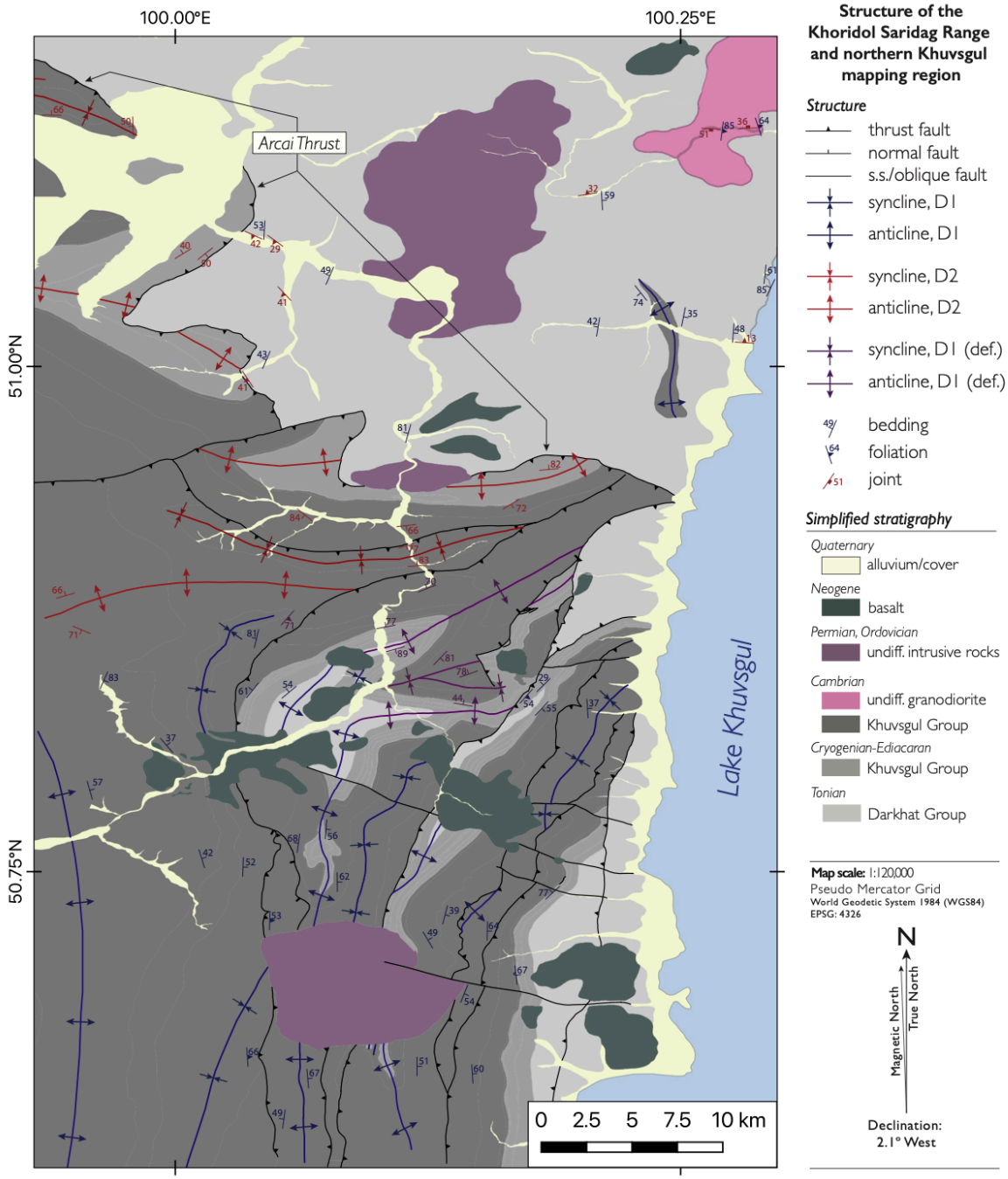

Figure 7: Simplified geological map of the Khoridol Saridag and a portion of the Northern mapping areas, highlighting structural data. Structures and data associated with dominantly E-W trending compression (D1) are colored dark blue, while structures and data associated with later NNE-SSW-trending compression (D2) are colored red. Purple structures and data indicate D1 structures that were subsequently deformed during D2. The position of the Arcai Thrust, which superimposes the para-allochthonous Khuvsgul Group strata that make up the Khoridol Saridag Range atop autocthonous Darkhat Group and Khuvsgul Group sequences, is indicated by the black arrows towards the top of the map.

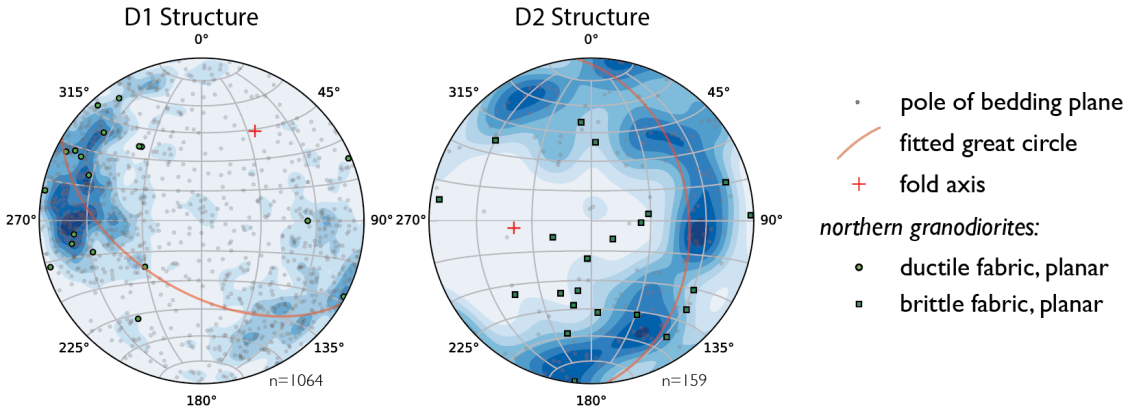

Figure 8: Stereonets showing orientation of km-scale folds in the Khoridol Saridag Range that are representative of D1 and D2 structures, respectively. Individual bedding measurements are depicted as poles to bedding planes. Ductile fabrics (dominantly folded foliation) observed in granodiorites from the Northern mapping region (including EAGC1942, 1943, and 1944) are shown on the D1 stereonet, while brittle fabrics (dominantly small-scale, cm-offset faults) observed in the same granodiorites are superimposed on the D2 stereonet. D1 structures are interpreted to be coeval with (or marginally postdate) the emplacement of the granodiorites, while D2 structures likely postdate granodiorite emplacement. The map locations of all major D1 and D2 structures in the Khoridol Saridag and northern mapping regions, as well as representative structural measurements, are presented in Figure 7.

D1 fold/thrust panels, and are well-developed in the northern and eastern portions of the Khoridol Saridag Range. Along the northern border of the range, fold axes trend more WNW-ESE, following the trace of the Arcai Gol Thrust. This generation of folds is accompanied by axial-parallel, S-dipping thrust faults.

The intersection of D1- and D2-generation folds results in domal structures observed throughout the region. These structures are exemplified by the Arcai Syncline, where a D1 N-S anticlinorium is cross-cut by a D2 E-W anticline, resulting in a domal antiform cored by the Darkhat Group (Figs. 3,7).

Apart from thrust-proximal outcrops, which typically exhibit fault-plane-parallel planar cleavage between 1–3 m on either side of observed fault surfaces, secondary fabrics are not pervasive across the Khoridol Saridag Range. Some axial planar cleavage is apparent

near fold axes, and on the limbs m- to cm-scale parasitic folds are present within well-bedded carbonate strata. Siliciclastic strata carry a weak cleavage that is typically subparallel to the nearest major fault plane orientation. Siliciclastic rocks also appear to mediate the location of many of the major thrusts in the region, with faults propagating along or near the contact between carbonate and siliciclastic strata. Furthermore, thrusts that juxtapose two carbonate panels often include entrained slivers of siliciclastic material (Fig. 11A).

Traces of E-dipping thrust faults are axial parallel with D1 folds, and those of S-dipping thrust faults are axial parallel with D2 structures (Fig. 7). An additional fault with a D1-parallel trace runs along the base of the easternmost Khoridol Saridag Range, and has a shallow westward dip (Figs. 3;7). Although poorly exposed, metasedimentary rocks that make up the footwall of the thrust have a well-developed, planar to undulating cleavage that is similar to that observed on the footwall of the Arcai Gol Thrust to the north (Fig. 11B).

The faults described above are crosscut by Ordovician and Permian intrusions, which are subsequently cross-cut by E-W trending, steeply dipping oblique sinistral normal faults with typical lateral offsets of a few hundred meters (Fig. 3,7). This fault set is further cut by east-dipping normal faults capped by Neogene basalts.

Structure of the northern map region

In the northern map region (Fig. 1C), exposure is generally poor, with heavy vegetation and frost-heave on exposed ridges restricting outcrop mapping opportunities to incised river valleys and high-relief ridgetops. Regionally, strata are folded into N-S trending, km-scale anticlinoria, plunging gently to the south (Figs. 7,9), with zones of

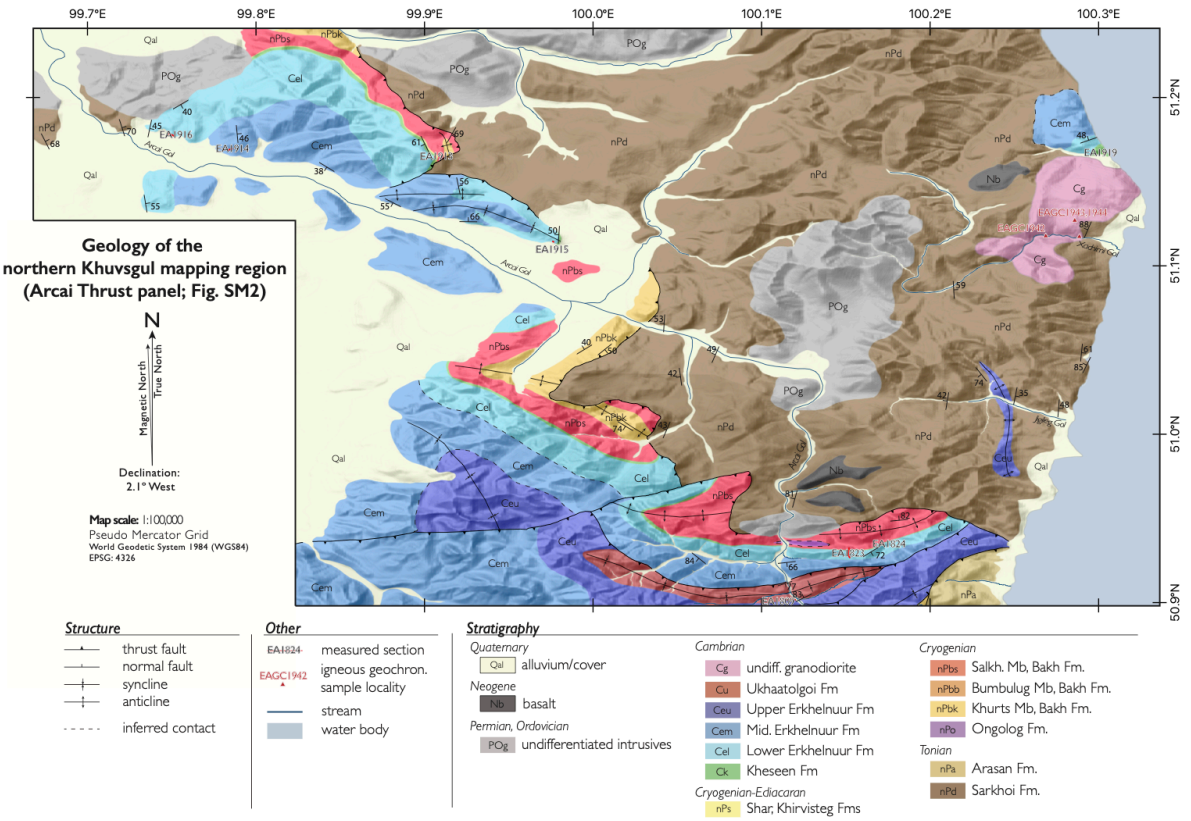

Figure 9: Geologic map of the Northern mapping region.

parasitic meter-to-decimeter-scale z-folds concentrated largely on the western limbs of these anticlinoria. Although granitic intrusions that cross-cut the larger-scale D1 folds are found throughout the broader Khuvsgul area, the northern map region also harbors pre-to-syn-D1-deformational intrusive bodies. In the Xachimi Gol drainage (Figs. 7,9), granodiorite plutons intrude the Sarkhoi Fm. At this locality, both the intrusive rocks and the country rock host meter-scale N-S folds and fold-axial-planar foliation.

Secondary fabrics are generally more apparent in northern map region outcrops than elsewhere in the greater Khuvsgul area, with slaty axial-planar cleavage observed in most outcrops that contain meter-to-decimeter scale folds. Darkhat Group exposures often feature a well-developed asymmetrical crenulation cleavage (Fig. 11B). This crenulation cleavage is most apparent in the southernmost portion of the northern map region (Fig. 1C, 7), where

D2-parallel cleavage cross-cuts bedding in outcrops within D1-parallel folds. Here, the resultant crenulation generally indicates a maximum stress direction for the D2 fabric that trends north-northeast - south-southwest: cleavage orientations broadly dip to the south-southwest, with lengthening of the south-southwest-dipping cleavage planes indicating top-to-the-north-northeast shear (Fig. 11B). Although there are only a few exposures of the fault contact, a majority of the footwall rocks at these outcrops feature a single, south-southwest dipping planar foliation, likely the result of intense fault-proximal deformation resulting in the obliteration of the earlier N-S axial-planar fabrics. Due to its proximity to the E-W trending portion of the Arcai Gol drainage, this fault system is referred to as the Arcai Gol Thrust (Fig. 7).

Structure of the Darkhat Valley map region

In the Darkhat Valley (Figs. 1C, 10), Khuvsgul Group rocks exhibit deformation similar to that observed in the other two map areas, including distinct D1 and D2 folds. D2 folds dominate the scattered outcrops found in the center of the Darkhat Valley, with D1 folds and fabrics predominantly observed along the fault bounded edges of the map region and in the limited outcrops of Darkhat Group rocks in the north Darkhat Valley.

Exposures along the southeast edge of the Darkhat Valley and the westernmost Khoridol Saridag Range preserve sets of tight D1 isoclinal folds and east-vergent chevron folds (Fig. 11C). These structures are located directly east of a west-dipping, D1-parallel fault plane bounded by several meters of cataclasite and fault breccia (Fig. 11D). This fault is inferred to continue north to the outlet of Arcai Gol, defining the western extent of the Khoridol Saridag Range (Fig. 1C).

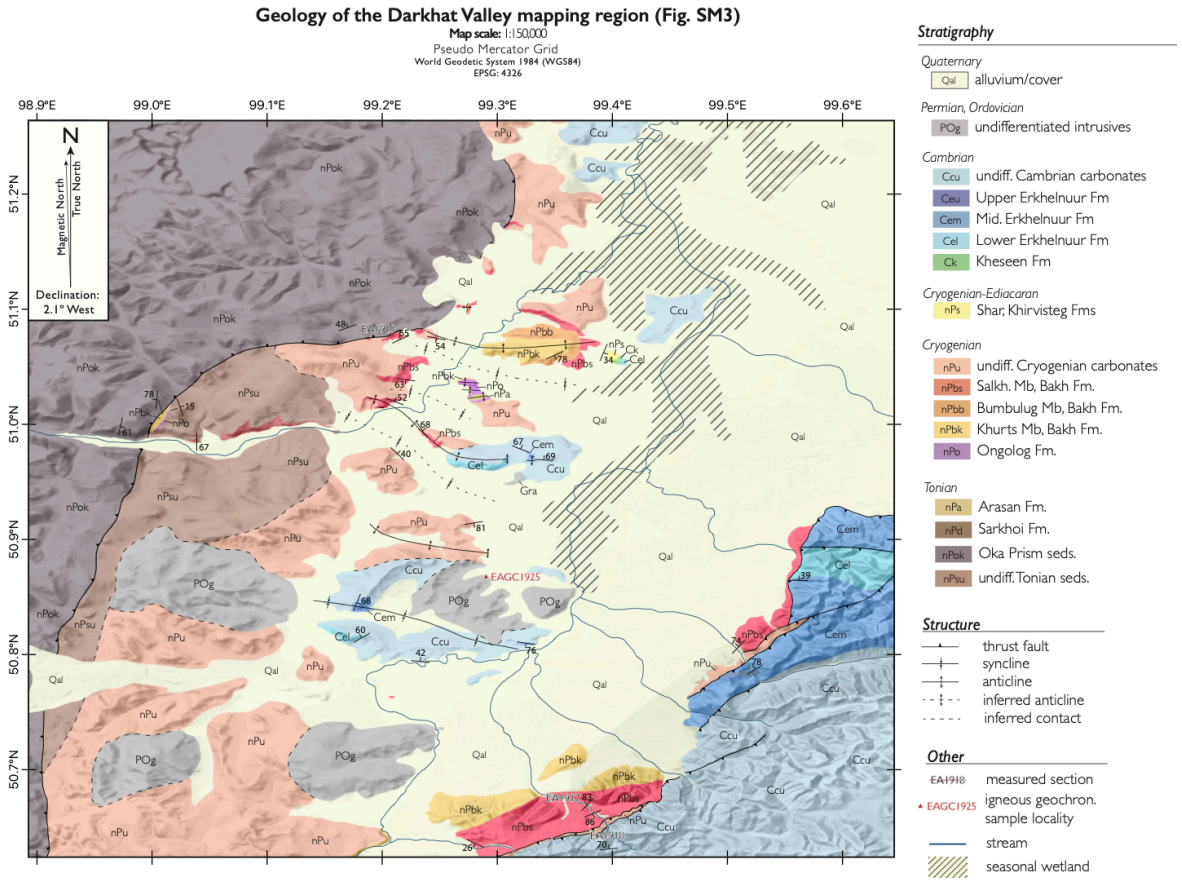

Figure 10: Geologic map of the Darkhat Valley mapping region.

On the western edge of the Darkhat Valley, D1 folds and fabrics dominate the structural motif, with a particularly well-developed cleavage observed near the footwall of a west-dipping, D1 fault that thrusts Tonian metasediments of the Oka Prism (Kuzmichev et al., 2007) atop Khuvsgul Group rocks. This cleavage is largely fault-plane parallel, and in many cases is sub-parallel to bedding, which at many outcrops in the westernmost Darkhat Valley appears to be overturned within an east-vergent drag fold along the footwall of the thrust.

Multiple intrusive bodies, ranging from monzogranites to granodiorites, outcrop throughout the Darkhat Valley, cross-cutting the folded Darkhat Group and Khuvsgul

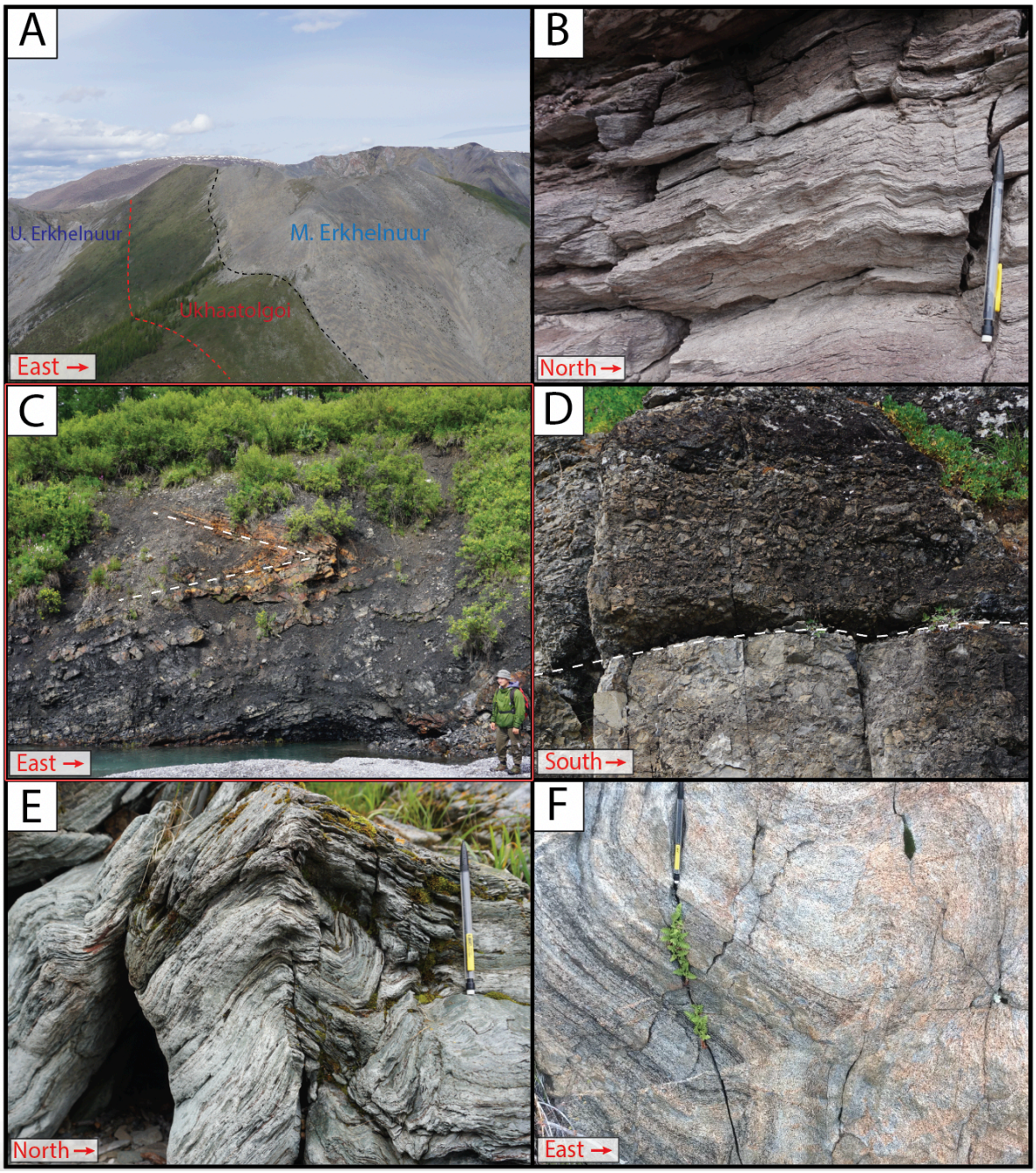

Figure 11: Field photographs detailing structural elements of the greater Khuvsgul study area. **A)** a laterally-discontinous sliver of Ukhaatolgoi Fm sediment forms the footwall of an east-dipping backthrust in the southeast Khoridol Saridag Range. **B)** crenulation cleavage in a fine-grained lithic wacke of a Sarkhoi Fm outcrop approximately 1 km north of the Arcai Gol Thrust. Elongated cleavage planes, dipping to the south-southwest, indicate shear in a top-to-the-north-northeast direction, consistent with the putative throw of the Arcai Gol Thrust. Primary bedding planes are dipping to the west (broadly into the page). **C)** chevron folds in the Salkhitai Mb of the Bakh Fm., eastern Darkhat Valley. Folds are broadly D1 parallel, and indicate eastward vergence, putatively associated with their proximity to **D)** cataclasites adjacent to a major E-dipping backthrust (fault surface highlighted with a white dashed line) running along the western margin of the Darkhat Valley and defining the western extent of the Khoridol Saridag Range. **E)** fabrics representative of those observed in siliciclastic lithologies across the Northern mapping area. **F)** foliations in granodiorite (EAGC1942) of the northern area are broadly axial-parallel to D1 structures.

Group. Several of these intrusions are inferred to be substantially larger in the subsurface than their current mappable outcrops suggest, as surrounding carbonate outcrops are marbleized, or have developed chaotic brecciation that has destroyed primary depositional fabrics in what is interpreted as the metamorphic aureole.

3.9.3. U-Pb Zircon Geochronology

Detrital zircon geochronology

Sixteen samples from throughout the Khuvsgul Basin yielded detrital zircon, the ages of which are depicted as normalized probability plots (Fig. 12). Samples are compiled by formation, with normalized probability plots representing compilations of four samples from the Sarkhoi Fm, one sample from the Khirvesteg Fm, two samples from the Kheseen Fm, and nine samples from the Ukhaatolgoi Fm (see Table A2, Appendix 2, for all detrital zircon ages and sample locations). The Sarkhoi Fm compilation reveals a strong peak at ~785 Ma, consistent with magmatic ages for volcanics of the Sarkhoi Fm (Kuzmichev and Larionov, 2011). The single detrital sample from the Khirvisteg Fm contains zircons younger than the peak of Sarkhoi magmatism, yielding a maximum depositional age constraint of 687.54 ± 2.05 Ma (LA-ICPMS, n=3). However, this sample is post-Marinoan, and thus must be younger than 635 Ma. A detrital sample from the Kheseen Fm (above the primary phosphorite strata) yielded a maximum depositional age of 525.19 ± 1.30 Ma (CA-ID-TIMS, n=4). Notably, these samples do not contain the 760-680 Ma detrital peaks observed in the Khirvesteg sample suggesting an exotic source. Finally, the Ukhaatolgoi Fm

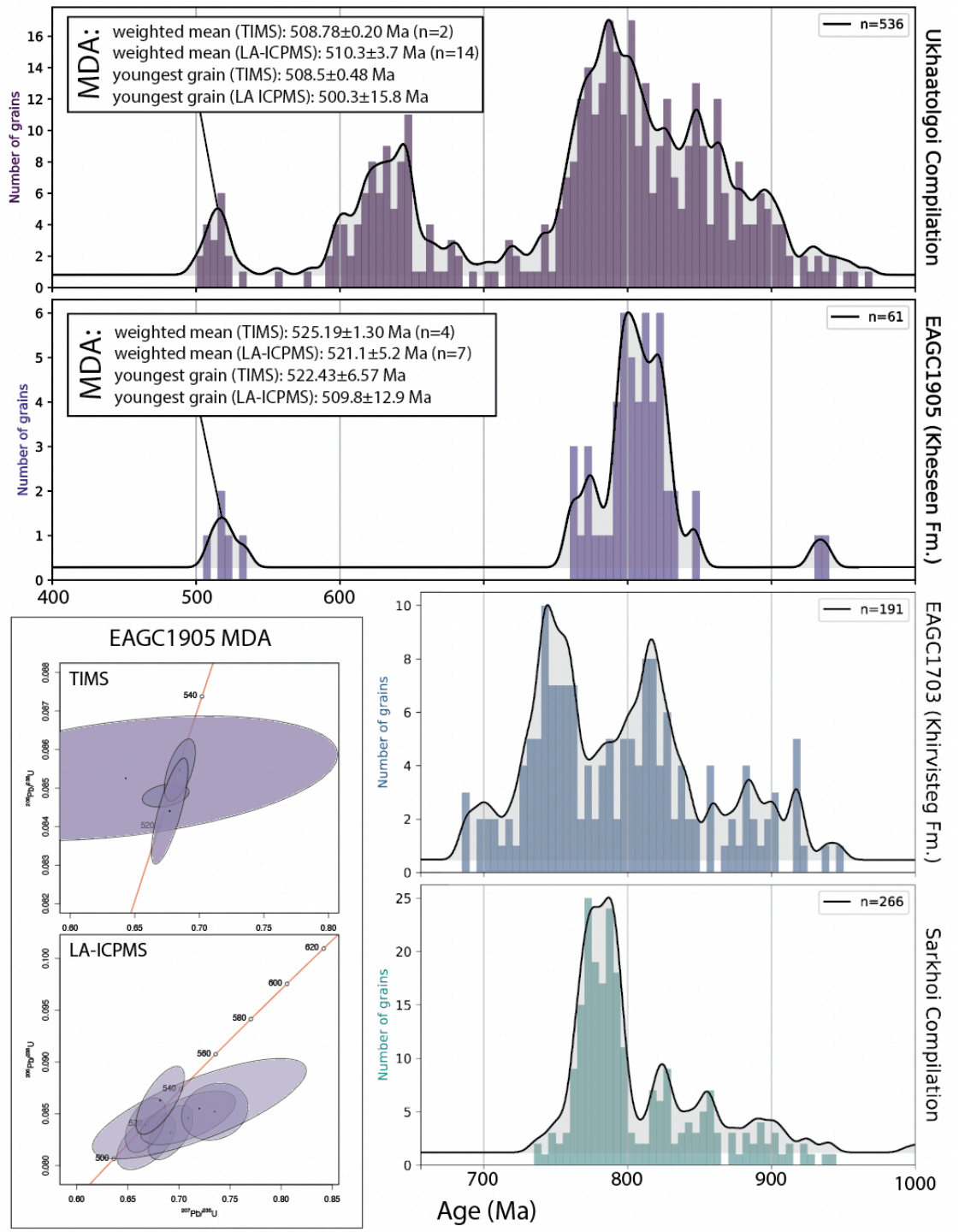

Figure 12: Detrital zircon age spectra from the Khuvsgul study area are arranged by relative stratigraphic height. Upper inset panels show maximum depositional age (MDA) constraints for the Kheseen Fm. (EAGC1905) and the Ukhaatolgoi Fm. (compilation of multiple samples) respectively, as determined by the youngest grain and youngest population of zircon analyzed by both CA-ID-TIMS and LA-ICPMS. Lower left inset: concordia diagrams for CA-ID-TIMS and LA-ICPMS analyses of youngest grains in EAGC1905. All sample locations and geochronological data are compiled in Appendix 2.

compilation includes peaks at ~780 Ma, ~630-640 Ma, and ~600 Ma, with a young peak at ~525 Ma and a maximum depositional age of 508.78 ± 0.20 Ma (CA-ID-TIMS, n=2).

Magmatic zircon geochronology

A rhyolite (KH01) from the Darkhat Valley yielded eighteen concordant young zircon grains, yielding a weighted mean age of 793.7±2.97 Ma. The large MSWD of these young grains is likely due to differential Pb-loss in several of the analyzed grains; alternatively, the younger population represents a true age and the older zircons can be largely interpreted as xenocrystic. As such, we do not attempt to isolate a statistically-homogenous magmatic zircon population from this sample. A rhyodacite (KH03) from the Sarkhoi Group, sampled in Darkhat Valley, yielded a weighted mean LA-ICPMS age of 810.9 ± 10.9 Ma (n=5; Fig. 13A). A foliated granodiorite (EAGC1942) from the region north of the Arcai Gol Thrust yielded an LA-ICPMS weighted-mean magmatic age of 498.8 ± 2.2 Ma (n=30). CA-ID-TIMS analysis of the five youngest grains from this sample yielded a 2-grain weighted mean magmatic age of 503.83 ± 0.13 Ma, and a single concordant young grain with an age of 503.22 ± 0.45 Ma (Fig. 13B). Other similar granodiorites from the same region (EAGC1943, 1944), yielded LA-ICPMS weighted mean ages of 501.3 ± 3.1 Ma (n=15) and 499.2 ± 1.5 Ma (n=88), respectively.

A monzogranite from the southern Darkhat Valley (EAGC1925) yielded an LA-ICPMS weighted-mean age of 447.9 ± 2.5 Ma (n=16), while a granodiorite and a tonalite from the Khoridol Saridag Range (EAGC1926B, 1917), yielded LA-ICPMS weighted-mean ages of 297.4 ± 0.6 Ma (n=210) and 276.59 ± 0.9 Ma (n=74) respectively (Fig. 13C). All

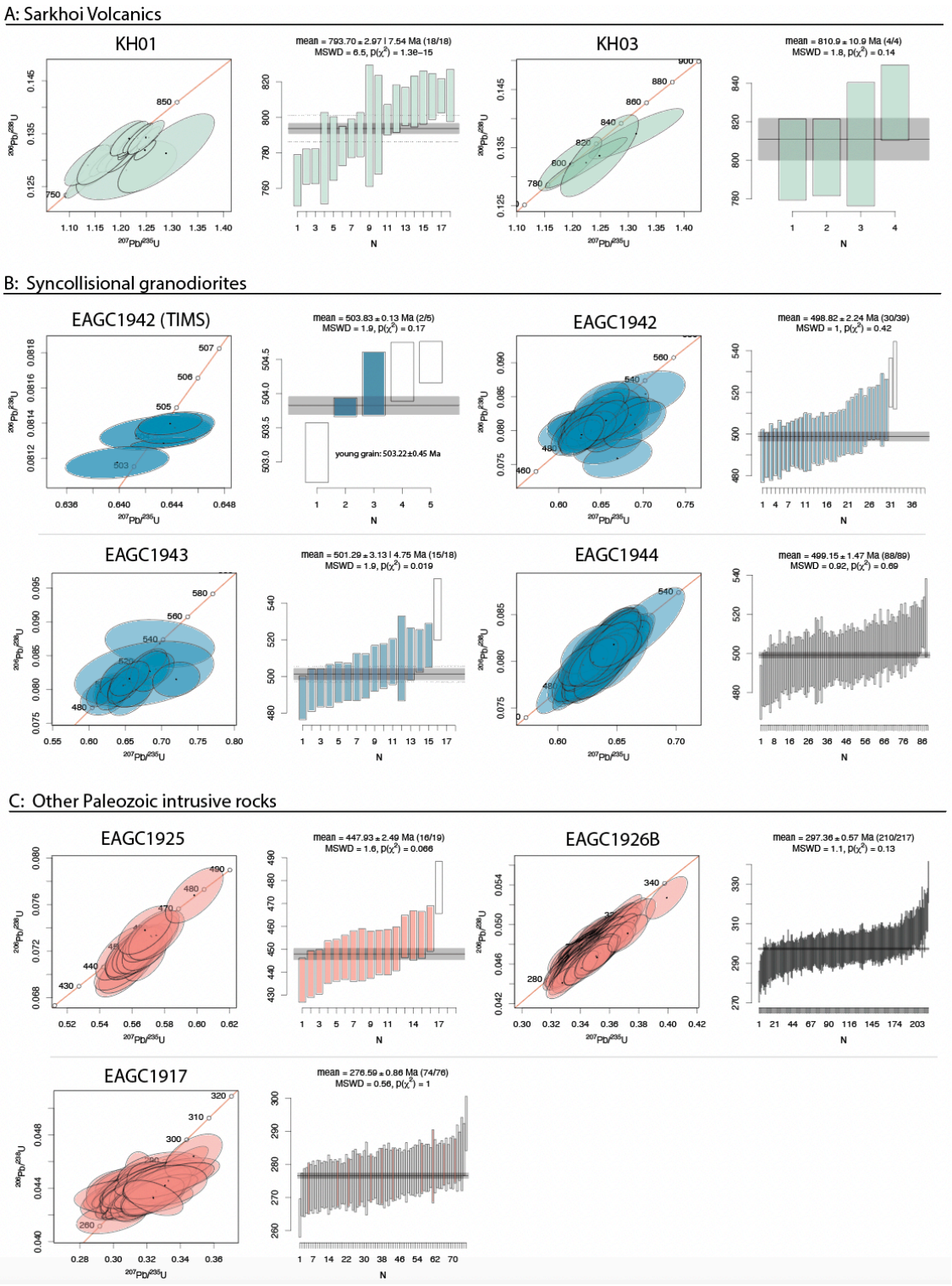

Figure 13: Concordia diagrams and weighted-mean plots for magmatic zircon populations from A) volcanics of the Sarkhoi Fm., B) granodiorites from the northern mapping area and C) igneous intrusive rocks postdating D1/D2 deformational events. LA-ICPMS and CA-ID-TIMS data are collated in the Supplementary Information.

magmatic zircon ages are visually summarized in Fig. 13, and are compiled and tabulated in Table A3, appendix 2.

3.9.4. Carbon isotope chemostratigraphy

At the base of the Cryogenian Khurts Mb of the Bakh Fm, $\delta^{13}C$ values reach a nadir of ~-6‰, before returning to values of ~0-2‰ (Fig. 4). The Bumbulug Mb is dominated by a positive $\delta^{13}C$ profile that sits around ~4‰ before briefly dipping toward negative values before a recovery to sustained, highly enriched (>6‰) values in the Salkhitai Mb (Fig. 4). In general, chemostratigraphically-correlated Cryogenian strata appear to expand to the WSW, with the thickest sections observed in the proximity of Agariin Gol/Bayan Zurgh (Fig. 1B). Above the Shar Diamictite, the basal Khirvesteg Fm hosts a distinctive decrease in $\delta^{13}C$, from 0 to -3‰, before a recovery to positive values (Fig. 4). In all sections that contain this isotopic profile, the initial decrease in $\delta^{13}C$ occurs in strata that host sheetcrack cements (fig 4D).

Condensed phosphorite facies of the Kheseen Fm host scattered $\delta^{13}C$ profiles with a negative excursion to ~-4‰ before a recovery to positive $\delta^{13}C$ values (Fig. 6). In the more expanded upper portions of the Kheseen Fm, $\delta^{13}C$ profiles are more directly correlated with global composite curves, and vary from -2 to +2‰.

A decrease of $\delta^{13}C$ values to ~-3‰, followed by a recovery to 0‰ is a profile diagnostic of the Lower Mb of the Erkhelnuur Fm (Fig. 6). In the Middle Mb, positive values of ~+2‰ are followed by a decrease to ~-1.5‰ (Fig. 6). These are followed a recovery in the Upper Mb to approximately 0 to +2‰, with these values persisting through the influx of Ukhaatolgoi Fm siliciclastics.

3.10. Discussion

3.10.1. Structural reconstruction of the Khuvsgul basin

The stratigraphic thickness of the Khuvsgul Group increases to the southwest, with lithofacies changes indicating deepening in the same direction (Figs. 4,6). Similarly, the relative abundance of terrigenous material in the easternmost exposures of the Kheseen and Erkhelnuur Fms suggest a terrestrial source, or at least a paleotopographic high, to the northeast. We suggest that the northern mapping area, which hosts the thinnest Cambrian strata, represents the most proximal region of the Khuvsgul basin, and sections in the Khoridol Saridag Range, Darkhat Valley, and further southwest represent increasingly distal depositional environments. In this model, the Northern mapping area is considered to be an autochthonous marginal component, and the fold-and-thrust architecture of the Khoridol Saridag Range map area is likely an amalgamation of parautochthonous platformal material that was folded and thrust-repeated during Paleozoic collision and accretion. The dominance of the north-south trending D1 structures in the Northern mapping region and the northern Darkhat Valley suggests a regional episode of east-west compression. The presence of ductile D1-parallel fabrics observed in granodiorites from the Northern mapping region (Fig. 8) constrain D1 to ≥503.87 ± 0.11 Ma (CA-ID-TIMS; Fig. 13). We suggest that this phase of deformation represents accretion along the western TMT margin and the final stages of a Cordilleran-style retro-arc foreland basin inversion that was also responsible for the earlier flysch deposition of the Ukhaatolgoi.

The west-dipping fault observed along the eastern foot of the Khoridol Saridag Range (Fig. 1C, Fig. 7) is interpreted as the main fault of the Khoridol Saridag Range thrust

system, with subsidiary east-dipping backthrusts propagating off this surface (Fig. 3). Repeated backthrusts break the Khoridol Saridag Range into distinct thrust panels, with the last major backthrust bounding the eastern edge of the Darkhat Valley (Fig. 1C; Fig. 11D). Tight, west-vergent isoclinal folds and chevron folds (Fig. 11C) in Khuvsgul Group strata exposed along the southeast edge of the Darkhat Valley reflect this area's position as the footwall of a major E-dipping backthrust.

A second major phase of deformation resulted in the generation of east-west trending D2 structures that both cross-cut and deform D1 structures in both the Khoridol Saridag Range, as well as a pervasive D2-parallel cleavage that cross-cuts D1-parallel bedding orientations in the northern mapping area. The propagation of the Arcai Gol Thrust (Figs. 1C, 7) along the southern margin of the autocthonous northern mapping area, resulting in the juxtaposition of Khuvsgul Group rocks atop older Sarkhoi volcanics, suggests that this area was already structurally above the basal Khoridol Saridag Range thrust sheet prior to the generation of the fault. North-northeast - south-southwest compression generated major D2 structures in the Khoridol Saridag Range, including anticlinal folds that crosscut D1 anticlinoria to form domal structures (Fig. 3). This compressional regime also generated widespread crenulation cleavage (Fig. 11B) in the southernmost portion of the northern mapping area, with cleavage orientations indicating reverse motion plane-parallel to the orientation of the Arcai Gol Thrust. Because Ordovician intrusions in the Khuvsgul region (including the c.a. 448 Ma EAGC1925) do not host any fabrics similar to those created by this event, this compressional stress regime likely occurred in the early Paleozoic. We suggest that the D2 deformation is associated with a late Cambrian to Ordovician collision between the northeastern margin of the TMT and Siberia

(Buslov et al., 2002; Kuzmichev, 2015; Domeier, 2018), with collision marked by *ca.* 490 Ma magmatic and metamorphic zircon ages from the Olkhon Terrane to the NE (Donskaya et al., 2017).

3.10.2 A new age model and chemostratigraphic framework for the Khuvsgul Group

Bulk carbonate $\delta^{13}C$ data from measured sections throughout the Khuvsgul Basin were used, in concert with lithostratigraphic, biostratigraphic, and structural context, to generate a basinal composite chemostratigraphic curve for the Khuvsgul Group (Fig.14A). The resultant composite curve was then correlated to contemporaneous, globally distributed $\delta^{13}C$ curves (Fig. 14B) by matching the peaks and nadirs of positive and negative $\delta^{13}C$ excursions from the Khuvsgul composite curve. Additional age constraints on these correlations are provided both by maximum depositional ages from detrital zircon samples, as well as biostratigraphic constraints from the first observed appearances of archaeocyatha in the Erkhelnuur Fm (Fig. 6; Fig. 14A). We adopt the nomenclature of the 2020 Geologic Timescale (Gradstein et al., 2020) and the Cambrian age model of Nelson et al. (2023), but also incorporate the regional Siberian timescale nomenclature for the basal Cambrian in our discussion and figures, as the bulk of previous work in the Khuvsgul region utilizes this framework.

We use $\delta^{13}C$ from carbonate strata as a tool for intra- and inter-basinal correlation, and acknowledge that diagenesis can alter primary carbon isotopic compositions in carbonates (Ahm et al., 2018), and can be driven by a variety of factors, including eustatic variability (Swart and Eberli, 2005) and fluid convection through carbonate platforms (Kohouts, 1965). Other potential drivers of variability include changes in the composition or

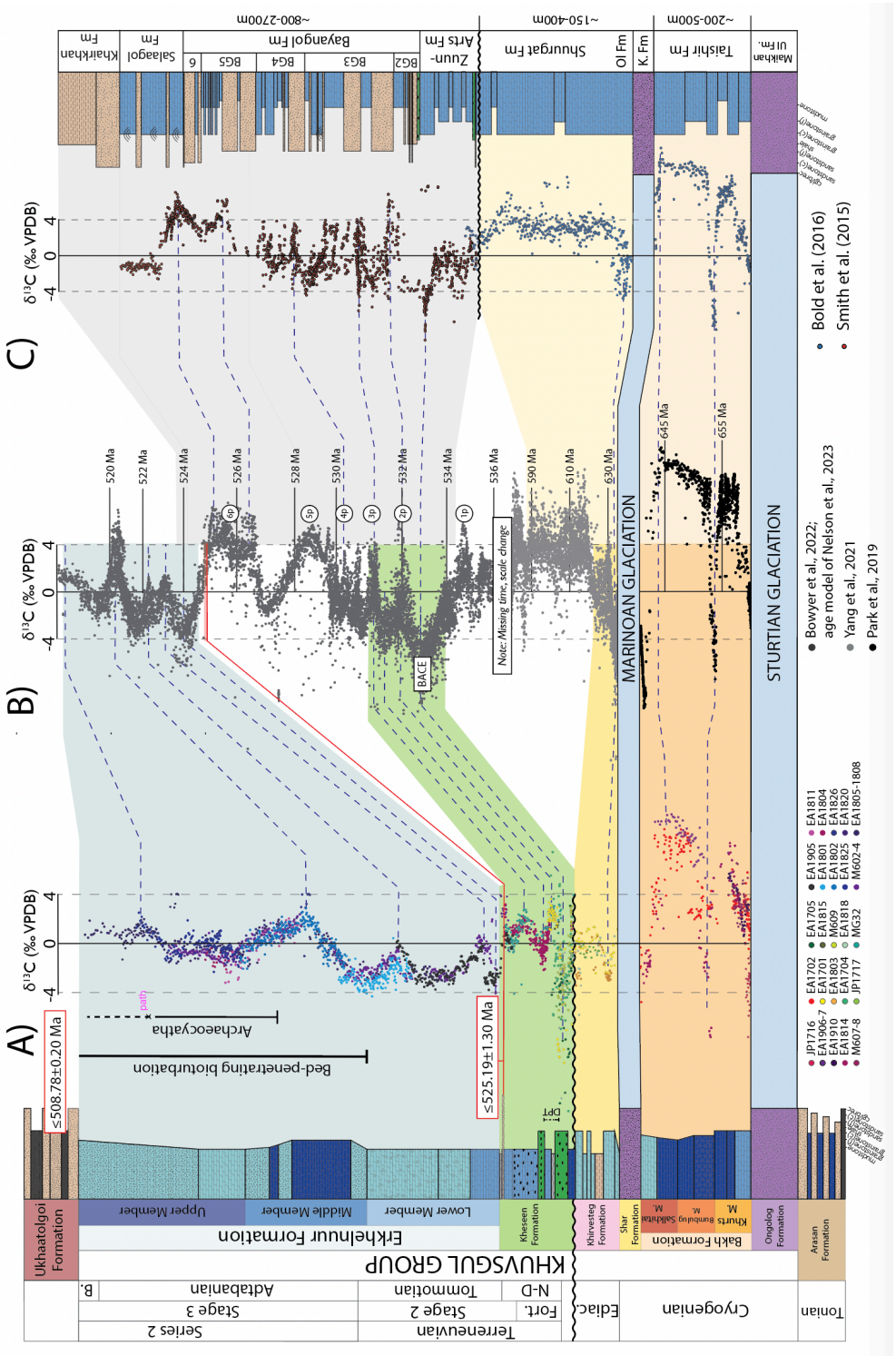

Figure 14: Age model and compiled chemostratigraphy for the Khuvsgul Group. **A)** a $\delta^{13}C$ compilation from the Khuvsgul group is correlated with **B)** a global $\delta^{13}C$ compilation and **C)** a composite $\delta^{13}C$ chemostratigraphy from Cryogenian-Cambrian strata of the Zavkhan Terrane. Note that while we use the global chemostratigraphic compilation of Bowyer et al. (2022), we utilize the Cambrian age model of Nelson et al. (2023).

volume of local carbon sources and sinks (Holmden et al., 1998), and changes in the dominant carbonate polymorph present in the depozone (e.g. aragonite vs. calcite, Romanek et al., 1992). However, given that both regional and global forcings, including tectonics, climate, and sea level changes, can influence these drivers, carbonate $\delta^{13}C$ chemostratigraphy can still serve as a valuable correlation tool both within and between basins at a regional or even global scale (Ahm and Husson, 2022).

Additional complexities are inherent in correlating $\delta^{13}C$ records from primary phosphogenic strata: compounded with issues of lateral discontinuity and stratigraphic condensation (Anttila et al, 2023; Follmi et al., 1995, 2017), remineralization and variable redox conditions associated with phosphogenesis may also drive local $\delta^{13}C$ gradients: phosphogenesis has been shown to occur in environments that promote the authigenic precipitation of carbonate near the sulfate reduction-methanogenic transitional zone (e.g. Cui et al., 2016; 2017), resulting in variable authigenic $\delta^{13}C$ compositions. Though some of the $\delta^{13}C$ values derived from this interval likely incorporate an authigenic component, texturally homogenous micritic cements within primary phosphogenic strata were targeted for $\delta^{13}C$ analysis whenever possible in order to minimize potential authigenic contamination.

3.10.3. Chronostratigraphy and Neoproterozoic-Cambrian evolution of the Khuvsgul Group

We combine our new age model with lithostratigraphic and facies observations summarized above to develop a model for the Neoproterozoic-Cambrian evolution of the Khuvsgul basin. A representative tectonic subsidence curve was calculated using a modified version of the backstripping model of Müller et al. (2018); all input data and assumed

lithological characteristics are summarized and tabulated in Table A4, Appendix 2. The model tectonic subsidence curve, and schematic cartoon outlining the tectonic evolution of the Khuvsgul basin(s) are shown in Fig. 15.

Cryogenian rift-drift transition: Following the emplacement of volcanics associated with the Sarkhoi/Zavkhan arc in the Tonian, and termination of arc magmatism on the margin, rifting allowed the deposition of the uppermost Sarkhoi and Arasan siliciclastic sequences. The variable thicknesses and facies of these units can be attributed to rift-related paleotopographic variability across the basin. The development of rift-related, localized accommodation space continued into deposition of the Ongolog Fm with a mid-Cryogenian rift-drift transition to passive-margin deposition through the early Ediacaran (Fig. 15A), as evidenced by a shift towards more gradational changes in formational thickness across the basin in the Bakh Fm and overlying Khirvesteg Fm. The development of a passive margin on the western margin of the TMT is corroborated by a lack of Cryogenian and Ediacaran magmatism and the exponential decay of tectonic subsidence (Fig. 15).

Ediacaran hiatus: A basinally-ubiquitous unconformity surface above basal Ediacaran strata (Figs. 6, 14A) across the Khuvsgul region is potentially related to accretion on the eastern margin of the TMT. An inferred collision is supported by ~630-620 Ma peaks in detrital zircon data from the Dzhida and Hamardavaa regions (Shkol'nik et al., 2016; terrane locations shown in Fig. 1), which also occur in detrital zircon spectra from younger Khuvsgul Group rocks in the Khoridol Saridag Range (Fig. 12). A similar hiatal surface is observed between the Shuurgat and Zuune Arts Fms. of the Tsagaan Oloom Group (Bold et

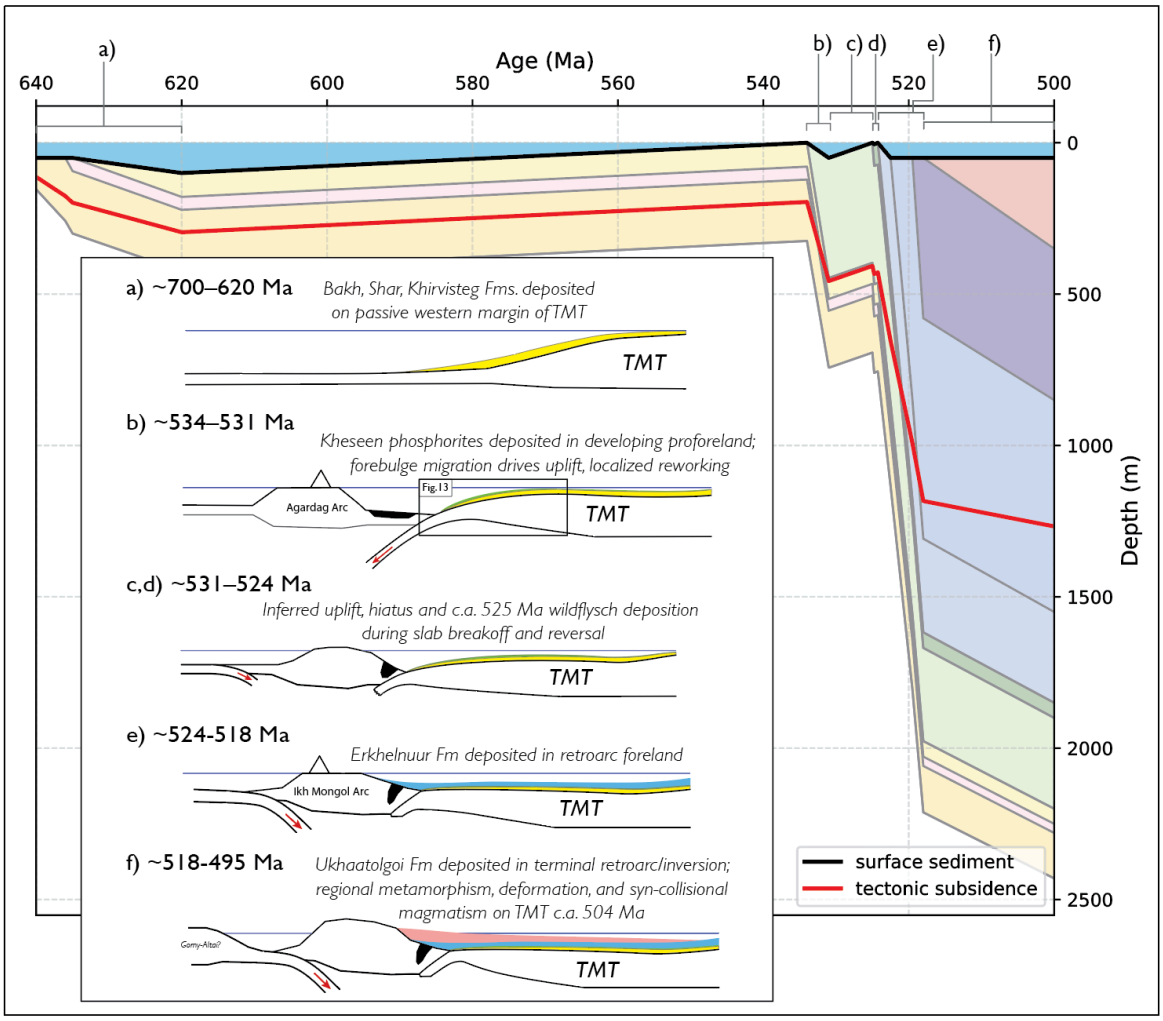

Figure 15: Tectonic subsidence model for the Khuvsgul Group, paired with a schematic tectonic model (inset panel) of the western margin of the Tuva-Mongolia Terrane in Khuvsgul Group time. **A)** passive margin deposition occurred along the western margin of the TMT during the Cryogenian and early Ediacaran, prior to a prolonged depositional hiatus along the margin. **B)** deposition of the fossilferous phosphorites of the Kheseen Fm occurred in a proforeland basin associated with the approaching Agardag Arc; see Fig. 16 for detailed schematic of phosphogenic environment. **C,D)** collision of the Agardag Arc resulted in slab breakoff and subduction polarity reversal; uplift associated with these events inverted the proforeland, caused putative erosion/hiatus, and resulted in the deposition of wildflysch in the eastern Khoridol Saridag Range. **E)** resumption of E-dipping subduction along the western margin results in Ikh-Mongol Arc magmatism, and the deposition of the Erkhelnuur Fm into the Ikh-Mongol retroarc foreland. **F)** collision along the western margin of the Ikh-Mongol arc resulted in regional metamorphism, inversion of the retroarc foreland, deposition of the Ukhaatolgoi Fm., and the emplacement of syn-deformational granodiorites c.a. 504 Ma.

al., 2016a, Smith et al., 2016), and is potentially related to accretion of the Bayankhongor ophiolite to the east.

A Cambrian phosphogenic pro-foreland basin: Above the Ediacaran unconformity surface, phosphatic strata of the basal Kheseen Fm were deposited into a nascent foreland basin associated with collision of the Agardag Arc above a west-dipping subduction zone along the western margin of the TMT (Fig. 15B). In the developing pro-foreland, localized zones of primary phosphogenesis experienced uplift and reworking, which we attribute to forebulge migration. Specifically, condensed primary phosphogenic zones on a paleotopographic high centered in the easternmost Khoridol Saridag Range likely sourced phosphatic and siliceous allochems that were redeposited in allodapic grainstones to the south and west (Figs. 6,16).The up-section decrease in phosphatic allochem frequency in the Kheseen Fm, as well as an overall trend towards deeper facies associations, suggests the onset of rapid subsidence associated with a developing foredeep, before an abrupt transition to coarse clastic debrites observed in section EAGC1905 at Kheseen Gol (Figs. 3, 5E, 6), and massive chert horizons elsewhere in the basin. We suggest that the Kheseen Gol debrites are a wildflysch associated with the inversion of the Kheseen pro-foreland during the terminal collision of the Agardag arc (Fig. 15c,d). As such, the debrites, which have a maximum depositional age of 525.19 ± 1.30 Ma (Fig. 12), are potentially associated with a significant depositional hiatus or erosional unconformity and may be temporally isolated from the underlying Kheseen Fm phosphorites.

Comparison of $\delta^{13}C$ data from the lower interval of the Kheseen Fm (Fig. 14a) with compiled global $\delta^{13}C$ records (Fig. 14b) provides an end-member age model for the Kheseen Fm. This model assumes significant depositional hiatus or erosional unconformity between

the upper Kheseen Fm phosphatic carbonates and the Kheseen Gol debrites, and draws an equivalency between a decrease in median $\delta^{13}C$ values in the basal Kheseen Fm, from approximately +3‰ to -4‰, with a similar decrease following Excursion 1p into the basal Cambrian carbon isotope excursion (BACE; Fig. 14b). The Kheseen phosphorites are broadly temporally equivalent to phosphatic strata of the Zuun-Arts Fm and BG2 Mb of the Bayan Gol Fm of the Zavkhan Terrane (Smith et al., 2016; Fig. 14c), and, considering radioisotopic constraints that have been proposed for the base of the Cambrian on other paleocontinents (Nelson et al., 2023), have a maximum age of ~534 Ma. This correlation (Fig. 14a,b) suggests that phosphogenesis in the Khuvsgul basin lasted ~3 Myr, which is comparable to the longevity of other phosphogenic environments in tectonically active Phanerozoic basins.

The presence of flysch deposits in the upper Kheseen Fm suggests a tectonic reorganization of the Khuvsgul basin associated with a collision. Uplift associated with slab breakoff and subduction polarity reversal could have resulted in significant hiatus or erosion, and driven the emplacement of terrigenous debrites across the terminal pro-foreland, prior to the resumption of subsidence in Erkhelnuur Fm time. Though these terrigenous debrites have thus far been described only at Kheseen Gol, *Cloudina*-bearing conglomerates and breccias of the Boxon Group (Khuvsgul-Group-equivalent strata of southern Siberia; Kheraskova and Samgin, 1992) suggest the widespread occurrence of coarse debrites in the early Cambrian.

Cambrian retro-arc foreland: The Erkhelnuur Fm was deposited into a rapidly subsiding retroarc foreland basin associated with east-dipping subduction along the western margin of the TMT (Fig. 15e), with carbonate platformal growth largely keeping pace with subsidence.

Shelf-slope transitional facies persist throughout the upper Erkhelnuur Fm (Fig. 6), with little evidence to suggest a long-term flooding stage or drowning of the platform anywhere in the Erkhelnuur stratigraphy. The interpretation of this basin as a retroarc foreland environment is supported by the influx of clastic sediments of the Ukhaatolgoi Fm, which feature facies characteristics of flysch deposition. Detrital zircon spectra from Ukhaatolgoi Fm samples contain Ediacaran and Cambrian grains from an exotic source, presumably the uplifted Agardag arc. In the Khuvsgul region, terminal foreland sedimentation was accompanied by the emplacement and deformation of 504-503 Ma granodiorites (Fig. 13), further supporting the interpretation of a retro-arc foreland environment, and potentially indicating the collision of another arc/terrane (likely the Gorny Altai Terrane; Dobretsov 2003; Buslov et al., 2013; Bold 2016b) along the western margin of the Ikh-Mongol arc.

3.10.4. Coevolution of the Khuvsgul Group and Neoproterozoic-Cambrian strata of the Zavkhan Terrane

With ties between the Neoproterozoic-Cambrian stratigraphy of the Zavkhan Terrane and the Khuvsgul Group proposed on the basis of lithostratigraphy (Macdonald and Jones, 2011), a new composite chemostratigraphy from the Khuvsgul Group allows us to refine these earlier correlations. The Cryogenian Bakh Fm hosts a carbon isotope profile similar to those from other Cryogenian non-glacial interlude platformal carbonate sequences around the world (Fig. 14). In particular, $\delta^{13}C$ values of +4 to +6‰ in the Khurts Mb of the Bakh Fm are followed by a -3 to -8‰ interval in the Bumbulug Mb, with a recovery to positive (+6 to +8‰) values observed in the upper Bumbulug and basal Salkhitai Mbs. These trends can be directly correlated (Fig. 14) to similar patterns observed in the Taishir Fm of the

Tsagaan Oloom Group of the Zavkhan Terrane, the type locality of the eponymous negative $\delta^{13}C$ excursion (Macdonald, 2009; Johnston et al., 2012; Bold et al., 2016a). This correlation supports the Sturtian and Marinoan affinities of the Ongolog and Shar Fms, respectively, and further bolsters arguments for a unified Khuvsgul and Zavkhan passive margin history during the Cryogenian. In addition to similarities in chemostratigraphy, the Bakh Fm is broadly similar, in terms of thickness, lithology, and facies association, to temporally-equivalent intervals of the Taishir Fm (Bold et el., 2016a). Barite crystal fans, sheet-crack cements, and affinities with underlying Marinoan diamictite sequences underscore the identification of the basal Khirvesteg and Ol Fms (Bold et al., 2016a) as Marinoan cap carbonate sequences within the Khuvsgul and Tsagaan Oloom Groups, respectively. Carbon isotope stratigraphy suggests a similar interpretation, with the basal portions of both formations hosting similar $\delta^{13}C$ profiles that dip to as low as -5‰ before recovering to ~0‰, a trend observed within Marinoan cap carbonates around the world (Bold et al., 2016a: Fig. 17, and references therein). Above the Marinoan cap carbonate sequence, on both terranes, early Ediacaran strata is truncated by an Ediacaran unconformity (Bold et al., 2016a; Macdonald et al., 2009).

Above the Ediacaran hiatal surface, the timing of deposition and lithological similarities begin to diverge. On the Zavkhan Terrane, the Zunn-Arts, Bayangol, Salaagol, and Khairkhan Fms formed during the latest Ediacaran to early Stage 2 of the Cambrian (~534-520 Ma) and are more siliciclastic-dominated (Smith et al., 2016). On the TMT, Khuvsgul Group strata are carbonate-dominated, and only the Kheseen Fm appears to have been deposited prior to Cambrian Stage 2, with the Erkhelnuur, and Ukhaatolgoi Fms deposited from Cambrian Stage 2 through Stage 3. These stratigraphic differences can be

attributed to the development of composite foreland basins during arc-continent collision, slab reversal, and accretion along the western TMT-Zavkhan margin.

3.10.5. Diachronous collision of a Cambrian arc and development of stacked forelands

Arc volcanism occurred west of both the TMT and the Zavkhan Terranes in the Ediacaran to Cambrian. In the south, the western margin of the Zavkhan Terrane is flanked by the oceanic Khantaishir Ophiolite, which formed *ca.* 570 Ma in a suprasubduction environment (Gianola et al., 2017, 2019), and arc-related igneous rocks. These include the Khantishir Magmatic Complex, which hosts continental arc lithologies that span ~524-495 Ma (Janousek et al. 2018). In the north, the ~570 Ma Agardag Tes-Chem ophiolite (Pfander and Kroner, 2004) lies west of the TMT, albeit inboard of island arc-related intrusives as young as 535 Ma (Rudnev et al., 2006) and ~522-518 Ma calc-alkaline granites of the East Tannu-Ola batholith (Rudnev et al., 2008; Mongush et al., 2011).

Janousek et al. (2018) argue that the Khantaishir Arc, Agardag Arc, and various other early Cambrian arc rocks located west of the TMT-Zavkhan margin were part of a single arc complex, which is termed the Ikh-Mongol Arc. In contrast, Smith et al. (2016) and Bold et al. (2016b) proposed ca. 540-520 Ma arc-continent collision along the composite TMT-Zavkhan margin, followed by slab breakoff and reversal. In schematic models of the Ikh-Mongol Arc, including those found within detailed studies of its components, the arc system is typically depicted as a continental or peri-continental arc over an east-dipping subduction zone (e.g. Fig. 19 of Janousek et al., 2018). However, most of the same studies (Janousek et al., 2018; Gianola et al., 2017, 2019) note geochemical signatures, particularly in older rocks, that describe an island-arc affinity, while the youngest rocks in the same

localities are more closely associated with continental arc compositions. Furthermore, the geometric relationship between the arc rocks of the Khantaishir Arc and the suprasubduction-origin interpretation of the Khantaishir ophiolite is inconsistent with east-dipping subduction at the time of ophiolite formation.

Here, parallel to interpretations of Khantaishir Arc subduction polarity suggested by Smith et al. (2016) and Bold et al. (2016b), we propose that the Ikh-Mongol Arc initiated over a west-dipping subduction zone, resulting in the emplacement of suprasubduction ophiolites oriented east of the main locus of arc volcanism. As the oceanic crust between the arc and the TMT-Zavkhan margin was consumed, the eastward progradation of the pro-foreland onto TMT-Zavkhan marginal crust resulted in the deposition of the Tsagaan-Oloom Group and the Kheseen Fm of the Khuvsgul Group. As the Agardag-Khantaishir Arc continued to approach and eventually collide with TMT-Zavkhan continental crust, suprasubduction-zone ophiolites were obducted and sandwiched between the arc and TMT-Zavkhan margin, with regional uplift along the margin resulting in the deposition of the Khairkhan Fm on the Zavkhan Terrane, and wildflysch deposits, erosion, and/or depostional hiatus in the upper Kheseen Fm on the TMT. Slab breakoff and reversal along the TMT-Zavkhan margin preceded the deposition of the Erkhelnuur and Ukhaatolgoi formations behind the ~522-518 Ma East Tannu-Ola batholith. Such a scenario is directly analogous to the present-day Taiwan margin (Teng et al., 2000; Clift et al., 2003).

Ikh-Mongol Arc accretion culminated with regional deformation (which manifested as D1 structures in the Khuvsgul Region) and the eastward migration of magmatism. Granulite metamorphism in the Sangilen region, which lies between the Agardag Arc and the TMT, occurred c.a. 515 Ma (Karmysheva et al., 2021), with lower temperature regional

metamorphism occurring between 505 and 495 Ma (Kozakov et al., 2021). This inferred accretionary orogeny is contemporaneous with the emplacement and subsequent deformation of ~504 Ma granodiorites in the autocthonous portion of the Khuvsgul basin (Fig. 8, 13). In the south, rocks in the Khantaishir Magmatic Complex began to host geochemical signatures consistent with a primitive continental arc after ~520 Ma (Janousek et al., 2018), while magmatism on the Zavkhan Terrane occurred between 509 and 507 Ma (Bold et al., 2016b).

Together, these data outline the diachronous development of composite foreland basins along the TMT-Zavkhan margin. The nascent stages of Ikh-Mongol Arc collision resulted in the deposition of the Zuun-Arts, Bayangol, Salaagol, and Khairkhan Fms of the Zavkhan Terrane and the Kheseen Fm of the Khuvsgul Group into pro-foreland basins between ~534 and ~524 Ma, with the latter strata experiencing a potentially-significant depositional hiatus or erosional unconformity (Fig. 14a) contemporaneous with continued deposition along the Zavkhan pro-foreland. Following slab reversal and reversal of subduction polarity, ~524-495 Ma foreland deposition on the Khuvsgul terrane occurred in a retroarc foreland basin setting.

3.10.6. Pro-foreland phosphogenesis

Differences in the style and tempo of foreland development (Sinclair and Naylor, 2012) along the TMT-Zavkhan margin likely had significant impacts on the style and extent of phosphogenesis at each locality. Siliciclastic material is much more abundant in Cambrian strata of the Zavkhan Terrane (Smith et al., 2016) than those of the TMT (Fig. 14c), and the relative proximity to (or availability of) terrigenous material in each locality

resulted in different grades and styles of phosphate mineralization. Phosphatic intervals in the Zuun-Arts Fm and BG2 Mb of the Bayangol Fm include phosphatic shales, rare phosphatic hardgrounds in carbonate strata, and lags of phosphatized small shelly fossils in carbonate grainstones (Smith et al., 2016). In general, the Zuun-Arts/BG2 phosphorite hosts lower phosphorus concentrations than the Kheseen phosphorites: on the Zavkhan Terrane, phosphogenesis manifested as diffuse phosphatic material in shale, or as concentrated but isolated phosphate precipitation around biogenous material.

In contrast, primary phosphogenesis in the Kheseen Fm (Fig. 16) is characterized by localized precipitation of concentrated phosphatic hardgrounds (Fig. 16 d,e). Although phosphatized microfossils and phosphatic allochems with biogenic textures (Anderson et al., 2017; 2019) have been identified in phosphatic grainstone beds (Fig. 16 b) of the Kheseen Fm, hardground-bearing zones in the basal Kheseen Fm are typically devoid of preexistent biological structures or substrates that would promote calcium fluorapatite (CFA) nucleation through biological mediation. Many of the phosphatic hardgrounds of the Kheseen Fm are found in close association with channelization, cross-stratification (Fig. 16c) and winnowed beds (Fig. 16 c-e), the cooccurrence of which is indicative of an energetic, sediment-starved environment. Importantly, many of the phosphatic horizons that initially appear to be hardgrounds are lags of granular phosphatic allochems that are cemented with a CFA matrix (red arrow, Fig. 5B), indicating that multiple generations of phosphate mineralization are present in many of the most concentrated phosphorite horizons. These observations are consistent with phosphogenic models associated with multigenerational winnowing and phosphate concentration (Baturin and Bezrukhov, 1979; Follmi et al., 1995; Anttila et al., 2023), as well models that invoke intermittent sediment starvation and low apparent

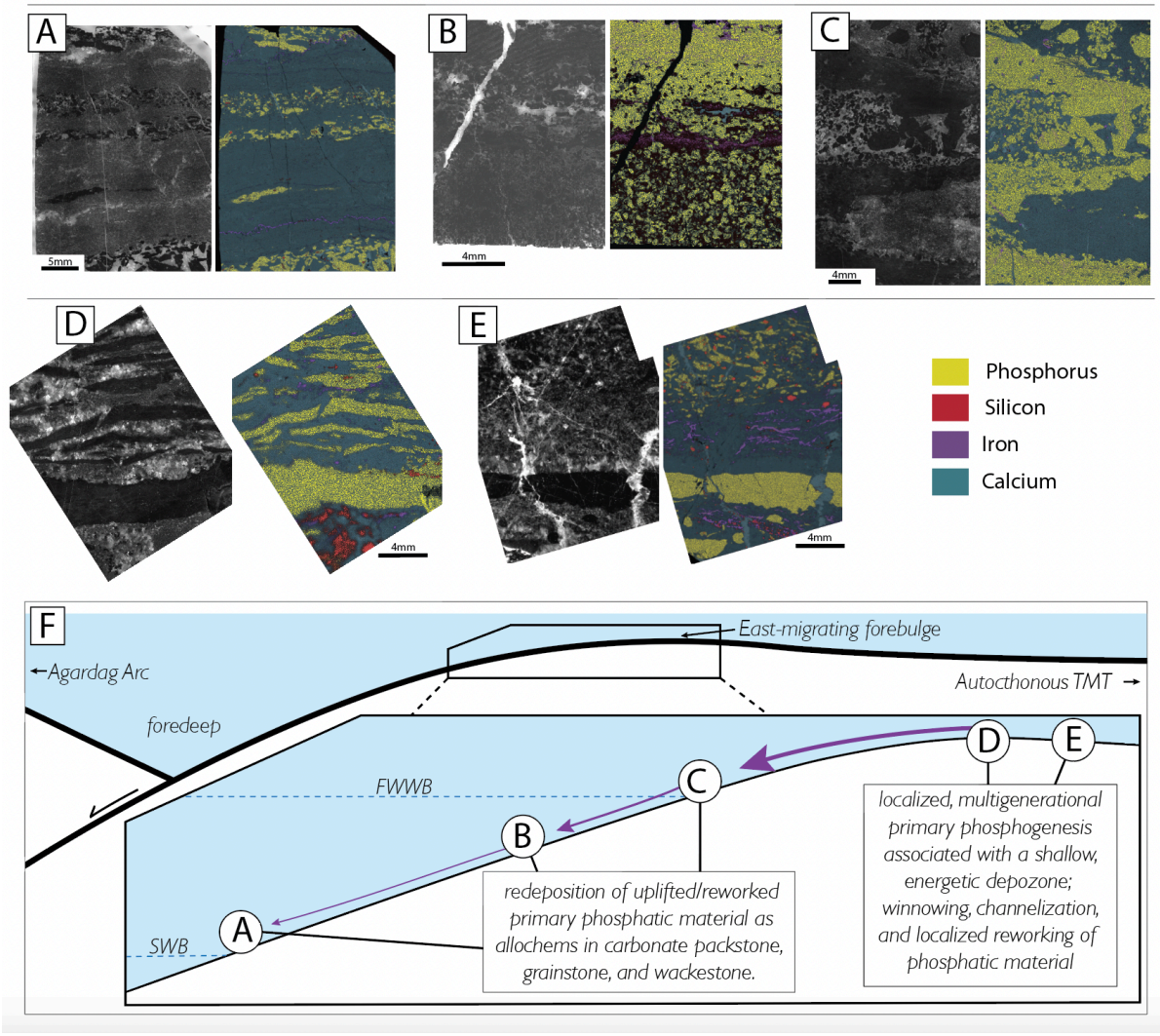

Figure 16: Kheseen Fm. phosphorite facies, presented as a thick-section photograph (left) and micro-XRF-derived elemental map (right). **A)** phosphatic allochems within grainstone horizons in interbedded limestone grainstone and mudstone. **B)** fining upward grainstone predominantly composed of phosphatic grains, with infrequent void-filling micritic cement. **C)** cross-bedded phosphatic wackestone and limestone grainstone. Note variably angular phosphatic clasts in coarsest wackestone horizon. **D)** Phosphatic hardground and overlying intraclast breccia, with tabular phosphatic clasts supported in a limestone grainstone matrix. Note siliceous cementation of limestone grainstone below basal phosphatic hardground. **E)** Phosphatic hardground, below limestone grainstone and wackestone with angular phosphatic and chert allochems. **F)** cartoon schematic model of the Kheseen Fm. phosphogenic sedimentary environment. The putative depositional environments of phosphorite facies A-E are shown, with predominantly-reworked facies (A-C) occurring at or below fair-weather-wave base (FWWB), and likely above storm-wave base (SWB). Facies D and E are indicative of primary, multigenerational phosphogenesis in a shallow, energetic environment, likely on a banktop or topographic high. The development of localized topography was likely mediated by the eastward migration of a forebulge associated with the collision of the Agardag-Khantaishir Arc.

sedimentation rates as primary drivers of ore-grade phosphate mineralization and concentration (Follmi et al., 2017).

Beyond providing an avenue for multigenerational phosphogenesis and mechanical concentration, the high-energy, low-sedimentation-rate environment inferred in the primary phosphogenic zones of the Kheseen Fm may also have promoted permeability barriers conducive to the accumulation of elevated porewater phosphate concentrations: multigenerational phosphatic horizons are often bounded by micrite laminae (Fig. 16 d,e), which may have provided a low porosity/permeability layer that restricted or focused porewater throughflow, as well as encouraged reducing conditions that increased the concentration of labile phosphate sourced from redox-sensitive mineral phases (Sundby et al., 1986). It has been demonstrated that both directional and oscillatory currents can create "armored", low-porosity horizons in sedimentary environments with silt-sand grainsize distributions (Wu et al., 2019), with coarser-grainsize layers bounded by finer, lower-permeability horizons. An analogous phenomenon occurred in Miocene phosphorites of the Monterey Fm, where silt- and clay-rich layers bound CFA-cemented lags of granule-pebble phosphatic clasts (Anttila et al., 2023). Additionally, the formation of authigenic and diagenetic phosphate minerals along these permeability barriers may function as a positive feedback through the addition of low-porosity, low-permeability material along a given horizon (Follmi et al., 2005).

3.10.7. Drivers of phosphogenesis and implications for a global Ediacaran-Cambrian phosphogenic event

Despite differences in phosphorite texture and grade, tectonically mediated paleotopography at both localities provided the necessary depositional conditions to accumulate phosphorus and precipitate/concentrate authigenic phosphate in the sediment column. We suggest that the eastward migration of a forebulge during the development of the Khuvsgul and Zavkhan pro-forelands drove the formation of paleotopographic highs (Fig. 16f), which host sedimentary conditions ideal for phosphogenesis. In many ways, this scenario is analogous to a model for authigenic Superior-type iron ore generation in foreland basin environments (e.g. Hoffman, 1987), in which the migration of foreland topography drives ore-generating conditions in a migrating, foredeep-axis-parallel band along the entire foreland margin. Phosphogenesis has occurred in foreland basin environments throughout the latest Neoproterozoic and Phanerozoic, including examples from the Ediacaran (Flicoteaux and Trompette., 1998; Moreira et al., 2021), Permian (Maughan, 1994), and Cretaceous (Föllmi, 1996). Along the TMT-Zavkhan margin, paleotopographic highs harbored energetic depositional environments that record evidence of abundant erosion and reworking (Fig. 16a-e), winnowing (Fig. 16d), and varying degrees of sediment starvation. These features are commonly observed in other Phanerozoic phosphorites (e.g. Follmi et al., 1996; Follmi et al., 2017; Anttila et al., 2023), and may be a critical component of condensed phosphorite formation: an energetic, winnowing depozone allows for the repetitive restructuring of the redoxocline at the sediment-water interface, which can greatly impact the lability and mineralogical association of phosphorus in the sediment column.

Phosphorus can be transferred from the water column to the sediment either with deposited organic material (Redfield et al., 1963), or as inorganic phosphate bound to metal oxyhydroxide minerals (Shaffer, 1986; Froelich, 1988). Both of these phosphorus shuttles are inherently redox-sensitive: the remineralization of organic matter (achievable through a variety of metabolic pathways) results in the liberation of organically-bound phosphorus (Froelich et al., 1982; Ingall and Van Capellen, 1990; Berner et al, 1993) as phosphate, while inorganic phosphate bound to Fe and Mn oxyhydroxide minerals becomes labile under reducing conditions (Sundby et al., 1986; O'brien et al., 1990). The recurrent process of sediment column redoxocline development (through repetitive deposition, hiatus, and reworking/removal) in winnowing sedimentary environments promotes the repeated remobilization of redox-sensitive mineral- and organic-bound phosphate, a fraction of which may precipitate as relatively-insoluble authigenic minerals in the sediment column (Föllmi, 1996, and references therein). These authigenic phosphate nodules or lamina are less susceptible to removal during winnowing than fine sediment or organic material, resulting in the relative immobility and eventual reburial of authigenic phosphatic material that can: a) serve as an ideal nucleation substrate for future authigenic or diagenetic phosphate precipitation (Van Cappellen et al., 1993), and; b) create low porosity/permeability layers that further concentrate pore-water phosphate (e.g. Föllmi et al., 2005).

In this model, the most critical factors governing phosphogenesis are: 1) the prevalence and abundance of shuttling mechanisms (e.g. organic material and redox-sensitive minerals) to efficiently transfer phosphate to or across the sediment-water-interface, and; 2) the effectiveness of the local depositional environment in modulating phosphate release, retention, and precipitation in the sediment column. We propose that

changes associated with these factors, rather than changes in gross marine phosphate abundance, are responsible for the global Ediacaran-Cambrian increase in phosphogenesis. Phosphorus concentrations in marine shales indicate that marine phosphate abundance was elevated to near-Phanerozoic levels by the Tonian (Planavsky et al., 2023), with shallow marine carbonates also recording elevated levels of marine phosphate in the early Neoproterozoic (Roest-Ellis et al., 2023). As such, the relative dearth of Tonian and Cryogenian phosphorites and the Ediacaran-Cambrian increase in phosphogenesis may instead reflect a change that affected the mechanism or locus of phosphate accumulation in marine sediments.

One potential such change is the increase in the oxidative potential in Earth's surface environments following the Cryogenian Snowball Earth events, which were associated with a return of iron formations in the geological record (Cox et al., 2013) and a crash in seawater sulfate (Hurtgen et al., 2002). We suggest that the Ediacaran-Cambrian increase in phosphogenesis reflects the opening of a taphonomic window, in which an increase in pO_2 increased terrestrial sulfide oxidation and the delivery of sulfate to the oceans (Lyons and Gill, 2010). This would have provided fuel for enhanced sulfate reduction of organic matter (Berner, 1977; Cui et al., 2017; Dodd et al., 2023), and increased the potential for labile phosphate in marginal marine environments. The diachroneity of Ediacaran-Cambrian phosphogenesis (Fig. 17), as well as the observation that many of these Ediacaran-Cambrian phosphorites were deposited into foreland basins, also implicates the role of tectonically-mediated depositional setting, rather than changes in marine phosphate abundance, in driving phosphogenesis.

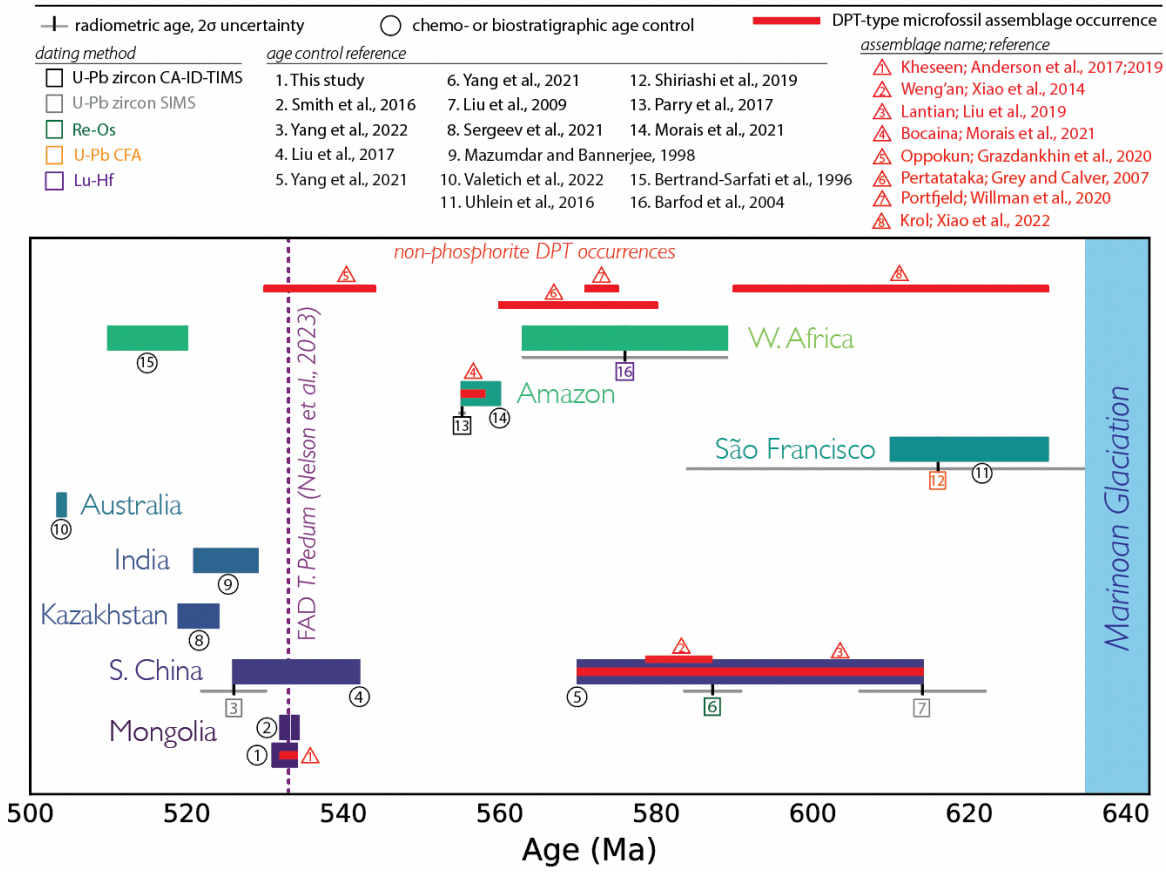

Figure 17: Age and duration of known Ediacaran and Cambrian phosphorite occurrences, grouped by craton. The temporal range of Doushantuo-Pertatataka-Type microfossil assemblages, including those not associated with phosphorites, are depicted in red.

3.10.8. Acanthomorphs of the Kheseen Fm: a long-lived biota

Microfossils, including Doushantuo-Pertatataka-Type acanthomorphic acritarchs, are found within reworked phosphorites of the Kheseen Fm the easternmost Khoridol Saridag Range (Anderson et al., 2017; 2019; locations in Fig. 3 and stratigraphic position in Fig. 11A). Doushantuo-Pertatataka-Type acanthomorphs were a cosmopolitan organism in the Ediacaran (Cohen and Macdonald, 2015) that appeared soon after the terminal Cryogenian (McFadden et al., 2009), and have been hypothesized (Xiao et al., 2014), albeit controversially (Cunningham et al., 2017), to represent early animal embryos. Doushantuo-Pertatataka-Type acanthomorphic acritarchs were initially thought to disappear from the fossil

record prior to or during the Shuram carbon isotope excursion (Zhou et al., 2017), a globally-synchronous phenomenon that occurred between 574 and 567 Ma (Rooney et al., 2020). However, discoveries of acanthomorphic achritarchs in putatively late-Ediacaran strata (Golubkova et al., 2015; Ouyang et al., 2017; Anderson et al., 2017) refuted this idea, with the occurrence of acanthromorphic acritarchs in late Ediacaran and basal Cambrian (544-530 Ma) strata of the Oppokun Fm of northern Siberia (Grazhdankin et al., 2020) confirming the long-lived nature of these taxa (Fig. 17). Our new chronostratigraphic model revises the age of the Kheseen Fm fossil assemblage described by Anderson et al. (2019) to be within the recovery of the BACE and prior to excursion 2p (Fig. 14 a,b), constraining the ages of this interval to between ~533-531 Ma, and making this assemblage one of the youngest known phosphatized Doushantuo-Pertatataka-Type fossil localities in the world (Fig. 17). Moreover, this age constraint demonstrates that Doushantuo-Pertatataka-type assemblages occurred, at localities around the globe, across a span of more than 90 million years.

3.11. Conclusions

New geological mapping, chemostratigraphy, biostratigraphy, and U-Pb zircon geochronology inform a new age and tectonic model for the Khuvsgul Group. The Khuvsgul Group was deposited into a series of stacked basins that developed along the western margin of the Tuva-Mongolia Terrane. The Cryogenian Ongolog, Bakh, Shar, and basal Ediacaran Khirvisteg Fms were deposited along a passive margin, prior to a prolonged depositional hiatus in the middle and late Ediacaran. Phosphorites of the fossiliferous Kheseen Fm were deposited into a nascent proforeland basin associated with the Agardag arc ca. 534 and 531

Ma; this age model provides new constraints on the Doushantuo-Pertatataka-Type assemblage hosted within the Kheseen Fm. Wildflysch deposition and several putative exposure surfaces observed around the basin at the top of the Kheseen Fm record slab breakoff, foreland inversion, and a *ca.* 525 Ma reversal in subduction polarity, prior to the deposition of the ~523-518 Ma Erkhelnuur Fm in a retroarc foreland. Collision along the western outboard margin of the Ikh-Mongol arc resulted in uplift and the emplacement of the Ukhaatolgoi Fm flysch, which directly preceded the emplacement of syn-collisional granodiorites on the autocthonous TMT. These folded intrusive rocks constrain the age of north-south trending structures in the Khuvsgul region to *ca.* 504 Ma, while a second set of north-northeast - south-southwest trending structures and fabrics indicates collision of the TMT with southern Siberia prior to 448 Ma.

The new age and tectonic model outlined above strengthens ties between the Khuvsgul Group and the Tsagaan Oloom Group of the Zavkhan Terrane, and supports the notion of a shared TMT-Zavkhan margin throughout the Neoproterozoic and Cambrian. The model also demonstrates that phosphogenesis occurred synchronously along this composite margin in the Terreneuvian, albeit with different phosphogenic styles: abundant siliciclastic input resulted in relatively diffuse phosphate mineralization on the Zavkhan Terrane, while sediment starvation and winnowing processes drove the deposition of highly-concentrated phosphate deposits in the Kheseen Fm of the Khuvsgul Group. Similar to other younger Phanerozoic phosphorites, phosphogenesis along the TMT-Zavkhan margin was tectonically modulated, with primary phosphogenesis occurring in shallow, energetic depozones putatively associated with the eastward migration of a forebulge. To this end, we suggest that the increase in Ediacaran-Cambrian phosphogenesis reflects the redox-driven

taphonomy of a tectonically-mediated depositional process, rather than a shift in global marine phosphate abundance: an increase in marine sulfate concentrations in the wake of the Cryogenian may have allowed microbial sulfate reduction (and redox conditions favorable to phosphogenesis) to expand into marginal marine environments that are likely to be preserved in the rock record.

* * *

ACKNOWLEDGEMENTS

This work was supported by the National Science Foundation (NSF) Frontier Research in Earth Science (FRES) Grant FRES1925990 and the National Aeronautics and Space Administration (NASA) Massachusets Institute of Technology (MIT) Astrobiology node NASA Geobiology grant NNH10ZDA001N-EXO. ESCA was additionally supported by National Science Foundation (NSF) Graduate Research Fellowship Program (GRFP) 2139319. We thank E. Baiarsaikhan, E. Erdene, Sam LoBianco, Peter Otness, and Judy Pu for assistance, stimulating conversations, and camaraderie in the field, and Uyanga Bold for guidance both scientifically and logistically. We thank Batsukh Erdene, M. Munkhbataar, and Ariunsanaa Dorj for logistical assistance, and the Ministry of Environment of Mongolia, and rangers and staff of the Khuvsgul Nuur National Park and Khoridol Saaridag Protected Zone for access. We thank Galen Halverson and Thi Hao Bui for usage of the stable isotope measurement facilities at McGill University, Ted Present and John Grotzinger for usage of the microXRF at California Institute of Technology, and Andrew Kylander Clark for

assistance with LA-ICPMS measurements at UC Santa Barbara. We thank Emmy Smith for helpful discussions.

* * *

REFERENCES, CHAPTER III, PART II

Ahm, A. S. C., Bjerrum, C. J., Blättler, C. L., Swart, P. K., & Higgins, J. A. (2018). Quantifying early marine diagenesis in shallow-water carbonate sediments. *Geochimica et Cosmochimica Acta*, *236*, 140-159. https://doi.org/10.1016/j.gca.2018.02.042

Ahm, Anne-Sofie, and Jon Husson. "Local and Global Controls on Carbon Isotope Chemostratigraphy." *Elements in Geochemical Tracers in Earth System Science* (2022). https://doi.org/10.1017/9781009028882

Anderson, R. P., Macdonald, F. A., Jones, D. S., McMahon, S., & Briggs, D. E. (2017). Doushantuo-type microfossils from latest Ediacaran phosphorites of northern Mongolia. *Geology*, *45*(12), 1079-1082. https://doi.org/10.1130/G39576.1

Anderson, R. P., McMahon, S., Macdonald, F. A., Jones, D. S., & Briggs, D. E. (2019). Palaeobiology of latest Ediacaran phosphorites from the upper Khesen Formation, Khuvsgul Group, northern Mongolia. *Journal of Systematic Palaeontology*, *17*(6), 501-532. https://doi.org/10.1080/14772019.2018.1443977

Anttila, E., Macdonald, F., & Bold, U. (2021). Stratigraphy of the Khuvsgul Group, Mongolia. Mongolian Geoscientist, 26(52), 2-15. https://doi.org/10.5564/mgs.v26i52.1516

Barfod, G. H., Vervoort, J. D., Montanez, I. P., & Riebold, S. (2004, June). Lu-Hf geochronology of phosphates in ancient sediments. In *GEOCHIMICA ET COSMOCHIMICA ACTA* (Vol. 68, No. 11, pp. A336-A336).

Banerjee, D. M., Basu, P. C., & Srivastava, N. (1980). Petrology, mineralogy, geochemistry, and origin of the Precambrian Aravallian phosphorite deposits of Udaipur and Jhabua, India. *Economic Geology*, *75*(8), 1181-1199. https://doi.org/10.2113/gsecongeo.75.8.1181

Baturin, G. N., & Bezrukov, P. L. (1979). Phosphorites on the sea floor and their origin. *Marine Geology*, *31*(3-4), 317-332. https://doi.org/10.1016/0025-3227(79)90040-9

Berner, R. A. (1977). Stoichiometric models for nutrient regeneration m anoxic sediments 1. *Limnology and Oceanography*, *22*(5), 781-786. https://doi.org/10.4319/lo.1977.22.5.0781

Berner, R. A., Ruttenberg, K. C., Ingall, E. D., & Rao, J. L. (1993). The nature of phosphorus burial in modern marine sediments. In *Interactions of C, N, P and S biogeochemical cycles and global change* (pp. 365-378). Springer Berlin Heidelberg. https://doi.org/10.1007/978-3-642-76064-8_15

Bertrand-Sarfati, J., Flicoteaux, R., Moussine-Pouchkine, A., & Ait Kaci, A. A. (1997). Lower Cambrian apatitic stromatolites and phospharenites related to the glacio-eustatic cratonic rebound (Sahara, Algeria). *Journal of Sedimentary Research*, *67*(5), 957-974. https://doi.org/10.1306/D426868A-2B26-11D7-8648000102C1865D

Bold, U., Smith, E. F., Rooney, A. D., Bowring, S. A., Buchwaldt, R., Dudás, F. Ő., ... & Macdonald, F. A. (2016a). Neoproterozoic stratigraphy of the Zavkhan terrane of Mongolia: The backbone for Cryogenian and early Ediacaran chemostratigraphic records. *American Journal of Science*, *316*(1), 1-63. https://doi.org/10.2475/01.2016.01

Bold, U., Crowley, J. L., Smith, E. F., Sambuu, O., & Macdonald, F. A. (2016b). Neoproterozoic to early Paleozoic tectonic evolution of the Zavkhan terrane of Mongolia: Implications for continental growth in the Central Asian orogenic belt. *Lithosphere*, *8*(6), 729-750. https://doi.org/10.1130/L549.1

Bold, U., Isozaki, Y., Aoki, S., Sakata, S., Ishikawa, A., Sawaki, Y., & Sawada, H. (2019). Precambrian basement, provenance implication, and tectonic evolution of the Gargan block of the Tuva-Mongolia terranes, Central Asian Orogenic Belt. *Gondwana Research*, *75*, 172-183. https://doi.org/10.1016/j.gr.2019.05.003

Bowring, J. F., McLean, N. M., & Bowring, S. A. (2011). Engineering cyber infrastructure for U-Pb geochronology: Tripoli and U-Pb_Redux. *Geochemistry, Geophysics, Geosystems*, *12*(6). https://doi.org/10.1029/2010GC003479

Bowyer, F. T., Zhuravlev, A. Y., Wood, R., Shields, G. A., Zhou, Y., Curtis, A., ... & Zhu, M. (2022). Calibrating the temporal and spatial dynamics of the Ediacaran-Cambrian radiation of animals. *Earth-Science Reviews*, *225*, 103913. https://doi.org/10.1016/j.earscirev.2021.103913

Buihover, B.N., Volkov, R. I., Ilyin, A.B., Pushlenkov, U.P., Savin, B.E., Semenova, O.A., Solyanikov, B.P., Spirkin, A.I., Tikhonova, O.K., Tikhonov, B.I., Uflayand, A.K. (1968). Geologic map, Khubsugul Aimag, Mongolia Peoples Republic. List M-47-IC,X,XI. Contract no. 1497 (in Russian).

Burchette, T. P., & Wright, V. P. (1992). Carbonate ramp depositional systems. *Sedimentary geology*, *79*(1-4), 3-57. https://doi.org/10.1016/0037-0738(92)90003-A

Buslov, M. M., Saphonova, I. Y., Watanabe, T., Obut, O. T., Fujiwara, Y., Iwata, K., ... & Kazansky, A. Y. (2001). Evolution of the Paleo-Asian Ocean (Altai-Sayan Region, Central Asia) and collision of possible Gondwana-derived terranes with the southern marginal part

of the Siberian continent. *Geosciences Journal*, *5*, 203-224. https://doi.org/10.1007/BF02910304

Buslov, M. M., Watanabe, T., Saphonova, I. Y., Iwata, K., Travin, A., & Akiyama, M. (2002). A Vendian-Cambrian island arc system of the Siberian continent in Gorny Altai (Russia, Central Asia). *Gondwana Research*, *5*(4), 781-800. https://doi.org/10.1016/S1342-937X(05)70913-8

Buslov, M. M., Ryabinin, A. B., Zhimulev, F. I., & Travin, A. V. (2009, October). Manifestations of the Late Carboniferous and Early Permian stages of formation of nappe-fold structures in the southern framework of the Siberian platform (East Sayany, South Siberia). In *Doklady Earth Sciences* (Vol. 428, No. 1, p. 1105). Springer Nature BV.

Buslov, M. M., Geng, H., Travin, A. V., Otgonbaatar, D., Kulikova, A. V., Ming, C., ... & Trofimova, D. A. (2013). Tectonics and geodynamics of Gorny Altai and adjacent structures of the Altai–Sayan folded area. *Russian Geology and Geophysics*, *54*(10), 1250-1271 https://doi.org/10.1016/j.rgg.2013.09.009

Clift, P. D., Schouten, H., & Draut, A. E. (2003). A general model of arc-continent collision and subduction polarity reversal from Taiwan and the Irish Caledonides. *Geological Society, London, Special Publications*, *219*(1), 81-98. https://doi.org/10.1144/GSL.SP.2003.219.01.04

Cohen, P. A., & Macdonald, F. A. (2015). The Proterozoic record of eukaryotes. *Paleobiology*, *41*(4), 610-632. https://doi.org/10.1017/pab.2015.25

Colman, A. S., & Holland, H. D. (2000). The Global Diagenetic Flux of Phosphorus from Marine Sediments to the Oceans: Redox Sensitivity and the Control of Atmospheric Oxygen Levels. https://doi.org/10.2110/pec.00.66.0053

Condon, D. J., Schoene, B., McLean, N. M., Bowring, S. A., & Parrish, R. R. (2015). Metrology and traceability of U–Pb isotope dilution geochronology (EARTHTIME Tracer Calibration Part I). *Geochimica et Cosmochimica Acta*, *164*, 464-480. https://doi.org/10.1016/j.gca.2015.05.026

Cook, P. J., & McElhinny, M. W. (1979). A reevaluation of the spatial and temporal distribution of sedimentary phosphate deposits in the light of plate tectonics. *Economic Geology*, *74*(2), 315-330. https://doi.org/10.2113/gsecongeo.74.2.315

Cook, P.J., and Shergold, J.H. (1986). *Phosphate Deposits of the World: Volume 1.* Cambridge University Press.

Cook, P. J. (1992). Phosphogenesis around the Proterozoic-Phanerozoic transition. *Journal of the Geological Society*, *149*(4), 615-620. https://doi.org/10.1144/gsjgs.149.4.0615

Cox, G. M., Halverson, G. P., Minarik, W. G., Le Heron, D. P., Macdonald, F. A., Bellefroid, E. J., & Strauss, J. V. (2013). Neoproterozoic iron formation: An evaluation of its temporal, environmental and tectonic significance. *Chemical Geology*, *362*, 232-249. https://doi.org/10.1016/j.chemgeo.2013.08.002

Cui, H., Xiao, S., Zhou, C., Peng, Y., Kaufman, A. J., & Plummer, R. E. (2016). Phosphogenesis associated with the Shuram Excursion: Petrographic and geochemical observations from the Ediacaran Doushantuo Formation of South China. *Sedimentary Geology*, *341*, 134-146 https://doi.org/10.1016/j.sedgeo.2016.05.008

Cui, H., Kaufman, A. J., Xiao, S., Zhou, C., & Liu, X. M. (2017). Was the Ediacaran Shuram Excursion a globally synchronized early diagenetic event? Insights from methane-derived authigenic carbonates in the uppermost Doushantuo Formation, South China. *Chemical Geology*, *450*, 59-80. https://doi.org/10.1016/j.chemgeo.2016.12.010

Cunningham, J. A., Vargas, K., Yin, Z., Bengtson, S., & Donoghue, P. C. (2017). The Weng'an Biota (Doushantuo Formation): an Ediacaran window on soft-bodied and multicellular microorganisms. *Journal of the Geological Society*, *174*(5), 793-802. https://doi.org/10.1144/jgs2016-142

Demidenko, Y. E., Zhegallo, E. A., Parkhaev, P. Y., & Shuvalova, Y. V. (2003). Age of phosphorites from the Khubsugul Basin (Mongolia).

Dobretsov, N. L., Buslov, M. M., & Vernikovsky, V. A. (2003). Neoproterozoic to Early Ordovician evolution of the Paleo-Asian Ocean: implications to the break-up of Rodinia. *Gondwana Research*, *6*(2), 143-159. https://doi.org/10.1016/S1342-937X(05)70966-7

Dodd, M. S., Shi, W., Li, C., Zhang, Z., Cheng, M., Gu, H., ... & Lyons, T. W. (2023). Uncovering the Ediacaran phosphorus cycle. *Nature*, 1-7. https://doi.org/10.1038/s41586-023-06077-6

Domack, E. W., & Hoffman, P. F. (2011). An ice grounding-line wedge from the Ghaub glaciation (635 Ma) on the distal foreslope of the Otavi carbonate platform, Namibia, and its bearing on the snowball Earth hypothesis. *Bulletin*, *123*(7-8), 1448-1477. https://doi.org/10.1130/B30217.1

Domeier, M. (2018). Early Paleozoic tectonics of Asia: Towards a full-plate model. *Geoscience Frontiers*, *9*(3), 789-862. https://doi.org/10.1016/j.gsf.2017.11.012

Donov, N. A., Edemsky, H. B. & Ilyin, A. V. (1967). Cambrian phosphorites of Mongolia Popular Republic. *Sovetskaya Geologia*, 3, 55–60

Donskaya, T. V., Gladkochub, D. P., Fedorovsky, V. S., Sklyarov, E. V., Cho, M., Sergeev, S. A., & Kim, J. (2017). Pre-collisional (> 0.5 Ga) complexes of the Olkhon terrane

(southern Siberia) as an echo of events in the Central Asian Orogenic Belt. *Gondwana Research*, *42*, 243-263. https://doi.org/10.1016/j.gr.2016.10.016

Flicoteaux, R., & Trompette, R. (1998). Cratonic and foreland Early Cambrian phosphorites of West Africa: Palaeoceanographical and climatical contexts. *Palaeogeography, Palaeoclimatology, Palaeoecology*, *139*(3-4), 107-120. https://doi.org/10.1016/S0031-0182(97)00141-7

Föllmi, K. B. (1990). Condensation and phosphogenesis: example of the Helvetic mid-Cretaceous (northern Tethyan margin). *Geological Society, London, Special Publications*, *52*(1), 237-252. https://doi.org/10.1144/GSL.SP.1990.052.01.17

Föllmi, K. B. (1996). The phosphorus cycle, phosphogenesis and marine phosphate-rich deposits. *Earth-Science Reviews*, *40*(1-2), 55-124. https://doi.org/10.1016/0012-8252(95)00049-6

Föllmi, K. B., Badertscher, C., de Kaenel, E., Stille, P., John, C. M., Adatte, T., & Steinmann, P. (2005). Phosphogenesis and organic-carbon preservation in the Miocene Monterey Formation at Naples Beach, California—The Monterey hypothesis revisited. *Geological Society of America Bulletin*, *117*(5-6), 589-619. https://doi.org/10.1130/B25524.1

Föllmi, K. B., Thomet, P., Lévy, S., KAENEL, E. D., Spangenberg, J. E., Adatte, T., ... & Garrison, R. E. (2017). The impact of hydrodynamics, authigenesis, and basin morphology on sediment accumulation in an upwelling environment: The Miocene Monterey Formation at Shell Beach and Mussel Rock (Pismo and Santa Maria basins, Central California, USA). *Journal of Sedimentary Research*, *87*(9), 986-1018. https://doi.org/10.1130/B32061.1

Froelich, P. N., Bender, M. L., Luedtke, N. A., Heath, G. R., & DeVries, T. (1982). Marine phosphorus cycle. *Am. J. Sci.;(United States)*, *282*(4). https://doi.org/10.2475/ajs.282.4.474

Froelich, P. N. (1988). Kinetic control of dissolved phosphate in natural rivers and estuaries: a primer on the phosphate buffer mechanism 1. *Limnology and oceanography*, *33*(4part2), 649-668. https://doi.org/10.4319/lo.1988.33.4part2.0649

Gerstenberger, H., & Haase, G. (1997). A highly effective emitter substance for mass spectrometric Pb isotope ratio determinations. *Chemical geology*, *136*(3-4), 309-312. https://doi.org/10.1016/S0009-2541(96)00033-2

Gianola, O., Schmidt, M. W., Jagoutz, O., & Sambuu, O. (2017). Incipient boninitic arc crust built on denudated mantle: the Khantaishir ophiolite (western Mongolia). *Contributions to Mineralogy and Petrology*, *172*, 1-18. https://doi.org/10.1007/s00410-017-1415-4

Gianola, O., Schmidt, M. W., Jagoutz, O., Rickli, J., Bruguier, O., & Sambuu, O. (2019). The Crust–Mantle Transition of the Khantaishir Arc Ophiolite (Western Mongolia). *Journal of Petrology*, *60*(4), 673-700. https://doi.org/10.1093/petrology/egz009

Golubkova, E. Y., Zaitseva, T. S., Kuznetsov, A. B., Dovzhikova, E. G., & Maslov, A. V. (2015, June). Microfossils and Rb-Sr age of glauconite in the key section of the Upper Proterozoic of the northeastern part of the Russian plate (Keltmen-1 borehole). In *Doklady Earth Sciences* (Vol. 462, pp. 547-551). Pleiades Publishing. https://doi.org/10.1134/S1028334X15060045

Gradstein, F. M., Ogg, J. G., Schmitz, M. D., & Ogg, G. M. (Eds.). (2020). *Geologic time scale 2020*. Elsevier.

Grazhdankin, D., Nagovitsin, K., Golubkova, E., Karlova, G., Kochnev, B., Rogov, V., & Marusin, V. (2020). Doushantuo-Pertatataka–type acanthomorphs and Ediacaran ecosystem stability. *Geology*, *48*(7), 708-712. https://doi.org/10.1130/G47467.1

Hartmann, J., & Moosdorf, N. (2011). Chemical weathering rates of silicate-dominated lithological classes and associated liberation rates of phosphorus on the Japanese Archipelago—Implications for global scale analysis. *Chemical Geology*, *287*(3-4), 125-157. https://doi.org/10.1016/j.chemgeo.2010.12.004

Hiess, J., Condon, D. J., McLean, N., & Noble, S. R. (2012). 238U/235U systematics in terrestrial uranium-bearing minerals. *Science*, *335*(6076), 1610-1614. https://doi.org/10.1126/science.1215507

Hoffman, P. F. (1987). Early Proterozoic foredeeps, foredeep magmatism, and Superior-type iron-formations of the Canadian Shield. *Proterozic lithospheric evolution*, *17*, 85-98. https://doi.org/10.1029/GD017p0085

Hoffman, P. F., Macdonald, F. A., & Halverson, G. P. (2011). Chapter 5 Chemical sediments associated with Neoproterozoic glaciation: iron formation, cap carbonate, barite and phosphorite. *Geological Society, London, Memoirs*, *36*(1), 67-80. https://doi.org/10.1144/M36.5

Holmden, C., Creaser, R. A., Muehlenbachs, K. L. S. A., Leslie, S. A., & Bergstrom, S. M. (1998). Isotopic evidence for geochemical decoupling between ancient epeiric seas and bordering oceans: implications for secular curves. *Geology*, *26*(6), 567-570. https://doi.org/10.1130/0091-7613(1998)026<0567:IEFGDB>2.3.CO;2

Horstwood, M. S., Košler, J., Gehrels, G., Jackson, S. E., McLean, N. M., Paton, C., ... & Schoene, B. (2016). Community-derived standards for LA-ICP-MS U-(Th-) Pb geochronology–Uncertainty propagation, age interpretation and data reporting. *Geostandards and Geoanalytical Research*, *40*(3), 311-332. https://doi.org/10.1111/j.1751-908X.2016.00379.x

Horton, F. (2015). Did phosphorus derived from the weathering of large igneous provinces fertilize the Neoproterozoic ocean? *Geochemistry, Geophysics, Geosystems*, *16*(6), 1723-1738. https://doi.org/10.1002/2015GC005792

Hurtgen, M. T., Arthur, M. A., Suits, N. S., & Kaufman, A. J. (2002). The sulfur isotopic composition of Neoproterozoic seawater sulfate: implications for a snowball Earth?. *Earth and Planetary Science Letters*, *203*(1), 413-429. https://doi.org/10.1016/S0012-821X(02)00804-X

Ilyin, A.V. and Zhuravleva, I.T., 1968, On the boundary between the Cambrian and the Precambrian at Prikhusugulie (Mongolian PR). *Dolkady Akademii Nauk SSSR,* v. 182, p. 1164-1166 (in Russian).

lyin, A. V. (1971). The Tuva–Mongolia Massif, Tr. *NIL Zarubezh-geologii (Proc. of NIL Zarubezhgeologiya), Nedra, Moskva*, *22*, 27-36

Ilyin, A. V. (1973). Khubsugul Phosphorite-Bearing Basin. *Geologicheskiy Institut, Akademiya Nauk SSSR*, Moscow (in Russian)

Ilyin, A. V., & Ratnikova, G. I. (1981). Primary, bedded, structureless phosphorite of the Khubsugul Basin, Mongolia. *Journal of Sedimentary Research*, *51*(4), 1215-1222. https://doi.org/10.1306/212F7E69-2B24-11D7-8648000102C1865D

Ilyin, A. V. (2004). The Khubsugul phosphate-bearing basin: New data and concepts. *Lithology and Mineral Resources*, *39*, 454-467. https://doi.org/10.1023/B:LIMI.0000040735.76025.80

Ingall, E. D., & Van Cappellen, P. (1990). Relation between sedimentation rate and burial of organic phosphorus and organic carbon in marine sediments. *Geochimica et Cosmochimica Acta*, *54*(2), 373-386. https://doi.org/10.1016/0016-7037(90)90326-G

Jackson, S. E., Pearson, N. J., Griffin, W. L., & Belousova, E. A. (2004). The application of laser ablation-inductively coupled plasma-mass spectrometry to in situ U–Pb zircon geochronology. *Chemical geology*, *211*(1-2), 47-69. https://doi.org/10.1016/j.chemgeo.2004.06.017

Janoušek, V., Jiang, Y., Burianek, D., Schulmann, K., Hanžl, P., Soejono, I., ... & Košler, J. (2018). Cambrian–ordovician magmatism of the Ikh-Mongol Arc system exemplified by the Khantaishir Magmatic Complex (Lake Zone, south–central Mongolia). *Gondwana Research*, *54*, 122-149. https://doi.org/10.1016/j.gr.2017.10.003

Johnston, D. T., Macdonald, F. A., Gill, B. C., Hoffman, P. F., & Schrag, D. P. (2012). Uncovering the Neoproterozoic carbon cycle. *Nature*, *483*(7389), 320-323. https://doi.org/10.1038/nature10854

Karmysheva, I. V., Vladimirov, V. G., Rudnev, S. N., Yakovlev, V. A., & Semenova, D. V. (2021). Syntectonic metamorphism of a collisional zone in the Tuva-Mongolian massif, Central Asian Orogenic belt: PT conditions, U-Pb ages and tectonic setting. *Journal of Asian Earth Sciences*, *220*, 104919. https://doi.org/10.1016/j.jseaes.2021.104919

Khain, E. V., Bibikova, E. V., Kröner, A., Zhuravlev, D. Z., Sklyarov, E. V., Fedotova, A. A., & Kravchenko-Berezhnoy, I. R. (2002). The most ancient ophiolite of the Central Asian fold belt: U–Pb and Pb–Pb zircon ages for the Dunzhugur Complex, Eastern Sayan, Siberia, and geodynamic implications. *Earth and Planetary Science Letters*, *199*(3-4), 311-325. https://doi.org/10.1016/S0012-821X(02)00587-3

Kherzaskova, T. N. & Samygin, S. G. (1992). Tectonic conditions in the East Sayan Vendian – Middle Cambrian terrigenous carbonate association. *Geotectonics*, 26, 445–458.

Kheraskova, T. N., Samygin, S. G., Ruzhentsev, S. V., & Mossakovsky, A. A. (1995). Late Riphean marginal-continental volcanic belt of East Gondwana: transactions of Russian Academy of Sciences. *Earth Sciences Section*, *342*, 661-664.

Khukhuudei, U., Kusky, T., Otgonbayar, O., & Wang, L. (2020). the early palaeozoic mega-thrusting of the gondwana-derived altay–lake zone in Western Mongolia: Implications for the development of the central asian orogenic belt and paleo-asian ocean evolution. *Geological Journal*, *55*(3), 2129-2149. https://doi.org/10.1002/gj.3753

Kohout, F. A. (1965). A hypothesis concerning cyclic flow of salt water related to geothermal heating in the Floridan aquifer. *Transactions of the New York Academy of Sciences*, *28*(2), 249-271.

Korobov, M.N., (1980). Lower Cambrian biostratigraphy and miomeran trilobites of Mongolia *Sovmestnaya Sovetsko-Mongol'skaya Geologicheskaya Ekspeditsiya, Trudy,* v. 26, p. 5–108. [in Russian]

Korobov, M.N., (1989). Lower Cambrian biostratigraphy and polymeran trilobites of Mongolia*. Sovmestnaya Sovetsko-Mongol'skaya Geologicheskaya Ekspeditsiya, Trudy,* v. 48, p. 1–204. [in Russian]

Korovnikov, I. V., & Lazarev, F. D. (2021). New findings of lower cambrian trilobites in the southern hövsgöl area (Mongolia) and their significance for stratigraphy and interregional correlation. *Russian Geology and Geophysics*, *62*(12), 1350-1358. https://doi.org/10.2113/RGG20204174

Kozakov, I. K., Kovach, V. P., Salnikova, E. B., Kröner, A., Adamskaya, E. V., Azimov, P. Y., ... & Plotkina, Y. V. (2021). Geochronology and Geodynamic Settings of Metamorphic Complexes in the Southwestern Part of the Tuva-Mongolian Terrane, Central Asian Foldbelt. *Stratigraphy and Geological Correlation*, *29*, 389-410. https://doi.org/10.1134/S0869593821030035

Kröner, A., Windley, B. F., Badarch, G., Tomurtogoo, O., Hegner, E., Jahn, B. M., ... & Wingate, M. T. D. (2007). Accretionary growth and crust formation in the Central Asian

Orogenic Belt and comparison with the Arabian-Nubian shield. https://doi.org/10.1130/2007.1200(11)

Kröner, A., Kovach, V., Belousova, E., Hegner, E., Armstrong, R., Dolgopolova, A., ... & Rytsk, E. (2014). Reassessment of continental growth during the accretionary history of the Central Asian Orogenic Belt. *Gondwana Research*, *25*(1), 103-125. https://doi.org/10.1016/j.gr.2012.12.023

Krogh, T. E. (1973). A low-contamination method for hydrothermal decomposition of zircon and extraction of U and Pb for isotopic age determinations. *Geochimica et Cosmochimica Acta*, *37*(3), 485-494. https://doi.org/10.1016/0016-7037(73)90213-5

Kuzmichev, A. B., Bibikova, E. V., & Zhuravlev, D. Z. (2001). Neoproterozoic (~ 800 Ma) orogeny in the Tuva-Mongolia Massif (Siberia): island arc–continent collision at the northeast Rodinia margin. *Precambrian Research*, *110*(1-4), 109-126. https://doi.org/10.1016/S0301-9268(01)00183-8

Kuzmichev, A., Sklyarov, E., Postnikov, A., & Bibikova, E. (2007). The Oka belt (southern Siberia and northern Mongolia): A Neoproterozoic analog of the Japanese Shimanto belt?. *Island Arc*, *16*(2), 224-242. https://doi.org/10.1111/j.1440-1738.2007.00568.x

Kuzmichev, A. B., & Larionov, A. N. (2011). The Sarkhoi Group in East Sayan: Neoproterozoic (~ 770–800 Ma) volcanic belt of the Andean type. *Russian Geology and Geophysics*, *52*(7), 685-700. https://doi.org/10.1016/j.rgg.2011.06.001

Kuzmichev, A. B. (2015). Neoproterozoic accretion of the Tuva-Mongolian massif, one of the Precambrian terranes in the Central Asian Orogenic Belt. *Composition and evolution of Central Asian Orogenic Belt: geology, evolution, tectonics, and models*, 66-92.

Kylander-Clark, A. R., Hacker, B. R., & Cottle, J. M. (2013). Laser-ablation split-stream ICP petrochronology. *Chemical Geology*, *345*, 99-112. https://doi.org/10.1016/j.chemgeo.2013.02.019

Laakso, T. A., Sperling, E. A., Johnston, D. T., & Knoll, A. H. (2020). Ediacaran reorganization of the marine phosphorus cycle. *Proceedings of the National Academy of Sciences*, *117*(22), 11961-11967. https://doi.org/10.1073/pnas.1916738117

Liu, P., Yin, C., Gao, L., Tang, F., & Chen, S. (2009). New material of microfossils from the Ediacaran Doushantuo Formation in the Zhangcunping area, Yichang, Hubei Province and its zircon SHRIMP U-Pb age. *Chinese Science Bulletin*, *54*(6), 1058-1064. https://doi.org/10.1007/s11434-008-0589-6

Liu, Z. R., & Zhou, M. F. (2017). Meishucun phosphorite succession (SW China) records redox changes of the early Cambrian ocean. *Bulletin*, *129*(11-12), 1554-1567. https://doi.org/10.1130/B31612.1

Liu, G., Qiao, X., Yu, P., Zhou, Y., Zhao, B., & Xiong, W. (2021). Rupture kinematics of the 11 January 2021 Mw 6.7 Hovsgol, Mongolia, earthquake and implications in the Western Baikal rift zone. *Seismological Research Letters*, *92*(6), 3318-3326. https://doi.org/10.1785/0220210061

Lyons, T. W., & Gill, B. C. (2010). Ancient sulfur cycling and oxygenation of the early biosphere. *Elements*, *6*(2), 93-99. https://doi.org/10.2113/gselements.6.2.93

Macdonald, F. A., Jones, D. S., & Schrag, D. P. (2009). Stratigraphic and tectonic implications of a newly discovered glacial diamictite–cap carbonate couplet in southwestern Mongolia. *Geology*, *37*(2), 123-126. https://doi.org/10.1130/G24797A.1

Macdonald, F. A., & Jones, D. S. (2011). Chapter 30 The Khubsugul Group, Northern Mongolia. *Geological Society, London, Memoirs*, *36*(1), 339-345. https://doi.org/10.1144/M36.30

Mattinson, J. M., Graubard, C. M., Parkinson, D. L., & McClelland, W. C. (1996). U-Pb reverse discordance in zircons: the role of fine-scale oscillatory zoning and sub-micron transport of Pb. *GEOPHYSICAL MONOGRAPH-AMERICAN GEOPHYSICAL UNION*, *95*, 355-370.

Mattinson, J. M. (2005). Zircon U–Pb chemical abrasion ("CA-TIMS") method: combined annealing and multi-step partial dissolution analysis for improved precision and accuracy of zircon ages. *Chemical Geology*, *220*(1-2), 47-66. https://doi.org/10.1016/j.chemgeo.2005.03.011

Maughan, E. K. (1994). Phosphoria Formation (Permian) and its resource significance in the western interior, USA.

Mazumdar, A., Banerjee, D. M., Schidlowski, M., & Balaram, V. (1999). Rare-earth elements and stable isotope geochemistry of early Cambrian chert-phosphorite assemblages from the Lower Tal Formation of the Krol Belt (Lesser Himalaya, India). *Chemical geology*, *156*(1-4), 275-297. https://doi.org/10.1016/S0009-2541(98)00187-9

McFadden, K. A., Xiao, S., Zhou, C., & Kowalewski, M. (2009). Quantitative evaluation of the biostratigraphic distribution of acanthomorphic acritarchs in the Ediacaran Doushantuo Formation in the Yangtze Gorges area, South China. *Precambrian Research*, *173*(1-4), 170-190. https://doi.org/10.1016/j.precamres.2009.03.009

McLean, N. M., Bowring, J. F., & Bowring, S. A. (2011). An algorithm for U-Pb isotope dilution data reduction and uncertainty propagation. *Geochemistry, Geophysics, Geosystems*, *12*(6). https://doi.org/10.1029/2010GC003478

McLean, N. M., Condon, D. J., Schoene, B., & Bowring, S. A. (2015). Evaluating uncertainties in the calibration of isotopic reference materials and multi-element isotopic

tracers (EARTHTIME Tracer Calibration Part II). *Geochimica et Cosmochimica Acta*, *164*, 481-501. https://doi.org/10.1016/j.gca.2015.02.040

Meert, J. G., Gibsher, A. S., Levashova, N. M., Grice, W. C., Kamenov, G. D., & Ryabinin, A. B. (2011). Glaciation and~ 770 Ma Ediacara (?) fossils from the lesser Karatau microcontinent, Kazakhstan. *Gondwana Research*, *19*(4), 867-880. https://doi.org/10.1016/j.gr.2010.11.008

Misi, A., & Kyle, J. R. (1994). Upper Proterozoic carbonate stratigraphy, diagenesis, and stromatolitic phosphorite formation, Irecê Basin, Bahia, Brazil. *Journal of Sedimentary Research*, *64*(2a), 299-310. https://doi.org/10.1306/D4267D84-2B26-11D7-8648000102C1865D

Mongolian Survey (1988) Geologic Map, Uranduush Uul. Geologic map M-47-45-A. (in Mongolian)

Mongush, A. A., Lebedev, V. I., Kovach, V. P., Sal'nikova, E. B., Druzhkova, E. K., Yakovleva, S. Z., ... & Serov, P. A. (2011). The tectonomagmatic evolution of structure-lithologic complexes in the Tannu-Ola zone, Tuva, in the Late Vendian–Early Cambrian (from geochemical, Nd isotope, and geochronological data). *Russian Geology and Geophysics*, *52*(5), 503-516. DOI: 10.1134/S1028334X11060328

Morais, L., Fairchild, T. R., Freitas, B. T., Rudnitzki, I. D., Silva, E. P., Lahr, D., ... & Trindade, R. I. F. D. (2021). Doushantuo-Pertatataka—like acritarchs from the Late Ediacaran Bocaina Formation (Corumbá Group, Brazil). *Frontiers in Earth Science*,1233. https://doi.org/10.3389/feart.2021.787011

Moreira, D. S., Uhlein, A., Uhlein, G. J., Sial, A. N., & Koester, E. (2021). Ediacaran/Early Cambrian Serra da Saudade Formation, Bambuí Group: the sedimentary record of a foreland basin in Southeastern Brazil. *Brazilian Journal of Geology*, *51*. https://doi.org/10.1590/2317-4889202120210029

Müller, R. D., Cannon, J., Williams, S., & Dutkiewicz, A. (2018). PyBacktrack 1.0: A tool for reconstructing paleobathymetry on oceanic and continental crust. *Geochemistry, Geophysics, Geosystems*, *19*(6), 1898-1909. https://doi.org/10.1029/2017GC007313

Munkhtsengel, B., Byambaa, J., & Tamiraa, A. (2021). Phosphate Deposits. *Mineral Resources of Mongolia*, 349-383. https://doi.org/10.1007/978-981-15-5943-3_12

Nelson, L.L., Crowley, J.L., Smith, E.F., Schwartz, D.M., Hodgin, E.B., Schmitz, M.D. (2023). Cambrian explosion condensed: High-precision geochronology of the lower Wood Canyon Formation, Nevada. *Proceedings of the National Academy of Science,* in press.

O'brien, G. W., Milnes, A. R., Veeh, H. H., Heggie, D. T., Riggs, S. R., Cullen, D. J., ... & Cook, P. J. (1990). Sedimentation dynamics and redox iron-cycling: controlling factors for the apatite—glauconite association on the East Australian continental margin. *Geological*

Society, London, Special Publications, *52*(1), 61-86. https://doi.org/10.1144/GSL.SP.1990.052.01.06

Osokin, P. V. & Tyzhinov, A. V. (1998). Precambrian Tilloids of the Oka- Khubsugul phosphorite-bearing basin (Eastern Sayan, Northwestern Mongolia). *Lithology and Mineral Resources*, 33, 142–154

Ouyang, Q., Guan, C., Zhou, C., & Xiao, S. (2017). Acanthomorphic acritarchs of the Doushantuo Formation from an upper slope section in northwestern Hunan Province, South China, with implications for early–middle Ediacaran biostratigraphy. *Precambrian Research*, *298*, 512-529. https://doi.org/10.1016/j.precamres.2017.07.005

Papineau, D. (2010). Global biogeochemical changes at both ends of the Proterozoic: insights from phosphorites. *Astrobiology*, *10*(2), 165-181. https://doi.org/10.1089/ast.2009.0360

Park, Y., Swanson-Hysell, N. L., MacLennan, S. A., Maloof, A. C., Gebreslassie, M., Tremblay, M. M., ... & Haileab, B. (2020). The lead-up to the Sturtian Snowball Earth: Neoproterozoic chemostratigraphy time-calibrated by the Tambien Group of Ethiopia. *GSA Bulletin*, *132*(5-6), 1119-1149. https://doi.org/10.1130/B35178.1

Parry, L. A., Boggiani, P. C., Condon, D. J., Garwood, R. J., Leme, J. D. M., McIlroy, D., ... & Liu, A. G. (2017). Ichnological evidence for meiofaunal bilaterians from the terminal Ediacaran and earliest Cambrian of Brazil. *Nature Ecology & Evolution*, *1*(10), 1455-1464. https://doi.org/10.1038/s41559-017-0301-9

Paton, C., Woodhead, J. D., Hellstrom, J. C., Hergt, J. M., Greig, A., & Maas, R. (2010). Improved laser ablation U-Pb zircon geochronology through robust downhole fractionation correction. *Geochemistry, Geophysics, Geosystems*, *11*(3). https://doi.org/10.1029/2009GC002618

Pfänder, J. A., & Kröner, A. (2004). Tectono-magmatic evolution, age and emplacement of the Agardagh Tes-Chem ophiolite in Tuva, Central Asia: crustal growth by island arc accretion. *Developments in Precambrian Geology*, *13*, 207-221. https://doi.org/10.1016/S0166-2635(04)13006-5

Planavsky, N. J., Asael, D., Rooney, A. D., Robbins, L. J., Gill, B. C., Dehler, C. M., ... & Reinhard, C. T. (2023). A sedimentary record of the evolution of the global marine phosphorus cycle. *Geobiology*, *21*(2), 168-174. https://doi.org/10.1111/gbi.12536

Redfield, A. C. (1958). The biological control of chemical factors in the environment. *American scientist*, *46*(3), 230A-221.

Reinhard, C. T., Planavsky, N. J., Gill, B. C., Ozaki, K., Robbins, L. J., Lyons, T. W., ... & Konhauser, K. O. (2017). Evolution of the global phosphorus cycle. *Nature*, *541*(7637), 386-389. https://doi.org/10.1038/nature20772

Roest-Ellis, S., Richardson, J. A., Phillips, B. L., Mehra, A., Webb, S. M., Cohen, P. A., ... & Tosca, N. J. (2023). Tonian Carbonates Record Phosphate-Rich Shallow Seas. *Geochemistry, Geophysics, Geosystems*, *24*(5), e2023GC010974. https://doi.org/10.1029/2023GC010974

Romanek, C. S., Grossman, E. L., & Morse, J. W. (1992). Carbon isotopic fractionation in synthetic aragonite and calcite: effects of temperature and precipitation rate. *Geochimica et cosmochimica acta*, *56*(1), 419-430. https://doi.org/10.1016/0016-7037(92)90142-6

Rooney, A. D., Cantine, M. D., Bergmann, K. D., Gómez-Pérez, I., Al Baloushi, B., Boag, T. H., ... & Strauss, J. V. (2020). Calibrating the coevolution of Ediacaran life and environment. *Proceedings of the National Academy of Sciences*, *117*(29), 16824-16830. https://doi.org/10.1073/pnas.2002918117

Rudnev, S.N., Vladimirov, A.G., Ponomarchuk, V.A., Bibikova, E.V., Sergeev, S.A., Plotkina, Y.V., Bayanova, T.B. (2006). The Kaakhem polychronous granitoid batholith, eastern Tuva: composition, age, sources, and geodynamic setting. *Litosfera*, 200, 3–33 (in Russian).

Rudnev, S. N., Borisov, S. M., Babin, G. A., Levchenkov, O. A., Makeev, A. F., Serov, P. A., ... & Plotkina, Y. V. (2008). Early Paleozoic batholiths in the northern part of the Kuznetsk Alatau: composition, age, and sources. *Petrology*, *16*, 395-419. https://doi.org/10.1134/S086959110804005X

Ruttenberg, K. C. The global phosphorus cycle, in *Treatise on Geochemistry* Vol. 8 (eds Holland, H. D. & Turekian, K. K.) 585–643 (Pergamon, 2003). https://doi.org/10.1016/B0-08-043751-6/08153-6

Ruzhentsev, S. V., & Burashnikov, V. V. (1995). Tectonics of the western Mongolian Salairides. *Geotectonics*, *29*(5), 379-394.

Sanders, C., & Grotzinger, J. (2021). Sedimentological and stratigraphic constraints on depositional environment for Ediacaran carbonate rocks of the São Francisco Craton: Implications for phosphogenesis and paleoecology. *Precambrian Research*, *363*, 106328. https://doi.org/10.1016/j.precamres.2021.106328

Sanders, C. B. (2023). *Geological and Geochemical Explorations of the Salitre Formation Phosphorite, Eastern Brazil* (Doctoral dissertation, California Institute of Technology). https://doi.org/10.7907/rd4m-7x08

Schulz, H. N., & Schulz, H. D. (2005). Large sulfur bacteria and the formation of phosphorite. *Science*, *307*(5708), 416-418. https://doi.org/10.1126/science.1103096

Sergeev, V. N., Schopf, J. W., & Kudryavtsev, A. B. (2020). Global microfossil changes through the Precambrian-Cambrian phosphogenic event: the Shabakta Formation of the

phosphorite-bearing Maly Karatau Range, South Kazakhstan. *Precambrian Research*, *349*, 105386. https://doi.org/10.1016/j.precamres.2019.105386

Shaffer, G. (1986). Phosphate pumps and shuttles in the Black Sea. *Nature*, *321*(6069), 515-517. https://doi.org/10.1038/321515a0

Sheldon, R. P. (1984). Ice-ring origin of the Earth's atmosphere and hydrosphere and late Proterozoic – Cambrian phosphogenesis*, Phosphorite, Geological Survey of India Special Publication*, 17, Udaipur, Rajasthan, India.

Shields, G., Stille, P., & Brasier, M. D. (2000). Isotopic records across two phosphorite giant episodes compared: the Precambrian-Cambrian and the late Cretaceous-recent. https://doi.org/10.2110/pec.00.66.0103

Shkol'nik, S. I., Stanevich, A. M., Reznitskii, L. Z., & Savelieva, V. B. (2016). New data about structure and time of formation of the Khamar-Daban terrane: U-Pb LA-ICP-MS zircon ages. *Stratigraphy and Geological Correlation*, *24*, 19-38. https://doi.org/10.1134/S086959381506009X

Shiraishi, F., Ohnishi, S., Hayasaka, Y., Hanzawa, Y., Takashima, C., Okumura, T., & Kano, A. (2019). Potential photosynthetic impact on phosphate stromatolite formation after the Marinoan glaciation: Paleoceanographic implications. *Sedimentary Geology*, *380*, 65-82. https://doi.org/10.1016/j.sedgeo.2018.11.014

Sinclair, H. D., & Naylor, M. (2012). Foreland basin subsidence driven by topographic growth versus plate subduction. *Bulletin*, *124*(3-4), 368-379. https://doi.org/10.1130/B30383.1

Sláma, J., Košler, J., Condon, D. J., Crowley, J. L., Gerdes, A., Hanchar, J. M., ... & Whitehouse, M. J. (2008). Plešovice zircon—a new natural reference material for U–Pb and Hf isotopic microanalysis. *Chemical Geology*, *249*(1-2), 1-35.https://doi.org/10.1016/j.chemgeo.2007.11.005

Smith, E. F., Macdonald, F. A., Petach, T. A., Bold, U., & Schrag, D. P. (2016). Integrated stratigraphic, geochemical, and paleontological late Ediacaran to early Cambrian records from southwestern Mongolia. *Bulletin*, *128*(3-4), 442-468. https://doi.org/10.1130/B31248.1

Southgate, P. N. (1980). Cambrian stromatolitic phosphorites from the Georgina Basin, Australia. *Nature*, *285*(5764), 395-397. https://doi.org/10.1038/285395a0

Spencer, C. J., Kirkland, C. L., & Taylor, R. J. (2016). Strategies towards statistically robust interpretations of in situ U–Pb zircon geochronology. *Geoscience Frontiers*, *7*(4), 581-589. https://doi.org/10.1016/j.gsf.2015.11.006

Sundby, B., Anderson, L. G., Hall, P. O., Iverfeldt, Å., van der Loeff, M. M. R., & Westerlund, S. F. (1986). The effect of oxygen on release and uptake of cobalt, manganese,

iron and phosphate at the sediment-water interface. *Geochimica et Cosmochimica Acta*, *50*(6), 1281-1288. https://doi.org/10.1016/0016-7037(86)90411-4

Swart, P. K., & Eberli, G. (2005). The nature of the δ13C of periplatform sediments: Implications for stratigraphy and the global carbon cycle. *Sedimentary Geology*, *175*(1-4), 115-129. https://doi.org/10.1016/j.sedgeo.2004.12.029

Szymanowski, D., & Schoene, B. (2020). U–Pb ID-TIMS geochronology using ATONA amplifiers. *Journal of Analytical Atomic Spectrometry*, *35*(6), 1207-1216. https://doi.org/10.1039/D0JA00135J

Teng, L. S., Lee, C. T., Tsai, Y. B., & Hsiao, L. Y. (2000). Slab breakoff as a mechanism for flipping of subduction polarity in Taiwan. *Geology*, *28*(2), 155-158. https://doi.org/10.1130/0091-7613(2000)28<155:SBAAMF>2.0.CO;2

Tyrrell, T. (1999). The relative influences of nitrogen and phosphorus on oceanic primary production. *Nature*, *400*(6744), 525-531. https://doi.org/10.1038/22941

Uhlein, G. J., Uhlein, A., Halverson, G. P., Stevenson, R., Caxito, F. A., Cox, G. M., & Carvalho, J. F. (2016). The Carrancas Formation, Bambuí Group: a record of pre-Marinoan sedimentation on the southern São Francisco craton, Brazil. *Journal of South American Earth Sciences*, *71*, 1-16. https://doi.org/10.1016/j.jsames.2016.06.009

Valetich, M., Zivak, D., Spandler, C., Degeling, H., & Grigorescu, M. (2022). REE enrichment of phosphorites: An example of the Cambrian Georgina Basin of Australia. *Chemical Geology*, *588*, 120654. https://doi.org/10.1016/j.chemgeo.2021.120654

Van Cappellen, P., Gaillard, J. F., & Rabouille, C. (1993). Biogeochemical transformations in sediments: kinetic models of early diagenesis. In *Interactions of C, N, P and S biogeochemical cycles and global change* (pp. 401-445). Springer Berlin Heidelberg. https://doi.org/10.1007/978-3-642-76064-8_17

Vermeesch, P. (2018). IsoplotR: A free and open toolbox for geochronology. *Geoscience Frontiers*, *9*(5), 1479-1493. https://doi.org/10.1016/j.gsf.2018.04.001

Wendt, I., & Carl, C. (1991). The statistical distribution of the mean squared weighted deviation. *Chemical Geology: Isotope Geoscience Section*, *86*(4), 275-285. https://doi.org/10.1016/0168-9622(91)90010-T

Wiedenbeck, M. A. P. C., Alle, P., Corfu, F. Y., Griffin, W. L., Meier, M., Oberli, F. V., ... & Spiegel, W. (1995). Three natural zircon standards for U-Th-Pb, Lu-Hf, trace element and REE analyses. *Geostandards newsletter*, *19*(1), 1-23. https://doi.org/10.1111/j.1751-908X.1995.tb00147.x

Wilde, S. A. (2015). Final amalgamation of the Central Asian Orogenic Belt in NE China: Paleo-Asian Ocean closure versus Paleo-Pacific plate subduction—A review of the evidence. *Tectonophysics*, *662*, 345-362. https://doi.org/10.1016/j.tecto.2015.05.006

Willman, S., Peel, J. S., Ineson, J. R., Schovsbo, N. H., Rugen, E. J., & Frei, R. (2020). Ediacaran Doushantuo-type biota discovered in Laurentia. *Communications Biology*, *3*(1), 647. https://doi.org/10.1038/s42003-020-01381-7

Windley, B. F., Alexeiev, D., Xiao, W., Kröner, A., & Badarch, G. (2007). Tectonic models for accretion of the Central Asian Orogenic Belt. *Journal of the Geological Society*, *164*(1), 31-47. https://doi.org/10.1144/0016-76492006-02

Wu, X., Baas, J. H., Parsons, D. R., Eggenhuisen, J., Amoudry, L., Cartigny, M., ... & Ruessink, G. (2018). Wave ripple development on mixed clay-sand substrates: effects of clay winnowing and armoring. *Journal of Geophysical Research: Earth Surface*, *123*(11), 2784-2801. https://doi.org/10.1029/2018JF004681

Xiao, S., Zhang, Y., & Knoll, A. H. (1998). Three-dimensional preservation of algae and animal embryos in a Neoproterozoic phosphorite. *Nature*, *391*(6667), 553-558. https://doi.org/10.1038/35318

Xiao, S., & Knoll, A. H. (1999). Fossil preservation in the Neoproterozoic Doushantuo phosphorite lagerstätte,South China. *Lethaia*, *32*(3), 219-238. https://doi.org/10.1111/j.1502-3931.1999.tb00541.x

Xiao, S., & Knoll, A. H. (2000). Phosphatized animal embryos from the Neoproterozoic Doushantuo formation at Weng'an, Guizhou, South China. *Journal of Paleontology*, *74*(5), 767-788. https://doi.org/10.1666/0022-3360(2000)074<0767:PAEFTN>2.0.CO;2

Xiao, W., Windley, B. F., Hao, J., & Zhai, M. (2003). Accretion leading to collision and the Permian Solonker suture, Inner Mongolia, China: Termination of the central Asian orogenic belt. *Tectonics*, *22*(6). https://doi.org/10.1029/2002TC001484

Xiao, S., Zhou, C., Liu, P., Wang, D., & Yuan, X. (2014). Phosphatized Acanthomorphic Acritarchs and Related Microfossils from the Ediacaran Doushantuo Formation at Weng'an (South China) and their Implications. *Journal of Paleontology*, *88*(1), 1-67. https://doi.org/10.1666/12-157R

Yang, C., Rooney, A. D., Condon, D. J., Li, X. H., Grazhdankin, D. V., Bowyer, F. T., ... & Zhu, M. (2021). The tempo of Ediacaran evolution. *Science advances*, *7*(45), eabi9643. https://doi.org/10.1126/sciadv.abi9643

Yang, C., Li, X. H., & Zhu, M. Y. (2022). Tectonic regime transition of the western South China Block in early Cambrian: Evidence from the Meishucun volcanic ash beds. *Palaeoworld*, *31*(4), 591-599. https://doi.org/10.1016/j.palwor.2022.03.003

Zhegallo, E. A. (2000). *Atlas of microorganisms from ancient phosphorites of Khubsugul (Mongolia)*. National Aeronautics and Space Administration, Marshall Space Flight Center.

Zhou, C., Xiao, S., Wang, W., Guan, C., Ouyang, Q., & Chen, Z. (2017). The stratigraphic complexity of the middle Ediacaran carbon isotopic record in the Yangtze Gorges area, South China, and its implications for the age and chemostratigraphic significance of the Shuram excursion. *Precambrian Research*, *288*, 23-38. https://doi.org/10.1016/j.precamres.2016.11.007

* * *

CHAPTER IV. TIMING AND TEMPO OF ORGANIC CARBON BURIAL IN THE MONTEREY FORMATION AND RELATIONSHIPS WITH MIOCENE CLIMATE

A version of this work has been published as:

[**Anttila, E.**, Macdonald, F.A., Szymanowski, D., Schoene, B., Kylander-Clark, A., Danhof, C. and Jones, D.S., 2023. *Timing and tempo of organic carbon burial in the Monterey Formation of the Santa Barbara Basin and relationships with Miocene climate.* Earth and Planetary Science Letters, v.620, 118343.]

ABSTRACT

Understanding the transfer of carbon between Earth's surface reservoirs is necessary for interpreting climate transitions in Earth history and predicting future climate change. Warming associated with the 16.9–14.7 Ma Miocene Climate Optimum and subsequent cooling during the 14.7–13.8 Ma Middle Miocene Climate Transition provide opportunities to study carbon cycle dynamics in the geologically recent past. The Monterey Hypothesis interprets the Middle Miocene Climate Transition cooling as part of a positive feedback in which enhanced organic carbon burial on the eastern Pacific margin drew down atmospheric CO_2. This idea has been supported by the correlation of organic-rich deposits in the Monterey Formation in coastal California with the mid-Miocene Monterey Event, a globally-observed positive shift in the $\delta^{13}C$ of marine carbonates that may be indicative of elevated burial of $\delta^{13}C$-depleted organic carbon. Here, we use 31 new U-Pb zircon laser ablation inductively coupled plasma mass spectrometry ages and 14 new isotope dilution thermal ionization mass spectrometry ages from volcanic ash beds in the Monterey

Formation along the Santa Barbara coast to constrain the timing and tempo of organic carbon mass accumulation in some of the most organic-rich rocks in California. The new age model demonstrates that peaks in organic carbon mass accumulation rate in the Monterey Formation do not coincide with the Monterey Event, and that total organic carbon content in the Miocene Santa Barbara Basin is inversely correlated with sedimentation rate. We propose that changes in organic carbon burial rates in the Monterey Formation were driven by a combination of sea-level change and local tectonically-mediated basin formation, which provided first-order controls on sedimentation rate, and that organic carbon burial in the Monterey Formation is better described as a response to, rather than a driver of, global climate.

4.1. Introduction

Organic-rich strata of the Monterey Formation were deposited in borderland basins along the western margin of North America during the Miocene, and are the primary source and reservoir rocks for California's hydrocarbon resources (Bramlette, 1946; Pisciotto and Garrison, 1981; Behl et al., 1999). Although the burial and preservation of organic material in the Monterey Formation has been investigated for more than half a century, attribution of the specific global and local processes that resulted in the distribution of organic-rich rocks in California remains a subject of debate. Deposition of the Monterey Formation spanned the Miocene Climatic Optimum [MCO, marked by peak Neogene temperatures (Moudestou et al., 2020) and a nadir of Antarctic ice extent (Foster et al., 2012)] through onset of the subsequent global cooling trend (Westerhold et al., 2020; Holbourn et al., 2014), motivating the hypothesis that organic carbon burial in the Monterey Formation and temporally-

equivalent units in the eastern Pacific drove Miocene climate change (Vincent and Berger, 1985; Flower and Kennett, 1993). Conversely, other workers have suggested that the MCO was marked by low marine organic carbon burial rates (Li et al., 2023; John et al., 2002), consistent with hypotheses suggesting that local preservation factors, rather than enhanced organic production and burial, were responsible for the elevated organic content of Monterey Formation shales (Isaacs, 1984; John et al., 2002; Föllmi et al., 2005).

These hypotheses can be assessed by quantifying the rate and timing of organic carbon burial in the Monterey Formation. Existing age models for the Monterey Formation rely primarily on biostratigraphy (John et al., 2002; Föllmi et al., 2005), with secondary constraints from chemostratigraphy and magnetostratigraphy. However, evidence of reworking and sedimentary condensation (Föllmi, 2005) complicates age assignment, as does variable preservation of calcareous skeletal material (Barron, 1986) and limited absolute age calibration for Californian marginal biozones (Crouch and Bukry, 1979). Carbon and oxygen isotope chemostratigraphic correlations of the Monterey Formation to global records (Flower and Kennett, 1993) are compromised by carbonate authigenesis (Blättler et al., 2015), and basin restriction (Isaacs, 2001; Hancock et el., 2019).

Here, we present precise U-Pb geochronology on zircon derived from volcanic ash beds intercalated within Monterey Formation strata. These dates anchor age models through four stratigraphic sections along the northern edge of the Santa Barbara Channel (Fig. 1). At the El Capitan and Naples sections, age models are paired with both new and previously published total organic carbon (TOC) measurements to constrain the rate of organic carbon burial. All age models are then integrated into a basinal chronostratigraphy to assess the synchronicity of lithostratigraphic change across the Santa Barbara Basin (SBB) and to

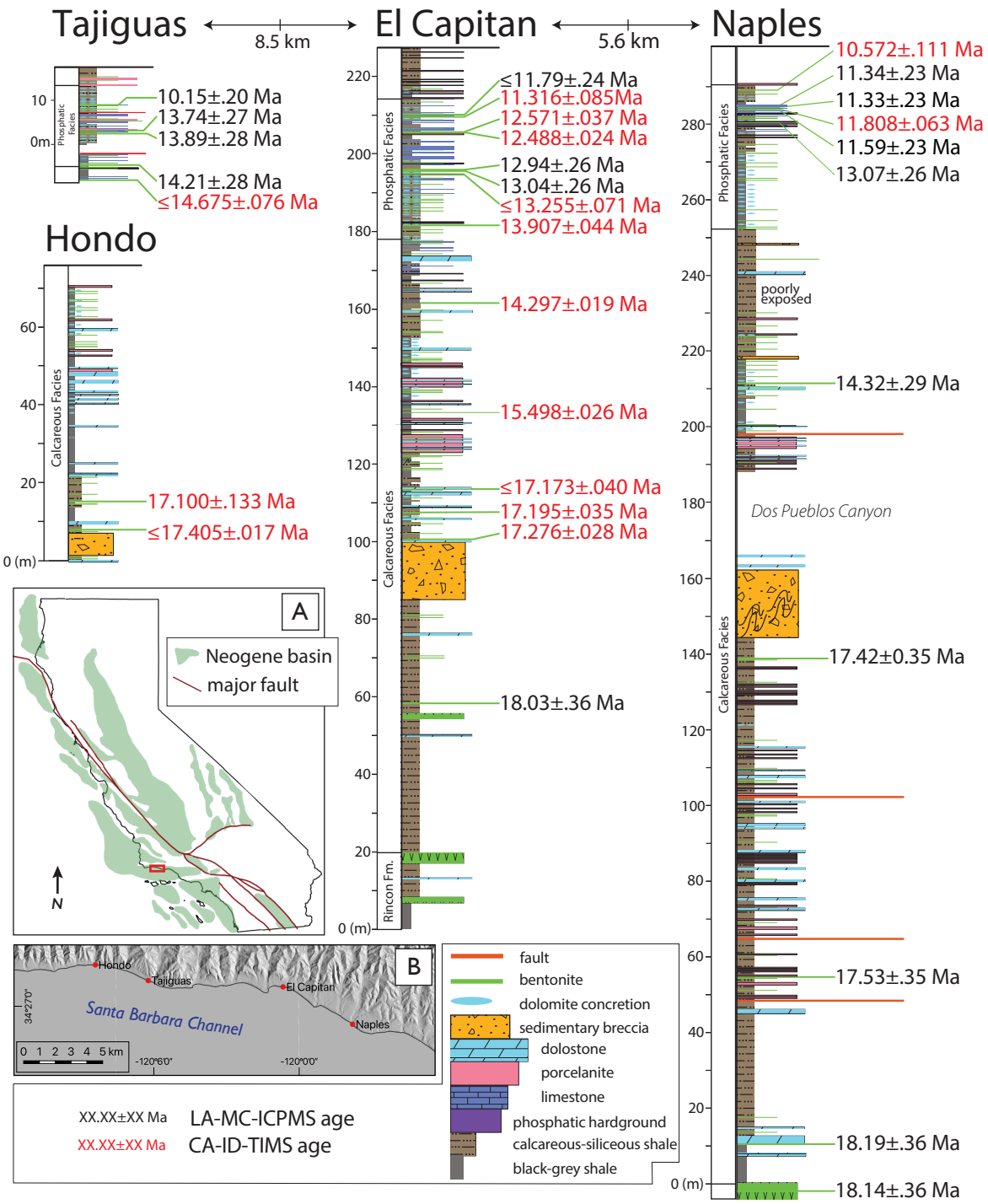

Figure 1: A) Neogene sedimentary basins of California, modified from Behl (1999), with study area highlighted in red and expanded in **B)**. **C)** Stratigraphic sections through outcrops at four beach-cliff exposures of the Monterey Formation, with U-Pb zircon ages appended onto the bentonites from which they were derived. Maximum depositional ages are represented with a ≤.

consider mechanisms for driving the accumulation of organic carbon. Within this chronostratigraphic framework, changes in TOC abundance and organic carbon mass accumulation rate (OCMAR) are compared with putative far-field drivers, and are used to assess the relationships between organic carbon burial in the Monterey Formation and Miocene climate change.

4.2. Geological background

The Monterey Formation of the SBB outcrops in beach cliff exposures along the northern edge of the Santa Barbara Channel (Fig. 1B; Isaacs, 1981). Shale, carbonate, and porcelanite (porous opaline silica) of the Monterey Formation broadly expand eastward with lateral variability in both thickness and facies over sub-km to km-scales, consistent with deposition within an active, fault-bounded transtensional borderland basin (Luyendyk et al., 1980). The thickness and facies changes within these coastal outcrops are a manifestation of similar variability spanning the greater SBB: the outcrops on the northern channel coast represent the condensed, banktop-proximal equivalents of thicker, siliceous basinal facies of the central Santa Barbara Channel (Hornafius, 1991). These basinal deposits are bounded to the south by another paleotopographic high (Isaacs, 1984), which now forms the Santa Barbara Channel Islands.

The Monterey Formation is subdivided into three lithostratigraphic units: the Calcareous Facies, Phosphatic Facies, and Siliceous Facies (Pisciotto and Garrison, 1981). The basal Calcareous Facies rests above the Rincon Shale and consists of calcareous-siliceous shales (Fig. 2A), interspersed with minor dolostone and porcelanite (Fig. 2B). The overlying Phosphatic Facies features darker, organic carbon-rich shale with abundant

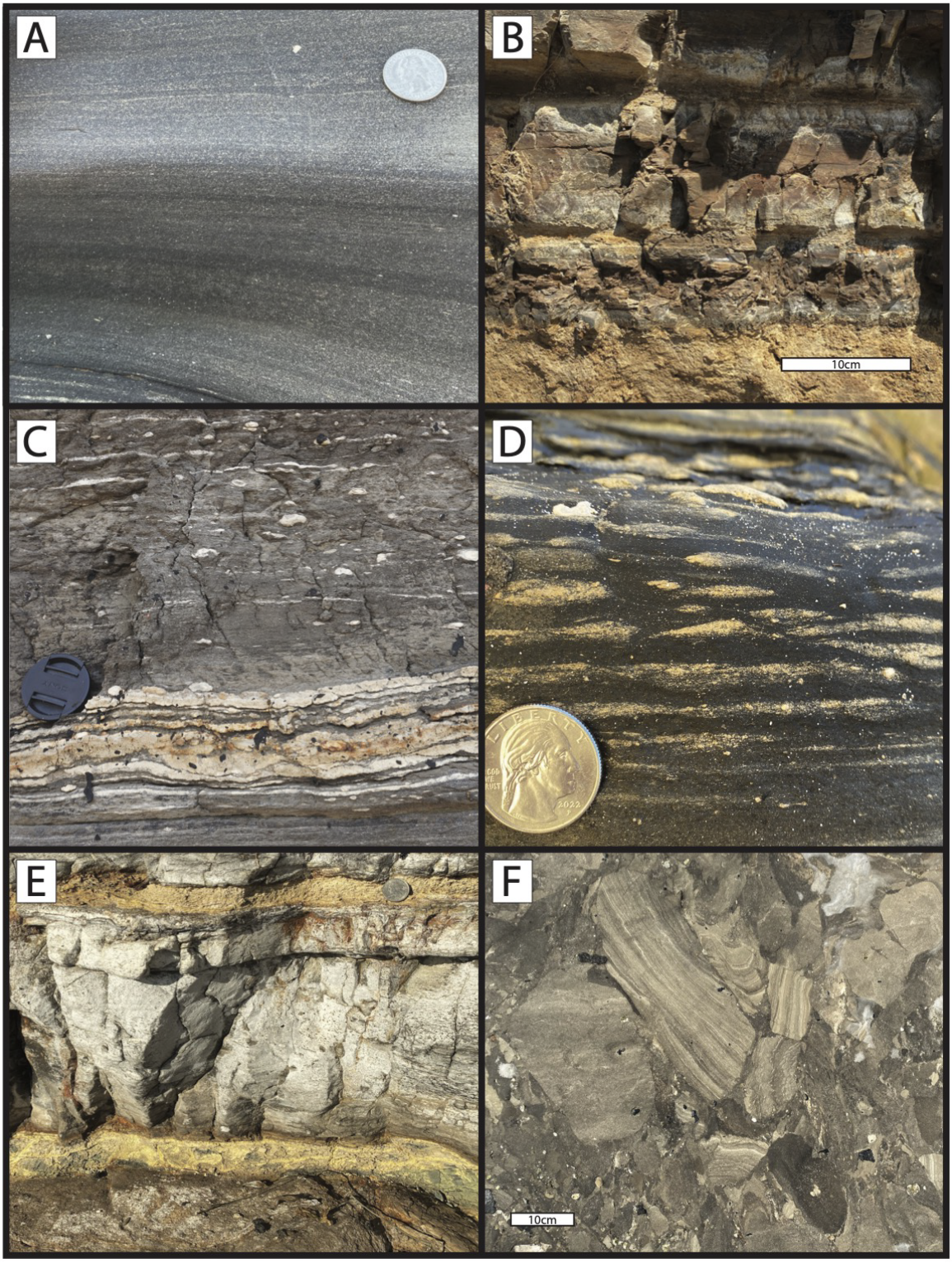
A
B
10cm
C
D
LIBERTY
2022
E
F
10cm

Figure 2: Field photographs of Monterey Formation outcrops from the Santa Barbara Basin. **A)** laminated shales, Tajiguas. Smaller, homogeneously distributed light specks are foraminifera and other calcareous fossil material, while larger white grains are angular granule-sized clasts of remobilized authigenic phosphate or dolomite. **B)** Massive shale (bottom) overlain by laminated porcelanite, middle Naples. **C)** Condensed phosphatic interval, Tajiguas Beach. Continuous white layers are lag deposits of authigenic phosphatic material cemented by additional phosphatic material. Note dispersed authigenic phosphate nodules in relatively expanded shale above the condensed horizons. **D)** reworked angular phosphatic grains in cross bedded shale matrix, Naples. High concentrations of phosphatic grains typically host secondary phosphatic cements. **E)** Bentonites in outcrop at Tajiguas, weathering yellow-to-ochre and separated by dark calcareous shale with a characteristic light gray weathering rind. Upper ash is EAGC2014, which sits at 3.0m in the composite Tajiguas section (Fig.1). **F)** Detail of the block breccia horizon, Naples. Note variable folding of reworked shale clasts, indicating variable lithification of the source shales prior to remobilization.

authigenic phosphatic and dolomitic nodules (Fig. 2C), reworked deposits of authigenic material (Fig. 2D), concentrated phosphorite beds (Fig. 2C), and rare lenticular dolomite (John et al., 2002; Föllmi et al., 2005; Isaacs et al., 2001; Bohacs and Swalbach, 1994). The uppermost Siliceous Facies is dominated by largely-featureless porcelanite beds, interrupted by subsidiary shale and marl horizons (Isaacs et al., 2001; Laurent et al., 2015).

The relative abundance of the biogenous, terrigenous, and authigenic components of the Monterey Formation can vary on centimeter scales within individual vertical sections (John et al., 2002; Föllmi et al., 2005) and on decimeter to kilometer scales along strike, following the compositional and facies variability described above. Bulk sedimentation rates broadly represent a combination of terrigenous and biogenous sediment fluxes to the depozone, with changes in the relative magnitude of these fluxes (as well as post-depositional authigenesis) resulting in the lithological variability observed throughout all three facies. Although the Miocene SBB was relatively distal from the continental margin, outer borderland paleotopographic highs (Hornafius, 1991; Marsaglia et al., 2006) may have provided local sediment sources, potentially augmented by fine current-borne suspended

terrigenous material from the continental margin (as observed in the modern Tanner Basin; Gorsline et al., 1968). Most shales within the Miocene SBB contain between ~20-50% terrigenous detrital material (Föllmi et al., 2005; Laurent et al., 2015). However, abundant Type II kerogen suggests a primarily marine origin for organic carbon in the Monterey Formation (Laurent et al., 2015). The occurrence of dominantly biogenous rocks, such as porcelanites and cherts, has been previously attributed to either exceptional productivity (Barron, 1986; Pisciotto and Garrison, 1981), or to punctuated episodes of high biogenic flux during periods of relatively minimal terrigenous input, resulting in less dilution of the biogenous material (Isaacs et al., 1984). Reworking and remobilization of these components must also be considered, as the removal of fine-grained material by winnowing currents and slumping/mass wasting events played a major role in concentrating coarser authigenic material, as evidenced by reworked, clast-supported beds of nodular phosphate within the Phosphatic Facies (Fig. 2C; John et al., 2002; Föllmi et al., 2005; Laurent et al., 2015).

In the SBB, all three facies are intercalated with volcanic ash beds, most of which have been altered to bentonite clay (Fig. 2E), that range from <1 cm to >1 m thick. Bentonites outcrop as recessive ochre, maroon, green, or blue-gray lamina within the surrounding strata. Some ashes in the SBB have been mineralogically or geochemically correlated within the SBB (Hornafius, 1994) and with potential eruptive sources (Knott et al., 2022), but few ash beds from the SBB have been dated with U-Pb geochronology (Fenton, 2018).

4.3. Methods

4.3.1. Field observations and sample collection

Between 2018 and 2022, stratigraphic sections were measured at multiple Monterey Formation outcrop localities on the northern edge of the Santa Barbara Channel. While all localities have been studied by previous workers, we measured our own sections to develop a consistent stratigraphic height framework across all localities, and to have reference points which we could use to compare our datasets to earlier measured sections. Within each section, bentonite samples were collected for U-Pb geochronology, with ~0.5kg of sample collected from each horizon. The locations and stratigraphic heights of all collected samples are compiled in Table A1, Appendix 3.

At the El Capitan section, fist-sized shale samples were collected for TOC and XRF analysis at ~1m intervals in the lower 100m of the section, and ~30cm intervals in the upper portion of the section. Sampling targeted fresh surfaces with minimal weathering rind (which are abundant due to active cliff retreat), and without visual evidence of hydrocarbon migration. TOC data from El Capitan is compiled in Table A4, Appendix 3, while XRF data are tabulated in Table A5, Appendix 3.

4.3.2. Geochronology sample preparation

Mineral Separation: Bentonite samples were combined with water and disaggregated with ~30s of pulsed blending in a standard kitchen blender. To remove mineral grains from the clay matrix and remove fine sediment, the resulting slurry was then poured into sonication/agitation equipment, following the methods of Hoke et al. (2014). 30 second pulses of sonication and constant circulation with magnetic stirrers were continued with

constant water flow through a series of two beakers, until the water in both beakers ran completely clear. The remaining sediment that accumulated on the bottom of both beakers was panned, and a heavy mineral fraction separated and placed in a large petri dish. We found that lightly scoring the bottom surface of the petri dish (effectively creating shallow riffles) and swirling/running the heavy mineral separate over the scored zone resulted in the concentration of zircon in and around the scored markings. Using these methods, we were able to recover ~100s of zircon crystals from most ~.5kg bentonite samples.

Picking, annealing, mounting, and imaging: Zircon crystals were picked (typically 150-200 in samples with abundant zircon) from the mineral separate of each sample with tweezers, transferred to crucibles, and annealed at 900ºC for 48 hours in a muffle furnace. Annealed zircon were then mounted in epoxy and polished. Polished mounts were subsequently imaged with cathodoluminescence (CL) using a Centaurus CL detector mounted on an FEI Quanta 400f field emission SEM at the University of California Santa Barbara (UCSB).

4.3.3. LA-ICPMS analyses

Laser ablation inductively coupled plasma mass spectrometry (LA-ICPMS) U-Pb geochronological analyses on zircon were completed at UC Santa Barbara using a Cetac/Photon Machines Analyte Excite 193 nm excimer laser attached to a Nu Plasma 3D multicollector ICPMS, following the methods of Kylander-Clark et al. (2013). Each zircon was ablated with a 20µm laser spot. The zircon 91500 (Wiedenbeck et al., 1995) was used for age calibration. Secondary zircon reference materials included 9435, AUSZ, Mudtank, GJ1 (Jackson et al., 2004), and Plesovice (Sláma et al., 2008). *Iolite* (Paton et al., 2010) was

used to correct for U-Pb mass bias and drift following the methods of Kylander-Clark et al. (2013) and Horstwood et al. (2016).

All LA-ICPMS data are compiled in Table SM2. $^{238}U/^{206}Pb$ ratios were corrected for ^{230}Th disequilibrium using measured zircon Th/U and an assumed Th/U(magma) of 3.5. Dates for each grain were calculated by importing reduced $^{238}U/^{206}Pb$ and $^{207}Pb/^{206}Pb$ ratios into *IsoplotR* (Vermeesch 2018). For each sample, a group of zircons with young (Miocene) $^{206}Pb/^{238}U$ dates were identified. This group of analyses was used to calculate a weighted-mean age: the oldest analyses were iteratively removed until a group of zircon ages conforming to statistical standards for a single population (Wendt and Carl, 1991) was acquired. The data used to calculate these weighted mean ages are in bold text and highlighted in grey in Table A2, Appendix 3, while older analyses that did not go into the weighted mean (likely representing either magmatic inheritance or detritus in the bentonite bed) are italicized. A blanket systematic uncertainty of 2% (accounting for all uncertainty criteria outlined in Horstwood et al., 2016) was then applied to the calculated weighted-mean ages. The weighted-mean age, and uncertainty, is utilized in our chronostratigraphic framework as the eruptive/depositional age and uncertainty for the measured bentonite horizon. Samples with a single young grain are treated as detrital, with the $^{206}Pb/^{238}U$ age of the youngest grain serving as the maximum depositional age (MDA) for the sampled horizon.

4.3.4. CA-ID-TIMS analyses

Chemical Abrasion: Individual grains from the population of zircons that make up the LA-ICPMS weighted mean age for each sample were analyzed with single zircon U-Pb

chemical abrasion isotope dilution thermal ionization mass spectrometry (CA-ID-TIMS) at Princeton University, following standard chemical abrasion methods modified from Mattinson (2005). Previously annealed single zircons were plucked from epoxy mounts, transferred to Teflon beakers, and rinsed with 3N HNO_3. Grains were removed from the acid rinse and loaded into 200µl Savillex microcapsules with ca. 90 µl 29M HF. Microcapsules were assembled in a Parr bomb and zircons were leached at 180ºC for 12 hours to remove domains in the crystal lattice that may have experienced lead loss.

Dissolution, spiking, and column chemistry: Following leaching, zircon grains were moved to Teflon beakers, and repeatedly rinsed in 3N HNO_3 and 6N HCl. The crystals were then transferred back to microcapsules, spiked with the EARTHTIME ^{205}Pb-^{233}U-^{235}U tracer (Condon et al., 2015; McLean et al., 2015) and placed back into a Parr bomb for dissolution in ca. 90 µl 29M HF for 60 h at 210ºC. The resulting solutions were then dried down, converted to chlorides in the Parr bomb overnight, and dried down once more on the hot plate. The samples were then redissolved in 3N HCl and placed into 50 µl microcolumns filled with AG-1 X8 resin, where U-Pb and trace element solutions were separated by anion exchange following methods modified from Krogh (1973). The U-Pb solution was dried down in a Teflon beaker on the hot plate with a microdrop of 0.015M H_3PO_4. Each aliquot was then redissolved in a silica gel emitter (Gerstenberger and Haase, 1997), and loaded with an ultrafine pipette onto a single outgassed zoned-refined rhenium filament.

Isotopic measurements: Lead and U isotopic measurements were performed with one of two Isotopx Phoenix thermal ionization mass spectrometers (TIMS) at Princeton University. Pb isotopes were measured using peak-hopping mode on a Daly photomultiplier ion-counter, while U isotopes were measured as UO_2 in static mode with Faraday cups

connected to traditional 10^{12} Ω amplifiers, or to ATONA amplifiers (Szymanowski and Schoene, 2020). Instrumental mass fractionation for Pb was corrected with a factor (0.14 or 0.18 %/amu) derived from a long-term compilation of in-run $^{202}Pb/^{205}Pb$ values of double-Pb-spiked Daly analyses on each instrument. The dead time of the Daly systems was kept constant throughout the period of the study but was monitored with analyses of NIST SRM 982 Pb isotope standard over a range of intensities. U runs were corrected for fractionation using the known $^{233}U/^{235}U$ of the spike and assuming a sample $^{238}U/^{235}U$ of 137.818 ± 0.045 (2σ; Hiess et al., 2012). An $^{18}O/^{16}O$ value of 0.00205 ± 2 (1σ) was used to correct for interferences in UO_2 analyses.

Data reduction: Data was compiled and reduced in *Tripoli* and *Redux* (Bowring et al., 2011; McLean et al., 2011). Initial ^{230}Th disequilibrium in the $^{206}Pb/^{238}U$ system was corrected for each grain by estimating $(Th/U)_{magma}$ using a fixed $(Th/U)_{zircon\text{-}magma}$ partition coefficient ratio of 0.19±0.06 (1s) based on a compilation of natural zircon–melt pairs, and uncertainties for the $(Th/U)_{magma}$ were propagated into final date uncertainty for each grain. Isotopic ratios, compositional data, and ages for all grains is available in Table A3, Appendix 3. Analytical uncertainty (±X) at the 95% confidence level for the U-Pb date of each grain was utilized for further weighted-mean age calculations and Bayesian eruptive age models. Weighted-mean ages were calculated in *Redux,* and are summarized in Table A1, Appendix 3. Bayesian eruptive age estimates were modeled using the package *Chron.jl* (Keller et al., 2018). While the ages reported in the manuscript utilize a uniform prior crystallization distribution, model ages calculated for several different prior crystallization distributions are tabulated in Table A1, Appendix 3.

4.3.5. Total Organic Carbon analyses

Shale samples were drilled with a 3/8" tungsten carbide bit on a drill press to generate ~15mL of unconsolidated shale powder. At Amherst College, aliquots of the powder were weighed, decarbonated with 3 N hydrochloric acid, rinsed with deionized water, dried in a 60°C oven, and reweighed. Dried insoluble residues were rehomogenized with mortar and pestle. Insoluble residue powders were loaded into tin capsules and combusted in a Costech ECS 4010 elemental analyzer interfaced with a Sercon 20-22 gas source stable isotope ratio mass spectrometer. Carbon content of samples was measured using beam area calibrated by a pure acetanilide standard. Acetanilide check standards were run after every fifth sample. TOC was calculated as the product of the percent insoluble residue of the whole rock and the percent carbon of the insoluble residue. Uncertainty in TOC measurement is +/- 1.8% (1 s.d.) based on replicate analyses of insoluble residues and replicate extractions of whole rock powders. Data is compiled in Table A4, Appendix 3.

TOC data from prior publications were extracted from published figures (John et al., 2002; Föllmi et al., 2005; Isaacs et al., 2001; Bohacs and Swalbach, 1994), and integrated into our measured sections by matching tie points from the measured sections in those publications to our stratigraphic framework. For each measured section, an exponential moving average (alpha of .05) was calculated with the compiled TOC data in order to characterize trends in TOC abundance, and appended with a 1σ analytical uncertainty envelope.

4.3.6 X-Ray Fluorescence analyses

Sample preparation: Shale powders were generated with a 3/8" tungsten carbide bit, following the same procedure detailed above for TOC analyses. 6-10mL aliquots of unconsolidated powder were placed into cylindrical Teflon pucks (32mm OD), the lower ends of which were covered with layer of transparent polypropylene thin film. The shale powder was firmly compacted against the thin film, using the capped top of a 20mL Falcon sample tube as a tamper. In addition to homogenizing the shale sample, powdering and compacting each sample minimized potential analytical variability due to matrix effects and/or crystal/grain orientation. Thicknesses of the resultant compacted shale powder always exceeded 2.7mm, or the maximum penetration depth of x-rays on a compacted substrate from the ThermoNiton XL5 Plus portable handheld XRF (pXRF) unit used to analyze the samples.

XRF measurements: Each compacted puck was placed into a shielded box attached to the emitting end of the pXRF unit, which was run in a benchtop configuration for all samples. Each measurement involved 30 seconds of analysis with the pXRF's Main filter, and subsequent 60 second analysis windows using the unit's integral Low, High, and Light filters for a total of ~210 seconds per sample. During each analysis session, a variety of shale standards, including USGS standards MAG-1, SCO-1, and SDC-1 (Gladney, 1980) and SDAR-L2 and SDAR-M2 (Wilson et al., 2021), were run multiple times at the beginning of each session (typically for ~20 minutes to allow the instrument's internal temperature to stabilize). Standards were subsequently interspersed amongst every ~8 unknowns.

Data reduction: Elemental abundances for each standard measurement were compiled, and compared to the published elemental abundance data for that standard (generated either by ICP-MS or via XRF). For each element, the relationships between published and measured abundances for each standard were plotted, and a linear model fit was applied. The standard deviation of each group of analyses for each element of each standard was calculated, and then averaged across all standards for each element, yielding an approximation of analytical uncertainty that more appropriately encapsulates external variables than the modeled analytical uncertainty provided by the pXRF's integral software. The standard deviation of the range of standard measurements for each element was doubled, and then added in quadrature to the elemental abundance uncertainties for each element of each unknown analysis. For elements with a model linear fit with a Pearson correlation coefficient of greater than .7, a linear calibration factor (the equivalent of correcting the model fit line to the 1:1 line) was applied to that elemental abundance in all measured unknowns. For elements with a model fit correlation coefficient of less than .7, no calibration factor was applied. Pearson correlation coefficients for linear fits for Al, Ca, Si, and Ti were calculated to be .53, .90, .96, and .97 respectively. For Al, multiple measurements from standards MAG-1, SDAR-M2, SDAR-L2, SCO-1, and SDC-1 overlapped, within uncertainty, the 1:1 line for Al. As such, no correction, other than additional uncertainty, was applied to measured Al abundances on unknowns. Calibrated elemental abundances of Al, Ca, Si, and Ti in El Capitan shales are summarized in Table A5, Appendix 3.

4.4. Results

4.4.1. Geochronology and age model

LA-ICPMS U-Pb dating resolved statistically-significant young magmatic zircon populations from 31 bentonite samples from the Monterey Formation. All weighted-mean ages calculated from these populations are stratigraphically consistent (younging upward), within 2σ uncertainty (Figs. 1, 3). 14 samples also analyzed with CA-ID-TIMS yielded modeled eruptive ages that are stratigraphically consistent and indistinguishable, within uncertainty, from LA-ICPMS weighted mean ages calculated for the same sample (Fig. 4A). The equivalence of LA-ICPMS and CA-ID-TIMS ages across all dually-measured samples suggests that despite differences in precision (Fig. 3), ages developed using both analytical techniques may be directly compared. Ages utilized in the chronostratigraphic framework are summarized in Fig.1.

Discrete bentonite beds without visible bedding structures were sampled for geochronology. Although these horizons are interpreted to have formed primarily as the result of volcanic airfall, some horizons were likely reworked during and soon after deposition, as corroborated by older detrital tails on all LA-ICPMS age spectra. Older grains are expected in airfall tuffs falling into an active siliciclastic depozone, either as inherited grains incorporated before or during eruption, or as detrital grains. For the LA-ICPMS data, the youngest coherent population of zircons derived from each bentonite is interpreted as the eruptive age of the ash horizon. However, CA-ID-TIMS analyses revealed variability within the uncertainty envelope of weighted mean-LA-ICPMS ages, including samples where the youngest dated grain is statistically distinct from the rest of the population. For these

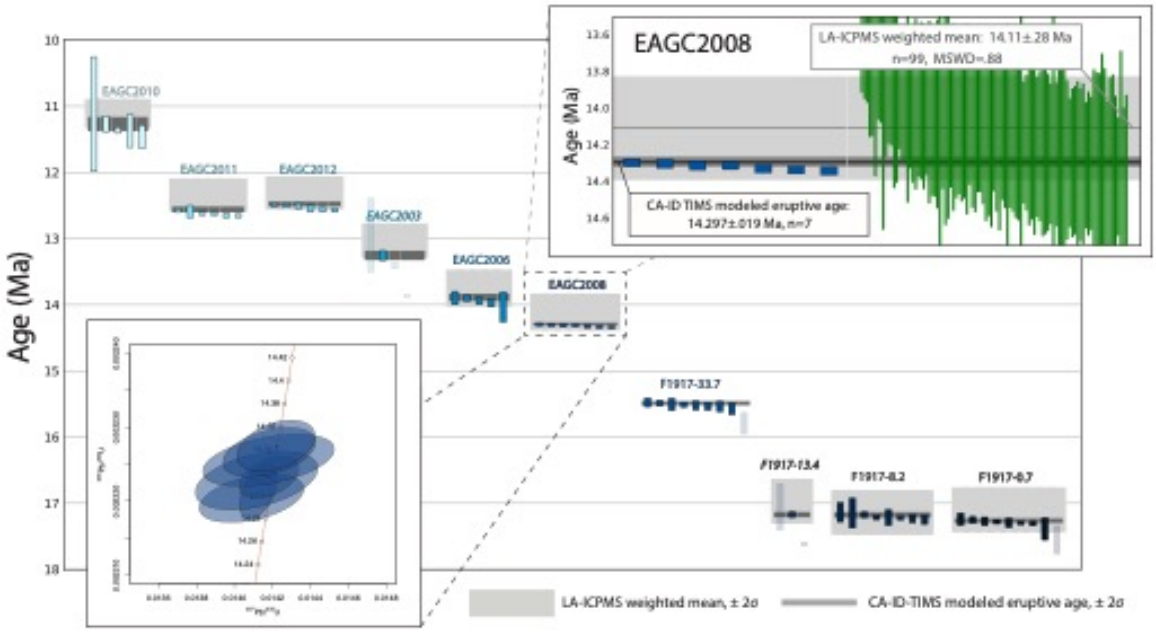

Figure 3: Th-corrected ^{206}Pb ^{-238}U dates, with 2σ uncertainty, from all zircons analyzed by CA-ID-TIMS from El Capitan, grouped by sample and plotted vs. age. Modeled TIMS eruptive ages (dark gray bars) and LA-ICPMS weighted-mean ages from each sample (light gray bars) are shown behind each group of individual analyses. Italicized labels indicate a sample for which TIMS analyses yielded a single young grain with good analytical precision, resulting in the characterization of the resultant TIMS age for that sample as a maximum depositional age for the sampled bentonite horizon. Left inset shows a Wetherill concordia plot of all CA-ID-TIMS analyses from sample EAGC2008, while the inset panel at right details the age and uncertainty of all individual analyses (CA-ID TIMS in blue, LA-ICPMS in green) used to calculate the age of sample EAGC2008. A summary of all geochronological data, including concordia diagrams and weighted-mean plots for all measured samples, can be found in the Supplementary Materials.

samples, the age of the youngest grain precisely analyzed with CA-ID-TIMS is treated as a maximum depositional age (MDA, Fig. 1).

Ages from El Capitan and Naples were input into a stratigraphic Markov-Chain Monte Carlo (MCMC) model in the Chron.jl package (Schoene et al., 2019). Four ash ages from El Capitan were correlated with specific ash horizons at Naples Beach based on previously described tephrochronological (Hornafius, 1994), biostratigraphic (John et al., 2002; Föllmi et al., 2005), and lithostratigraphic similarities between sections. These ages

were incorporated into the Naples age model with additional (±1.5m) vertical uncertainty to account for potential miscorrelation. For horizons with multiple age constraints (e.g. a TIMS modeled eruptive age and a LA-ICPMS weighted mean age), the age with the least analytical uncertainty was chosen as the model constraint. For the three horizons at El Capitan where a weighted-mean or modeled-eruptive age was not calculated (due to a distinct young grain in a LA-ICPMS sample, or a single young grain in a group of TIMS analyses), the resultant MDA was utilized in the age model. All ages utilized in the Chron.jl framework are in bold text in Table SM1, and depicted in Fig. 1. The model was run at a vertical resolution of 0.2m, with 30,000 steps (10,000 runs discarded for burn-in), and 95% credible intervals were calculated (Figs. 4B, 5A).

Sedimentation rates and 68% credible intervals (Fig. 4D, 5C) were calculated in the Chron.jl age-height model framework using an overlapping binned approach. Here, we utilize a shifting bin size of (age)/10, with a 10-bin overlap in order to minimize spurious spikes or rapid transitions in sedimentation rate observed with narrower bins. Regardless of the binning method, the trends and mean modeled sedimentation rates are comparable, and consistently approach values expected for linear sedimentation rates between age constraints.

4.4.2. Organic carbon mass accumulation rate

TOC measurements on shales from El Capitan Beach range from 1–24 wt% TOC (Fig. 4C). The trends of this new dataset largely agree with earlier measurements from El Capitan by John et al. (2002), as well as with TOC datasets from Naples Beach (Fig. 5B; Föllmi et al., 2005; Isaacs et al., 2001, Bohacs and Swalbach, 1994). TOC data from prior

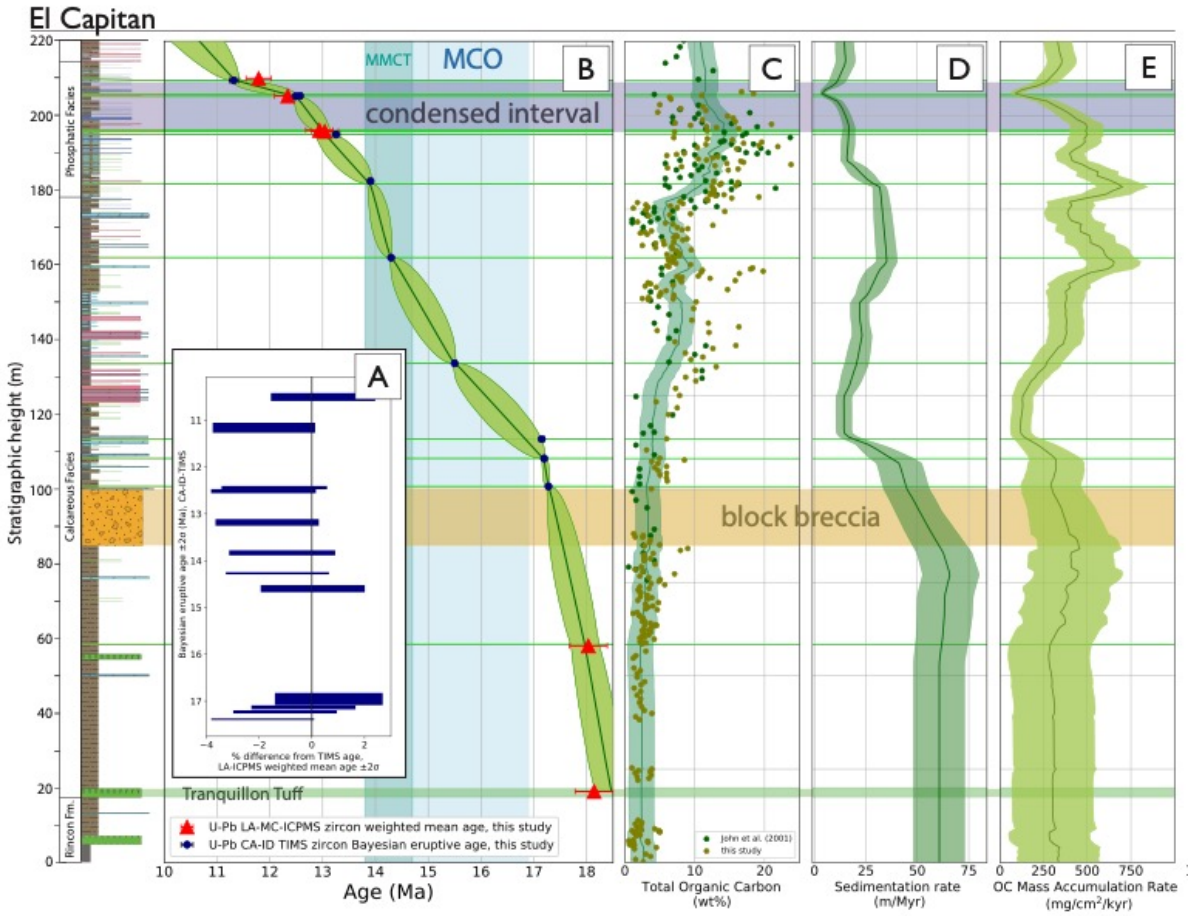

Figure 4: Age model and modeled organic carbon mass accumulation rate (OCMAR) for El Capitan. **A)** CA-ID-TIMS ages vs. LA-ICPMS ages derived from the same bentonite sample, illustrating that both methods yield ages that may be directly compared. **B)** age vs. height model for El Capitan, showing the 95% credible interval envelope of modeled age-height relationships. Vertical bars illustrate the temporal extent of the Miocene Climatic Optimum (MCO) and mid-Miocene Climatic Transition (MMCT). **C)** Compiled total organic carbon (TOC) data (from this study and from John et al., 2002) from El Capitan, with a moving average through all data depicted as a solid line with 1σ analytical uncertainty envelope. **D)** Modeled sedimentation rate for El Capitan, with 68% credible interval envelope. **E)** Modeled OCMAR curve and 68% credible interval envelope for El Capitan, plotted vs stratigraphic height.

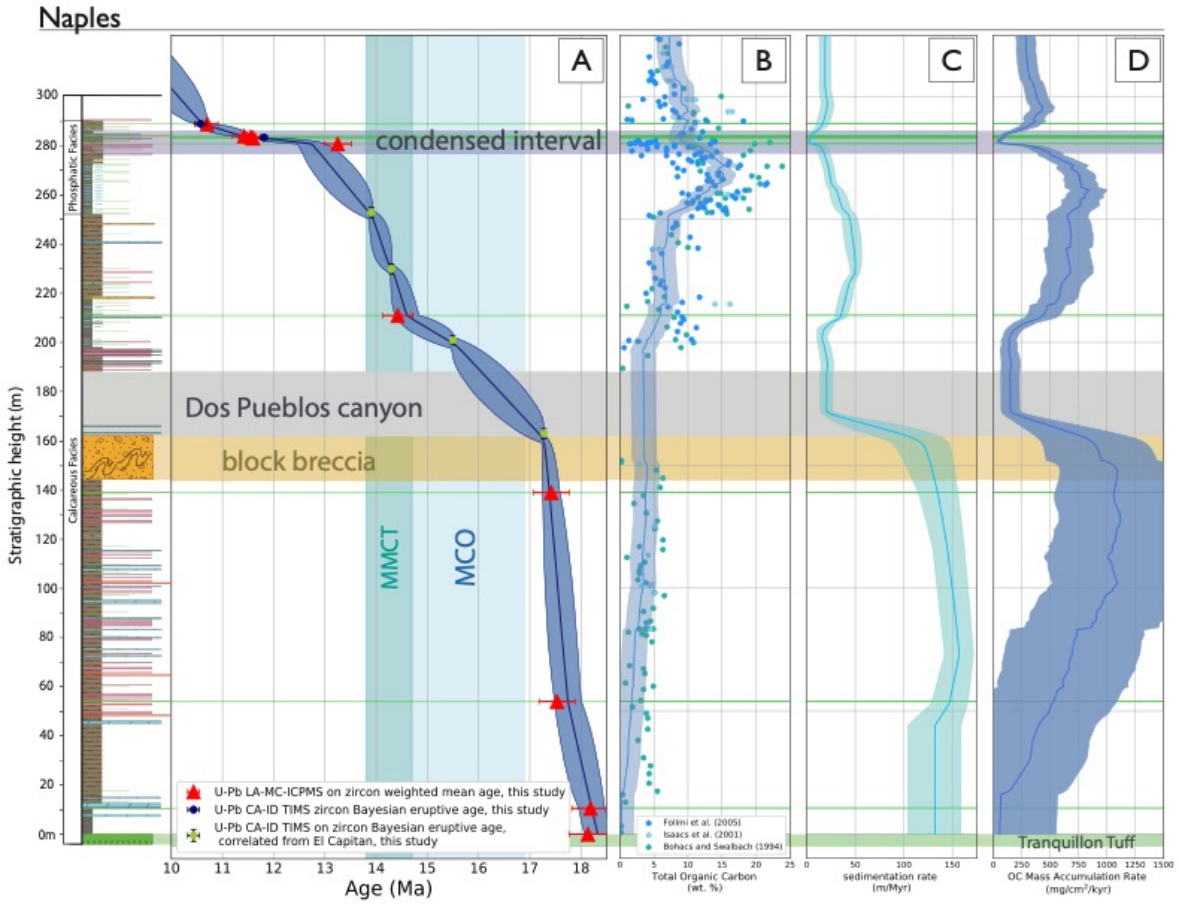

Figure 5: Age model and modeled organic carbon mass accumulation rate (OCMAR) for Naples. **A)** age vs. height model for Naples, showing the 95% credible interval envelope of modeled age-height relationships. Note the usage of four ages correlated from the El Capitan section. The El Capitan ash ages were correlated to specific ash horizons at Naples Beach based on extant tephrochronological (Hornafius, 1994), biostratigraphic (John et al., 2002; Föllmi et al., 2005), and lithostratigraphic similarities between sections. However, they were incorporated into the age model with additional (±1.5m) vertical uncertainty to account for potential miscorrelation. The temporal extents of the MCO and MMCT are represented by vertical bars. **B)** TOC data from Naples compiled from Föllmi et al. (2005), Isaacs et al. (2001), and Bohacs and Swalbach (1994), with a moving average through the data depicted as a solid line with 1σ analytical uncertainty envelope. **C)** Modeled sedimentation rate for Naples with 68% credible interval envelope. **D)** Modeled OCMAR curve and 68% credible interval envelope for Naples, plotted vs. stratigraphic height.

publications was integrated into our measured sections by matching tie points from the measured sections into our stratigraphic framework. For each measured section, an exponential moving average was calculated with the compiled TOC data in order to characterize trends in TOC abundance, and appended with a 1σ analytical uncertainty envelope (Figs. 3C, 4B).

Organic carbon mass accumulation rate (OCMAR, mg/cm^2/kyr) is calculated using the following equation:

$$\boxed{\mathrm{OCMAR} = S * Ctot * \rho} \quad \text{(Eq. 1)}$$

where S (m/Myr) is modeled sedimentation rate, C_{tot} (wt%) is organic carbon (in this case an exponential moving average of TOC measurements taken through the section), and ρ (g/cm^3) is an assumed shale density of 2.1g/cm^3. 1σ uncertainty is propagated using the following equation:

$$\frac{\sigma\mathrm{OCMAR}}{\mathrm{OCMAR}} = \sqrt{\left(\frac{\sigma S}{S}\right)^2 + \left(\frac{\sigma Ctot}{Ctot}\right)^2 + \left(\frac{\sigma\rho}{\rho}\right)^2} \quad \text{(Eq.2)}$$

where σS is 1σ uncertainty in sedimentation rate generated by Chron.jl; $\sigma Ctot$ is 1.8%, the 1σ analytical uncertainty associated with our TOC measurements, and $\sigma\rho$ is 0.2 g/cm^3, or the estimated 1σ uncertainty associated with potential variability in shale density through the section. OCMARs for both El Capitan and Naples are plotted both against stratigraphic height (Figs. 4E, 5D) and time (Fig. 6A).

Usage of post-compaction average shale density accounts for compaction-related change in both density and apparent sedimentation rate in OCMAR estimates. This is

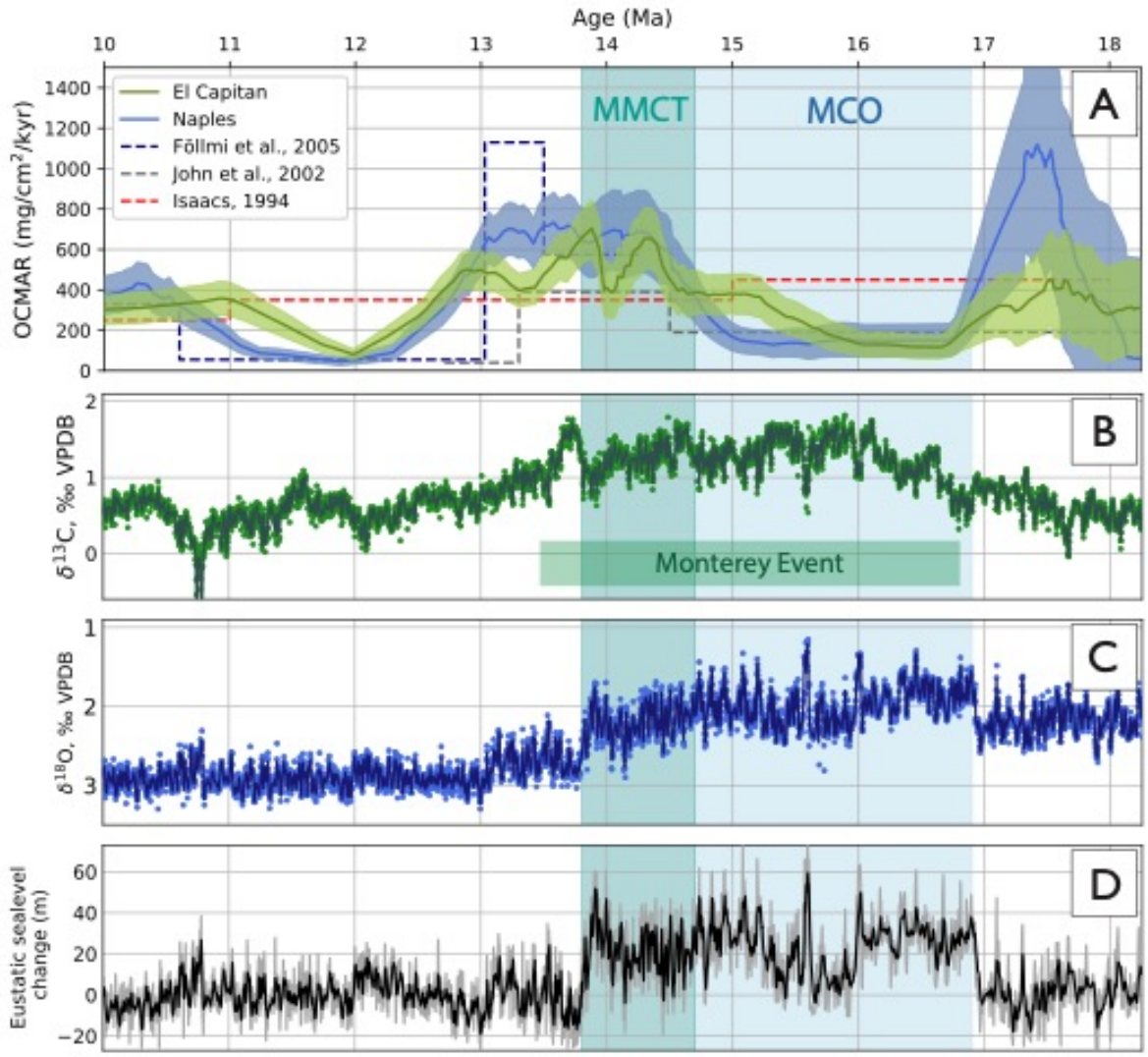

Figure 6: A) Organic carbon mass accumulation rates (OCMARs) and 68% credible interval envelopes for El Capitan and Naples, plotted vs. time, with blue and teal intervals demarcating the temporal extent of the Miocene Climatic Optimum (MCO) and mid-Miocene Climatic Transition (MMCT) (Steinthorsdottir et al., 2020). Note relatively low OCMAR during the MCO. Previous estimates for OCMAR in the Santa Barbara Basin are shown as dashed lines. **B)** Compiled $\delta^{13}C$ from benthic foraminiferal tests plotted vs. time (ODP cores 1337-1338, Westerhold et al., 2020), with the temporal extent of the Monterey Event positive $\delta^{13}C$ isotope shift (Vincent and Berger, 1985) depicted as a green box. **C)** Compiled $\delta^{18}O$ from benthic foraminifera plotted vs time (Westerhold et al., 2020). **D)** Modeled global eustatic sea level change, in meters (Miller, 2020).

particularly important in porcelanite-dominated intervals (e.g. ~120-140 m at El Capitan and ~190-200 m at Naples): the thickness of porcelanites derived from diatomaceous biogenous material can be reduced by a factor of 7 from their depositional thickness (given an initial

porosity of 90% at deposition and a post-burial porosity of 10%; Isaacs, 1984). However, a density of 2.5g/cm^3, the upper 2σ bound of density estimates utilized in our OCMAR calculation, is roughly equivalent to a pure diatomaceous porcelanite at 6.5% porosity, which is significantly less than porosities for measured porcelanites in the SBB (Isaacs, 1983), and mitigates potential compaction-related underestimates of OC accumulation rate through this interval. Overall, our mean assumed density is higher than average shale density through the section, resulting in a conservative overestimate of MAR through each section, and bolstering the argument for relatively low rates of OC burial in the Miocene SBB. This overestimate is further enhanced in silica-dominated intervals by the preferential sampling of shale: silica-rich porcelanites were not targeted for TOC sampling, and as a result the calculated average TOC content through porcelanite-dominated intervals is likely an overestimate.

4.4.3. Shale elemental abundances

The Al/Si ratio, Ti content, Ca content, and Si/Ti ratio of El Capitan shales are plotted against TOC content in Fig. 7. All XRF-derived elemental abundances of Al, Ca, Si, and Ti are compiled in Table S4. Al/Si ratios (Fig. 7B), a proxy for clay abundance and mineral surface area (Galy et al., 2008; Hoang et al., 2010), show a positive relationship with TOC content, as does Ti content (Fig. 7C), which is a redox-insensitive proxy for the abundance of terrigenous material in shale (Calvert and Pedersen, 2007). Meanwhile, both Ca abundance and the Si/Ti ratio have a broadly negative relationship with TOC (Fig. 7D, E). Ca serves as a proxy for $CaCO_3$ abundance (Rothwell and Croudace, 2015), which, in

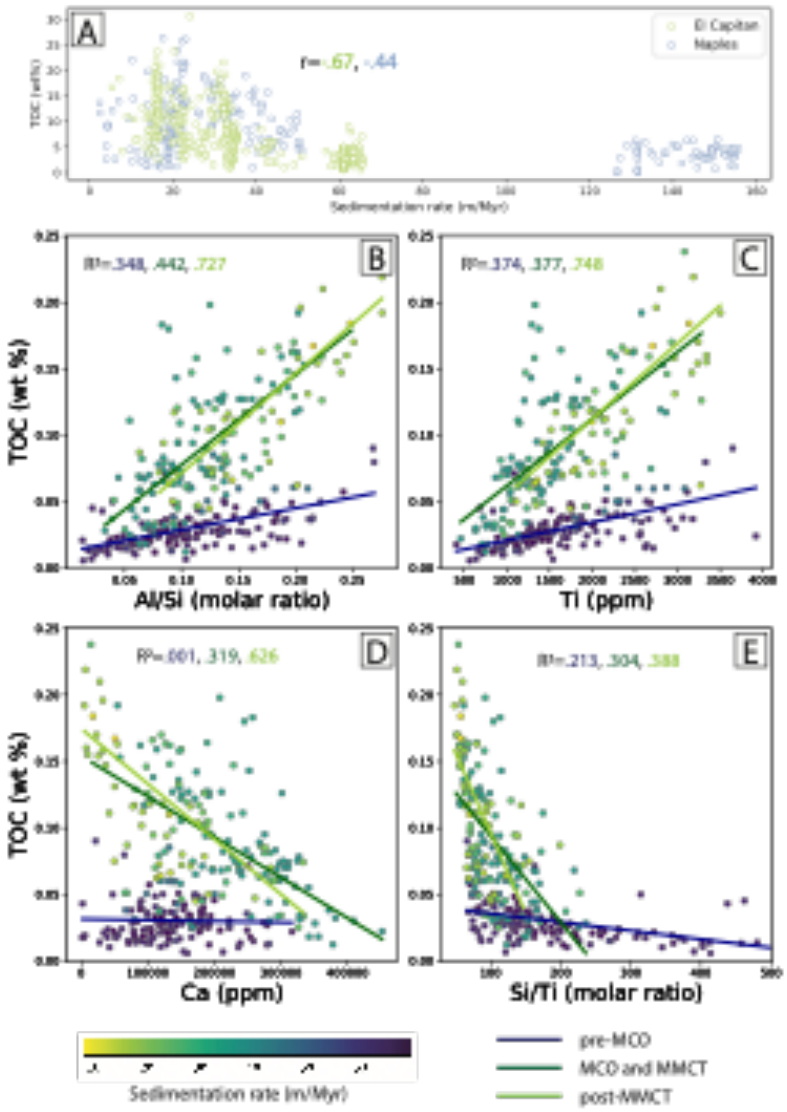

Figure 7: A) Relationships between modeled sedimentation rate and TOC content at El Capitan and Naples, showing an inverse correlation at both localities (r values of -0.68 and -0.44, respectively). Comparison of TOC and elemental proxy data from El Capitan shales, including **B)** Al/Si ratio, a proxy for mineral surface area and clay abundance (Kennedy et al., 2002) plotted vs TOC. Higher Al/Si ratios generally indicate smaller grain size, more abundant clay, and a higher total mineral surface area. **C)** Ti abundance, a proxy for terrigenous flux variation (Rothwell and Croudace, 2015) with Ti increasing with increased terrigenous contributions, plotted vs TOC. **D)** Ca abundance and **E)** Si/Ti ratios, both proxies for biogenous vs terrigenous sediment flux changes (Rothwell and Croudace, 2015), plotted vs TOC. All data is shaded by modeled sedimentation rate at the sample height in the El Capitan section. Linear fits of the data for the pre-MCO, MCO+MMCT, and post-MMCT intervals are plotted to illustrate the importance of sedimentation rate in determining TOC abundance across different depositional regimes.

Monterey Formation shales, is strongly influenced by the occurrence biogenous material (Föllmi et al., 2005). Si/Ti ratios indicate the relative prevalence of biogenous versus terrigenous silica sources, with higher ratios indicating a larger biogenous component (e.g. Aghinotri et al., 2008).

4.5. Discussion

4.5.1. Drivers of organic carbon accumulation in the Monterey Formation

High-TOC intervals within Monterey Formation sections of the SBB have been interpreted to represent enhanced organic carbon (OC) burial associated with upwelling-related increases in primary productivity (Flower and Kennett, 1993). This interpretation predicts synchronous increases in TOC and biogenous sediment flux that are uncommon in the SBB, as evidenced by inverse relationships between biogenous proxies and TOC at El Capitan (Fig. 7C,D) and elsewhere (Föllmi et al., 2005; Laurent et al., 2015). Rather, TOC content is the result of the collective influence of several driving factors, including: 1) productivity, which delivers an initial flux of OC to the depozone; 2) dilution, which reduces the relative portion of organic carbon in a sediment through the deposition of non-organic material, and 3) preservation, which results in the survival and retention of only a fraction of initially-deposited OC. Although syn- and early-post-depositional preservational processes may have been important in modulating TOC content at El Capitan and Naples, evidence of minimal burial diagenesis at both localities (Isaacs, 1981) suggests that later post-depositional degradation or migration of locally-deposited OC is likely negligible. OCMAR, the flux of OC buried in a sedimentary sequence, represents the combined effects of productivity, dilution, and preservation over time. Our new age model allows us to

quantify changes in OCMAR through Monterey Formation sections, and directly compare the timing of OCMAR variability with the timing of putative regional and global drivers.

The MCO and MMCT are defined by shifts in the $\delta^{18}O$ composition of benthic foraminifera (Steinthorsdottir et al., 2021), which reflect a combination of seawater temperature and ice volume (Chappel and Shackleton, 1986). Peaks in OCMAR in the Monterey Formation occur prior to the onset of the MCO and during and after the MMCT (Fig. 6). These peaks could be interpreted to be consistent with the Monterey Hypothesis, as increased organic burial in Monterey strata is coincident with cooler intervals in the climatic proxy record (Fig. 6), potentially indicative of enhanced positive feedbacks between cooling, thermocline development, upwelling, and primary productivity (Vincent and Berger, 1985). Alternatively, OC burial in the Monterey Formation could be controlled by eustatically- and climatically-induced changes that extend beyond enhanced upwelling and productivity. These changes include shifts in regional hydrology (changing fluxes of nutrients or clay to the basin), basinal redox state (expansion/contraction of oxygen minima, changes in redox gradient depth), or basinal circulation (changing winnowing currents or upwelling), all of which can influence TOC abundance in Monterey Formation sediments.

Similarly, the coincidence between a drop in OCMAR and the onset of the MCO (Fig. 6) suggests a relationship, but the causality can again be interpreted in several ways: 1) warming or other climate-induced environmental changes could have caused a change in the magnitude or locus of upwelling and/or productivity, which could have driven a reduction in biogenous flux in the SBB during the MCO, or 2) sea-level rise could have caused changes in total sediment delivery to the borderland environment, which would manifest as reduced

syn-MCO terrestrial flux to borderland depozones. These scenarios are considered within the context of a depositional model for the Monterey Formation in Section 5.3.

4.5.2 Relationships between sedimentation rate and TOC

Despite differences in the magnitude of both TOC content and sedimentation rate in contemporaneous intervals of the El Capitan (Fig. 4) and Naples (Fig. 5) sections, OCMAR at both localities is comparable in terms of both magnitude and variability (Fig. 6). Sedimentation rate and TOC abundance are inversely correlated at both locations (r-values of -0.67 and -0.44, respectively; Fig. 7A), yielding relatively low OCMARs in high-TOC intervals, and vice-versa, consistent with previous OCMAR estimates (John et al., 2002; Föllmi et al., 2005).

Secular differences in the relationships between TOC and various sediment component flux proxies observed in high- and low-sedimentation rate intervals at El Capitan (Figure 7B-E) suggest that sedimentation rate influences processes that can control TOC abundance. Al/Si ratios, which serve as a proxy for clay abundance (Galy et al, 2008), are positively correlated with TOC, indicating the importance of clay shielding (Kennedy et al., 2002) as a preservation mechanism for TOC in the Miocene SBB. Furthermore, the slope of that positive correlation is dependent on sedimentation rate: lower sedimentation rates result in a much stronger relationship between clay and TOC than higher sedimentation rates, despite similar Al/Si ratios across all modeled sedimentation rates (Fig. 7B). This trend, which is also observed in Ti abundance (Fig. 7C), is consistent with the observed negative correlation between sedimentation rate and TOC abundance. At high sedimentation rates, dilution plays a dominant role in determining TOC abundance through the addition of

material that either does not contain OC, or does not contribute to the preservation of organic material in the depozone. Conversely, at low sedimentation rates, strong relationships between clay proxies and TOC indicate the importance of preservation in determining TOC content. Indeed, the most linear relationship between TOC and clay abundance occurs during the post-MMCT interval at El Capitan (Fig. 7B), which features the lowest sedimentation rates observed in the section.

Relationships between TOC and biogenous flux proxies (Fig. 7D, E) are also dependent on sedimentation rate. Thus, as sedimentation rate affects a variety of factors that control the abundance of TOC, factors that control sedimentation rate were fundamental in determining the TOC content of Miocene Santa Barbara Basin strata. Importantly, in Holocene-to-modern Californian borderland basins, topographic variability and eustatic sea-level modulate sedimentation rates across the margin (Gorsline et al., 1968, Covault and Sharman, 2019).

4.5.3. Depositional model for organic carbon accumulation in the Santa Barbara Basin

With modern analogs in mind, we propose that a combination of local tectonics and eustasy were primary controls on Monterey Formation depositional systems, sedimentation rates, and organic carbon accumulation, with organic carbon deposition responding to, rather than driving, climatic variability. Changes in sea-level exacerbated the depositional effects of changing paleotopography in the tectonically evolving Miocene SBB, resulting in substantial changes in sedimentation rate and TOC abundance through both time and space (Fig. 8).

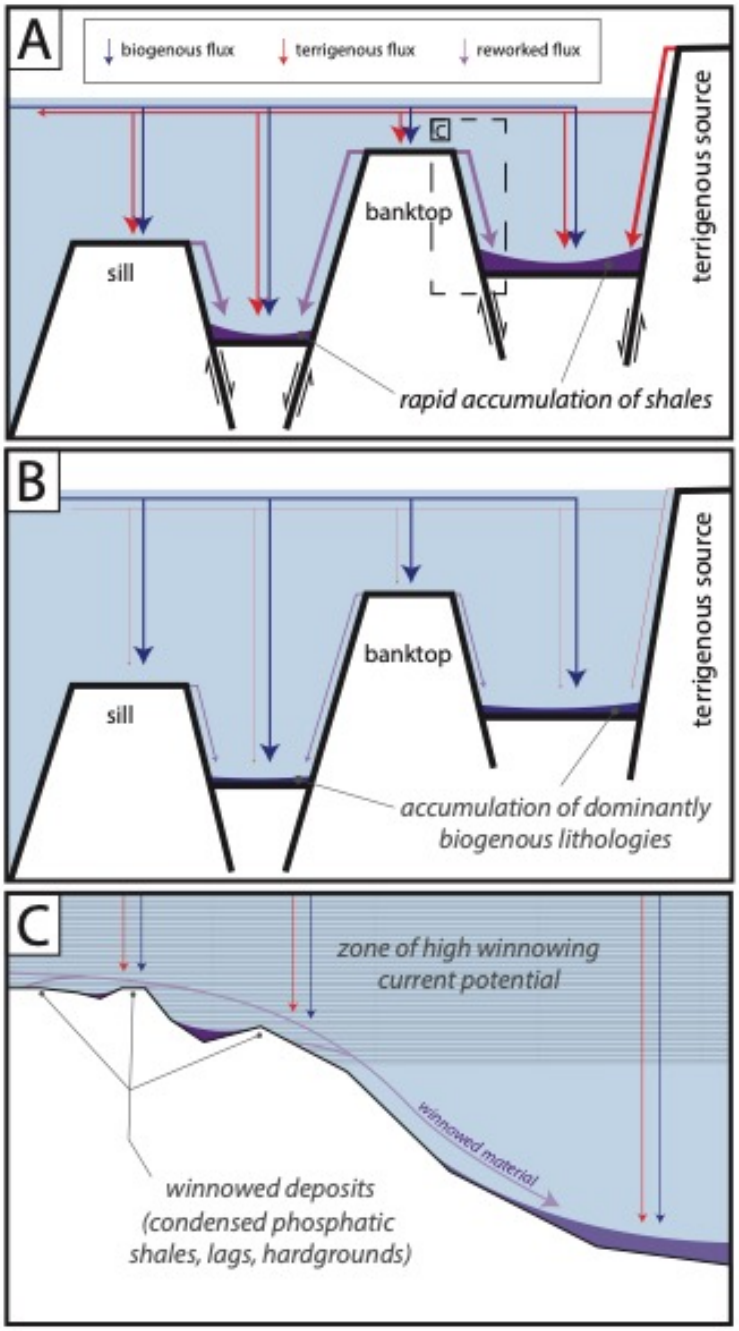

Figure 8: Cartoon depiction of sedimentation patterns across the SBB, as controlled by tectonic and eustatic changes. Arrow sizes are proportional to flux magnitude. **A)** Low sea level and active tectonism result in the deposition of both primary and remobilized sediment into newly created accommodation space. High sedimentation rates, dominated by remobilized sediment flux, result in thick shales with relatively low TOC content. Dashed box shows area detailed in panel C. **B)** High sea level reduces terrigenous flux to the depozone, as well as diminishes the ability of shallow current action to rework material on submerged paleotopographic highs. Biogenous flux becomes the dominant sediment source, resulting in deposition of biogenous lithologies. **C)** Detail of a submerged paleotopographic high, illustrating topographic control on thickness and lithologic variability.

Low sea level, high sedimentation rate: In this model, high sedimentation rates are most common during relative eustatic minima, when sediment sources (either terrigenous sources or banktops/shelves) are most likely to be exposed to processes, such as gravitational instability, subaerial exposure, or current action, that mobilize and deposit sediment into available accommodation space (Fig. 8A). This is especially prevalent during periods of active faulting in the basin, during which time material accumulating on local topographic highs is frequently remobilized and redeposited into actively-generated accommodation space through mass-wasting processes. Shales (Fig. 8A), both massive and laminated, dominate intervals of the Miocene SBB with high post-compaction sedimentation rates. Although stepwise changes in terrigenous flux have been argued to be responsible for shifts in both sedimentation rate and OCMAR in the Miocene SBB (Isaacs, 1984), Monterey Formation shales contain a terrigenous component fraction that is consistently variable between ~20-60% throughout most of the Calcareous and Phosphatic Facies (Föllmi et al., 2005; Laurent et al., 2015), an interval which encompasses the full range of sedimentation rates modeled for the SBB (Figs. 4,5). Similarly, Ti and Ca abundances express similar ranges of variability across a variety of sedimentation rates at El Capitan (Fig. 7C,D). This could be indicative of consistent, concomitant changes in independent biogenic and terrigenous fluxes to the depozone, yielding similar shale compositions at a variety of different sedimentation rates. Alternatively, shale deposition represents the remobilization of material previously deposited on shelves or banktops that is later distributed (purple arrows, Fig. 8) to depozones on the slope or shelf-slope transition, resulting in reworked, redeposited shales with compositions that reflect prior mixing of biogenous and terrigenous fluxes (blue and red arrows respectively, Fig. 8) in a shelf or banktop environment. This scenario agrees

with the interpretations of Föllmi et al. (2005), who argue that most mudstones and shales observed at Naples Beach are the product of gravity-flow deposition, rather than vertical rain-out from distal suspended sediment load.

The highest sedimentation rates and lowest sustained TOC concentrations observed in this study are hosted within the pre-MCO basal Monterey Formation, which is dominated by shale lithologies (Fig. 2A). The elevated sedimentation rates through this interval drive relationships between TOC and proxies for clay, terrigenous, and biogenous sediment abundance that are distinct from those in younger intervals with lower, albeit more variable sedimentation rates (Fig. 7). Importantly, this interval contains abundant evidence of active tectonism and basinal evolution: large thickness differences between sections (Fig. 1) suggest variable generation of accommodation space likely related to normal faulting on the interior margin of the basin along present day Santa Cruz Island (Hornafius, 1991), culminating with the deposition of slumped block breccias (Fig. 2F) found across the SBB at ~17.0 Ma (Fig. 1). It is unclear whether the block breccia horizon represents a single event (e.g., a seismite) or is the result of tectonically- or eustatically-induced instability. While debris flows occur along the modern Californian margin during intervals of both sea-level rise and fall, debris flows that occurred during transgressions are most common (Covault and Graham, 2010). The temporal proximity of the onset of the MCO with the block breccia horizon suggests a potential association with the transgression at the onset of the MCO. Furthermore, the occurrence of a coarse litharenitic sandstone within the breccia horizon at the El Capitan locality is indicative of the presence of a likely-proximal terrigenous sediment source to the Miocene SBB. However, similar to the modern Californian margin, the throughflow of coarse clastic material to basinal depozones may have been largely

restricted to submarine canyons (Covault and Sharman, 2019), resulting in the observed dearth of coarse clastic material in the northern SBB outcrops.

High sea level, low sedimentation rate: During relative sea level maxima, potential sediment sources are inundated, resulting in a reduction of both terrigenous material and remobilized banktop material to the depozone (Fig. 8B). Biogenous material becomes the most voluminous contribution to the depozone, resulting in the accumulation of dominantly biogenous lithologies.

This model scenario is best represented in the SBB by a decrease in apparent sedimentation rate at ~17.0 Ma that is concomitant with a shift in dominant lithology from calcareous shale to porcelanite beds (Fig. 1; Fig. 2B), as well as low-to-moderate TOC and a decrease in OCMAR. The base of this interval aligns temporally with the onset of the MCO (Herbert et al., 2022; Westerhold et al, 2020) and a eustatic sea-level rise at ~16.9 Ma of ~40 m (Miller et al., 2020). This scenario supports previously proposed models for the occurrence of biogenous lithologies as the result of reduced detrital input (Isaacs, 1984), and suggests that reduced terrigenous input, rather than a reduction in primary productivity, is responsible for reduced OCMAR across the early MCO interval. Additionally, the low TOC measured through this interval can potentially be explained by the reduction of detrital material to the depozone, thereby limiting clay-mediated preservation of TOC and resulting in concomitant local minima in sedimentation rate and TOC abundance that are not observed elsewhere in the section. Alternatively, the high porosity and permeability of dominantly biogenous material in a pre-compaction setting could have resulted in the relatively poor

preservation of OC, driving both low TOC and low post-compaction apparent sedimentation rate.

Low sea level, low sedimentation rate: When material is transferred from relatively high topography (e.g. sills or banktops, Fig. 8) into adjacent accommodation space, highly condensed stratigraphy and/or unconformities will develop along those topographic highs (Fig. 8C). During periods of rapid uplift or topographic generation, gravitational mass wasting will remobilize most material found on banktops, regardless of grainsize, density or hydraulic stability. When the dominant source of sediment remobilization is current action, however, material above a certain grain size, density, or hydraulic stability threshold will remain in-situ, while more easily-mobilized material is scoured and redeposited elsewhere. As a result, lowstand intervals during which banktops, shelves, and slopes are exposed to persistent winnowing currents will feature condensed regions with extremely low sedimentation rates and a high probability of significant unconformity surfaces.

This scenario is exemplified in the SBB by rocks of the Phosphatic Facies (Fig. 1), which host both the lowest sedimentation rates and highest TOC contents measured in the basin. A ~60 m sea-level fall associated with East Antarctic Ice Sheet (EAIS) growth beginning at ~13.8 Ma (Holbourn et al., 2014; Miller et al., 2020) may have amplified paleotopographic variability across banktop highs (Hornafius, 1991) in the northern SBB. This variability drove the deposition of discontinuous lag deposits of reworked authigenic phosphatic nodules and phosphatic hardgrounds (Fig. 2C), which define the condensed interval of the Phosphatic facies. Differences in condensation between sections are significant, resulting in this interval containing the only long-lived decoupling of OCMARs

between El Capitan and Naples beaches (Fig. 6). At El Capitan and Naples, the condensed interval interval spans 13.25 Ma to just younger than 11.32 Ma, while hardgrounds appear before 14.27 Ma at Tajiguas Beach, and are abundant between 13.89 Ma and 10.15 Ma (Fig. 1). The Phosphatic Facies contains evidence of sediment reworking (Fig. 2D) and variable hydrodynamic conditions across sub-decimeter lateral distances, with authigenic calcareous and phosphatic material forming clast-supported conglomeratic lags in regions where finer material has been winnowed away (Fig. 2C).

A strong positive relationship between Al/Si ratio and TOC through this interval (Fig. 7A) suggests that even in a winnowing environment, clay abundance plays a significant role in determining the abundance of organic carbon. While this may seem counterintuitive for an environment wherein fine-grained material is preferentially removed, both directional currents and waves can concentrate clays in the shallow subsurface of the sediment, resulting in a clay-enriched layer that is more resistant to hydraulic removal than adjacent, clay-poor horizons (Wu et al., 2018). The development of an "armored" clay-rich layer provides a mechanism for maintaining clays in an actively-winnowing environment, and also provides an avenue for porosity reduction in the upper sediment column. Föllmi et al. (2005) argue that porosity reduction during phosphogenesis provides enhanced preservational potential for OC by limiting porewater throughput and decreasing oxidative remineralization potential below low-porosity horizons. The exceptional TOC content (and resultant variable OCMAR) of the post MMCT interval may therefore be a function of preservation both by clay shielding as well as by porosity reduction associated with both winnowing-related clay armoring and phosphogenesis, with the locus of winnowing and phosphogenesis controlled by basinal topography (Föllmi et al., 2005; Föllmi et al., 2017).

4.5.4. Timing and magnitude of organic carbon accumulation in the Monterey Formation

The age model presented here demonstrates that these TOC-rich sections along the SBB coast that were used to argue for increased organic burial during the MCO and MMCT (Flower & Kennett, 1993) have moderate OCMARs because they are condensed. This does not necessarily imply that all Monterey Formation exposures that formed in other settings will have the same record of organic burial, as different depositional systems will respond differently to sea-level change. For example, during low-stands, when upper slope and banktop sections are winnowed, more fine material, including clay, may be delivered to deeper-water sections, promoting enhanced carbon burial (Fig. 8A). Indeed, seismic profiles across the Santa Barbara channel suggest significant thickening of units contemporaneous with the condensed interval of the northern SBB Phosphatic Facies (Hornafius, 1991). Thus, for the Monterey Hypothesis to be retained, exceptional organic carbon burial would have had to have occurred elsewhere on the California margin, away from the northern SBB sections in offboard deposits.

Exceptional rates of organic carbon burial are not the baseline in the Miocene SBB: the maximum OCMAR observed at Naples Beach, which precedes the MCO, is within the range of OCMARs measured along Holocene productive margins (Fig. 9). In general, SBB strata host OCMARs more akin to those observed on lower productivity margins or within the modern California borderland basins (between ~250–1650 mg/cm^2/kyr, Jahnke, 1990). Estimated OCMARs from the Belridge Field of the San Joaquin Basin, an expanded, clastic-rich Monterey Formation locality, are similar to those of the SBB sections and modern Californian borderland basins (Fig. 9), ranging between ~490–2200 g/cm^2/kyr (see

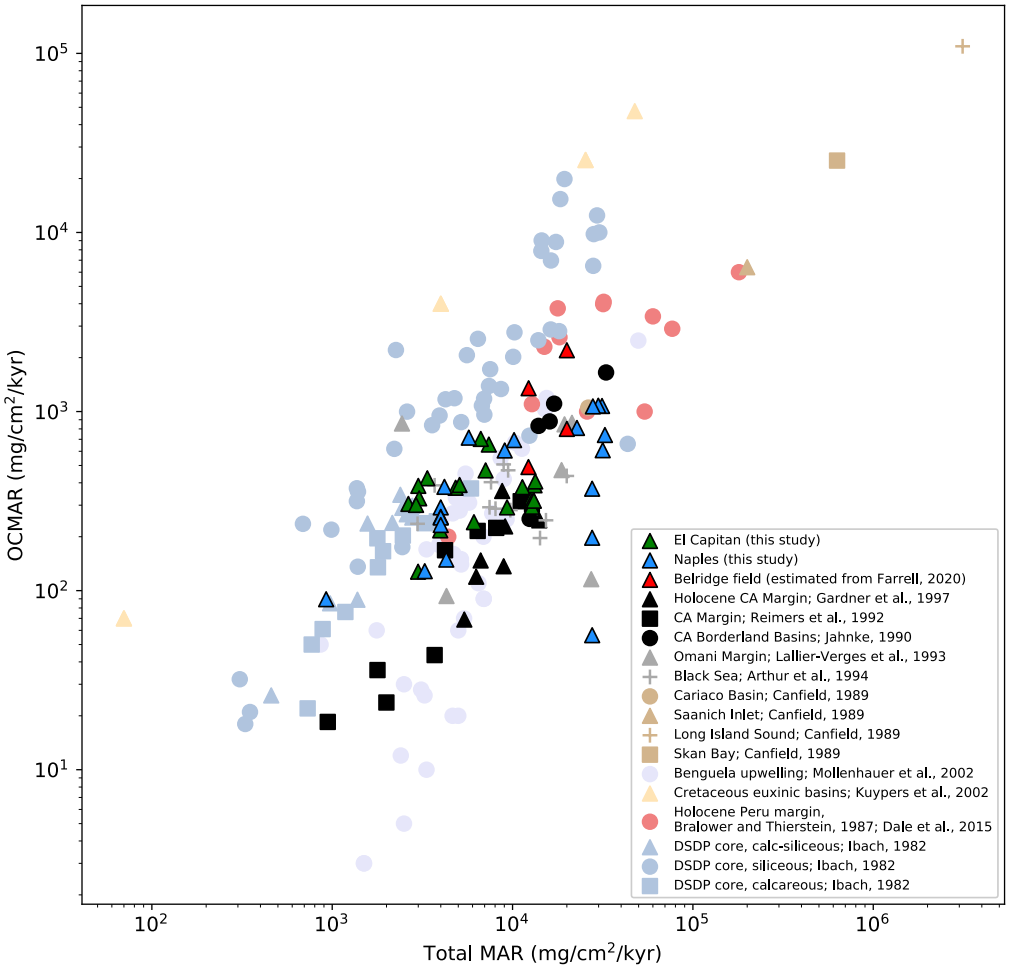

Figure 9: Ranges of OCMAR from El Capitan and Naples, as well as estimated OCMARs from the Belridge oil field of the San Joaquin Valley, plotted against total mass accumulation rate (MAR). Note log scale. Also included are OCMAR vs total MAR for a variety of different localities, including the Californian Margin (Gardner et al., 1997; Reimers et al., 1992), California Borderland Basins (Jahnke, 1990), the Omani Margin (Lallier and Verges, 1993), the Black Sea (Arthur et al., 1994), the Cariaco Basin, Saanich Inlet, Long Island Sound, and Skan Bay (Canfield, 1989), the southwestern African margin (Mollenhauer et al., 2002), Cretaceous euxinic basins (Kuypers et al., 2002), the Holocene Peruvian margin (Bralower and Theirstein, 1987; Dale et al., 2015), and data compiled from various Deep Sea Drilling Project (DSDP) cores (Ibach, 1982). Figure adapted from Gardner et al., 1997. Note the overlap of calculated Monterey Formation OCMAR ranges with typical values from the modern California margin and Borderland Basins.

Appendix 3 for additional discussion). However, the current age model for Belridge Field strata (Scheirer and Magoon, 2007) suggests that the highest OCMARs in this interval postdate the end of the MMCT, undermining arguments for a driving relationship between OC burial in the Monterey Formation and the onset of Miocene cooling.

4.5.5. Organic burial in the Monterey Formation and the Monterey Event

A core tenet of the Monterey Hypothesis is the proposed correlation between positively-shifted $\delta^{13}C$ values of the Monterey Event with enhanced episodes of organic burial in the Monterey Formation (Vincent and Berger, 1985; Flower and Kennett, 1993). The Monterey Event is characterized by a +1‰ shift in the $\delta^{13}C$ of foraminiferal tests (interpreted to record changes in the isotopic composition of marine dissolved inorganic carbon, or DIC) from marine sediment cores around the globe. The $\delta^{13}C$ of DIC is set by the sum of the isotopic composition and fluxes of inputs and outputs of carbon into the global marine reservoir, and can be schematically represented with a simple single-box model (Fig. 10A). On timescales longer than the residence time of carbon in the deep ocean, this model can be simplified by assuming a steady state, with the magnitude and composition of output fluxes balancing those of the input (Kump and Arthur, 1999):

$$\delta^{13}C_{in} = (\delta^{13}C_{org} \times f_{org}) + \delta^{13}C_{carb} \times (1 - f_{org}) \quad \text{(Eq. 3)}$$

Here, f_{org} represents the fraction of carbon that is removed from the marine reservoir as organic carbon, while $\delta^{13}C_{in}$, $\delta^{13}C_{org}$, and $\delta^{13}C_{carb}$ represent the isotopic compositions of carbon input into the marine system, buried organic carbon, and carbon in buried carbonates,

respectively. Although this relationship is an oversimplification of the dynamic global carbon cycle, this mass balance model provides a quantitative test of hypotheses related to changes in organic carbon burial. Here, we use this framework to assess the significance of the rates of organic carbon burial in the Monterey Formation relative to the mass-balance requirements of the ~1‰ $\delta^{13}C$ excursion of the Monterey Event.

Assuming an input isotopic composition of -6‰ (roughly the composition of volcanogenic CO_2; Shields and Mills, 2017) and an average $\delta^{13}C_{org}$ composition of -23‰, which approximates the average $\delta^{13}C$ of global Miocene organic carbon (Katz et al., 2005) as well as $\delta^{13}C_{org}$ of the Monterey Formation (mean $\delta^{13}C_{org}$ of -23.18‰ in El Capitan shales, Table SM4; Laurent et al., 2015) the ~1‰ shift in the $\delta^{13}C$ of DIC observed during the Monterey Event could have been driven by an increase in f_{org} of ~10% (from 0.277 to 0.306), with no appreciable change in total C flux in or out of the global surface system. Given an assumed conservative average global carbon burial flux of ~0.6 GtC/yr (Li et al., 2023), this shift in f_{org} requires an additional 0.017 GtC/yr flux of organic carbon out of the marine system. If all this additional flux was accommodated by organic burial in the Monterey Formation (assuming a depositional area of ~180,000 km^2, equivalent to the total area of Neogene basins outlined in Fig. 1A), an OCMAR of 9,440 $mg/cm^2/kyr$ would need to have been sustained across all Californian Neogene basins during Monterey Event time. Expanding depositional area to an estimate of total circum-Pacific Neogene basin area (~600,000 km^2; Vincent and Berger, 1985) yields a sustained OCMAR of 2833 $mg/cm^2/kyr$. This rate is higher than those reported anywhere in the Monterey Formation, and substantially higher than those observed in the SBB during early Monterey Event time

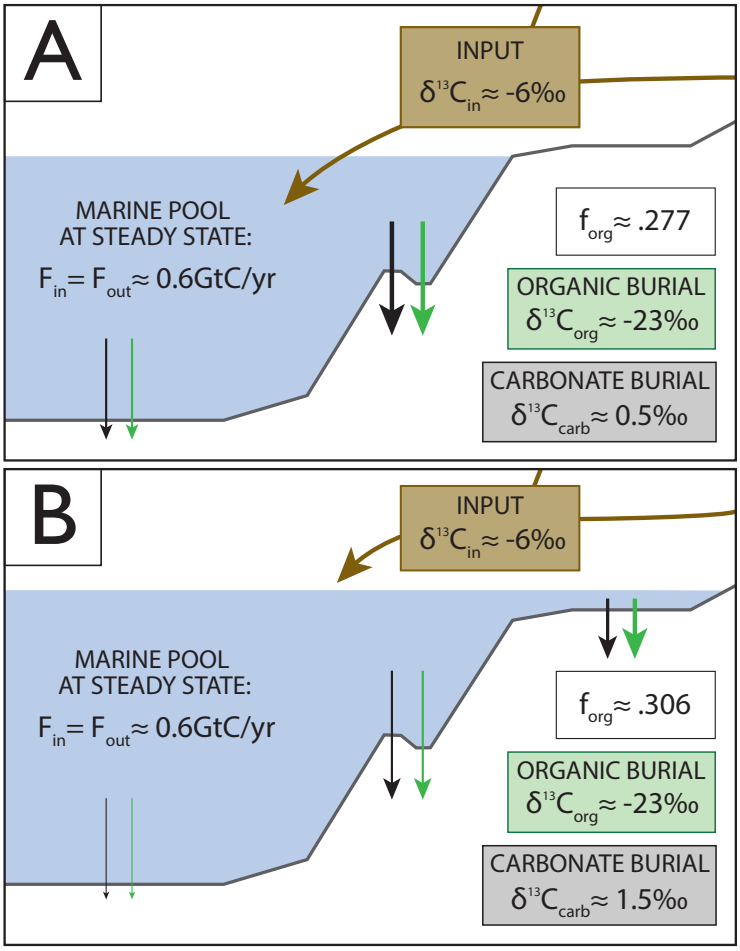

Figure 10: Cartoon depiction of a simple box model describing the isotopic mass balance required to set the $\delta^{13}C$ of the marine dissolved inorganic carbon (DIC) pool. Both panels represent steady state conditions, with F_{in} (total flux of carbon input into the marine pool from all sources) set equal to F_{out} (total flux of carbon output from the marine pool, which is the sum of organic burial and carbonate burial fluxes). Input/output flux is assumed to be ~0.6GtC/yr. Panel **A)** represents a pre-Monterey Event scenario with carbonate burial ($\delta^{13}C_{carb}$) isotopic compositions of ~0.5‰, requiring a ratio of organic to carbonate burial (f_{org}) of ~.277. **B)** represents a syn-Monterey Event scenario, in which $\delta^{13}C_{carb}$ is driven to ~1.5‰ by an increase in f_{org} to ~.306. We suggest that some of the implied increase in organic carbon burial was accommodated by burial in proximal, supra-shelf environments during the syn-MCO transgression. In both panels, the scale of the black (carbonate) and green (organic) arrows schematically represents the relative magnitude of carbon burial in deep marine (left), distal marginal (center) and proximal/supra-shelf (right) environments. Note that during the MCO, a relocation of a fraction of organic burial to newly-inundated epicontinental settings may have balanced decreases in deep marine organic burial rates, consistent with the observations of Li et al. (2023).

(<250mg/cm^2/kyr from 15.75-16.75 Ma, Fig. 6). A simple sensitivity test (see Appendix 3 for expanded discussion) shows that this relationship is replicated by a range of reasonable estimated $\delta^{13}C_{in}$ and $\delta^{13}C_{org}$ values. It is therefore unlikely that organic burial in the Monterey Formation, or indeed in all circum-Pacific basins, was the primary driver of the positive isotopic excursion of the Monterey Event.

4.5.6. Alternative drivers of the Monterey Event

Similar to the Monterey Formation, global rates of organic carbon burial may have responded to, rather than driven, changes in global climate. The positively-shifted foraminiferal $\delta^{13}C$ values of the Monterey Event begin during the MCO, and lag an abrupt shift in foraminiferal $\delta^{18}O$ values (Fig. 6) associated with warming, ice loss, and sea-level rise at the beginning of the MCO (Holbourn et al., 2014). Eustatic sea level models suggest a ~40 m syn-MCO transgression (Miller et al., 2020), providing support for hypotheses that propose enhanced organic carbon burial on continental shelves during eustatic maxima (Fig. 10B) as a driver of positive marine $\delta^{13}C$ excursions (Compton et al., 1990; Bjerrum et al., 2006; Sosdian et al., 2020). Inundation of continental shelves may have produced an increase in shallow marine depositional environments that can support more efficient organic burial than the deep ocean (Hedges and Keil, 1995). This hypothesis is supported by the mid-Miocene geological record: estuarine coals on the Sunda Shelf record evidence of enhanced organic carbon deposition in nearshore marginal environments (Fikri et al., 2022;), while phosphorites on the eastern seaboard of North America have been interpreted as the product of organic-rich deposits that were emplaced during syn-MCO highstands and subsequently oxidized during lowstands (Compton et al., 1990).

This hypothesis is distinct from that of Li et al. (2023), who present a global compilation of Neogene organic carbon burial rates in deep marine environments, and argue that a decrease in marine organic burial during the Middle Miocene is indicative of low global organic carbon burial rates and anemic global f_{org}. However, the locations that make up this compilation largely sample open marine depositional environments that represent a small fraction of global organic burial (Hedges and Keil, 1995). Thus, the organic carbon burial record of Li et al. (2023), and indeed in the Monterey Formation, could be interpreted as a syn-MCO fractional shift in the locus of marine primary productivity, export, and burial from deeper marine environments to shallower, marginal environments associated with changes in sea level. The apparent decrease in deep marine OC burial would therefore be compensated by the increased burial and/or recycling of organic carbon in proximal environments, consistent with the shelf-inundation hypotheses discussed above.

4.5.7 Organic carbon burial and Miocene Climate

Although organic carbon burial in the Monterey Fm and equivalent circum-Pacific basinal deposits cannot explain the Monterey Event alone, the isotopic shift of the Monterey Event may have been related to transgression and organic carbon burial over a broader continental shelf area, and can be achieved without changing the total global carbon burial flux. In this scenario, changes in the inorganic carbon cycle must be invoked to exert influence on global carbon mass balance and drive climate change, to which a dynamic organic carbon cycle would then respond. Potential inorganic drivers of the MCO warming include the outgassing of CO_2 associated with the eruption of the Columbia River Flood Basalts, with weathering of the resultant basaltic edifice contributing to subsequent cooling

(Hodell and Woodruff, 1994) for several million years after the cessation of volcanism at ca. 15.9 Ma (Kasbohm and Schoene, 2018). Additional changes in inorganic carbon sources from slowing seafloor spreading rates (Herbert et al., 2022) or changes in sinks from enhanced silicate weathering in the tropics (Park et al., 2020) have been proposed as contributors to Miocene cooling. Our data from the Monterey Formation are consistent with hypotheses for inorganic geological drivers of long-term climate change, and support the notion that organic carbon burial in the Miocene responded to, rather than drove, global climate.

4.6. Conclusions

A new age model for the Monterey Formation incorporates 31 new LA-ICPMS and 14 CA-ID-TIMS U-Pb zircon ages from the northern coast of the Santa Barbara Channel. Modeled sedimentation rates from this age model were combined with TOC data from sections at El Capitan and Naples to assess the magnitude and timing of OCMAR in the Miocene Santa Barbara Basin, and show that peaks in SBB OCMAR do not correspond with the Monterey Event shift in the global $\delta^{13}C_{DIC}$ record from a timing or mass-balance perspective. Rather than driving climate, TOC burial in the Monterey Formation was controlled by changes in sedimentation rate, which was in turn controlled by a combination of local tectonics and eustasy. Thus, contrary to the driving relationship postulated by the Monterey Hypothesis, organic carbon deposition in the Monterey Formation was largely a response to basin formation and climate change.

* * *

ACKNOWLEDGEMENTS

This project was funded by American Chemical Society (ACS) PRF #65256-ND8 to FAM. ESCA was additionally supported by an NSF Graduate Research Fellowship. We thank Scott Hornafius and Jim Boles for stimulating conversations and constructive feedback, and thank Caroline Newell and Brian Mo for their assistance with sample preparation.

* * *

REFERENCES, CHAPTER IV

Agnihotri, R., Altabet, M.A., Herbert, T.D. and Tierney, J.E., 2008, Subdecadally resolved paleoceanography of the Peru margin during the last two millennia: Geochemistry, Geophysics, Geosystems, 9(5). doi:10.1029/2007GC001744

Arthur, M.A., Dean, W.E., Neff, E.D., Hay, B.J., King, J. and Jones, G., 1994, Varve calibrated records of carbonate and organic carbon accumulation over the last 2000 years in the Black Sea: Global Biogeochemical Cycles, 8(2), p. 195-217. doi:10.1029/94GB00297

Barron, J.A., 1986, Paleoceanographic and tectonic controls on deposition of the Monterey Formation and related siliceous rocks in California: Palaeogeography, Palaeoclimatology, Palaeoecology, 53(1), p. 27-45. doi:10.1016/0031-0182(86)90037-4

Behl, R.J., Moores, E.M., Sloan, D. and Stout, D.L., 1999, Since Bramlette (1946): The Miocene Monterey Formation of California revisited: Classic Cordilleran Concepts: A View from California: Geological Society of America, Special Paper, 338, p. 301-313.

Blättler, C.L., Miller, N.R. and Higgins, J.A., 2015, Mg and Ca isotope signatures of authigenic dolomite in siliceous deep-sea sediments: Earth and Planetary Science Letters, 419, p.32-42. doi:10.1016/j.epsl.2015.03.006

Bjerrum, C.J., Bendtsen, J. and Legarth, J.J.F., 2006, Modeling organic carbon burial during sea level rise with reference to the Cretaceous: Geochemistry, Geophysics, Geosystems, 7(5). doi:10.1029/2005GC001032

Bohacs, K.M. and Schwalbach, J.R., 1994, Natural gamma-ray spectrometry of the Monterey Formation at Naples Beach, California: insights into lithology, stratigraphy, and source-rock quality, *in* Field Guide to the Monterey Formation between Santa Barbara and Gaviota, California: AAPG Pacific Section, p. 85-94.

Bowring, J.F., McLean, N.M. and Bowring, S.A., 2011, Engineering cyber infrastructure for U-Pb geochronology: Tripoli and U-Pb_Redux: Geochemistry, Geophysics, Geosystems, 12(6).

Bralower, T.J. and Thierstein, H.R., 1987, Organic carbon and metal accumulation rates in Holocene and mid-Cretaceous sediments: palaeoceanographic significance: Geological Society, London, Special Publications, 26(1), p.345-369. doi:10.1144/GSL.SP.1987.026.01.23

Bramlette, M.N., 1946, The Monterey Formation of California and the origin of its siliceous rocks (Vol. 212): Washington D.C., US Government Printing Office, 57 p.

Calvert, S.E. and Pedersen, T.F., 2007, Chapter fourteen elemental proxies for palaeoclimatic and palaeoceanographic variability in marine sediments: interpretation and application: Developments in marine geology, 1, p.567-644. doi:10.1016/S1572-5480(07)01019-6

Canfield, D.E., 1989, Sulfate reduction and oxic respiration in marine sediments: implications for organic carbon preservation in euxinic environments. Deep Sea Research Part A. Oceanographic Research Papers, 36(1), p. 121-138. doi:10.1016/0198-0149(89)90022-8

Chappell, J. and Shackleton, N., 1986, Oxygen isotopes and sea level: Nature, 324(6093), p.137-140. doi:10.1038/324137a0

Compton, J.S., Snyder, S.W. and Hodell, D.A., 1990. Phosphogenesis and weathering of shelf sediments from the southeastern United States: Implications for Miocene δ13C excursions and global cooling. *Geology*, *18*(12), pp.1227-1230.

Covault, J.A. and Graham, S.A., 2010, Submarine fans at all sea-level stands: Tectono-morphologic and climatic controls on terrigenous sediment delivery to the deep sea: Geology, 38(10), p.939-942. doi:10.1130/G31081.1

Covault, J.A. and Sharman, G.R., 2019. Tectonostratigraphic Evolution of the Inner California Borderland: Template for Fill-and-Spill Sedimentation, *in* The Sedimentary Basins of the United States and Canada, p.511-528. Elsevier. doi:10.1016/B978-0-444-63895-3.00012-7

Crouch, J.K. and Bukry, D., 1979, Comparison of Miocene provincial foraminiferal stages to coccolith zones in the California Continental Borderland: Geology, 7(4), p.211-215. doi: 10.1130/0091-7613(1979)7<211:COMPFS>2.0.CO;2

Dale, A.W., Sommer, S., Lomnitz, U., Montes, I., Treude, T., Liebetrau, V., Gier, J., Hensen, C., Dengler, M., Stolpovsky, K. and Bryant, L.D., 2015, Organic carbon production, mineralisation and preservation on the Peruvian margin: Biogeosciences, 12(5), p.1537-1559. doi: 10.5194/bg-12-1537-2015

Fenton, N.C., 2018, Zircon U-Pb Dating of Tuff in the Monterey Formation of California by Laser Ablation Inductively Coupled Plasma Mass Spectrometry [Doctoral dissertation]: San Diego State University, 99 p.

Fikri, H.N., Sachsenhofer, R.F., Bechtel, A. and Gross, D., 2022. Organic geochemistry and petrography in Miocene coals in the Barito Basin (Tutupan Mine, Indonesia): Evidence for astronomic forcing in kerapah type peats. *International Journal of Coal Geology*, *256*, p.103997. https://doi.org/10.1016/j.coal.2022.103997

Flower, B.P. and Kennett, J.P., 1993, Relations between Monterey Formation deposition and middle Miocene global cooling: Naples Beach section, California: Geology, 21(10), p. 877-880. doi: 10.1130/0091-7613(1993)021<0877:RBMFDA>2.3.CO;2

Föllmi, K.B., Badertscher, C., de Kaenel, E., Stille, P., John, C.M., Adatte, T. and Steinmann, P., 2005, Phosphogenesis and organic-carbon preservation in the Miocene Monterey Formation at Naples Beach, California—The Monterey hypothesis revisited: Geological Society of America Bulletin, 117(5-6), p. 589-619.

Föllmi, K.B., Thomet, P., Lévy, S., De Kaenel, E., Spangenberg, J.E., Adatte, T., Behl, R.J. and Garrison, R.E., 2017: The impact of hydrodynamics, authigenesis, and basin morphology on sediment accumulation in an upwelling environment: the Miocene Monterey Formation at Shell Beach and Mossel Rock (Pismo and Santa Maria Basins, Central California, USA): Journal of Sedimentary Research, 87(9), p.986-1018. doi:https://doi.org/10.2110/jsr.2017.57

Foster, G.L., Lear, C.H. and Rae, J.W., 2012, The evolution of pCO^2, ice volume and climate during the middle Miocene: Earth and Planetary Science Letters, 341, p. 243-254. doi:https://doi.org/10.1016/j.epsl.2012.06.007

Galy, V., France-Lanord, C., & Lartiges, B. (2008). Loading and fate of particulate organic carbon from the Himalaya to the Ganga–Brahmaputra delta. *Geochimica et Cosmochimica Acta*, *72*(7), 1767-1787. https://doi.org/10.1016/j.gca.2008.01.027

Gardner, J.V., Dean, W.E. and Dartnell, P., 1997, Biogenic sedimentation beneath the California Current system for the past 30 kyr and its paleoceanographic significance: Paleoceanography, 12(2), p. 207-225. doi:https://doi.org/10.1029/96PA03567

Gerstenberger, H. and Haase, G., 1997, A highly effective emitter substance for mass spectrometric Pb isotope ratio determinations: Chemical geology, 136(3-4), p. 309-312.

Gladney, E.S., 1980, Compilation of elemental concentration data for the United States Geological Survey's six geochemical exploration reference materials (No. LA-8473-MS): Los Alamos Scientific Lab., NM (USA).

Gradstein, F.M., Ogg, J.G., Schmitz, M.D. and Ogg, G.M. (eds.), 2020, Geologic time scale 2020: Elsevier. doi:https://doi.org/10.1016/B978-0-12-824360-2.00002-4

Gorsline, D.S., Drake, D.E. and Barnes, P.W., 1968, Holocene sedimentation in Tanner Basin, California continental borderland: Geological Society of America Bulletin, 79(6), p.659-674. doi:https://doi.org/10.1130/0016-7606(1968)79[659:HSITBC]2.0.CO;2

Hancock, L.G., Hardisty, D.S., Behl, R.J. and Lyons, T.W., 2019, A multi-basin redox reconstruction for the Miocene Monterey Formation, California, USA: Palaeogeography, Palaeoclimatology, Palaeoecology, 520, p.114-127. doi:https://doi.org/10.1016/j.palaeo.2019.01.031

Hedges, J.I. and Keil, R.G., 1995, Sedimentary organic matter preservation: an assessment and speculative synthesis: Marine chemistry, 49(2-3), p.81-115. doi:https://doi.org/10.1016/0304-4203(95)00008-F

Herbert, T.D., Dalton, C.A., Liu, Z., Salazar, A., Si, W. and Wilson, D.S., 2022, Tectonic degassing drove global temperature trends since 20 Ma: Science, 377(6601), p.116-119. doi:10.1126/science.abl4353

Hiess, J., Condon, D.J., McLean, N. and Noble, S.R., 2012, 238U/235U systematics in terrestrial uranium-bearing minerals: Science, 335(6076), p.1610-1614.

Hodell, D.A. and Woodruff, F., 1994, Variations in the strontium isotopic ratio of seawater during the Miocene: Stratigraphic and geochemical implications: Paleoceanography, 9(3), p. 405-426. doi:https://doi.org/10.1029/94PA00292

Hoke, G.D., Schmitz, M.D. and Bowring, S.A., 2014, An ultrasonic method for isolating nonclay components from clay-rich material: Geochemistry, Geophysics, Geosystems, 15(2), p. 492-498.

Holbourn, A., Kuhnt, W., Lyle, M., Schneider, L., Romero, O. and Andersen, N., 2014. Middle Miocene climate cooling linked to intensification of eastern equatorial Pacific upwelling. *Geology*, *42*(1), pp.19-22. doi:https://doi.org/10.1130/G34890.1

Hornafius, J.S., 1984. Origin of remanent magnetization in dolomite from the Monterey Formation, *in* Garrison, R.E., Kastner, M. and Zenger, D.H., eds. 1984, Dolomites of the

Monterey Formation and Other Organic-Rich Units: Pacific Section, SEPM, Vol 41, p. 195-212.

Hornafius, J.S., 1991, Facies analysis of the Monterey Formation in the northern Santa Barbara Channel: AAPG bulletin, 75(5), p. 894-909.

Hornafius, J.S., 1994, ed., Field Guide to the Monterey Formation between Santa Barbara and Gaviota, California: Bakersfield, CA, AAPG Pacific Section, 123 p.

Horstwood, M.S., Košler, J., Gehrels, G., Jackson, S.E., McLean, N.M., Paton, C., Pearson, N.J., Sircombe, K., Sylvester, P., Vermeesch, P. and Bowring, J.F., 2016, Community-derived standards for LA-ICP-MS U-(Th-) Pb geochronology–Uncertainty propagation, age interpretation and data reporting: Geostandards and Geoanalytical Research, 40(3), p. 311-332.

Ibach, L.E.J., 1982, Relationship between sedimentation rate and total organic carbon content in ancient marine sediments: AAPG Bulletin, 66(2), p.170-188. doi:https://doi.org/10.1306/03B59A5D-16D1-11D7-8645000102C1865D

Isaacs, Caroline M, 1981, Porosity reduction during diagenesis of the Monterey Formation, Santa Barbara coastal area, California, *in* Garrison, R.E., Douglas, R.G., Pisciotto, K.E., Isaacs, C.M., and Ingle, J.C., eds., The Monterey Formation and related siliceous rocks of California: Los Angeles, CA, Pacific Section, Soc. Of Economic Paleontologists and Mineralogists, p. 257-271.

Isaacs, C.M., 1983, Compositional variation and sequence in the Miocene Monterey Formation, Santa Barbara coastal area, California *in* Larue, D.K. & Steel, R.J., (eds.), Cenozoic Marine Sedimentation, Pacific margin, USA. Pacific Section, Soc. econ. Paleo. Min., Bakersfield. p. 117-32.

Isaacs, C.M., 1984, Hemipelagic deposits in a Miocene basin, California: Toward a model of lithologic variation and sequence: Geological Society, London, Special Publications, 15(1), p. 481-496. doi:https://doi.org/10.1144/GSL.SP.1984.015.01.31

Isaacs, C.M., Pollastro, R.M., Barron, J.A., Ingle Jr. J.C., Bukry, D., Dunbar, R.B., Keller, M.A., Tomson, J.H., Lewan, M.D., 2001, Geologic and Paleontologic Features of Rock Samples in the Cooperative Monterey Organic Geochemistry Study, Naples Beach and Lions Head Sections, California, *in* Isaacs, C.M., and Rulkötter, J., (eds.), The Monterey Formation: From Rocks to Molecules, Columbia University Press, New York. p. 373-392.

Jackson, S.E., Pearson, N.J., Griffin, W.L. and Belousova, E.A., 2004, The application of laser ablation-inductively coupled plasma-mass spectrometry to in situ U–Pb zircon geochronology: Chemical geology, 211(1-2), p. 47-69.

Jahnke, R.A., 1990, Early diagenesis and recycling of biogenic debris at the seafloor, Santa Monica Basin, California: Journal of marine research, 48(2), p. 413-436. doi:https://doi.org/10.1357/002224090784988773

John, C.M., Follmi, K.B., De Kaenel, E., Adatte, T., Steinmann, P. and Badertscher, C., 2002, Carbonaceous and phosphate-rich sediments of the Miocene Monterey formation at El Capitan State Beach, California, USA: Journal of Sedimentary Research, 72(2), p. 252-267. doi:https://doi.org/10.1306/080701720252

Kasbohm, J. and Schoene, B., 2018, Rapid eruption of the Columbia River flood basalt and correlation with the mid-Miocene climate optimum: Science advances, 4(9), p.8223. doi:10.1126/sciadv.aat8223

Katz, M.E., Wright, J.D., Miller, K.G., Cramer, B.S., Fennel, K. and Falkowski, P.G., 2005. Biological overprint of the geological carbon cycle. *Marine Geology*, *217*(3-4), pp.323-338. https://doi.org/10.1016/j.margeo.2004.08.005

Keller, C.B., Schoene, B., Samperton, K.M. (2018), A stochastic sampling approach to zircon eruption age interpretation: Geochem. Persp. Let. 8, p. 31–35.

Kennedy, M.J., Pevear, D.R. and Hill, R.J., 2002. Mineral surface control of organic carbon in black shale. *Science*, *295*(5555), pp.657-660. doi:10.1126/science.1066611

Knott, J.R., Sarna-Wojcicki, A.M., Barron, J.A., Wan, E., Heizler, L. and Martinez, P., 2022. Tephrochronology of the Miocene Monterey and Modelo Formations, California: Understanding the Monterey Formation and Similar Biosiliceous Units across Space and Time, 556, p. 187. doi:https://doi.org/10.1130/2022.2556(08)

Krogh, T.E., 1973, A low-contamination method for hydrothermal decomposition of zircon and extraction of U and Pb for isotopic age determinations: Geochimica et Cosmochimica Acta, *37*(3), pp.485-494.

Kump, L.R. and Arthur, M.A., 1999. Interpreting carbon-isotope excursions: carbonates and organic matter. *Chemical Geology*, *161*(1-3), pp.181-198.

Kuypers, M.M., Pancost, R.D., Nijenhuis, I.A. and Sinninghe Damsté, J.S., 2002, Enhanced productivity led to increased organic carbon burial in the euxinic North Atlantic basin during the late Cenomanian oceanic anoxic event: Paleoceanography, 17(4), p. 3-1. doi:https://doi.org/10.1029/2000PA000569

Kylander-Clark, A.R., Hacker, B.R. and Cottle, J.M., 2013, Laser-ablation split-stream ICP petrochronology: Chemical Geology, 345, p. 99-112.

Lallier-Verges, E., Bertrand, P. and Desprairies, A., 1993. Organic matter composition and sulfate reduction intensity in Oman Margin sediments: Marine Geology, 112(1-4), p. 57-69. doi:https://doi.org/10.1016/0025-3227(93)90161-N

Laurent, D., de Kaenel, E., Spangenberg, J.E. and Föllmi, K.B., 2015, A sedimentological model of organic-matter preservation and phosphogenesis in the Miocene Monterey Formation at Haskells Beach, Goleta (central California): Sedimentary Geology, 326, p.16-32. doi:https://doi.org/10.1016/j.sedgeo.2015.06.008

Li, Z., Zhang, Y.G., Torres, M. and Mills, B.J., 2023, Neogene burial of organic carbon in the global ocean: Nature, 613(7942), p.90-95. doi:https://doi.org/10.1038/s41586-022-05413-6

Luyendyk, B.P., Kamerling, M.J. and Terres, R., 1980, Geometric model for Neogene crustal rotations in southern California: Geological Society of America Bulletin, 91(4), p. 211-217. doi:https://doi.org/10.1130/0016-7606(1980)91<211:GMFNCR>2.0.CO;2

Marsaglia, K.M., Davis, A.S., Rimkus, K. and Clague, D.A., 2006, Evidence for interaction of a spreading ridge with the outer California borderland: Marine geology, 229(3-4), p.259-272. doi:https://doi.org/10.1016/j.margeo.2006.02.006

Mattinson, J.M., 2005, Zircon U–Pb chemical abrasion ("CA-TIMS") method: combined annealing and multi-step partial dissolution analysis for improved precision and accuracy of zircon ages: Chemical Geology, 220(1-2), p. 47-66.

McLean, N.M., Bowring, J.F. and Bowring, S.A., 2011, An algorithm for U-Pb isotope dilution data reduction and uncertainty propagation: Geochemistry, Geophysics, Geosystems, 12(6).

Miller, K.G., Browning, J.V., Schmelz, W.J., Kopp, R.E., Mountain, G.S. and Wright, J.D., 2020, Cenozoic sea-level and cryospheric evolution from deep-sea geochemical and continental margin records: Science advances, 6(20), eaaz1346. doi:10.1126/sciadv.aaz1346

Modestou, S.E., Leutert, T.J., Fernandez, A., Lear, C.H. and Meckler, A.N., 2020, Warm middle Miocene Indian Ocean bottom water temperatures: Comparison of clumped isotope and Mg/Ca-based estimates: Paleoceanography and Paleoclimatology, 35(11), p.e2020PA003927. doi:https://doi.org/10.1029/2020PA003927

Mollenhauer, G., Schneider, R.R., Müller, P.J., Spieß, V. and Wefer, G., 2002, Glacial/interglacial variablity in the Benguela upwelling system: Spatial distribution and budgets of organic carbon accumulation: Global Biogeochemical Cycles, 16(4), p. 81-1. doi:https://doi.org/10.1029/2001GB001488

Park, Y., Maffre, P., Goddéris, Y., Macdonald, F.A., Anttila, E.S. and Swanson-Hysell, N.L., 2020, Emergence of the Southeast Asian islands as a driver for Neogene cooling: Proceedings of the National Academy of Sciences, 117(41), p. 25319-25326. doi:https://doi.org/10.1073/pnas.2011033117

Paton, C., Woodhead, J.D., Hellstrom, J.C., Hergt, J.M., Greig, A. and Maas, R., 2010, Improved laser ablation U-Pb zircon geochronology through robust downhole fractionation correction: Geochemistry, Geophysics, Geosystems, *11*(3).

Pisciotto, K.A. and Garrison, R.E., 1981, Lithofacies and depositional environments of the Monterey Formation, California, *in* Garrison, R.E., Douglas, R.G., Pisciotto, K.E., Isaacs, C.M., and Ingle, J.C., eds., The Monterey Formation and related siliceous rocks of California: Los Angeles, CA, Pacific Section, Soc. Of Economic Paleontologists and Mineralogists, p. 97-122.

Reimers, C.E., Jahnke, R.A. and McCorkle, D.C., 1992, Carbon fluxes and burial rates over the continental slope and rise off central California with implications for the global carbon cycle: Global Biogeochemical Cycles, 6(2), p. 199-224. doi:https://doi.org/10.1029/92GB00105

Rothwell, R.G., 2015,Twenty years of XRF core scanning marine sediments: What do geochemical proxies tell us? *in* Micro-XRF studies of sediment cores. p.25-102. Springer, Dordrecht. doi:https://doi.org/10.1007/978-94-017-9849-5_2

Scheirer, A.H. and Magoon, L.B., 2007, Age, distribution, and stratigraphic relationship of rock units in the San Joaquin Basin Province, California: Petroleum systems and geologic assessment of oil and gas in the San Joaquin Basin province, California: US Geologic Survey Professional Paper. doi:10.1126/science.aau2422

Schoene, B., Eddy, M.P., Samperton, K.M., Keller, C.B., Keller, G., Adatte, T. and Khadri, S.F., 2019, U-Pb constraints on pulsed eruption of the Deccan Traps across the end-Cretaceous mass extinction: Science, 363(6429), p. 862-866. doi:10.1126/science.aau2422

Shields, G.A. and Mills, B.J., 2017. Tectonic controls on the long-term carbon isotope mass balance. *Proceedings of the National Academy of Sciences*, *114*(17), pp.4318-4323. https://doi.org/10.1073/pnas.1614506114

Sláma, J., Košler, J., Condon, D.J., Crowley, J.L., Gerdes, A., Hanchar, J.M., Horstwood, M.S., Morris, G.A., Nasdala, L., Norberg, N. and Schaltegger, U., 2008, Plešovice zircon—a new natural reference material for U–Pb and Hf isotopic microanalysis*:* Chemical Geology, 249(1-2), p. 1-35.

Steinthorsdottir, M., Coxall, H.K., De Boer, A.M., Huber, M., Barbolini, N., Bradshaw, C.D., Burls, N.J., Feakins, S.J., Gasson, E., Henderiks, J. and Holbourn, A.E., 2021, The Miocene: the future of the past: Paleoceanography and Paleoclimatology, 36(4), p.e2020PA004037. doi:https://doi.org/10.1029/2020PA004037

Sosdian, S.M., Babila, T.L., Greenop, R., Foster, G.L. and Lear, C.H., 2020. Ocean carbon storage across the middle Miocene: A new interpretation for the Monterey Event. *Nature Communications*, *11*(1), p.134. https://doi.org/10.1038/s41467-019-13792-0

Szymanowski, D. and Schoene, B., 2020, U–Pb ID-TIMS geochronology using ATONA amplifiers: Journal of Analytical Atomic Spectrometry, 35(6), p. 1207-1216.

Vermeesch, P., 2018, IsoplotR: A free and open toolbox for geochronology: Geoscience Frontiers, 9(5), p. 1479-1493.

Vincent, E. and Berger, W.H., 1985, Carbon dioxide and polar cooling in the Miocene: The Monterey hypothesis: The carbon cycle and atmospheric CO2: Natural variations Archean to present, *32*, p. 455-468. doi:https://doi.org/10.1029/GM032p0455

Wendt, I. and Carl, C., 1991, The statistical distribution of the mean squared weighted deviation: Chemical Geology: Isotope Geoscience Section, 86(4), p. 275-285.

Westerhold, T., Marwan, N., Drury, A.J., Liebrand, D., Agnini, C., Anagnostou, E., Barnet, J.S., Bohaty, S.M., De Vleeschouwer, D., Florindo, F. and Frederichs, T., 2020, An astronomically dated record of Earth's climate and its predictability over the last 66 million years: Science, 369(6509), p. 1383-1387. doi:10.1126/science.aba6853

Wiedenbeck, M.A.P.C., Alle, P., Corfu, F.Y., Griffin, W.L., Meier, M., Oberli, F.V., Quadt, A.V., Roddick, J.C. and Spiegel, W., 1995, Three natural zircon standards for U-Th-Pb, Lu-Hf, trace element and REE analyses: Geostandards newsletter, 19(1), p. 1-23.

Wilson, S.A., Potts, P.J. and Webb, P.C., 2021, Three New Geochemical Reference Materials for Mineral Exploration and Environmental Contamination Studies: SdAR-L2, SdAR-M2 and SdAR-H1: Geostandards and Geoanalytical Research, 45(2), p. 359-367.

Wu, X., Baas, J.H., Parsons, D.R., Eggenhuisen, J., Amoudry, L., Cartigny, M., McLelland, S., Mouazé, D. and Ruessink, G., 2018, Wave ripple development on mixed clay-sand substrates: effects of clay winnowing and armoring: Journal of Geophysical Research: Earth Surface, 123(11), p.2784-2801. doi:https://doi.org/10.1029/2018JF004681

* * *

APPENDIX 1

Supplementary materials for

CHAPTER II: THE REAL MCCOY: GREAT UNCONFORMITY SOURCE TO SINK ON THE RIFTED PASSIVE MARGIN OF LAURENTIA

SUMMARY

All data and code for this work is accessible within the following GitHub repository:

https://github.com/eliel-anttila/Anttila_Thesis/tree/e1a68dda7b2d398a7e05bb4909f29d5a154cb1da/Chapter2

The repository includes a summary of parameters and inputs for the tectonic subsidence model utilized in Chapter II (SubsParam.docx), all chemostratigraphic data and section locations (Table A1), geochronological data and sampling coordinates (Table A2), a tabulated summary of tectonic subsidence model inputs (Table A3), and two 1:24,000 scale maps of the Egan and Schell Creek Range field areas (Map_A1.pdf and Map_A2.pdf, respectively).

APPENDIX 2

Supplementary materials for

CHAPTER III: CAMBRIAN FORELAND PHOSPHOGENESIS IN THE KHUVSGUL BASIN, MONGOLIA

SUMMARY

All data, and code for this work is accessible within the following GitHub repository:

https://github.com/eliel-anttila/Anttila_Thesis/tree/e1a68dda7b2d398a7e05bb4909f29d5a154cb1da/Chapter3

This repository includes several tables detailing the locations of all measured sections referenced in the text (Table A1), all carbonate chemostratigraphic data (Table A2), all geochronological data (Table A3), and all parameters used to build the tectonic subsidence model for the Khuvsgul Group (Table A4).

APPENDIX 3

Supplementary materials for

CHAPTER IV: TIMING AND TEMPO OF ORGANIC CARBON BURIAL IN THE MONTEREY FORMATION OF THE SANTA BARBARA BASIN AND RELATIONSHIPS WITH MIOCENE CLIMATE

SUMMARY

Calculations of organic carbon mass accumulation rates for the Monterey Formation in the Belridge Field of the San Joaquin Basin, referenced in the main text of Chapter IV, are outlined below in Section A. A sensitivity test of the carbon isotope box model discussed in the main text of Chapter IV is outlined in Section B, and visually summarized in Fig. SM5.

All additional supplementary material (including figures), data, and code for this work is accessible within the following GitHub repository:

https://github.com/eliel-anttila/Anttila_Thesis/tree/e1a68dda7b2d398a7e05bb4909f29d5a154cb1da/Chapter4

This repository includes geochronological sample locations (Table A1), LA-ICPMS (Table A2), CA-ID-TIMS (Table A3), TOC (Table A4), and XRF (Table A5) data tables, and visualizations of geochronological data used to generate U-Pb ages (Figs. SM1-SM4).

SECTION A: ORGANIC CARBON MASS ACCUMULATION RATES IN THE BELRIDGE FIELD

Estimated organic carbon mass accumulation rates (OCMARs) from the Belridge Field of the San Joaquin Basin, an expanded, clastic-rich Monterey Formation locality, are similar to those of the Santa Barbara Basin Monterey Formation sections and modern

Californian borderland basins (Fig. 9, main text). The Macdonald Shale and Antelope Shale are members of the Monterey Formation found in the Belridge oil field (Schwartz, 1988), with the Macdonald Shale interpreted as a hemipelagic, deepwater deposit (Graham and Williams, 1985). Together, the Macdonald and Antelope shales are over 500 m thick (from Well 856C-7 in Farrell, 2020), with deposition of the Macdonald Shale occurring between ~13.5–10 Ma and the Antelope Shale between ~10–6.5 Ma (Scheirer and Magoon, 2007). Using these rough age constraints and member thicknesses from Farrell (2020), the Macdonald and Antelope shales have average sedimentation rates of 55.7 m/Myr and 90.57 m/Myr respectively. Farrell (2020) calculates average TOC contents for several different facies of an interval including the top of the Macdonald Shale and majority of the Antelope Shale, with values ranging from 4–11%. Using these values as approximate maxima and minima for average TOC content, and assuming a relatively high bulk shale density of 2.2 g/cm^3, OCMAR for the Macdonald Shale ranges from ~490–1350 $g/cm^2/kyr$, and ~800–2200 $g/cm^2/kyr$ for the Antelope Shale. While these values are generally higher than those observed in the coastal SBB, they are still within the range of values expected for OCMAR on productive margins (Fig. 9, main text).

SECTION B: SENSITIVITY TEST OF $\delta^{13}C$ BOX MODEL

In order to assess the impact of different input variables on the results of the steady-state carbon isotopic box model outlined in Section 5.5 of the main text, we input ranges of $\delta^{13}C_{in}$ and $\delta^{13}C_{org}$ values (between -12 and 0‰, and -27 and -19‰, respectively) into Eq. 3. Results of this sensitivity test are shown as contour plots in Fig S5, with a red triangle

denoting the position of the results provided by the assumed compositions for $\delta^{13}C_{in}$ (-6‰) and $\delta^{13}C_{org}$ (-23‰) that are currently utilized in the main text. Fig. SM5A depicts calculated f_{org} values for a pre-Monterey Event scenario, the above $\delta^{13}C_{in}$ and $\delta^{13}C_{org}$ compositional ranges, given a steady-state total carbon burial flux of 0.6GtC/yr and a $\delta^{13}C_{carb}$ composition of 0.5‰. Calculated f_{org} values for Monterey Event conditions, with a $\delta^{13}C_{carb}$ composition of 1.5‰ and all other input variables identical to those in the previous panel, are shown in Fig. SM5B. Fig. SM5C depicts the change in f_{org} required to shift from pre- to syn-Monterey Event $\delta^{13}C_{carb}$ compositions for a given combination of $\delta^{13}C_{in}$ and $\delta^{13}C_{org}$ values. Note that while the combination of enriched input carbon and organic carbon isotopic compositions results in the lowest f_{org} (Fig. SM5A,B), this region of the parameter space also results in the largest Δf_{org} required to drive a ~1‰ shift in marine $\delta^{13}C$ (Fig. SM5C).

In Fig. SM5D, we examine the impact of various $\delta^{13}C_{in}$ and $\delta^{13}C_{org}$ values on the sustained OCMAR, distributed across the entire area of Neogene circum-Pacific basins (~600,000km^2, Vincent and Berger, 1985) that would be required to drive the ~1‰ $\delta^{13}C$ shift of the Monterey Event. In general, more-enriched input carbon and organic carbon compositions result in higher required organic burial fluxes, with only the most depleted putative $\delta^{13}C_{in}$ values (<~-11‰) generating required OCMARs below 2000 mg/cm^2/kyr.

Changes in the magnitude of total carbon burial flux (conservatively estimated to be ~0.6GtC/yr, following Li et al., 2023), would have a linear impact on the magnitude of the required burial fluxes described above: a smaller total carbon burial flux would necessitate a proportionally smaller OC burial flux. However, for the range of $\delta^{13}C_{in}$ and $\delta^{13}C_{org}$

compositions considered in this sensitivity test, halving the total estimated C burial flux (to ~0.3GtC/yr) results in sustained OCMARS required across Neogene circum-Pacific basins that are still higher than most OCMARs observed anywhere in the SBB, and that are between ~5-10 times larger than the OCMARS observed in syn-MCO SBB strata. As such, we suggest that even for a range of potential $\delta^{13}C_{in}$, $\delta^{13}C_{org}$, and global carbon burial fluxes, organic carbon burial in the Monterey Formation and similar circum-Pacific basins along cannot explain the ~1‰ marine $\delta^{13}C$ shift of the Monterey Event.

* * *

REFERENCES, APPENDIX 3

Farrell, J.C., 2020, Lateral Variation of Fine-Grained, Organic-Rich Sediments of the Miocene Monterey Formation, Belridge Field Area, California [Masters thesis]: California State University, Long Beach, 81p.

Graham, S.A. and Williams, L.A., 1985, Tectonic, depositional, and diagenetic history of Monterey Formation (Miocene), central San Joaquin basin, California: AAPG bulletin, 69(3), p. 385-411. doi:https://doi.org/10.1306/AD4624F7-16F7-11D7-8645000102C1865D

Li, Z., Zhang, Y.G., Torres, M. and Mills, B.J., 2023, Neogene burial of organic carbon in the global ocean: Nature, 613(7942), p.90-95. doi:https://doi.org/10.1038/s41586-022-05413-6

Scheirer, A. H., & Magoon, L. B. (2007). Age, distribution, and stratigraphic relationship of rock units in the San Joaquin Basin Province, California. *Petroleum systems and geologic assessment of oil and gas in the San Joaquin Basin province, California: US Geologic Survey Professional Paper*.

Schwartz, D.E., 1988, Characterizing the lithology, petrophysical properties, and depositional setting of the Belridge diatomite, South Belridge field, Kern County, California, *in* Graham, Sephan A., (ed.), Studies of the Geology of the San Joaquin Basin: Pacific Section SEPM, 60, p. 281-301.

Vincent, E. and Berger, W.H., 1985, Carbon dioxide and polar cooling in the Miocene: The Monterey hypothesis: The carbon cycle and atmospheric CO2: Natural variations Archean to present, *32*, p. 455-468. doi:https://doi.org/10.1029/GM032p0455

* * *